Reduced Dimensional Modeling of the Entire Human Lung

Mahmoud M. Ismail

Bericht Nr. 19 (2014)
Lehrstuhl für Numerische Mechanik
Professor Dr.-Ing. Wolfgang A. Wall
Technische Universität München

ISBN 978-3-00-046790-5

Berichte können bezogen werden über:

Lehrstuhl für Numerische Mechanik
Technische Universität München
Boltzmannstrasse 15
D-85747 Garching bei München
http://www.lnm.mw.tum.de

Alle Rechte, insbesondere das der Übersetzung in andere Sprachen, vorbehalten. Ohne Genehmigung des Autors ist es nicht gestattet, dieses Buch ganz oder teilweise auf photomechanischem, elektronischem oder sonstigem Wege zu kommerziellen Zwecken zu vervielfältigen.

All rights reserved. In particular the right to translate the text of this thesis into another language is reserved. No part of the material protected by this copyright notice may be reproduced or utilized in any form or by any means, electronic or mechanical, including photocopying, recording or by any other information storage and retrieval system, without written permission of the author.

TECHNISCHE UNIVERSITÄT MÜNCHEN

Lehrstuhl für Numerische Mechanik

Reduced Dimensional Modeling of the Entire Human Lung

Mahmoud M. Ismail

Vollständiger Abdruck der von der Fakultät für Maschinenwesen der Technischen Universität München zur Erlangung des akademischen Grades eines

Doktor-Ingenieurs (Dr.-Ing.)

genehmigten Dissertation.

Vorsitzender: Univ.-Prof. Dr.-Ing. Michael W. Gee

Prüfer der Dissertation:

1. Univ.-Prof. Dr.-Ing. Wolfgang A. Wall
2. Prof. Perumal Nithiarasu, Ph.D.
   Swansea University, Swansea / UK

Die Dissertation wurde am 05.03.2014 bei der Technischen Universität München eingereicht und durch die Fakultät für Maschinenwesen am 25.06.2014 angenommen.

Abstract

In 2008, the American Lung Association released a report showing that deaths due to lung diseases are increasing whilst deaths due to other diseases such as heart and cancer are declining.

Many factors, including mechanical factors, make lungs susceptible to a wide range of diseases, both in everyday life and in the intensive care unit. Despite the plethora of research, the precise dynamics of mechanical failure of the lung still remains to be fully elucidated. For example, Acute Lung Injury (ALI) and Acute Respiratory Distress (ARDS) patients are associated with high mortality rates due to mechanical failure caused by mechanical ventilation. Unfortunately, these rates remain high even when preventative measures are taken.

A major challenge of understanding lung mechanics lies in the inhomogeneous nature of lung damage. This leads to difficulties in identifying which of the mechanical factors are responsible for the damage. As such, the aim of this work was to develop a reduced dimensional *in silico* model of the entire human lung that can measure mechanical variations and oxygen ventilation within the lungs at levels *in vivo* and *ex vivo* methods cannot reveal. Thereby, it aims to a better understanding of lung mechanics and improve the diagnosis of lung failure.

For this purpose, the lung is modeled as a whole by including the entire respiratory and circulatory systems. The respiratory system starts at the tracheal inlet and ends at the peripheral alveoli, which in turn are inter-dependent due to the physical attachments between them. The pulmonary circulatory system considers the entire path of blood starting from the pulmonary valve, passing through pulmonary capillaries and ending in the main pulmonary vein. Finally, the two systems are coupled at the alveolar level to facilitate the consistent consideration of inhomogeneous O_2 exchange, thereby allowing for a previously unachieved level of modeling detail and precision.

The novelty of this work is achieved by developing the only comprehensive entire lung model based on patient-specific anatomy. While the lung geometry and the major airways are segmented from a patients computer tomography images, the unsegmentable airways are predicted using a pre-existing volume filling approach. The alveoli and the acini are generated in an inverse manner using novel 0D acinar and parenchymal models. The inter-acinar neighborhoods are detected using a brute force search algorithm, while the pulmonary veins and arteries are generated using novel anatomic-based algorithms. The first 4 generations of the conducting airways are modeled using 3D flow models wheres as the remaining sections of the lungs are modeled using reduced-dimensional (reduced-D) models. The reduced-D models include pre-existing 1D and novel 0D models. The coupling between the 3D and reduced-D domains is achieved via a novel method that guaranteed stability and pressure matching at the coupling interface. Furthermore, the circulatory and the respiratory system are coupled by detecting which capillaries belong to which acini. In this way, consistent O_2 transport between air and blood is achieved.

All novel generated lung components and models are derived mathematically, fitted to physiological measurements and investigated intensively. The various lung components are shown to match the measurements reported in anatomy, morphology and physiology.

Finally all of the lung components are assembled together into one entire-lung framework and investigated under various external conditions and lung health stages. The simulated results showed a deeper insight into local phenomena such as hypoxia, volume competition between neighboring acini and volutrauma at a level never achieved before. Thus paving the way to optimizing mechanical ventilation techniques that reduce mechanical damage without compromising the oxygen delivery to various sections of the lung.

Zusammenfassung

Im Jahre 2008 hat die amerikanische Lungen-Organisation (American Lung Association) einen Bericht veröffentlicht, laut dem die Sterblichkeitsrate durch Lungenkrankheiten stetig zunimmt, während sich die Sterblichkeitsrate durch andere Krankheiten (Herz, Krebs etc.) immer weiter verringert.

Bedingt durch zahlreiche (unter anderem auch mechanische) Faktoren ist die menschliche Lunge empfindlich für eine weite Bandbreite an Krankheiten, sowohl im alltäglichen Leben, als auch auf der Intensivstation.

Trotz intensiver Forschung ist es uns bis heute nicht gelungen, die präzise Dynamik des mechanischen Lungenversagens zu erforschen. Zum Beispiel weisen Patienten mit akuter Lungenverletzung (ALI) oder akutem Atemnotsyndrom (ARDS) eine extrem hohe Sterblichkeitsrate durch das Versagen von mechanischen Ventilationsgeräten auf. Trotz diverser präventiver Manahmen bleiben diese Raten ungewöhnlich hoch.

In der inhomogenen Natur des Lungendefektes liegt die wesentliche Herausforderung zum tiefgründigen Verständnis der Lungenmechanik. Die Identifizierung der mechanischen Faktoren, die für den jeweiligen Defekt verantwortlich sind, bleibt daher weiterhin schwierig. Ziel dieser Dissertation ist deshalb ein multiskalares in silico-Modell der gesamten menschlichen Lunge zu entwickeln, welches es erlaubt, die mechanischen Variationen und die Sauerstoffventilation innerhalb der Lunge präziser als mit den gängigen in vivo- und ex vivo- Methoden messen zu können und somit zu einem besseren Verständnis der Lungenmechanik allgemein und zu einer verbesserten Diagnose von Lungenkrankheiten im Besonderen beizutragen.

Hierfür wurde die Lunge als Ganzes inklusive ihrer respiratorischen und zirkulatorischen Systeme modelliert. Das respiratorische System verläuft vom Trachealeingang bis hin zur peripheren Alveoli, die durch physikalische Vorgänge miteinander verbunden sind. Das pulmonalzirkulatorische System besteht aus den Blutbahnen und verläuft von der Pulmonalklappe durch die Pulmonalkapillaren bis hin zur Hauptpulmonalvene. Durch die Kuppelung der beiden Systeme auf Höhe der Alveole kann der inhomogene Sauerstoffaustausch im Modell berücksichtigt und somit ein bis dato nicht erreichtes Level an Präzision und Detail erzielt werden.

Diese Dissertation stellt das erste einheitliche Lungenmodell vor, welches die spezifische Anatomie von Patienten berücksichtigt. Hierfür wurden die Geometrie der Lunge und ihre Hauptatemwege anhand von Computertomograhiebildern eines Patienten segmentiert. Die nicht segmentierbaren Atemwege wurden durch eine bereits existierende Annäherung der Volumenfüllung berechnet.

Die Alveoli und Azini wurden im Umkehrverfahren durch neuartige 0D azinäre und parenchymale Modelle errechnet. Die interazinären Gegenden wurden durch einen Brachialgewalt-Suchalgorithmus ermittelt und die Pulmonalvenen und arterien durch neuartige -auf die Anatomie basierende- Algorithmen generiert. Die ersten vier Generationen der leitenden Atemwege wurden anhand von 3D-Strömungsmodellen modelliert, während die restlichen Lungenabschnitte anhand von reduzierten dimensionalen (reduced-D) Modellen modelliert wurden. Die reduzierten D-Modelle bestehen aus bereits existierenden 1D- und neuartigen 0D-Modellen. Die Kupplung der 3D mit den reduzierten D-Domänen wurde durch eine neuartige Methode erzielt, bei der die Stabilität und der Druck an dem Kupplungsrand angeglichen werden konnte. Durch das Ermitteln der Kapillaren, die zu den Azini gehören, konnten die zirkulatorischen und respiratorischen Systeme miteinander verbunden werden. Auf diese Art und Weise konnte der konstante O_2-Transport durch Luft und Blut sichergestellt werden.

Alle neukonzipierten Modelle wurden mathematisch abgeleitet, intensiv geprüft und stimmen mit den physiologische Messwerten überein. Die Modelle der diversen Lungenkomponenten stimmen mathematisch mit den bekannten Messwerten aus der Anatomie, Morphologie und Physiologie überein. Zu aller Letzt wurden alle Komponente in ein ganzheitliches Lungenmodell zusammengefügt und unter diversen externen Bedingungen und verschiedenen Gesundheitsstadien der Lunge geprüft. Die simulierten Resultate geben eine bisher nicht erreichte Einsicht in lokale Phänomene wie die Hypoxie, die Volumenkonkurrenz zwischen benachbarten Azini und Volumentrauma. Schlussendlich ebnet diese Dissertation den Weg für die Optimierung von mechanischen Ventilationstechniken ohne die Sauerstoffzufuhr in die verschiedenen Lungenregionen zu gefährden.

”You are every image, and yet
I’m homesick for you.”
- Jalal ad-Din Muhammad Rumi, 13th century

To my parents and my siblings

Acknowledgment

”The smallest act of kindness is worth more than the grandest intention.”

- Oscar Wilde

First of all, I would like to thank my supervisor Prof. Dr.-Ing. Wolfgang A. Wall for the opportunity to become a member of the Institute for Computational Mechanics (LNM) and for giving me the chance to delve into my favorite topic.

What made my time at LNM so special is the amazing work culture and the excellent coffee machine that kept us awake when facing crucial deadlines. I therefore wish to express my gratitude to all of my colleagues in the past five and a half years who were always willing to help me and turned my stay at LNM into a constant learning experience. I would not have achieved this PhD without you. Special thanks go to: Dr.-Ing. Lena Yoshihara and Dr. Andrew Comerford for the fruitful discussions, positive feedback and for being my mentors. Dr.-Ing. Volker Gravemeier for supervising my work on inflow conditions in fluid mechanics. Mr. M. Hamman de Vaal for the valuable technical and linguistic remarks on this manuscript and for introducing me to *The Far Side* comics. Mr. Sudhakar Yogaraj for helping me with MetaPost and structuring my thoughts. Dr.-Ing. Peter Gamnitzer for his patience and the enormous help with LNMs in-house code *BACI*. Dr.-Ing. Andreas Maier for being a great office mate, an amazing mountain biking partner and for the best *Steckerlfisch* I ever had. Ms. Renata Nagl for her precious help with tons of bureaucracy and her tips on healthy lifestyle.

I further wish to thank: Prof. Dr.-Ing. Kai-Uwe Bletzinger for recommending me to the LNM. Prof. Dr.-Ing. Michael W. Gee for supervising part of my work on vascular mechanics and for accepting to be the head of my PhD examination committee. Prof. Perumal Nithiarasu, Ph.D, for accepting, along with Prof. Dr.-Ing. Wall, to be the referee of this work and for traveling all the way from Swansea to take part in my PhD defense. My students Mr. Ali Azizi for his great help with setting up the LNM’s firewall, Ms. Ilona Trübswetter for her help with segmenting 1D and 3D human arterial networks, and Mr. Moritz Werb for the many discussions on transport of Oxygen in pulmonary systems.

Finally, I wish as well to express my gratitude to my dearest friends and beloved ones: Ms. Electra Stavropoulou and Mr. Majid Hojjat for their ongoing support and inspiring discussions on Fluid-Structure Interaction, Adjoint methods or Finite-Element methods during our countless cooking sessions. Dr.-Ing. Amin Moosaie for sharing his profound knowledge on Fluid Mechanics, which he gladly explained each time we had a cup of tea together. Mr. Ramses Sala for the best *Kaiserschmarrn* recipe and for the countless discussions on how to not to give up and successfully survive a PhD thesis. Mr. Omran Al-Zoubi, (Trauma Surgeon) and Mr. Samer Al-Barazanchi, (Radiologist) for all the *One-Pan Roast Chicken and Potatoes* and for the countless nights spent on discussing human anatomy/physiology, which formed my core understanding of pulmonary physiology. Ms. Nina Stolle for her constant support, her corrections and for generously treating me with my favorite chocolates.

Last but not least, I wish to express my highest gratitude to my siblings for their support and to my parents for their enormous sacrifices, patience and endless support, that brought me to where I am today.

Munich, August 2014 Mahmoud M. Ismail

Contents

1. Introduction 3
   1.1. History and motivation 3
   1.2. Anatomy and physiology of the human lung 6
   1.3. Modeling approach 11

2. Geometry 15
   2.1. 3D airway and lung geometry 15
   2.2. Conductive airways 17
   2.3. Respiratory airways 18
      2.3.1. Acini 18
      2.3.2. Inter-acinar tissue 22
   2.4. Pulmonary blood vessels 25
      2.4.1. Generate nodal translation vectors 26
      2.4.2. Generate pulmonary arteries 26
      2.4.3. Generate pulmonary veins 27
      2.4.4. Generate pulmonary capillaries 27
   2.5. Oxygen exchange interface 32

3. Mathematical formulations 39
   3.1. 3D fluid domains 39
   3.2. 1D pipe flow domain 41
      3.2.1. Conservation of mass 42
      3.2.2. Balance of momentum 43
      3.2.3. Wall mechanics 43
      3.2.4. Compatibility conditions (characteristic variables) 44
      3.2.5. Boundary conditions 46
   3.3. 0D pipe flow domain 49
      3.3.1. Conservation of mass 50
      3.3.2. Wall mechanics 50
      3.3.3. Balance of momentum 51
   3.4. 0D alveolar domain 51
      3.4.1. 0D alveolar duct 52
      3.4.2. 0D acinus 53
   3.5. 0D inter-acinar tissue 53
   3.6. 1D scalar transport 55
      3.6.1. Boundary conditions and junctions 56
   3.7. Oxygen exchange interface 57

3.8. Coupling of multi-dimensional fluid domains . . . 58

4. Parameter identification 63
4.1. Ventilatory system . . . 63
4.1.1. Conductive airways . . . 63
4.1.2. Respiratory airways (0D acinar model) . . . 73
4.1.3. Inter-acinar dependencies . . . 77
4.2. Pulmonary circulatory system . . . 87
4.2.1. Pulmonary capillary networks . . . 87
4.2.2. Pulmonary arteries and veins . . . 87
4.3. Oxygen transport . . . 88
4.3.1. O_2 concentration in air . . . 89
4.3.2. O_2 concentration in blood . . . 89
4.3.3. Model validation of the oxygen transport . . . 90
4.4. Coupling 3D and reduced-D domains . . . 92
4.4.1. Treatment of inertial effects in airflow (towards a matching boundary pressure) . . . 96

5. The Entire Lung Model 109
5.1. Relaxed spontaneous breathing . . . 110
5.1.1. Respiratory system . . . 110
5.1.2. Circulatory system . . . 111
5.1.3. Oxygen transport . . . 114
5.2. Mechanical ventilation - Supine position . . . 115
5.2.1. Respiratory system . . . 116
5.2.2. Oxygen transport . . . 117
5.3. Coupled 3D/0D ventilatory system . . . 117

6. Summary and Discussion 125
6.1. Comprehensive model of the human . . . 125
6.2. Anatomically representative model . . . 125
6.3. Parameter identification and physiological results . . . 126
6.4. Deeper insight into regional ventilation, volume competition and heterogeneities 127
6.5. Prediction of volutrauma and hypoxia . . . 127
6.6. Stability of coupled 3D/reduced-D problems and boundary pressure matching . 128

7. Outlook and Limitations 129
7.1. Outlook . . . 129
7.2. Limitations . . . 130

A. Numerical discretization of the 3D flow domain 133

B. Numerical discretization of 1D pipe flow domain 135

C. Numerical discretization of 0D pipe flow domain 137

D. Numerical discretization of 0D parenchyma domain **139**
D.1. 0D acinus 139
D.2. 0D inter-acinar linker 140

E. Numerical discretization of 0D impedance tree domain **141**

F. Radial mapping of a non-circular convex surface to circular surface **143**

Nomenclature

General styles for scalars, vectors and tensors

u, U	Scalar values
$\mathbf{x}$, $\mathbf{n}$	Vector values

Operators

$\|\cdot\|_2$	Second norm
$\|\cdot\|_{\mathrm{L}_2}$	L_2 norm
$\times$	Cross or vector product
$\langle\cdot,\cdot\rangle$	Dot, scalar or inner product
$(\bar{\cdot})$	Time averaged value
$(\tilde{\cdot})$	Length averaged value

Domains and boundaries

Γ	Surface boundary
∂S	Curve boundary
Ω	Spatial domain

0D pipe flow domain

C	Capacitance
I	Inductance
R	Resistance

1D pipe flow domain

A	Area
α	Momentum correction factor
β	Wall stiffness constant
c	Characteristic wave speed
E	Young's modulus of elasticity
f	Wall shear forces
F	Total external forces
γ	Velocity profile power constant
h	Wall thickness
l	Length
$\mathbf{L}$	Eigenvalue matrix
Λ	Eigenvalue vector
λ	Eigenvalue
μ	Dynamic viscosity
P	Space averaged dynamic pressure
ψ	Pressure area algebraic relationship
Q	Flow rate
r	Radial coordinate
R	Radius
R_{f}	Wave reflection factor
ρ	Fluid density
s	Curve scalar coordinate value
W	Riemann wave speed
$\mathbf{W}$	Pseudo-characteristic Riemann waves
u	Velocity
U	Space averaged velocity
x	Straight scalar coordinate value

3D fluid domain

ε	Rate of deformation tensor
$\mathbf{f}$	Body forces
$\mathbf{h}$	Neumann boundary condition
ν	Fluid kinematic viscosity
p	Scalar kinematic fluid pressure
Re	Reynolds number
$\mathbf{u}$	Cartesian velocity vector

1D scalar transport

c_{s}	Scalar transport concentration
D	Diffusion coefficient

Oxygen exchange interface

$A^{\mathrm{I}}_{\mathrm{O}_2}$	Oxygen interface surface area
$h^{\mathrm{I}}_{\mathrm{O}_2}$	Oxygen interface wall thickness
$D^{\mathrm{I}}_{\mathrm{O}_2}$	Oxygen diffusion constant
$D^{\mathrm{I}}_{\mathrm{T}}$	Total interface oxygen diffusion constant
Q_{O_2}	Oxygen flow rate

Superscripts and subscripts

$(\cdot)^{\mathrm{air}}$	Air
$(\cdot)^{\mathrm{bld}}$	Blood
$(\cdot)_{\mathrm{D}}$	Dirichlet
$(\cdot)^{\mathrm{e}}$	Elastic
$(\cdot)^{\mathrm{ext}}$	External
$(\cdot)^{\mathrm{F}}$	Fluid
$(\cdot)^{\mathrm{Hb}}$	Hemoglobin
$(\cdot)^{\mathrm{I}}$	Interface
$(\cdot)_{\mathrm{in}}$	At inflow
$(\cdot)^{n}$	Time step n
$(\cdot)_{\mathrm{n}}$	Normal
$(\cdot)_{\mathrm{N}}$	Neumann
$(\cdot)_{\mathrm{O}_2}$	Oxygen
$(\cdot)_{\mathrm{out}}$	At outflow
$(\cdot)_{\mathrm{s}}$	Reduced dimensional structure
$(\cdot)^{\mathrm{S}}$	Structure
$(\cdot)^{\mathrm{v}}$	Viscous

Acini

a	Edge length of an octahedron
α	Ratio of alveolar volume over parenchymal volume
A_{duct}	Duct area of an alveolar duct
A_{oct}	Area of an octahedron
B	Alveolar duct viscosity
B_{a}	Alveolar duct airway resistance
d	Distance
E_1	Alveolar duct elastance
E_2	Alveolar duct associated visco-elastance
K_{ac}	Acinar volumetric stiffness
N_{ad}	Number of alveolar duct
$N_{\text{Oct}}^{\text{Duct}}$	Number of octahedra per duct of an alveolar duct
P_{intr}	Intra-pleural pressure
P_{tp}	Transpulmonary pressure
r_{i}	Radius of an acinus i
r_{ij}	Sum of radii of acini i and j
V_{ac}	Volume of an acinus
V_{alv}	Total volume of alveoli
V_{duct}	Total duct volume of respiratory airways
V_{par}	Total volume of parenchyma
V_{tis}	Total volume of parenchymal tissue
V^{LB}	Volume of a lung lobe
$V_{\text{ac}}^{\text{LB}}$	Total air volume of the lobar acini
$V_{\text{alv}}^{\text{LB}}$	Total air volume of the lobar alveoli
$V_{\text{par}}^{\text{LB}}$	Total volume of the lobar parenchyma
ζ	Ratio of duct volume over alveolar volume

Blood vessels

$\mathbf{a}_i$	Arterial translation vectors
$\mathbf{m}_i$	Nodal coordinate of a vein junction
r_{art}	Radius of an artery
r_{art_0}	Radius of the main pulmonary artery
r_{ven}	Radius of a vein
r_{ven_0}	Radius of the main pulmonary vein
V_{blood}	Total volume of blood vessels
$\mathbf{v}_i$	Venous translation vectors
$\mathbf{w}_i$	Airway translation unit vectors

Capillaries

α_{dp}	Ratio of daughter to parent radius
lr_{a}	Length to radius ratio of arterioles
L_{a}	Length of an arteriole
lr_{v}	Length to radius ratio of venules
L_{v}	Length of a venule
r_{d}	Radius of a daughter capillary
r_{p}	Radius of a parent capillary
r_{ter}	Terminal arteriole radius
$\hat{r}_{\mathrm{ter}}$	Actual terminal arteriole radius
r_{va}	Ratio of venule radius over arteriole radius
V_{a}	Total volume of arterioles in a capillary network
V_{a_0}	Total volume of root arteriole in a capillary network
V_{cap}	Volume of a capillary network
V_{v}	Total volume of venules in a capillary network
V_{v_0}	Total volume of root venule in a capillary network
ξ	Murray's power constant

Conductive airways

$A_{\mathrm{t}}^{\mathrm{l}}$	Total area of terminal conducting airways in a lobe
$\hat{A}_{\mathrm{art}}^{\mathrm{G}}$	Average area of all arteries with the same generation number
$\hat{A}_{\mathrm{ven}}^{\mathrm{G}}$	Average area of all veins with the same generation number
$\mathrm{AW}_{i,j}$	Airway located between nodes i and j
G	Airway generation number
l_{t}	Maximum length of terminal airways
$\mathbf{n}_{\mathrm{br}_i}$	Vector from terminal of a parent airway to centroid of a daughter sub-volume
$\mathbf{n}_{\mathrm{pc}_i}$	Vector from terminal of a parent airway to centroid of a parent sub-volume
$\mathbf{n}_{\mathrm{SP}_i}$	Normal of a split plane
$\hat{r}_{\mathrm{art}}^{\mathrm{G}}$	Average radius of all veins with the same generation number
$\hat{r}_{\mathrm{art}}^{\mathrm{G}}$	Average radius of all arteries with the same generation number
r_{aw}	Radius of an airway
r_{t}	Maximum radius of terminal airways
$\mathbf{u}_i$	Unit direction vector of an airway branch
$\hat{V}_{\mathrm{art}_{\mathrm{T}}}$	Total volume of arteries
$V_{\mathrm{art}_{\mathrm{T}}}$	Total volume of patient's arteries
V_{aw}	Total volume of conducting airways
V_{lung}	Total volume of a lung volume
$V_{\mathrm{ven}_{\mathrm{T}}}$	Total volume of patient's veins
$\hat{V}_{\mathrm{ven}_{\mathrm{T}}}$	Total volume of veins
$\mathbf{x}_{\mathrm{c}_i}$	Centroid of a lobar sub-volume

Abbreviations

0D	Zero-dimensional
1D	One-dimensional
3D	Three-dimensional
Ac	Acinus
AD	Alveolar duct
ALI	Acute lung injury
ARDS	Acute respiratory distress syndrome
AS	Alveolar sac
BL	Bronchiole
BR	Bronchus
CO_2	Carbon dioxide
CT	Computer tomography
FRV	Functional residual volume
Hb	Hemoglobin
ICU	Intensive care unit
LA	Left atrium
LB	Lung lobe
LV	Left ventricle
MV	Mechanical ventilation
O_2	Oxygen
PEEP	Positive end expiratory pressure
PV	Pressure volume
RA	Right atrium
RBL	Respiratory bronchiole
RBVMM	Residual-based variational multiscale finite element method
Re	Reynolds number
Reduced-D	Reduced-dimensional
RTV	Residual tidal volume
RV	Residual volume
SP	Splitting plane
SV	Sub-volume
TBL	Terminal bronchiole
TLC	Total lung capacitance
TLV	Total lung volume
TV	Tidal volume
VALI	Ventilator associated lung injury
VC	Vital capacitance
VILI	Ventilator induced lung injury
ZEEP	Zero end expiratory pressure

1. Introduction

> ”The substance of the lung is dilatable and extensible like the tinder made from a fungus. But it is spongy and if you press it, it yields to the force which compresses it, and if the force is removed, it increases again to its original size.”
>
> - Leonardo da Vinci, late 15th century

1.1. History and motivation

Lungs are organs whose main function is gas exchange between the outside atmosphere and the living organism’s internal circulatory system. Their mechanics has received considerable attention both experimentally and computationally. However despite this plethora of research the precise dynamics still remains to be fully elucidated. On average, a human being takes over 500 million breaths throughout his/her lifespan, inhaling over 250 million liters of air. Without oxygen no living being can survive. But why is breathing so vital for humans? and why is their mechanics of such importance?

The study of pulmonology goes back to the ancient Greeks who believed that the lungs were like bellows cooling down or heating up the heart. The heart was considered as a furnace set on fire the moment a living being is born and put off the moment a living being dies [59]. The aforementioned Galenic assumption lasted for more than 1.5 millennia until the mid 17th century, outlasting the Islamic golden era and Europe’s dark ages. In *The Canon of Medicine*[1], Avicenna described blood as being heated by the *bilious humor* coming from the whole body and that the gaseous products within the *bilious humor* are the reason behind the accumulation of moisture in lungs [55]. The Galenic definition of the lung was so embedded that no one could think outside of it until an English chemist called John Mayow discovered in the 17th century the first evidence of oxygen (O_2), which he named *ingeo-aereal particles* [75]. Mayow made his discovery after he noticed that a mouse or a sparrow would die shortly after it was trapped in a jar to which fresh air was prevented. However, he failed to recognize the role of carbon dioxide (CO_2) in breathing, which was discovered earlier by the Belgian chemist Jan Baptist van Helmont. A century after Mayow, Antoine Lavoisier, a French chemist, successfully described the chemistry of respiration as is known today [34]. Together with Pierre-Simon Laplace, Lavoisier designed a calorie meter thanks to whom they concluded that respiration is in fact a slow combustion process, in which O_2 is inhaled and combusted to produce CO_2 which in turn is exhaled. Lavoisier’s only mistake, he assumed the combustion process took place in the pulmonary bronchioles.

In the past century, many works were dedicated to investigate pulmonology down to the cell level. However, when it comes to understanding the various causes of pulmonary diseases and developing effective treatments, many gaps still need to be bridged. A recent report released by the American Lung Association showed that deaths due to lung diseases are increasing while deaths due to other diseases such as heart and cancer are declining [4]. Thus again emphasizing how complex lungs are and how susceptible they are to a wide range of diseases, both in everyday life and in the intensive care unit. For example, pulmonary diseases might lead to Acute Lung Injury (ALI), asthma, or Acute Respiratory Distress Syndrome (ARDS). ALI and ARDS are of particular interest to this work since it is hypothesized that they can be caused due to Ventilatory Associated Lung Injury (VALI), i.e. a mechanical insult to the lung [115]. Recent statistics showed that 7% of all Intensive Care Unit (ICU) patients and 16% of all mechanically ventilated patients suffer from ARDS, with mortality rates of 49% and 58% for ALI and ARDS, respectively [142]. Such high mortality rates led to two open questions, that might pave the way to better understanding of these diseases and improve their treatments: firstly, how flow and pressure vary through the lung? i.e. how to properly ventilate human lungs. Secondly, how the different levels of the lung interact with each other? i.e. how to minimize lung damage? [4]

---

[1] *The Canon of Medicine* was taught in Europe untill the mid 17th century.

ALI and ARDS (most severe form of ALI) are life-threatening pulmonary diseases that have a form of an inflammatory response to direct and indirect insults to the lung. Both ALI and ARDS are characterized by severe hypoxemia, hypercapnia, diffuse infiltration in the chest X-ray, and a substantial reduction in pulmonary compliance [115]. Patients with ALI and ARDS cannot breathe by themselves and are thus assisted via Mechanical Ventilation (MV). However, MV can cause VALI, which can accelerate the lung damage through triggering a pulmonary systematic inflammatory reaction [115]. While ventilated ARDS and ALI patients can suffer from VALI, VALI can also induce ALI and ARDS in patients through mechanical insults such as baro-trauma due to Zero End Expiratory Pressure (ZEEP) [4], volutrauma due to ventilating with high Tidal Volume (TV) [113; 117; 141], cyclic collapse of the peripheral airways [32], biotrauma due to inflammatory mediators release by shear stress [18] and O_2-toxiticy [20]. Indeed, reducing the aforementioned mechanical factors via preventive MV techniques significantly reduced mortality rates among ARDS patients from 39% to 30% [4]. Such techniques involved lowering TV, using Positive End Expiratory Pressure (PEEP), and/or using pressure-release ventilators [4]. However 30% mortality rate is nonetheless very high.

Many *in vivo* and *ex vivo* experiments aimed to pave a better understanding of the nature of lung damage. However, reproducing the lung behavior in an *ex vivo* environment or measuring lung damage in an *in vivo* environment was shown to be a big challenge. That is because the damage of ventilated ill lungs has an inhomogeneous nature [24] and occurs at very small scale within the peripheral regions. This made it difficult to identify or reproduce the mechanical factors that are responsible for the progression of lung damage. The inhomogenities also added another challenge of how to properly ventilate patients such that the lung damage is minimized while the oxygen delivery to the various regions of the lungs is not compromised.

Alternative experiments to those of *in vivo* and *ex vivo* were achieved via *in silico* patient-specific models. Such models have been recently successfully utilized for understanding various complex biological phenomena. For instance, computational methods successfully gave a better insight into biomechanics [14; 47; 65; 132; 149; 150], tuned and reproduced patient-specific measurements [12; 67], predicted unmeasurable internal stresses [45; 47; 117], predicted whether patients require surgical interventions [88–90; 94; 116; 120], improved medical devices [36; 44; 112], improved drug delivery [21; 76; 77; 165–167], and pre-planned surgeries [138].

In lungs computational methods were used successfully to predict local phenomena and gave more insight into immeasurable inhomogeneties [7; 22; 48; 50; 66; 85–87; 131; 160], investigated flow patterns and turbulent effects [23; 82], modeled lung parenchyma [117–119; 129; 157; 158] and airway tissue [70; 130]. However, most of the *in silico* models focused either on a small section of the lung or on impedance analysis and pressure-volume (PV) curves of the lung [7; 8; 50; 57; 85; 105; 130], thus a limited spatial representation of the lung ventilation was achieved.

As such the aim of this work is to develop a unique comprehensive patient-specific *in silico* model of the entire human lung. The purpose of this model is to reproduce the patient-specific pulmonary physiology and to capture both local and global pulmonary phenomena with affordable computational costs. Thus giving a deeper insight into the patient's pulmonary physical and physiological state. And by that improve the understanding of how damage progresses and leads to reduction in O_2 ventilation (i.e. hypoventilation). In hope to improve mechanical ventilation techniques and reduce mortality rates.

The novelty of this work was achieved by developing the only comprehensive entire lung model based on patient-specific anatomy that included the entire pulmonary circulatory and respiratory systems. Furthermore, the O_2 transportation is integrated into the entire lung model to show for the first time how O_2 is delivered to the various regions of the lung in health and disease.

The model is achieved through a sum of previously published (and in-press) works of the author that started by developing the first detailed respiratory system of the healthy human lungs in [66]. The author successfully showed the spatial representation of pressure and flow in the respiratory system. The entire respiratory system was composed of 3D, 0D, and coupled 3D/0D airway trees, modeling the entire respiratory system from the tracheal inlet until the peripheral alveoli. The author has then observed that the consistent stable 3D/0D coupling approach in [66] resulted in pressure mismatch. This was thus resolved in a novel manner by the author et al. in [68], where for the first time a full coupled 3D/0D respiration was achieved. The respiration incorporated both inspiration and expiration and resulting in a matching pressure at the coupling boundary and physiological flow rates. Furthermore, the author observed that the inter-acinar dependencies within all of the pre-existing models were only achievable via the airway trees, i.e. via pendelluft flows [58]. Together with others, the author developed a novel inter-acinar dependency model in [69]. Considering the inter-acinar dependencies, the author successfully simulated the entire lung while applying the pleural pressure only onto the sub-pleural acini and successfully captured neighboring acini competing for pleural volume. The author also showed that neighboring acini became more competitive in mechanically ventilated lungs and even more competitive in mechanically ventilated ill lungs. Finally, the author developed a novel method to generate pulmonary circulatory system using the geometry of the respiratory system and incorporated it in an entire lung model with 1D O_2 transport model. The respiratory and the pulmonary circulatory systems were merged together within one novel frame work, thanks to which spatial distribution of O_2 and O_2-toxicity were investigated under different external conditions and lung health states.

1.2. Anatomy and physiology of the human lung

Developing a comprehensive model of the entire human lung required a proper knowledge of the pulmonary anatomy and physiology. In this section the lung is divided into two systems, the respiratory and the circulatory system. Thus distinguishing between the regions through which air flows and the regions through which blood flows. In addition to that, the O_2 exchange interface and its physiology are distinguished.

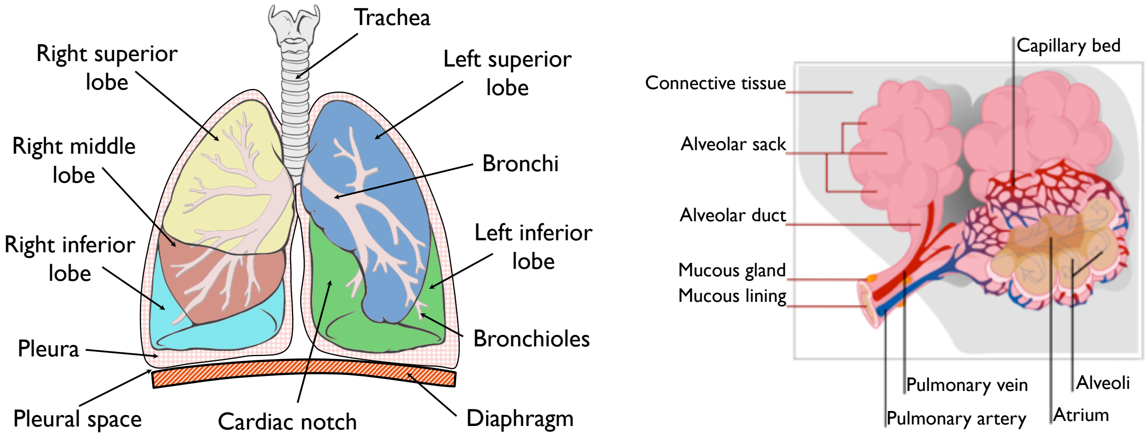
Trachea
Right superior lobe
Left superior lobe
Right middle lobe
Bronchi
Left inferior lobe
Right inferior lobe
Bronchioles
Pleura
Pleural space
Cardiac notch
Diaphragm
Capillary bed
Connective tissue
Alveolar sack
Alveolar duct
Mucous gland
Mucous lining
Pulmonary vein
Alveoli
Pulmonary artery
Atrium

(a)

(b)

Figure 1.1.: Two diagrams showing (a) the anatomy of human lungs[2] and (b) the anatomy of lung parenchyma at the alveolar level.

Anatomically lungs are part of, both, the respiratory system and the circulatory system. A healthy human being has two lungs; see Figure 1.1(a). The right lung is composed of a three lobes whereas the left lung is composed two lobes. Furthermore, the left lung has a hollowed section called the a cardiac notch, where the heart is positioned. Both lungs are covered by a pleura, which is a serous membrane surrounded by the pleural space. The pleural space (or the thoracic cavity) is a cavity bounded mainly by the rib cage and the diaphragm. The pressure inside the pleural cavity of a healthy human being is mostly negative. Under healthy conditions, the pleural pressure varies between $-2\,\mathrm{cmH_2O}$, at peak forced expiration, and $-30\,\mathrm{cmH_2O}$ at total lung volume/capacitance (TLV/TLC). The negative pleural pressure keeps the lungs inflated all the time and prevents them from collapsing. As matter of fact, under normal conditions, humans are not able to deflate their lungs beyond the residual volume (RV), which in a healthy adult human ranges between 1 and 1.5 liters. At rest conditions, healthy adult humans have 2.5 to 3.5 liters of air in their lungs, which is called the functional residual volume (FRV). During spontaneous breathing, a healthy adult human being has a pleural pressure varying from $-8\,\mathrm{cmH_2O}$ at end expiration to $-5\,\mathrm{cmH_2O}$ at peak inspiration. Table 1.1 shows in detail the volume of air versus the pleural pressure in healthy adult human lungs. During inhalation, the rib cage and/or the diaphragm expand the pleural cavity. The expansion in the pleural cavity decreases the pleural pressure, which in turn leads to expansion of the lungs and thus the inhalation of air. During expiration, the rib cage and/or the diaphragm collapse the pleural cavity, which intern increases the pressure inside the pleural space and thus air is forced outside the lung by the recoil forces inside the lung tissue. At rest conditions, a healthy adult inhales roughly $0.5\,\mathrm{l}$ of air per breath. This means that at each breath humans ventilate roughly 15% of the air in their lungs.

---

[2] This diagram is reproduced from Patrick J. Lynch, medical illustrator; C. Carl Jaffe, MD, cardiologist.

Table 1.1.: Average pleural pressure versus volume of air in a healthy adult human lung.

Lung Volume	Volume of Air (l) [103]		Pleural Pressure
	male	female	$(\mathrm{cmH_2O})$
Total lung capacity (TLC)	5.40 - 7.06	3.71 - 4.95	-30.0 [155]
Functional residual volume (FRV)	2.65 - 4.01	1.81 - 2.79	- 5.3 [43]
Residual volume (RV)	1.58 - 2.62	1.19 - 1.95	-2.0 [78]
Resting tidal volume (RTV)	0.43 - 0.89	0.39 - 0.71	[-8.3,-5.3] [43]

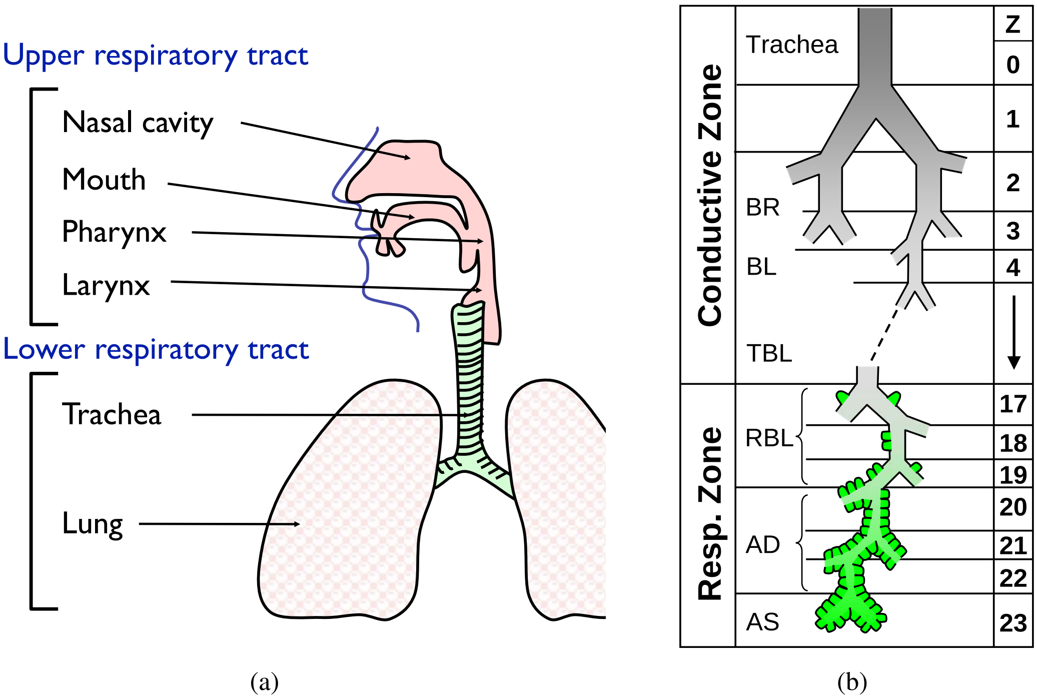
Respiratory System
Upper respiratory tract
Nasal cavity
Mouth
Pharynx
Larynx
Lower respiratory tract
Trachea
Lung
Conductive Zone
Resp. Zone
Trachea
BR
BL
TBL
RBL
AD
AS
Z
0
1
2
3
4
17
18
19
20
21
22
23

(a) (b)

Figure 1.2.: Sketch diagrams of (a) the human respiratory tract and (b) the human airways according to Weibel's model[3]. Z = airway generation; BR = bronchus; BL = bronchiole; TBL = terminal bronchiole; RBL = respiratory bronchiole; AD = alveolar duct; AS = alveolar sac. Note that the RBL, AD, and AS make up the transitional and respiratory zone.

The respiratory system (or ventilatory system) is a biological system, whose main function is to facilitate the flow of air inside lungs. Anatomically, a respiratory system is composed of upper respiratory tract and lower respiratory tract; see Figure 1.2(a). The upper respiratory tract is composed of the nasal cavity, mouth, pharynx, and larynx. The lower respiratory tract is composed of a tree of conducting and respiratory airways; see Figure1.2(b). The conducting airways, which form up the dead zone, start at the trachea and extend down to 17 generations. The dead zone stands for the region of the airways in which no gas exchange occurs [56]. The dead zone of a healthy adult human being has a volume of roughly $150\,\mathrm{ml}$ [56], peripheral airway radii of $1.5\,\mathrm{mm}$ [153], and is attached at the periphery to around 30,000 respiratory airway networks called acini [154]. The respiratory airways (acini) extend up to 7 generations and make up the respiratory zone, at which gas exchange occurs. The respiratory region is composed of alveolar ducts and alveoli; see Figure 1.1(b). A pulmonary alveolus is a hollow anatomical structure locate at the periphery of a respiratory tree. The alveolar membrane is made of a two cell layer. The first layer is made of epithelium cells and is exposed to the air side. The second layer is made of endothelium cells and is exposed to blood vessel. Such a two cell layer facilitates the gas exchange between air and blood. The average alveolar wall thickness in a healthy human being is around $6\,\mu\mathrm{m}$. On average a human being has roughly 500 million alveoli [106], which make up a gas exchange area of $80 - 150\,\mathrm{m}^2$, of which 90% is surrounded by blood capillaries [155]. The volume of air inside a respiratory zone of an average human being at end expiration is around $2.5\,\mathrm{liters}$ [56] and the volume of alveoli is 2 to 3 times that of the stress free state [27].

Pulmonary Circulatory System

The pulmonary circulation is the part of the blood circulation happening inside the lungs. In total, the human pulmonary circulatory system is composed of 15-17 generation trees of pulmonary arteries and veins [61; 140]. At the periphery the pulmonary circulatory system is connected to over 10 generations of arterioles and venules. In total, the pulmonary system makes around 9% of the total amount of blood within a human body [56]. Figure 1.3 shows a sketch of the entire circulatory system inside the human body and distinguishes between pulmonary and systemic circulation. Blood vessels colored in red indicate that they carry blood rich in O_2. Blood vessels colored in blue indicate that they carry blood poor in O_2. The blood circulation goes as follows. O_2 rich blood is pumped by the left ventricle into the systemic arteries. Blood travels through the network of bifurcating arteries and arterioles. At the end of the arterioles blood enters a network of tiny and thin capillaries within the body tissue. Once in capillaries, hemoglobin (Hb) of the O_2 rich blood (HbO_2) releases O_2 molecules to the surrounding tissue cells and attracts the carbon dioxide molecules (CO_2) from the surrounding tissue cells. The CO_2 rich blood ($HbCO_2$) then travels through a network of venules and veins until in reaches the right atrium. Blood inside the right atrium then flows to the right ventricle, mostly via pressure drop between the right atrium and the right ventricle. The right ventricle pumps the CO_2 rich blood into the lungs through a network of pulmonary arteries and arterioles all the way into the tiny thin capillaries aligned along the pulmonary alveoli. Once inside the alveolar capillaries, Hb releases CO_2 and and gains O_2. The O_2 rich blood then flows through a network of pulmonary venules and veins

---

[3] Picture reproduced from Weibel [153].

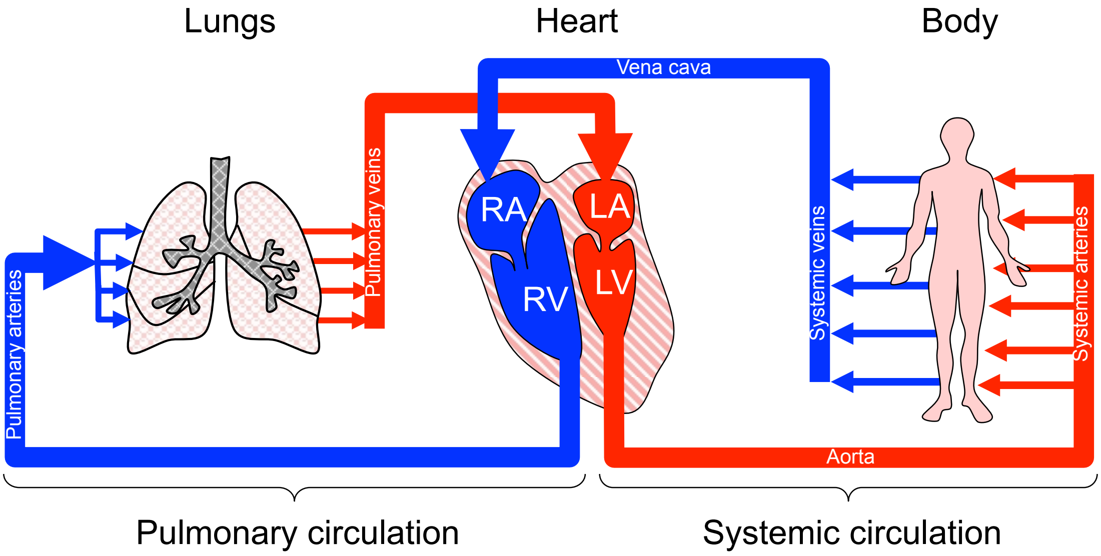

Figure 1.3.: Sketch diagrams of the human circulatory system showing the systemic circulation and the pulmonary circulation. LA = left atrium; LV = left ventricle; RA = right atrium; RV = right ventricle.

into the left atrium. Finally, blood flows from the left atrium into the left ventricle by the positive pressure gradient between the left atrium and the left ventricle and the atrial contraction. The cycle through which blood travels from the right ventricle to the left atrium is called pulmonary circulation. In short, pulmonary circulation is a circulation through which blood flows through the lungs to gain O_2 and give away CO_2.

Oxygen exchange interface

The human body gains O_2 and and loses CO_2 through the gaseous diffusion occurring between the blood in the pulmonary capillaries and the air inside the alveoli. The gaseous diffusion thus occurs through the alveolar wall due to wall permeability and gaseous concentration gradient across the wall. In physiology, the concentrations of O_2 and CO_2 are measured by their atmospheric partial pressure $\mathrm{P}_{\mathrm{O}_2}$ and $\mathrm{P}_{\mathrm{CO}_2}$, respectively. In healthy humans pulmonary arterial blood has $P_{\mathrm{O}_2} = 40\,\mathrm{mmHg}$ and $P_{\mathrm{CO}_2} = 45\,\mathrm{mmHg}$. At sea level, atmospheric air is inspired with $P_{\mathrm{O}_2} = 150\,\mathrm{mmHg}$ and $P_{\mathrm{CO}_2} = 40\,\mathrm{mmHg}$. Once atmospheric air reaches the respiratory zone the P_{O_2} of the respiratory zone increases whereas the P_{CO_2} drops. At this stage, O_2 starts to diffuse from the alveoli into the Hb of the capillary blood coming from the pulmonary arteries. At the same time, Hb of the capillary blood coming from the pulmonary arteries releases CO_2. The released CO_2 then diffuses through the alveolar wall into the alveolar air. Typically, under healthy resting conditions, this process takes less than $0.3\,\mathrm{s}$, i.e. blood needs to only travel one third of the alveolar capillaries to fully saturate with O_2 and release its CO_2. Figure 1.4 shows how the vascular P_{O_2} increases to match that of air's whereas vascular P_{CO_2} drops to match that of air's. The values reported in Figure 1.4 are for a healthy adult with a breathing rate of $6\,\mathrm{l/mim}$.

---

[4] These data curves were reproduced from Guyton [56].

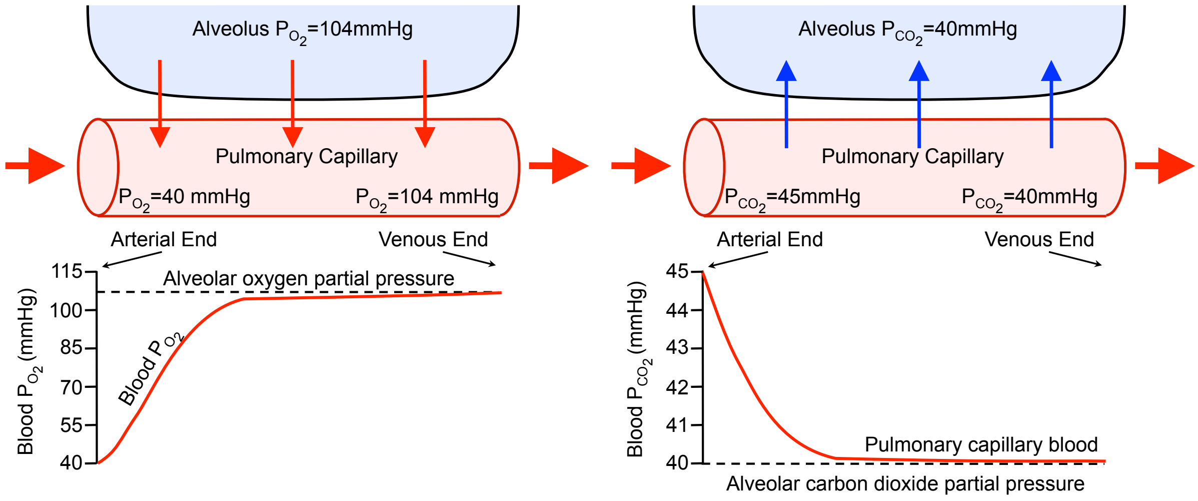
Alveolus P_{O_2}=104mmHg
Pulmonary Capillary
P_{O_2}=40 mmHg
P_{O_2}=104 mmHg
Arterial End
Venous End
Alveolar oxygen partial pressure
Blood P_{O_2}
Blood P_{O_2} (mmHg)
115
100
85
70
55
40
Alveolus P_{CO_2}=40mmHg
Pulmonary Capillary
P_{CO_2}=45mmHg
P_{CO_2}=40mmHg
Arterial End
Venous End
Blood P_{CO_2} (mmHg)
45
44
43
42
41
40
Pulmonary capillary blood
Alveolar carbon dioxide partial pressure

(a) (b)

Figure 1.4.: Gas exchange in pulmonary capillaries showing (a) the Diffusion of O_2 from an alveolus into pulmonary blood and (b) the diffusion of CO_2 from pulmonary blood into the alveolus[4]. Values reported at a breathing rate of $6\,\mathrm{l/min}$.

The final expired $P_{O_2} \approx 104\,\mathrm{mmHg}$ and $P_{CO_2} \approx 45\,\mathrm{cmH_2O}$. The pulmonary vascular P_{O_2} increased from ≈ 40 to ≈ 104. The pulmonary vascular P_{CO_2} dropped from $\approx 45\,\mathrm{cmH_2O}$ to $\approx 40\,\mathrm{cmH_2O}$ [56]. Furthermore, the O_2 saturation of Hb in healthy human blood is detailed in Figure 1.5. Interestingly, while the human body is required to raise its vascular P_{O_2} from 40 to at least $80\,\mathrm{mmHg}$, the Hb saturation is only raised from 75% to at least 95%. This means that the human body requires high O_2 levels but manages to only consume 20 to 25% of the O_2 supplied to it.

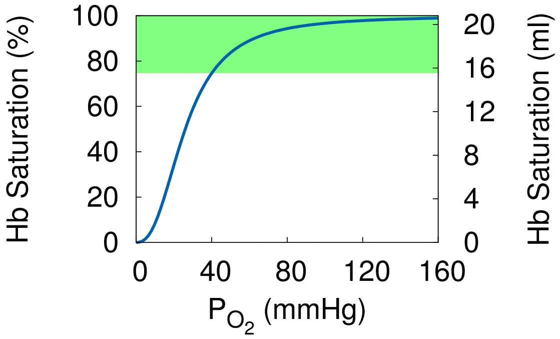

Figure 1.5.: Hemoglobin O_2 saturation curve in $100\,\mathrm{ml}$ of human blood. The zone marked in green shows the range of O_2 in healthy human being blood.

1.3. Modeling approach

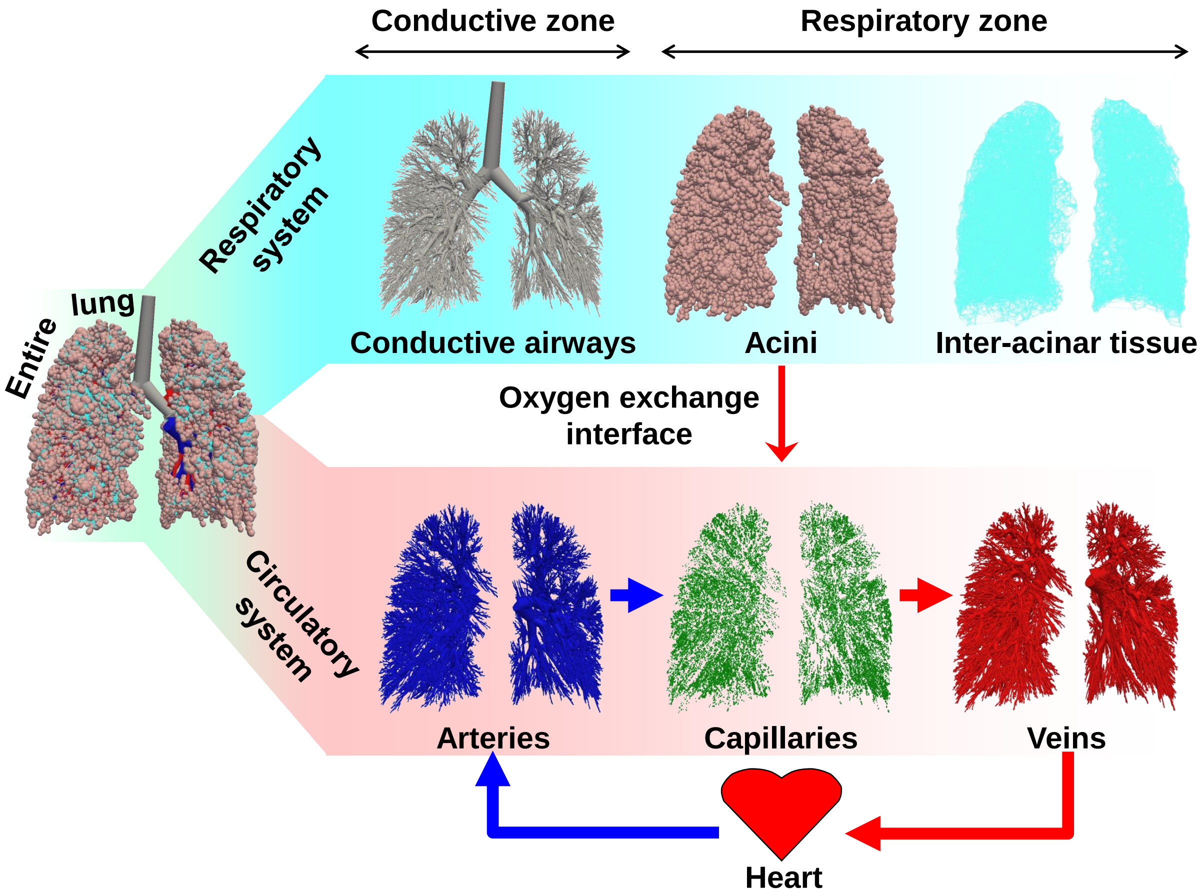
Conductive zone
Respiratory zone
Respiratory system
Entire lung
Conductive airways
Acini
Inter-acinar tissue
Oxygen exchange interface
Circulatory system
Arteries
Capillaries
Veins
Heart

Figure 1.6.: A detailed representation of the entire lung model showing the different model components.

Considering the described pulmonary anatomy and physiology, the entire lung model shown in Figure 1.6 is developed. This is achieved by dividing the lung into two systems; a respiratory system and a circulatory system. The respiratory system is broken down into three different sections; the conducting airways, the respiratory airways and the inter-acinar tissue. The circulatory system is also broken down into three sections; the large arteries, the large veins and the capillary network. Furthermore, an O_2 exchange interface is defined, through which O_2 is allowed to diffuse between the respiratory zone and the capillary networks.

The main challenge in establishing the comprehensive model of Figure 1.6 lies in the huge range of relevant scales within the lung model. To put it into numbers, human lungs are composed of 17 generations of conducting airways, 17 generation of arteries, and 17 generation of veins. At the peripheral regions conducting airways are connected to 6 generation trees of respiratory airways whereas the arteries and veins are connected to a capillary network of arterioles and venules, each 10 generations at least. As such the scale of the pulmonary fluid networks ranges from $1.5\,\mathrm{cm}$ in radius outside the lung to few tens of micrometers at the peripheries. The parenchyma consists of more than 500 million of interconnected alveoli, each having a radius of few tens of micrometers. When summed up, the alveoli cover up to $150\,\mathrm{m}^2$ of gas exchange area [155]. The inhomogeneous behavior of the ventilation induced pulmonary damages indicated that different scales and domains of the lung highly interact and influence each other. Thus, to better understand the involved processes and to develop protective strategies, a full model of the lung incorporating different scales and domains is a necessity.

Earlier attempts to model the lung using 3D models were covered in [25; 54; 82; 84; 149; 166; 167]. More recently, such models were extended towards modeling larger sections of conducting airways in 3D representations using idealized geometries [48; 76]. However none of these works were able to model the entire lung in 3D. That is because the large variation in scales within the lung made it impossible to model with the currently available computer resources. Fortunately, adequate reduced-dimensional (reduced-D) models, such as 1D and 0D models, were shown to well capture averaged behavior of full 3D models. This was indeed demonstrated earlier via 1D models [1; 2; 13; 31; 35; 37–40; 92; 100; 102; 107–109; 121; 125; 126; 145; 151], 0D models [3; 5; 66; 81; 111; 122; 134; 135; 147], and impedance models [8; 22; 50; 85; 86; 105; 130; 148] for different physiological flow networks. More advanced *in silico* models have incorporated the various modeling scales together in a coupled 3D-1D-0D frame work [13; 22; 35; 37; 40; 53; 68; 83; 86; 114; 124; 143; 148; 164]. This allowed the fine scale physics to be captured using 3D models whereas the boundaries of the 3D region were modeled using a combination of 1D, 0D, and impedance models. Furthermore, coupling of 3D domain with reduced-D domain was shown to produce more correct flow and pressure distribution within a 3D *in silico* model of the lung [22; 66].

Despite such an extensive research in the field of reduced-D modeling, most of the applications in pulmonary mechanics focused mainly on a small section or impedance analysis and pressure-volume (PV) curves of the lung [57]. One main goal of such analyses was to show the effect of global and local conditions onto the lung impedance curves (such as, total lung compliance and airway resistance) [7; 8; 50; 85; 105; 130]. However, the lung was nonetheless looked at as a single compartment model.

As such, this work proposed a novel approach that achieves the entire lung model shown in Figure 1.6, by building the entire respiratory model out of trees of 3D and 0D airways coupled to 0D acini. The neighboring acini were inter-connected with inter-acinar tissue by including novel inter-acinar dependencies. The pulmonary vessels were constructed using a network of 3D, 1D and 0D blood vessels and connected to the airway at the gas exchange interface. Thus allowing the diffusion of O_2 from air to blood. Furthermore, the influence of various external conditions (gravity and tracheal pressure) and internal condition (pleural pressure and lung health) onto the respiratory system and the circulatory system were also modeled and included within the system.

The outline of the remainder of this work is as follows. Each of the six different components in Figure 1.6 are either segmented from a patients Computer Tomography (CT)-scan images in Chapter 2 or generated using novel anatomic-based algorithms. The mathematical formulation of the six components are covered in Chapter 3. The identification of the various material and physical and material parameters are detailed and compared against measurements from human physiology in Chapter 4. In Chapter 5, all of the six components are assembled together and tested under physiological conditions including spontaneous breathing and mechanical ventilation. Furthermore, a comparison between mechanically ventilating diseased and healthy lungs are also detailed in Chapter 5. Finally, a summary and a discussion are covered in Chapters 6 whereas future outlook and limitations are proposed in Chapter 7.

2. Geometry

> ”I profess to learn and to teach anatomy not from books but from dissections, not from the tenets of Philosophers but from the fabric of Nature.”
>
> - William Harvey, 1628

The aim of this chapter is to develop a method that models the various sections of the lung geometrically. This is achieved by firstly segmenting the lung lobes and the tracheobronchial geometry from patient specific Computer Tomography (CT) images. The sections which are unsegmentable, due to the limited CT resolution, are then generated using morphological and anatomical based algorithms. These sections included the peripheral conducting airways, the respiratory airways, the blood vessels and the capillaries. The unsegmentable conducting airways are generated using a space filling algorithm. The respiratory airways are generated inversely by matching the patient’s lungs volume to the morphological measurements of fixated human lungs. The blood vessels are created using well known relationships between the morphology of airways and the morphology of pulmonary blood vessels.

2.1. 3D airway and lung geometry

The 3D lung components are segmented from end-expiratory CT data supported by Barkow and Strohmaier [6] (slice thickness and pixel size $0.7344\,\mathrm{mm}$; see Figure 2.1(a,b)) using the commercially available segmentation software Mimics[5] (Materialise). The CT resolution allowed for the extraction of a 3D tracheobronchial geometry starting at the level of the trachea, downstream of the laryngeal region, and progresses up to the 5th generation of the bronchial tree (at the approximate location where the airway enters one of the five lobes of the lung). Furthermore, the 5 lung lobes are also identified in the CT images and segmented separately; see Fig 2.1(c).

Due to the limited CT resolution, only the first four airway generations are properly visible. The peripheral airways have to be generated using a space filling algorithm. For this purpose anatomically based space filling algorithm developed by the author et al. [66], which is an improved version of [137], is used. This was achieved as following:

1. A group of points are randomly generated inside each lobe.

---

[5] http://biomedical.materialise.com/mimics

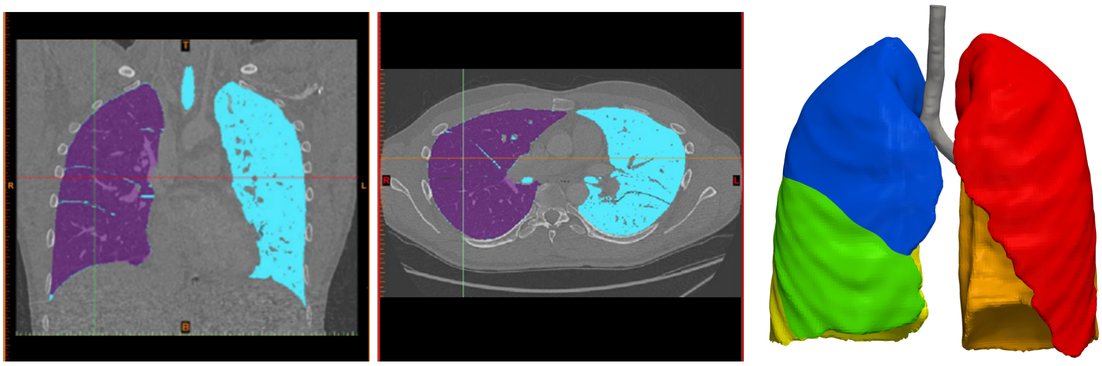

(a) (b) (c)

Figure 2.1.: Patient-specific lung geometry showing (a) coronal slice of the patient's CT-scan, (b) transverse slice on the lung patient's CT-scan, and (c) segmented lobes and tracheobronchial airways. The CT images are supported by [6]

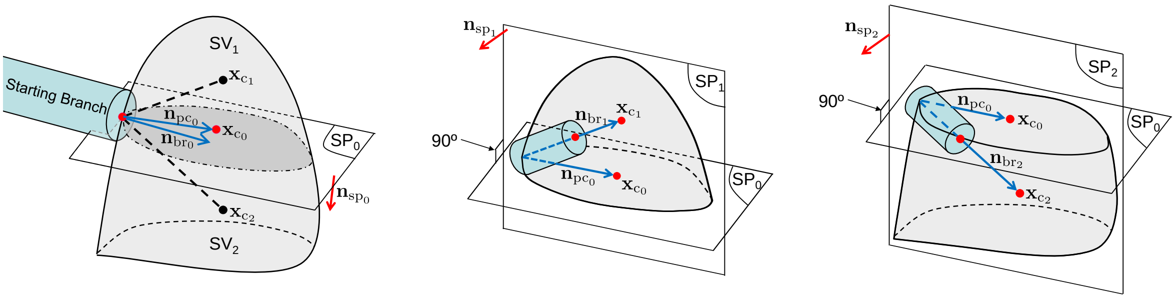
SV_1
$\mathbf{x}_{c_1}$
Starting Branch
$\mathbf{n}_{pc_0}$
$\mathbf{x}_{c_0}$
$\mathbf{n}_{br_0}$
SP_0
$\mathbf{n}_{sp_0}$
$\mathbf{x}_{c_2}$
SV_2
$\mathbf{n}_{sp_1}$
SP_1
$\mathbf{n}_{br_1}$
$\mathbf{x}_{c_1}$
90°
$\mathbf{n}_{pc_0}$
$\mathbf{x}_{c_0}$
SP_0
$\mathbf{n}_{sp_2}$
SP_2
90°
$\mathbf{n}_{pc_0}$
$\mathbf{x}_{c_0}$
SP_0
$\mathbf{n}_{br_2}$
$\mathbf{x}_{c_2}$

(a) (b) (c)

Figure 2.2.: Visualization of the tree growing algorithm showing (a) the initial split plane and a lobar volume, (b) the upper split sub-volume and its corresponding bronchial branch, and (c) the lower split sub-volume and its corresponding branch.

2. The center of mass of a lobe ($\mathbf{x}_\mathrm{c}$) is evaluated by averaging the coordinates of all points inside the lobe as

$$\mathbf{x}_\mathrm{c} = \frac{1}{N_\mathrm{p}} \sum_{i=1}^{N_\mathrm{p}} \mathbf{x}_i, \tag{2.1}$$

where N_p is the total number of points inside a lobe.

3. A splitting plane is defined to split a lobe into two sub-volumes. The starting splitting plane (SP_0) is defined by the vector normal to the outlet surface of the 3D airway geometry ($\mathbf{n}_{\mathrm{br}_0}$) and the vector connecting the 3D airway outlet centroid to the center of mass of the lobe ($\mathbf{n}_{\mathrm{pc}_0}$). In other words SP_0 is defined by the normal vector $\mathbf{n}_{\mathrm{sp}_0} = \mathbf{n}_{\mathrm{pc}_0} \times \mathbf{n}_{\mathrm{br}_0}$ and the point $\mathbf{x}_{\mathrm{c}_0}$ (see Figure 2.2(a)).

4. The lobar volume is split into two sub-volumes (SV_1 and SV_2) using the splitting plane SP_0 (see Figure 2.2(a)).

5. The centroids of the two sub-volumes ($\mathbf{x}_{c_1}$ and $\mathbf{x}_{c_2}$) are evaluated using eq (2.1). The two daughter airway branches are grown from the end of the parent airway in the direction of the centroids, i.e. along the vectors $\mathbf{n}_{\mathrm{br}_1}$ and $\mathbf{n}_{\mathrm{br}_2}$. The length of each daughter airway is set to be 40% of the distance between the centroid of the sub-volumes and the starting point of the daughter branches, i.e. first branch is extended with $0.4\|\mathbf{n}_{\mathrm{br}_1}\|_2$ whereas the second branch is extended with $0.4\|\mathbf{n}_{\mathrm{br}_2}\|_2$ (see Figure 2.2(a)). Daughter airways that ended outside the sub volume are trimmed such that they do not grow outside the sub-region.
6. In each sub-volume a new splitting plane, for example SP_1 and SP_2 in Figure 2.2(b,c), is evaluated using three points: (i) The parent volume centroid, (ii) the parent airway distal point, and (iii) the sub-volume's centroid (see Figure 2.2(b) and (c)).
7. The process is repeated from Step 4 until one of the termination criteria is met.

2.2. Conductive airways

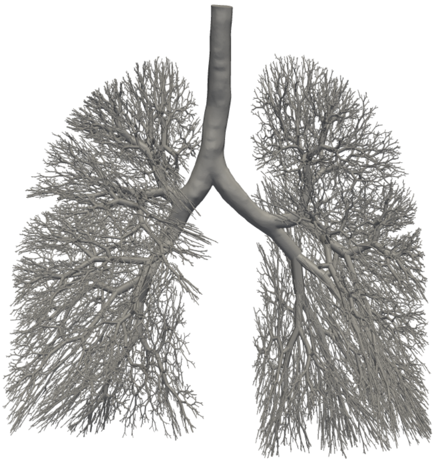

Figure 2.3.: 3D representation of a tree of 16 generations of conducting airways

The termination criteria used in this work are an airway length ($l_{\mathrm{t}} = 1.2\,\mathrm{mm}$), airway radius ($r_{\mathrm{t}} = 0.2\,\mathrm{mm}$) or node termination criteria (no nodes left for sub-division). The daughter to parent branch scaling of the radii for the left and right branches of the tree are 0.876 and 0.686, respectively; these values are based on the morphologically measured values in human lungs as reported in [91]. Figure 2.3 shows the patient's generated tree of conducting airways. Figure 2.4(a) shows the amount of all airways in each generation. Figure 2.4(b) shows the number of terminal airways for different generations. The statistical values of the diameter, length and length-to-radius ratios are detailed in Figure 2.5. Furthermore, the airway diameters and lengths in Figure 2.5(a) and (b) show a very good match between the generated bronchial tree and the morphological measurements of [154]. The length-to-radius ratio in Figure 2.5(c) is only 15% off the one measured by [154]. Table 2.1 shows the volumetric details of the segmented lobes and the artificially generated tree. The total volume of the generated dead space $(132.9\,\mathrm{ml})$ agreed with that measured in morphology $(150\,\mathrm{ml})$ [56].

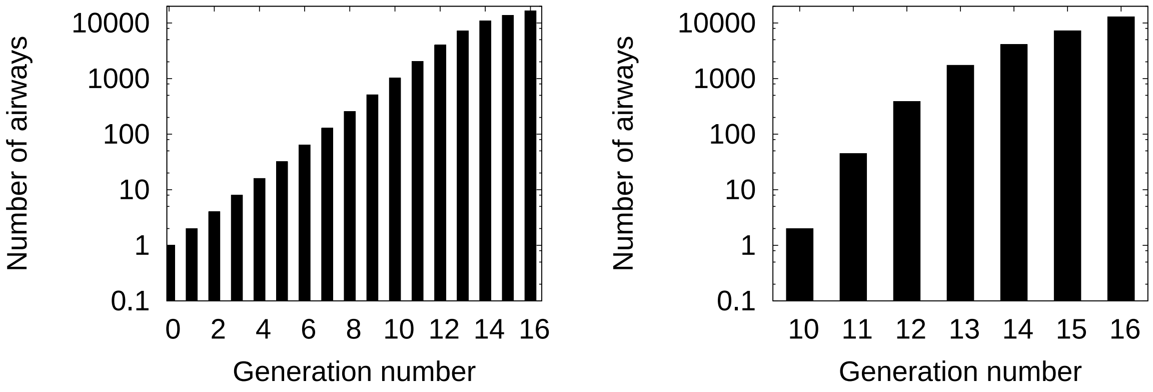

(a) (b)

Figure 2.4.: The amount of conducting airways in each generation showing (a) all the airways and (b) how many branches of the tree end at different generations.

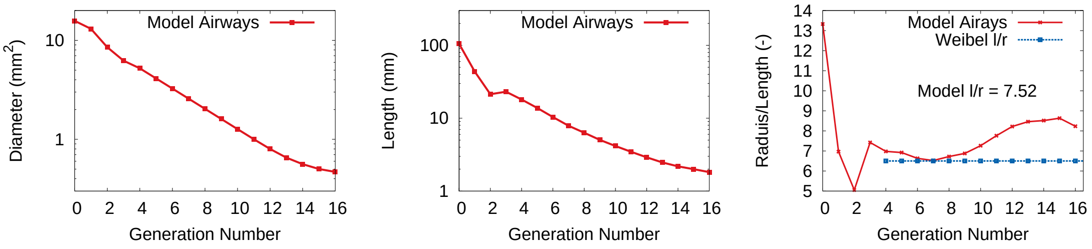

(a) (b) (c)

Figure 2.5.: The amount of conducting airways in each generation showing (a) all the airways and (b) how many branches of the tree end at different generations.

2.3. Respiratory airways

2.3.1. Acini

To evaluate the number of alveoli inside the segmented lungs two things are required: the volume of alveolar air and the transpulmonary pressure (i.e. the stress state under which the alveoli are). For this purpose the ratio of total air volume over the ration of total lung volume is estimated from the alveolar volume measurements of Ochs et al. [106], who in turn observed that the volume of the human alveoli at a tranpulmonary pressure $P_{\mathrm{tp}} = 25\,\mathrm{cmH_2O}$ is independent of

Table 2.1.: Lobar and airway information of the space filled lung showing V^{LB} the lobar volume, $V^{\mathrm{LB}}_{\mathrm{aw}}$ the lobar airway volume, and $A^{\mathrm{LB}}_{\mathrm{TBL}}$ the total cross-sectional area of terminal airways in a lobe

Section	Segmented volume (l) (V^{LB})	Airway volume (l) ($V^{\mathrm{LB}}_{\mathrm{aw}}$)	Terminal area ($10^2\mathrm{cm}^2$) ($A^{\mathrm{LB}}_{\mathrm{TBL}}$)
Trachea	0.040	0.0406	–
Right superior lobe	0.837	0.0148	8.74
Right middle lobe	0.398	0.0085	4.42
Right inferior lobe	1.066	0.0253	12.3
Left superior lobe	1.107	0.0230	12.4
Left inferior lobe	0.929	0.0207	10.1
Total volume	4.297	0.1329	48.0

their location in the lung and equal to $4.2\times10^{-3}\mathrm{mm}^3$ (range: 3.3–$4.8\times10^{-3}\mathrm{mm}^3$). Ochs et al. [106] also observed that the mean volume of an alveolus in a human lung is independent of the number of alveoli in the lung. As such they defined the volume of the lung as

$$V_{\mathrm{lung}} = V_{\mathrm{aw}} + V_{\mathrm{blood}} + V_{\mathrm{par}}, \tag{2.2}$$

where V_{aw} is the volume of large airways, V_{blood} the volume of large blood vessels, and V_{par} the volume of the parenchyma. The parenchyma is defined as the gas exchange region, excluding large blood vessels and bronchi, i.e.

$$V_{\mathrm{par}} = V_{\mathrm{tis}} + V_{\mathrm{duct}} + V_{\mathrm{alv}},$$

where V_{tis} is the volume of parenchymal tissue, V_{duct} the volume of respiratory ducts and V_{alv} the volume of the alveoli. The total volume of the tissue is considered to be independent of the volume of the lung and the ratio of the alveolar duct volume to the volume of alveoli is taken to be $\zeta = V_{\mathrm{duct}}/V_{\mathrm{alv}} = 0.13$ [28]. In other words the total volume of tissue is rewritten as

$$V_{\mathrm{tis}} = V_{\mathrm{par}} - (1+\zeta)\,V_{\mathrm{alv}}.$$

The segmented lungs used in this work are taken from a lying patient at end-expiration, which meant that the pleural pressure is around $-5.3\,\mathrm{cmH_2O}$ and the alveolar pressure is around $0\,\mathrm{cmH_2O}$ [43], i.e. the transpulmonary pressure is $P_{\mathrm{tp}} = 5.3\,\mathrm{cmH_2O}$. To match the alveolar measurements of Ochs et al. [106] (at $P_{\mathrm{tp}} = 25\,\mathrm{cmH_2O}$) and the patients alveoli used in this work (at $P_{\mathrm{tp}} = 5.3\,\mathrm{cmH_2O}$), the assumed constant lung tissue volume yields the following

$$\left(V_{\mathrm{par}} - (\zeta+1)\,V_{\mathrm{alv}}\right)\big|_{5.3\mathrm{cmH_2O}} = \left(V_{\mathrm{par}} - (\zeta+1)\,V_{\mathrm{alv}}\right)\big|_{25\mathrm{cmH_2O}}\,. \tag{2.3}$$

A variable $\alpha = V_{\mathrm{alv}}/V_{\mathrm{par}}$ is defined to change the relationship in eq (2.3) to

$$\alpha|_{5.3\mathrm{cmH_2O}} = \left(\frac{V_{\mathrm{alv}}|_{25\mathrm{cmH_2O}}}{V_{\mathrm{alv}}|_{5.3\mathrm{cmH_2O}}} \left(\frac{1}{\alpha|_{25\mathrm{cmH_2O}}} - 1 - \zeta \right) + 1 + \zeta \right)^{-1}. \tag{2.4}$$

From Ochs et al. [106], the ratio of paranchymal volume over the lung volume at $P_{\mathrm{tp}} = 25\,\mathrm{cmH_2O}$ are found to be

$$\left.\frac{V_{\mathrm{par}}}{V_{\mathrm{lung}}}\right|_{25\mathrm{cmH_2O}} = 0.9$$

and the ratio of total alveolar volume over the lung volume at $P_{\mathrm{tp}} = 25\,\mathrm{cmH_2O}$

$$\left.\frac{V_{\mathrm{alv}}}{V_{\mathrm{lung}}}\right|_{25\mathrm{cmH_2O}} = 0.64.$$

The ratio α at a $P_{\mathrm{tp}} = 25\,\mathrm{cmH_2O}$ is found to be

$$\alpha|_{25\mathrm{cmH_2O}} = 0.71.$$

Using the *in silico* results of Denny and Schroter [29] (see Table 2.2), the ratio of the alveolar volume at $P_{\mathrm{tp}} = 5.3\,\mathrm{cmH_2O}$ over the alveolar volume at $P_{\mathrm{tp}} = 25\,\mathrm{cmH_2O}$ is found to be

$$\frac{V_{\mathrm{alv}}|_{5.3\,\mathrm{cmH_2O}}}{V_{\mathrm{alv}}|_{25\,\mathrm{cmH_2O}}} = 0.6.$$

Substituting all of the above ratios in Eq (2.4) resulted in α at $P_{\mathrm{tp}} = 5.3\,\mathrm{cmH_2O}$

$$\alpha|_{5.3\,\mathrm{cmH_2O}} = 0.63.$$

Table 2.2.: The quasi-static change of the alveolar volume with respect to the change in the transpulmonary pressure (* Values under dynamic loading) [29]

P_{tp} ($\mathrm{cmH_2O}$)	0	5.3*	30
Volume ($\times 10^{-3}\mathrm{mm}^3$)	1.03	2.897*	5.165

The volume of blood inside the pulmonary circulation is found to be 450 ml [56]. Substituting the blood volume and patient's segmented volumes (reported in Table 2.1) in eq (2.2) yields the following ratio

$$\frac{V_{\mathrm{par}}|_{5.3\,\mathrm{cmH_2O}}}{V_{\mathrm{lung}}|_{5.3\,\mathrm{cmH_2O}}} = 0.86.$$

This means that ratio of total alveolar volume over the total volume of lungs at $P_{\mathrm{tp}} = 25\,\mathrm{cmH_2O}$

$$\frac{V_{\mathrm{alv}}|_{5.3\,\mathrm{cmH_2O}}}{V_{\mathrm{lung}}|_{5.3\,\mathrm{cmH_2O}}} = 0.86 \times 0.6 = 0.54.$$

The final lung volume percentages of parenchyma and alveolar air at a transpulmonary pressures of $5.3\,\mathrm{cmH_2O}$ and $25\,\mathrm{cmH_2O}$ are reported in Table 2.3.

Table 2.3.: Volume composition of the lung at different transpulmonary pressures. * Values measured and reported by [106]. ** Values, evaluate in this section.

Lung Section	$25\,\mathrm{cmH_2O}$ [106]	$5.3\,\mathrm{cmH_2O}$
Parenchyma	$90\%^*$	$88\%^{**}$
Alveoli	$64\%^*$	$54\%^{**}$

The evaluated percentages in Table 2.3 are applied onto the segmented volumes of Table 2.1. The resulted patient's volumes at $P_{\mathrm{tp}} = 5.3\,\mathrm{cmH_2O}$ are reported in Table 2.4.

Table 2.4.: Detailed information of different lobes within the space filled lung at a transpulmonary pressure $P_{\mathrm{tp}} = 5.3\,\mathrm{cmH_2O}$. $V^{\mathrm{LB}}_{\mathrm{par}}$ is the evaluated parenchymal volume, $V^{\mathrm{LB}}_{\mathrm{alv}}$ the evaluated alveolar volume, and $V^{\mathrm{LB}}_{\mathrm{ac}}$ the evaluated acinar volume

Section name	Section V^{LB} (l)	Parenchyma $V^{\mathrm{LB}}_{\mathrm{par}}$ (l)	Alveoli $V^{\mathrm{LB}}_{\mathrm{alv}}$ (l)	Functional residual $V^{\mathrm{LB}}_{\mathrm{ac}}$ (l)
Right superior lobe	0.837	0.731	0.448	0.504
Right middle lobe	0.398	0.347	0.213	0.240
Right inferior lobe	1.026	0.897	0.550	0.618
Left superior lobe	1.107	0.967	0.593	0.667
Left inferior lobe	0.929	0.811	0.497	0.560
Total volume	4.297	3.755	2.302	2.590

The acinar volumes are distributed among the terminal airways by first evaluating the total terminal airways cross-sectional area ($A^{\mathrm{LB}}_{\mathrm{TBL}}$) of a lobe (see Table 2.1 for the lobar values of $A^{\mathrm{LB}}_{\mathrm{TBL}}$). Then the volume of each acinus ($V^{\mathrm{i}}_{\mathrm{ac}}$) connected to a terminal airway of cross-sectional area $A^{\mathrm{i}}_{\mathrm{TBL}}$ is evaluated as

$$V^{\mathrm{i}}_{\mathrm{ac}} = V^{\mathrm{LB}}_{\mathrm{ac}} \frac{A^{\mathrm{i}}_{\mathrm{TBL}}}{A^{\mathrm{LB}}_{\mathrm{TBL}}},$$

where $V^{\mathrm{LB}}_{\mathrm{ac}}$ is the total acinar volume of a lobe shown in Table 2.4. The patient's detailed respiratory zone values, shown in Table 2.5, are evaluated using the information above, the acinar air volume and the geometric details of the alveolar duct of [28]. In total the patient is estimated to have 797 million alveoli, a total gas exchange area of $86\,\mathrm{m}^2$ at $P_{\mathrm{tp}} = 5.3\,\mathrm{cmH_2O}$ and a functional residual volume of 2.59 liters. The residual volume is estimated o be 1.06 liters from the PV curves of [29] by finding the volume of air at $P_{\mathrm{tp}} = 2.0\,\mathrm{cmH_2O}$ [78].

Table 2.5.: Simulated results of spontaneous breathing. * Results during dynamic loading. ** Values based on the quasi-static pressure/volume (PV) curve produced by Denny and Schroter [29]

Number of acini	28778
Number of alveoli	797 million
Total gas exchange surface area (at $P_{\mathrm{tp}} = 5.3\,\mathrm{cmH_2O}$)	$85.9\,\mathrm{m}^2$
Functional residual volume (at $P_{\mathrm{tp}} = 5.3\,\mathrm{cmH_2O}$)*	2.59 l*
Residual volume (at $P_{\mathrm{tp}} = 2\,\mathrm{cmH_2O}$)	1.06 l**
Complete lung volume (at $P_{\mathrm{tp}} = 25\,\mathrm{cmH_2O}$)	5.9 l**

The patient's spatial distribution of the acinar volume is shown in Figure 2.6.

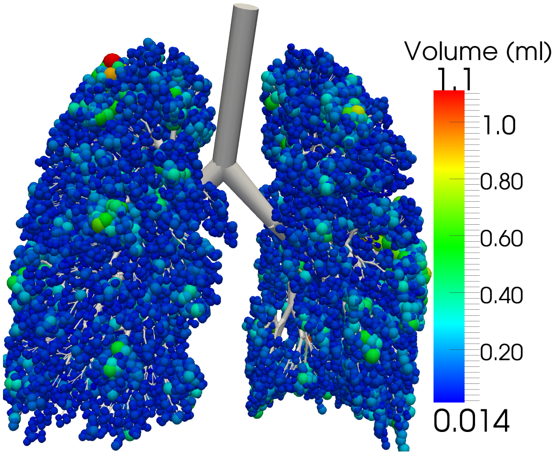

Figure 2.6.: Distributed volume of acini.

2.3.2. Inter-acinar tissue

In anatomy, neighboring alveoli share the same wall. This can be imagined as if neighboring alveoli have two walls that are sutured into each other. As such, the physics of an alveolus can be dependent on the physics of its neighbors. For this purpose, the approach developed by the author et al. [69] is used to detect the acinar neighborhoods within the geometry of Figure 2.6. The neighborhoods are defined by inter-acinar linkers, which link the neighboring acini to each other.

The inter-acinar linkers are detected using algorithm 1. For this purpose the 3D segmented geometry in Figure 2.1 is firstly meshed. Then the pleura is distinguished using mimics. Finally, the 3D mesh is used to detect which 0D acini are interconnected to each other (see Figure 2.7). Figure 2.8 shows all detected pleural acini for an axial cut through the left lung. The inter-acinar

Algorithm 1 Generate inter-acinar dependencies

```
Find which 3D elements correspond to which 0D Acinus:
Mesh 3D lung geometry and distinguish the pleural space (see Figure 2.7(a))
loop over all 3D elements
    Find the nearest 0D acinus $i$ to the current 3D element.
    Label the current 3D element with $i$ (see Figure 2.7(b))
    Find a volume set $k$ with 3D elements labeled with $i$
    if volume set $k$ does not exist then
        Create a new volume set $k$
    end if
    Add current element to volume set $k$ (see Figure 2.7(c))
    Add 0D acinus $i$ to volume set $k$ (see Figure 2.7(d))
end loop
loop over all 0D acini
    Get 0D acinus number $i$
    if 0D acinus $i$ does not belong to any volume set (see Figure 2.7(d)) then
        Find the nearest volume set $k$ to 0D acinus $i$
        Add 0D acinus $i$ to volume set $k$ (see Figure 2.7(e))
    end if
end loop
Detect 3D neighborhoods:
loop over all 3D volume sets
    Find the 3D volume set boundaries (see Figure 2.7(c))
end loop
loop over all 3D volume sets $k_1$
    loop over all volume sets $k_2$ (Such that $k_2 \neq k_1$)
        if volume set $k_1$ and volume set $k_2$ share a common boundary element then
            Set volume set $k_1$ and volume set $k_2$ as neighbors
        end if
    end loop
    if volume set $k_1$ share a common boundary with the pleura then
        Set volume set $k_1$ as a subpleural volume set
    end if
end loop
Detect 0D neigborhoods:
loop over all volume sets
    Interconnect all of the 0D acini of the current volume set to each other (see Figure 2.7(f)
    Interconnect all of the 0D acini of the current volume set to the 0D acini of the neighboring volume sets (see Figure 2.7(f)
    if volume set is connected to the pleura (see Figure 2.7(g) then
        Connect all of the 0D acini of the current volume set to the pleura (see Figure 2.7(h)
    end if
end loop
```

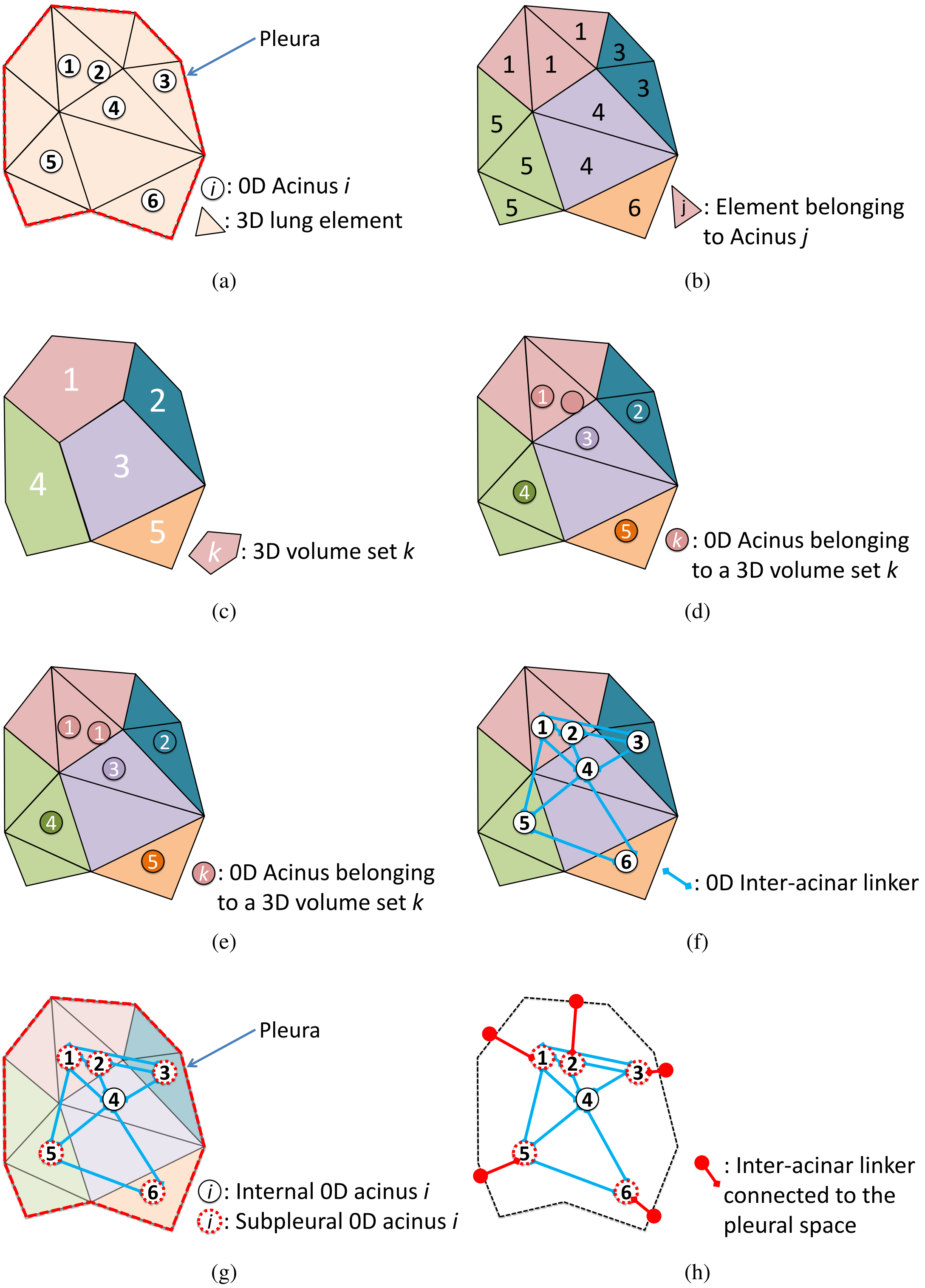
Pleura
ⓘ: 0D Acinus i
: 3D lung element
1 2 3 4 5 6
j: Element belonging to Acinus j
k: 3D volume set k
k: 0D Acinus belonging to a 3D volume set k
: 0D Inter-acinar linker
ⓘ: Internal 0D acinus i
i: Subpleural 0D acinus i
: Inter-acinar linker connected to the pleural space
(a)
(b)
(c)
(d)
(e)
(f)
(g)
(h)

Figure 2.7.: The evolution of the 0D inter-acinar dependency algorithm.

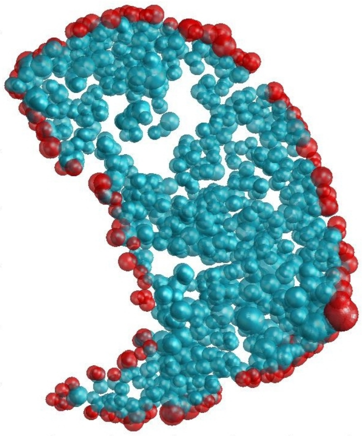

Figure 2.8.: An axial plane view through left lung showing non-pleural acini in blue and pleural acini in red.

neighborhood detecting Algorithm 1 is applied onto the geometry in Figure 2.6 and the 3D meshed geometry of Figure 2.1. The resulting tree of inter-acinar linkers is shown in Figure 2.9. In total the algorithm detected $28,681$ 3D volume sets, $134,155$ internal inter-acinar linkers and $5,980$ pleural inter-acinar linkers. Figure 2.9 shows the computed network of inter-acinar linkers.

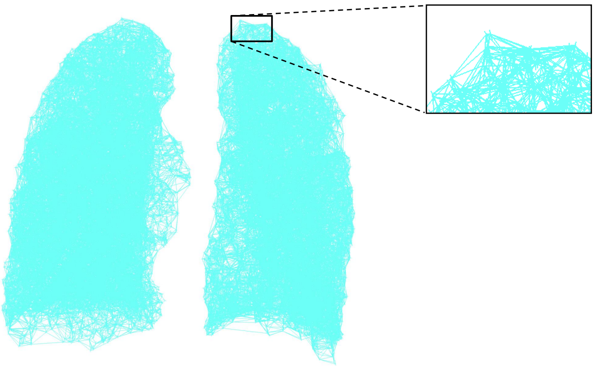

Figure 2.9.: Detected inter-acinar linkers of the entire lung.

2.4. Pulmonary blood vessels

In humans, pulmonary arteries arise from right ventricle and branch perpendicularly into the right and left lung. The pulmonary vascular branches join the bronchi while still in the mediastinum and remain in close association with the branching airway tree. This means that pulmonary all arteries, which are inside the lung, branch and lie parallel to the airways [154]. Pulmonary veins, on the other hand, lie between the two pairs of airways and pulmonary arteries [154].

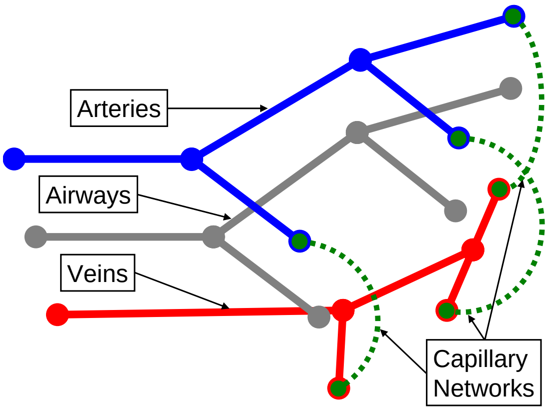

Figure 2.10.: A schematic showing pulmonary blood vessels generated from an airway tree

Based on the anatomical knowledge, pulmonary blood vessels are generated from the airway tree, as shown in Figure 2.10. For this purpose, an algorithm is developed to do the following:

1. The nodes of the airways are copied to form the nodes of arteries and nodes.
2. A group of translation vectors are generated, using Algorithm 2, to translate the copied nodes into an arterial or a venous geometry.
3. The translation vectors are used to create the pulmonary arteries using Algorithm 3.
4. The translation vectors are used to create a pseudo-venous geometry. The pseudo venous geometry is then modified to produce the anatomical venous geometry, using Algorithm 4.
5. Symmetric trees of capillaries are produced between terminal arteries and their nearest terminal veins, using Algorithm 5.

2.4.1. Generate nodal translation vectors

To generate the nodal translation vectors, the bifurcating tree of airways in Figure 2.11(a) is assumed. The airway nodal numbers are circled, whereas the airway branch numbers are shown in squares. Each branching node i is assumed to have two daughter airways numbered as j and k. The daughter airways j and k are assumed to have orientation vectors labeled as $\mathbf{u}_j$ and $\mathbf{u}_k$, respectively (see Figure 2.11). Following these assumptions, the nodal translation vectors are evaluated using Algorithm 2.

2.4.2. Generate pulmonary arteries

The pulmonary arteries have to follow the airways. Their average radii follow a logarithmic law

$$r_{\mathrm{art}_G} = r_{\mathrm{art}_0} 2^{-G/3},$$

where r_{art_0} is the radius of pulmonary artery at generation zero and G is the generation number [154]. Algorithm 3 is developed to reproduce the mean arterial diameters according to [154],

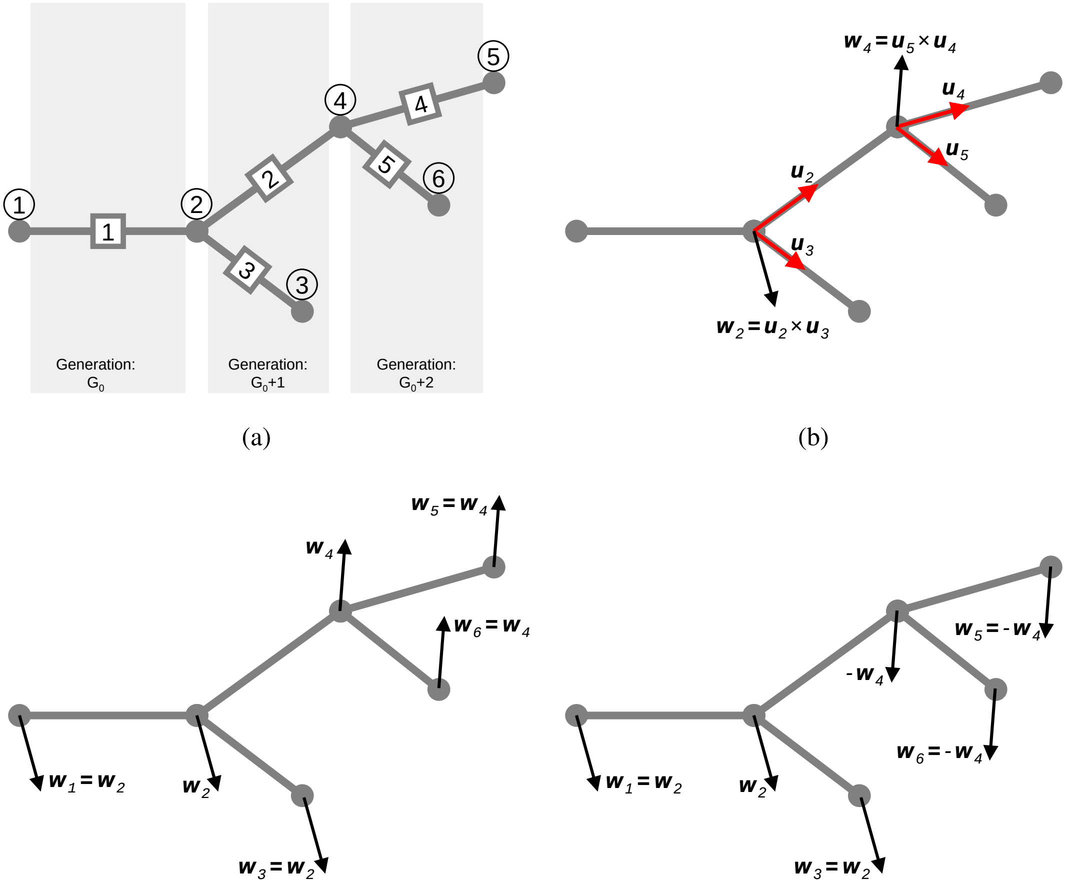
①
1
②
③
3
2
④
4
⑤
5
⑥
Generation: G_0
Generation: G_0+1
Generation: G_0+2
$w_4 = u_5 \times u_4$
u_4
u_5
u_2
u_3
$w_2 = u_2 \times u_3$
$w_5 = w_4$
w_4
$w_6 = w_4$
$w_1 = w_2$
w_2
$w_3 = w_2$
$w_5 = -w_4$
$-w_4$
$w_6 = -w_4$
$w_1 = w_2$
w_2
$w_3 = w_2$

(a) (b)

(c) (d)

Figure 2.11.: Step by step schematic showing how to generate a set of copy vectors for a random tree of airways

while maintaining the natural asymmetry in the arterial tree. This is achieved by multiplying the arteries radius by a ratio. The arterial ratio is evaluated by dividing the artery's corresponding airway radius by the mean airway radius of the entire corresponding generation.

2.4.3. Generate pulmonary veins

Just like the arteries, pulmonary veins follow a similar logarithmic law [60]. However they grow between the two pairs of airways and pulmonary veins. Algorithm 4 is developed to reproduce the anatomical structure of veins, the mean venous diameter and maintain the natural asymmetry in the venous tree.

2.4.4. Generate pulmonary capillaries

The pulmonary capillary networks are generated using Algorithm 5. Knowing that a capillary network has a volume of V_{cap_i} and using the measurements reported by Townsley [140], the

Algorithm 2 Generate nodal translation vectors

```
Find the translation vectors on bifurcation nodes:
loop over all nodes
    if node $i$ is a bifurcation node then
        find orientation vectors $\mathbf{u}_j$ and $\mathbf{u}_k$ of the daughter branches
        set $\mathbf{w}_i = \mathbf{u}_j \times \mathbf{u}_k$ (see Figure 2.11(b))
        scale $\mathbf{w}_i$ to unit vector ($\mathbf{w}_i = \mathbf{w}_i / \|\mathbf{w}_i\|_2$)
    end if
end loop
Find the translation vectors of the terminal nodes:
loop over all nodes
    if node $i$ is not a bifurcation node then
        find airway $\mathrm{AW}_{i,m} \mid \text{nodes } \{i, m\} \in \mathrm{AW}$
        set $\mathbf{w}_i = \mathbf{w}_m$ (see Figure 2.11(c))
    end if
end loop
Prevent overlapping of the translated and airway geometry:
set Generation = $G_0$
for Generation < $G_{\max}$ do
    loop over all airways in current Generation
        Get an airway $\mathrm{AW}_{m,n} \mid \text{nodes } \{m, n\} \in \mathrm{AW}_{m,n}$
        if $\langle \mathbf{w}_m, \mathbf{w}_n \rangle < 0$ then
            set $\mathbf{w}_n = -\mathbf{w}_m$ (see Figure 2.11(d))
        end if
    end loop
    set Generation = Generation + 1
end for
```

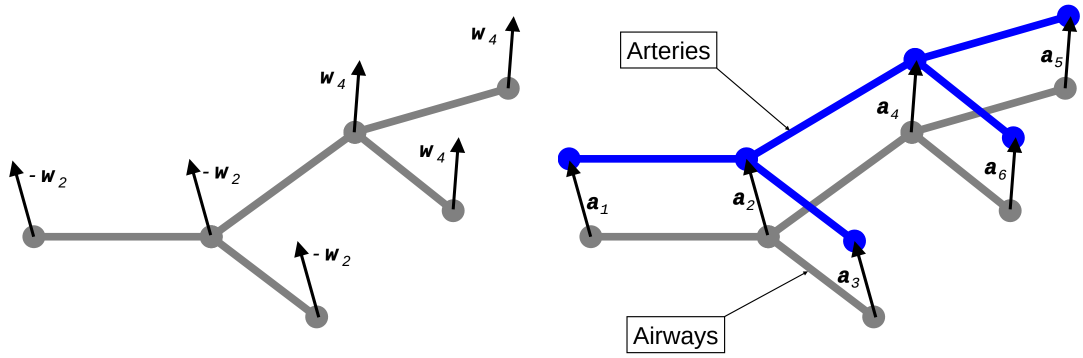

(a) (b)

Figure 2.12.: Step by step schematic showing how to generate pulmonary arteries from a random tree of airways

Algorithm 3 Generate pulmonary arteries

```
copy all airway geometry (see Figure 2.12(a))
set the arteries to the copied airway geometry
Find the normalized arterial radii:
set artery radius at generation $0$ to $r_0 = 1$
loop over all generations
    evaluate the average area of airways $\hat{A}^G_{\text{aw}}$ in generation $G$
    evaluate the average airway radius $\hat{r}^G_{\text{aw}} = \sqrt{\hat{A}^G_{\text{aw}}/\pi}$ of a generation $G$
    evaluate average arterial radius $\hat{r}^G_{\text{art}} = r_0 2^{-G/3}$ of generation $G$ [154]
    loop over all arteries in generation $G$
        get artery $i$
        evaluate arterial radius $r^G_{\text{art}_i} = \hat{r}^G_{\text{art}} \left(r^G_{\text{aw}_i}/\hat{r}^G_{\text{aw}}\right)$
    end loop
end loop
Correct arterial radii to match the wanted arterial volume:
get the volume of all arteries $\hat{V}_{\text{art}_\text{T}}$
get patient's actual arterial volume $V_{\text{art}_\text{T}}$
evaluate $\alpha_{\text{corr}} = V_{\text{art}_\text{T}}/\hat{V}_{\text{art}_\text{T}}$
scale cross-sectional area of all arteries by $\alpha_{\text{corr}}$
Scale the translation vector to prevent arteries from overlapping with airways:
loop over all nodes
    Find airway radius at $i$, $r_{\text{aw}_i}$
    Find arterial radius at $i$, $r_{\text{art}_i}$
    Evaluate translation vector $\mathbf{a}_i = \left(r_{\text{aw}_i} + r_{\text{art}_i}\right)\mathbf{w}_i$
    Shift the current node by $\mathbf{a}_i$ (see Figure 2.12(b))
end loop
```

model of the capillary network is grown between a terminal artery and a terminal vein in an iterative manner to produce the network shown in Figure 2.15. This is achieved by assuming that:

- Blood capillaries in human body are made of bifurcating trees [109].
- The length-to-radius ratios $\text{lr}_\text{a} = 12$ and $\text{lr}_\text{v} = 14$ are fixed for arterioles and venules, respectively [140].
- The terminating blood capillary radius is taken to be $4\,\mu\text{m}$ [16].
- The tree of capillaries is assumed to be symmetric. Since the spatial distribution of blood in capillaries is not of an interest in this work.
- The ratio of venules' radius to arterioles radius is taken to be $r_{\text{va}} = 1.44$ [140]
- The parent to daughter radius relationship is assumed to follow Murray's law [99].

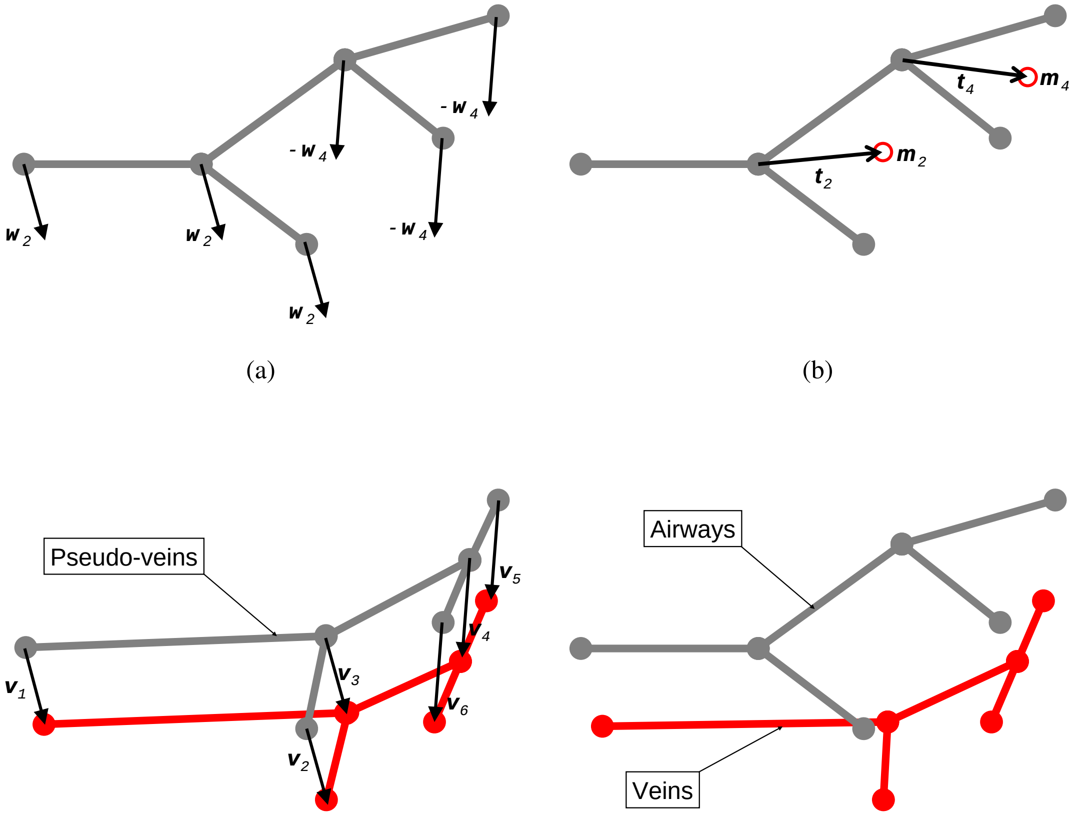

(a) (b)

(c) (d)

Figure 2.13.: Step by step schematic showing how to generate pulmonary veins from a random tree of airways

Murray's law states that

$$r_{\mathrm{p}}^{\xi} = r_{\mathrm{d}_1}^{\xi} + r_{\mathrm{d}_2}^{\xi},$$

where r_{p} is the radius of parent blood vessel, r_{d_1} the radius of the first daughter blood vessel, r_{d_2} the radius of the second daughter blood vessel, and $6/2 \leq \xi \leq 7/3$ [144]. The optimal value of ξ is $7/3$ and $6/2$ for turbulent and laminar flows, respectively. However since flow in small blood vessels is laminar ξ is taken to be 3. Thus the radial daughter to parent ratio of capillaries yields

$$\alpha_{\mathrm{dp}} = \frac{r_{\mathrm{d}_i}}{r_{\mathrm{p}}} = \left(\frac{1}{2}\right)^{1/\xi} \tag{2.5}$$

Following the definition of a capillary network, the volume of arterioles is analytically evaluated as:

$$V_{\mathrm{a}} = V_{\mathrm{a}0} \sum_{n} \alpha_{\mathrm{pd}}^{3n} 2^n,$$

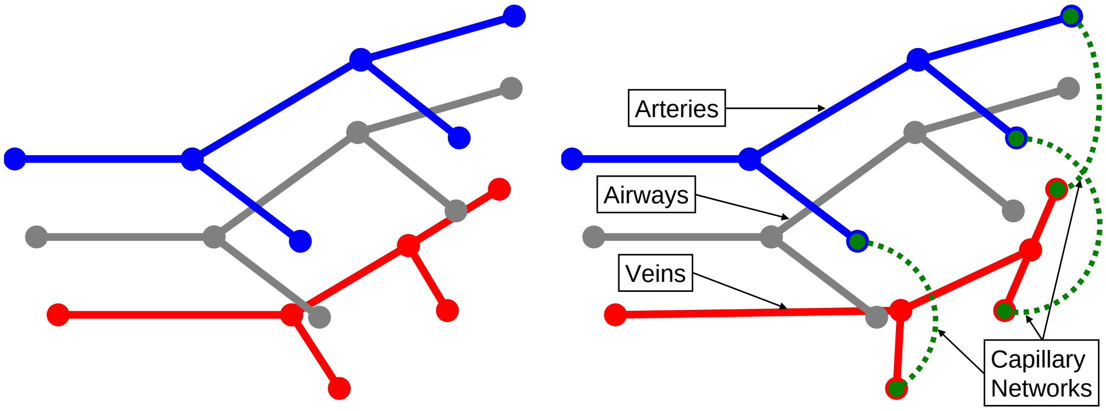
Arteries
Airways
Veins
Capillary Networks

(a) (b)

Figure 2.14.: Step by step schematic showing how to generate pulmonary capillary networks from generated pulmonary arteries and veins

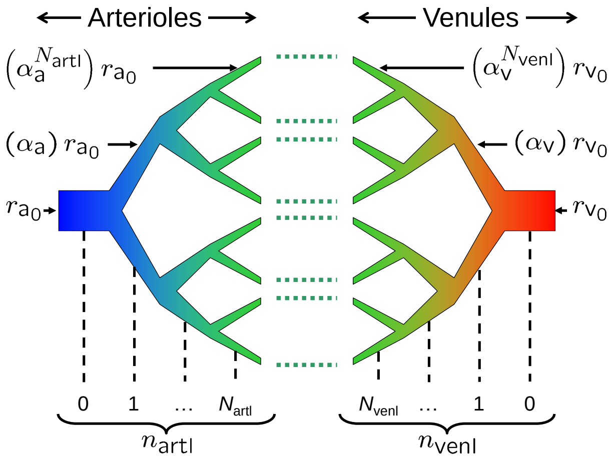
Arterioles
Venules
$\left(\alpha_{a}^{N_{artl}}\right) r_{a_0}$
$\left(\alpha_{v}^{N_{venl}}\right) r_{v_0}$
$(\alpha_a)\, r_{a_0}$
$(\alpha_v)\, r_{v_0}$
r_{a_0}
r_{v_0}
0
1
...
N_{artl}
N_{venl}
...
1
0
n_{artl}
n_{venl}

Figure 2.15.: A schematic of a pulmonary capillary network

where V_{a} is the total volume of arterioles and $V_{\mathrm{a}_0} = \pi r_{\mathrm{a}_0}^2 L_{\mathrm{a}_0}$ is the volume of the root arteriole in a tree of capillaries. However since the length-to-radius ratio is taken to be constant ($\mathrm{lr}_{\mathrm{a}} = 12$), then the total volume of a tree of arterioles yields

$$V_{\mathrm{a}} = \pi r_{\mathrm{a}_0}^3 \mathrm{lr}_{\mathrm{a}} \sum_{n=0} \alpha_{\mathrm{pd}}^{3n} 2^n \tag{2.6}$$

Similar to the arterioles, the volume of the venules is deduced to be

$$V_{\mathrm{v}} = \pi r_{\mathrm{v}_0}^3 \mathrm{lr}_{\mathrm{v}} \sum_{n=0} \alpha_{\mathrm{pd}}^{3n} 2^n$$

where V_v is the total volume of venules and V_{v_0} is the volume of the root venule in a tree of capillaries. Furthermore, since $r_{\mathrm{v}_0} = 1.44 r_{\mathrm{a}_0}$ then the volume of venules can be rewritten as

$$V_\mathrm{v} = \pi r_{\mathrm{a}_0}^3 \left(r_\mathrm{va}\right)^3 \mathrm{lr}_\mathrm{v} \sum_n \left(\alpha_\mathrm{pd}^{3n} 2^n\right). \tag{2.7}$$

Summing the total volume of arterioles and venules, i.e. eq (2.6) and eq (2.7), resulted in the following model of the capillary tree volume

$$V_\mathrm{cap} = \pi r_{\mathrm{a}_0}^3 \left(\mathrm{lr}_\mathrm{a} + \left(r_\mathrm{va}\right)^3 \mathrm{lr}_\mathrm{v}\right) \sum_n \left(\alpha_\mathrm{pd}^{3n} 2^n\right). \tag{2.8}$$

The root arterial radius of a capillary tree is found from eq (2.8)

$$r_{\mathrm{a}_0} = \left(\frac{V_\mathrm{cap}}{\pi \left(\mathrm{lr}_\mathrm{a} + \left(r_\mathrm{va}\right)^3 \mathrm{lr}_\mathrm{v}\right) \sum_n \left(\alpha_\mathrm{pd}^{3n} 2^n\right)} \right)^{1/3}. \tag{2.9}$$

The terminal arterioles in a symmetric capillary tree have a radius $\hat{r}_\mathrm{term} = r_{\mathrm{a}_0} \left(\alpha_\mathrm{pd}\right)^{n_\mathrm{max}}$. This meant that eq (2.9) is solved iteratively by finding n_max that minimizes $|\hat{r}_\mathrm{term} - r_\mathrm{term}|$.

The total volumes of blood in pulmonary arteries, veins, and capillaries are set to $V_{\mathrm{art}_\mathrm{T}} = 135\,\mathrm{ml}$, $V_{\mathrm{ven}_\mathrm{T}} = 235, \mathrm{ml}$ and $V_{\mathrm{cap}_\mathrm{T}} = 80\,\mathrm{ml}$, respectively [146]. Algorithms 2, 3, 4, and 5 are applied onto the airway geometry in Figure 2.3 and Figure 2.6. The resulting pulmonary circulatory system are shown in Figure 2.16. The detailed cross-sectional areas and the lengths of the arteries and veins are shown in Figure 2.17. The detailed capillary network number of generation, terminal arteriole radii, and capillary tree volumes are also detailed in Figure 2.17. The results in Figure 2.17 show a very good agreement between the model and the morphologically reported measurements [154].

2.5. Oxygen exchange interface

In the current work, each terminal airway is connected to one and only one acinus, one terminal artery, and one terminal vein. This means that each acinus has one and only one tree of capillaries with whom O_2 is exchanged. Therefore, each acinus is connected to the closest network of capillaries as shown in Figure 2.18. Based on morphological information, this work defined the O_2 exchange surface as the alveolar surface in contact with the blood capillaries. Knowing that 90% of the alveolar surface is in contact with blood capillaries [56], the O_2 exchange surface is simply defined as 90% of the total alveolar surface. In this work, the respiratory zone is defined in Section 2.2 as a volume filled with the alveolar ducts of Denny and Schroter [28] (see also Figure 3.8(a)) and related to the acinar volume.

Each alveolar duct is composed of $N_\mathrm{oct}^\mathrm{ad} = 36$ truncated octahedra among which $N_\mathrm{oct}^\mathrm{AS} = 32$ built up the alveolar sacs and the remaining $N_\mathrm{oct}^\mathrm{Duct} = 4$ built up the duct. This means that, the sum of all alveolar surface areas is estimated as the total area of 32 alveoli minus the area removed for the duct (see A_duct in Figure 2.18(b)). The area of the duct made of $N_\mathrm{oct}^\mathrm{Duct}$ of

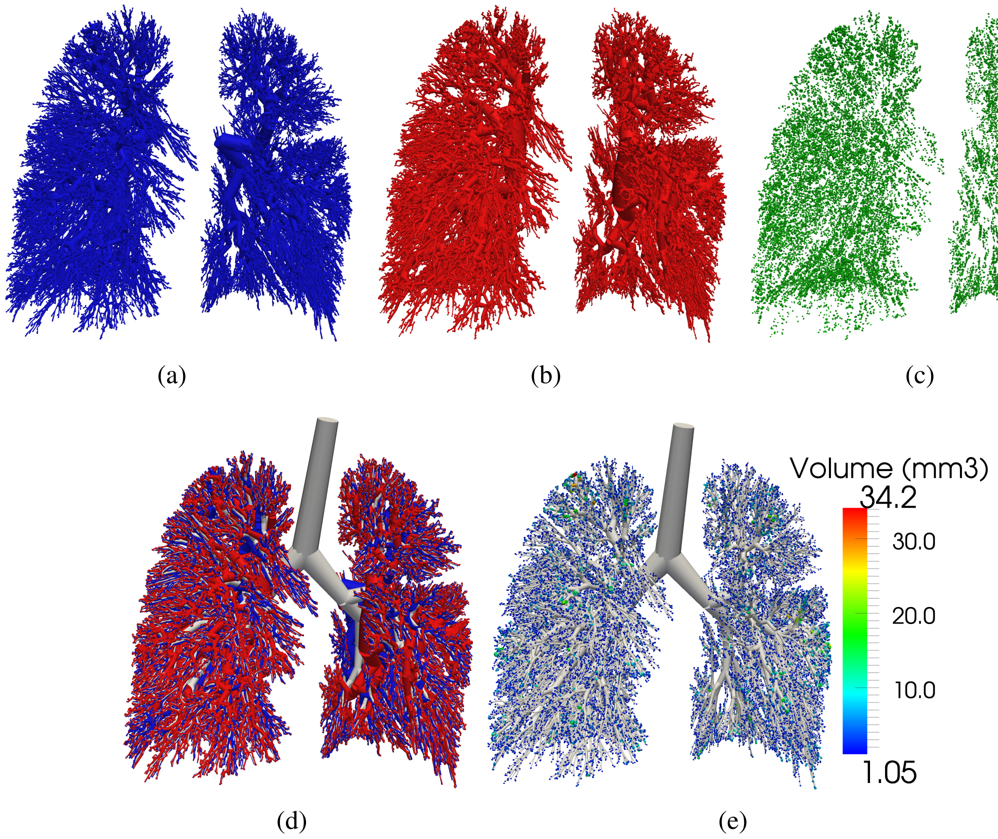

(a) (b) (c)

(d) (e)

Figure 2.16.: Generated trees of (a) pulmonary arteries, (b) pulmonary veins, and (c) pulmonary capillaries. The airway tree shown together with (d) pulmonary arteries and veins and (e) pulmonary capillaries.

truncated octahedra is equal to

$$A_{\text{duct}} = N_{\text{oct}}^{\text{Duct}} A_{\text{oct}} - \left(2N_{\text{oct}}^{\text{Duct}} - 2\right) \left(\frac{3\sqrt{3}}{2}\right) a^2,$$

where a is the edge length of a truncated octahedron and $A_{\text{oct}} = \left(6 + 12\sqrt{3}\right) a^2$ the area of a truncated octahedron. The alveolar duct used in this work has $N_{\text{oct}}^{\text{Duct}} = 4$, thus the duct area is

$$A_{\text{duct}} = 4A_{\text{oct}} - 9\sqrt{3}a^2.$$

Therefore, the alveolar duct used in this work has a total area of

$$A_{\text{ad}} = N_{\text{oct}}^{\text{AS}} A_{\text{oct}} - A_{\text{duct}} = 32A_{\text{oct}} - \left(4A_{\text{oct}} - 9\sqrt{3}a^2\right),$$

i.e.

$$A_{\text{ad}} = \left(168 + 345\sqrt{3}\right) a^2. \tag{2.10}$$

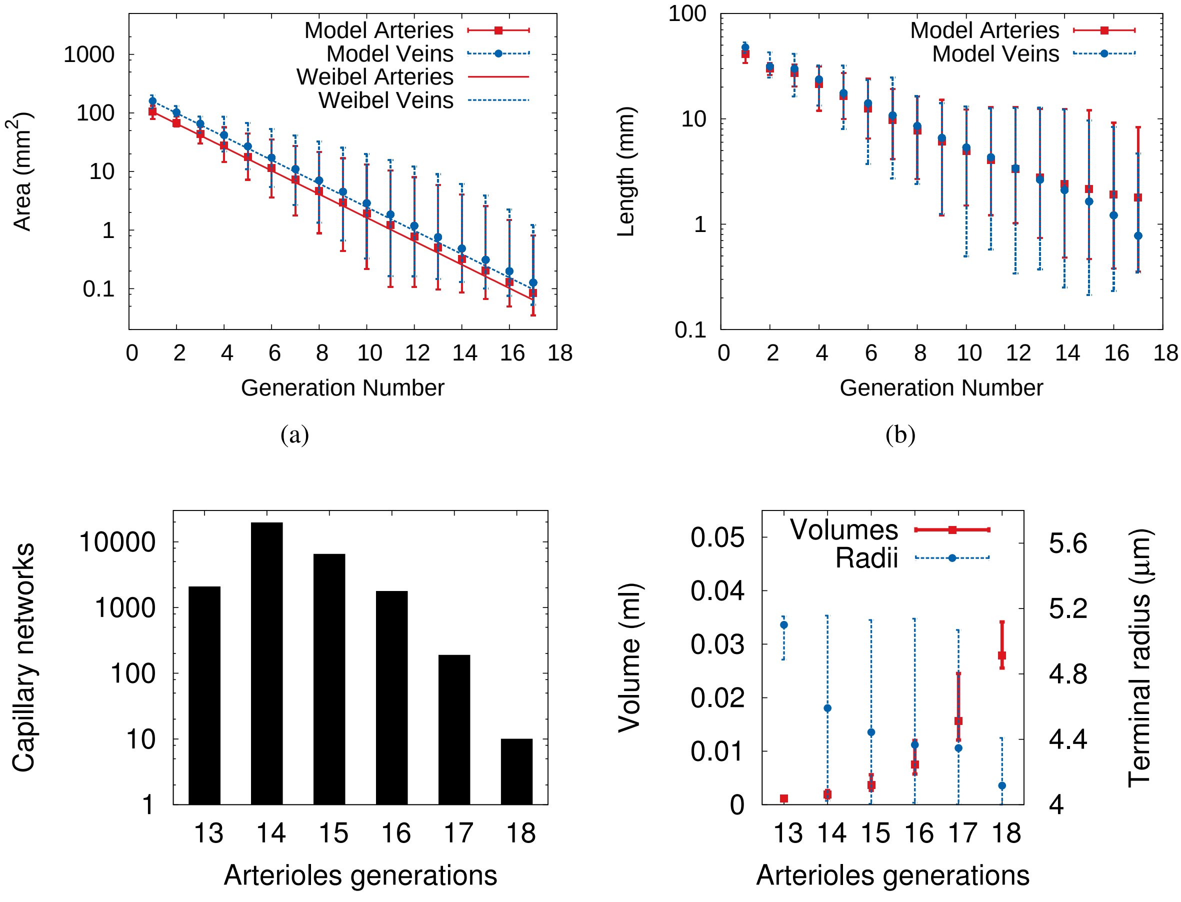

(a) (b)

(c) (d)

Figure 2.17.: Detailed (a) pulmonary arterial and venous cross-sectional areas, (b) pulmonary arterial and venous lengths for different generation numbers. Detailed total number of arteriole generations within the generated capillary trees versus (c) number of capillary trees, (d) volumes of capillary trees and arteriole terminal radius.

The alveolar duct surface area is related to the alveolar duct volume through the edge length a as following:

$$V_{\mathrm{ad}} = N_{\mathrm{oct}} V_{\mathrm{oct}} = 36 \left(8\sqrt{2}\right) a^3 = \left(288\sqrt{2}\right) a^3,$$

i.e. the edge length is deduced to be

$$a = \left(\frac{V_{\mathrm{ad}}}{288\sqrt{2}}\right)^{1/3}. \tag{2.11}$$

substituting eq (2.11) in eq (2.10) resulted in the following relationship between the alveolar duct area and volume

$$A_{\mathrm{ad}} = \left(168 + 345\sqrt{3}\right)\left(\frac{V_{\mathrm{ad}}}{288\sqrt{2}}\right)^{2/3}. \tag{2.12}$$

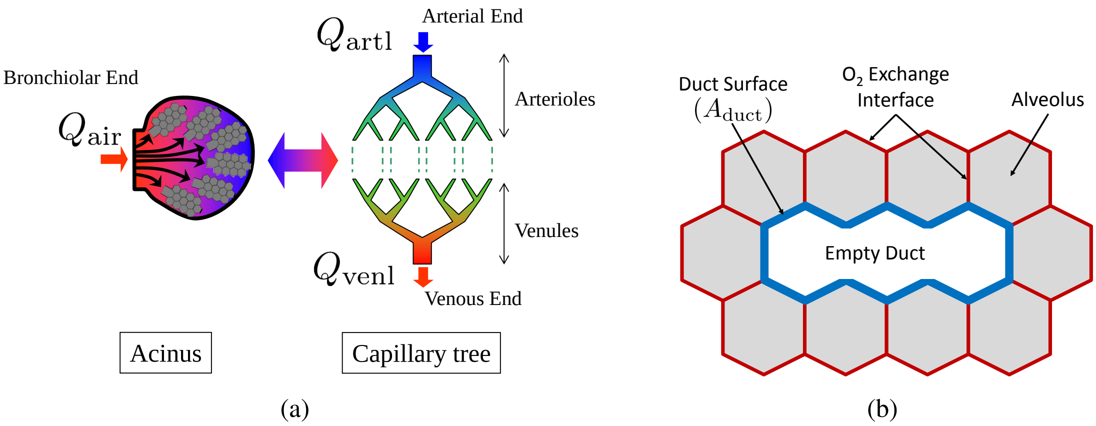
Bronchiolar End
Q_{air}
Arterial End
Q_{artl}
Arterioles
Venules
Q_{venl}
Venous End
Acinus
Capillary tree
(a)
Duct Surface
(A_{duct})
O_2 Exchange
Interface
Alveolus
Empty Duct
(b)

Figure 2.18.: Oxygen exchange interface (a) between an acinus and a tree of capillaries and (b) with in an alveolar duct

The area and the volume of an acinus are defined in this worked as the number of alveolar ducts an acinus has multiplied by the area and volume of an alveolar duct, respectively. Thus substituting the area and the volume of an acinus in eq (2.12) resulted in the following relationship between total alveolar surface area and total volume of air within an acinus

$$A_{\mathrm{ac}} = N_{\mathrm{ad}} \left(168 + 345\sqrt{3}\right) \left(\frac{V_{\mathrm{ac}}}{288 N_{\mathrm{ad}} \sqrt{2}}\right)^{2/3},$$

where N_{ad} is the number of alveolar ducts in an acinus. Finally, the acinar O_2 exchange interface area is found to be

$$A^{\mathrm{I}}_{\mathrm{O}_2} = 0.9 A_{\mathrm{ac}} = 0.9 N_{\mathrm{ad}} \left(168 + 345\sqrt{3}\right) \left(\frac{V_{\mathrm{ac}}}{288 N_{\mathrm{ad}} \sqrt{2}}\right)^{2/3}. \tag{2.13}$$

Algorithm 4 Generate pulmonary veins

```
Create the pseudo-veins:
copy airway geometry (see Figure 2.13(a))
invert $\mathbf{w}_i$ vectors ($\mathbf{w}_i = -\mathbf{w}_i$)
set the veins to the copied airway geometry
Evaluate the vectors that will translate the pseudo-veins into veins:
loop over all venous nodes
    get current node coordinates $\mathbf{x}_i$
    if node $i$ is a bifurcation node then
        get the other two daughter branches' nodal coordinates $\mathbf{x}_j$ and $\mathbf{x}_k$
        evaluate the midpoint node of nodes $j$ and $k$ ($\mathbf{m}_i = (\mathbf{x}_j + \mathbf{x}_k)/2$)
        evaluate artery-to-vein nodal translation vector $\mathbf{m}_i = \mathbf{m}_i - \mathbf{x}_i$
        set artery-to-vein nodal translation vector $\mathbf{t}_i = \mathbf{0}$
    end if
end loop
Translate the pseudo-veins into veins geometry:
loop over all venous nodes
    get node $i$
    translate all venous nodes by $\mathbf{t}_i$ (see Figure 2.13(b))
end loop
Evaluate the venous normalized radii:
set venous radius at generation $0$ to $r_0 = 1$
loop over all generations
    evaluate the average area of airways $\hat{A}_{\text{aw}}^{G}$ in generation $G$
    evaluate the average airway radius $\hat{r}_{\text{aw}}^{G} = \sqrt{\hat{A}_{\text{aw}}^{G}/\pi}$ of a generation $G$
    evaluate average venous radius $\hat{r}_{\text{ven}}^{G} = r_0 2^{-G/3}$ of generation $G$ [60; 154]
    loop over all veins in generation $G$
        get vein $i$
        evaluate the vein's radius $r_{\text{ven}_i}^{G} = \hat{r}_{\text{ven}}^{G}\left(r_{\text{aw}_i}^{G}/\hat{r}_{\text{aw}}^{G}\right)$
    end loop
end loop
Correct venous radii to match the wanted venous volume:
get the volume of all veins $\hat{V}_{\text{ven}_\text{T}}$
get patient's actual venous volume $V_{\text{ven}_\text{T}}$
evaluate $\alpha_{\text{corr}} = V_{\text{ven}_\text{T}}/\hat{V}_{\text{ven}_\text{T}}$
scale cross-sectional area of all veins by $\alpha_{\text{corr}}$
Scale the translation vector to prevent veins from overlapping with airways:
loop over all nodes
    find airway radius at $i$, $r_{\text{aw}_i}$
    find vein's radius at $i$, $r_{\text{ven}_i}$
    evaluate translation vector $\mathbf{v}_i = \left(r_{\text{aw}_i} + r_{\text{ven}_i}\right)\mathbf{w}_i$
    shift all venous nodes by $\mathbf{v}_i$ (see Figure 2.13(c))
end loop
```

Algorithm 5 Generate pulmonary capillaries

```
get patient's capillary blood volume ($V_{\mathrm{cap}_\mathrm{T}}$)
evaluate the total volume of air in the respiratory zone ($V_{\mathrm{ac}_\mathrm{T}}$)
Generate capillary trees:
loop over all terminal airways
    find the corresponding acinar tree
    find the corresponding terminal artery
    find the corresponding terminal vein
    get the volume of the corresponding acinar tree ($V_{\mathrm{ac}_i}$)
    evaluate the volume of the corresponding capillary tree ($V_{\mathrm{cap}_i} = V_{\mathrm{cap}_\mathrm{T}} (V_{\mathrm{ac}_i} / V_{\mathrm{ac}_\mathrm{T}})$)
    grow a tree of arterioles and venules
    connect capillary tree between the corresponding terminal artery and terminal vein (see Figure 2.14(b))
end loop
```

3. Mathematical formulations

> ”There is nothing that can be said by mathematical symbols and relations which cannot also be said by words. The converse, however, is false. Much that can be and is said by words cannot be put into equations because it is nonsense.”
>
> - Clifford A. Truesdell, 1966

This section is dedicated to the mathematical formulations of the different lung components and materials. The 3D formulation of the blood and air domains is initially presented. The 3D formulation is then used to deduce the 1D pipe flow formulation, which in turn is used to deduce the 0D pipe flow formulation. The lung parenchyma is formulated as groups of 0D acinar elements and 0D inter-acinar linkers. Finally, the 1D transport of O_2 in blood and air and the 1D diffusion of O_2 between air and blood are described.

3.1. 3D fluid domains

The two fluid domains considered in this work are air and blood. Air is a compressible Newtonian fluid. However, due to low Mach flow of air in lungs (<0.1 in physiology), air has incompressible flow characteristics [66]. Under normal room conditions, air gains most of its temperature and moist from the upper airways (nose and mouth) [165]. This means that air enters the trachea at a temperature close to 37°C. This also means that air density is considered to be constant within the entire lung. Blood is an incompressible non-Newtonian fluid whose viscosity is highly dependent on the hematocrit number and the blood shear rate. Under healthy conditions, bloods hematocrit is 40%. Furthermore, in large arteries blood is exposed to high shear rates. Thus, for all healthy large arteries blood behaves like a Newtonian fluid [43; 159]. As such, throughout this work, blood in large blood vessels and air inside the lung airways are considered to be incompressible Newtonian fluids.

To start with, the boundary value problem of Figure 3.1 is assumed. The flow is described using the incompressible Navier-Stokes equations, representing the motion of fluid in domain Ω

$$\nabla \cdot \mathbf{u} = 0, \tag{3.1}$$

$$\frac{\partial \mathbf{u}}{\partial t} + \mathbf{u} \cdot \nabla \mathbf{u} + \nabla p - 2\nu \nabla \cdot \varepsilon\left(\mathbf{u}\right) = \mathbf{f}, \tag{3.2}$$

where $\mathbf{u}$ is the velocity, p the kinematic pressure, $\mathbf{f}$ the body forces and ν the kinematic viscosity. The rate-of-deformation tensor $\varepsilon\left(\mathbf{u}\right)$ is defined as

$$\varepsilon\left(\mathbf{u}\right) = \frac{1}{2}\left(\nabla \mathbf{u} + \left(\nabla \mathbf{u}^{\mathrm{T}}\right)\right).$$

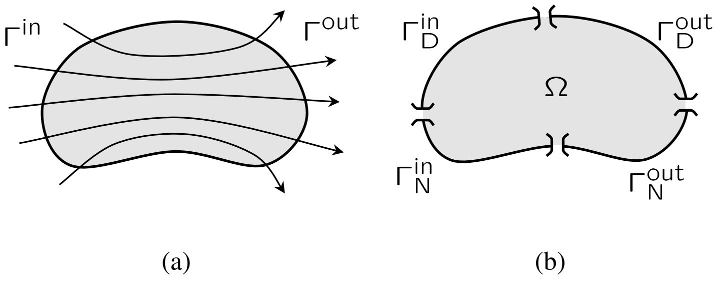

Γ^{in}
Γ^{out}
$\Gamma_{\text{D}}^{\text{in}}$
$\Gamma_{\text{D}}^{\text{out}}$
Ω
$\Gamma_{\text{N}}^{\text{in}}$
$\Gamma_{\text{N}}^{\text{out}}$
(a)
(b)

Figure 3.1.: Illustration of the boundary value problem of a flow through domain Ω.

Inflow and outflow parts of the domain are denoted by Γ^{in} and Γ^{out}, respectively:

$$\Gamma^{\text{in}} = \{\mathbf{x} \in \Gamma \mid u_{\text{n}}(\mathbf{x}, t) \leq 0\},\ \Gamma^{\text{out}} = \Gamma - \Gamma^{\text{in}},$$

where

$$u_{\text{n}} = \mathbf{u} \cdot \mathbf{n},$$

with $\mathbf{n}$ denoting the unit normal vector pointing outward from the boundary and u_{n} the normal velocity on the boundary. The Dirichlet part Γ_{D} and the Neumann part Γ_{N} of the boundary are distinguished such that $\Gamma_{\text{D}} \cap \Gamma_{\text{N}} = \emptyset$, $\Gamma_{\text{D}} \cup \Gamma_{\text{N}} = \Gamma$, $\Gamma_{\text{D}}^{\text{in/out}} = \Gamma_{\text{D}} \cap \Gamma^{\text{in/out}}$ and $\Gamma_{\text{N}}^{\text{in/out}} = \Gamma_{\text{N}} \cap \Gamma^{\text{in/out}}$. On the Dirichlet boundary Γ_{D}, the velocity is directly prescribed

$$\mathbf{u} = \mathbf{u}_{\text{D}}.$$

On the Neumann boundary Γ_{N}, the conditions are differently prescribed on in- and outflow boundaries as is consistently derived in [53] based on a method originally proposed in [64]): For the inflow Neumann boundary, the total momentum flux is prescribed: $\Gamma_{\text{N}}^{\text{in}}$,

$$-u_{\text{n}}\mathbf{u} - p\mathbf{n} + 2\nu\varepsilon(\mathbf{u}) \cdot \mathbf{n} = \mathbf{h}^{\text{in}}, \tag{3.3}$$

and for the $\Gamma_{\text{N}}^{\text{out}}$ only the traction:

$$-p\mathbf{n} + 2\nu\varepsilon(\mathbf{u}) \cdot \mathbf{n} = \mathbf{h}^{\text{out}}. \tag{3.4}$$

As such, the Neumann boundary condition is described in a unified form as follows:

$$-u_{\text{n}}^{\text{in}}\mathbf{u} - p\mathbf{n} + 2\nu\varepsilon(\mathbf{u}) \cdot \mathbf{n} = \mathbf{h}, \tag{3.5}$$

where

$$u_{\text{n}}^{\text{in}} = \frac{u_{\text{n}} - |u_{\text{n}}|}{2},$$

which yields to u_{n} on $\Gamma_{\text{N}}^{\text{in}}$ and zero elsewhere. For sufficiently high Reynolds numbers, the viscous term in (3.5) is negligible as compared to the other terms and is neglected throughout this work.

3.2. 1D pipe flow domain

Under certain physical and geometrical assumptions, airways and blood vessels can be modeled using cylindrical compliant pipes [125; 126]. The physical assumptions are that blood vessels and airways have axi-symmetric velocity profiles and their walls are not deformable in the length direction, i.e. they are subjected to plane strain conditions. The geometric assumption is that blood vessels and airways are axi-symmetric in shape, as shown in Figure 3.2(a). As such, airways or blood vessels are reduced to the pipe model shown in Figure 3.2(b).

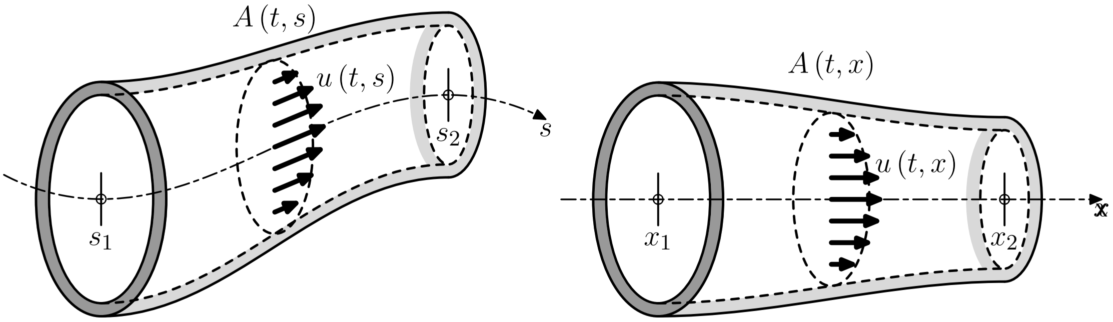

(a) Curved circular pipe having s as a centerline (b) Straight circular pipe having x as a centerline

Figure 3.2.: Illustration of blood vessels and airways using axi-symmetric pipes.

Mathematically, the flow symmetry is represented with a power-law velocity profile

$$u(x,r,t) = \frac{\gamma+2}{\gamma} U \left(1 - \left(\frac{r}{R}\right)^{\gamma}\right),$$

where $u(r,x,t)$ is the fluid velocity at (r,x,t), r the local radial coordinate, R the local pipe radius, γ an even number and U the mean velocity normal to a cross-sectional area $A(x,t)$. Figure 3.3 shows the influence of γ on the velocity profile, where $\gamma = 2$ led to a parabolic velocity profile and $\gamma = \infty$ to a flat velocity profile.

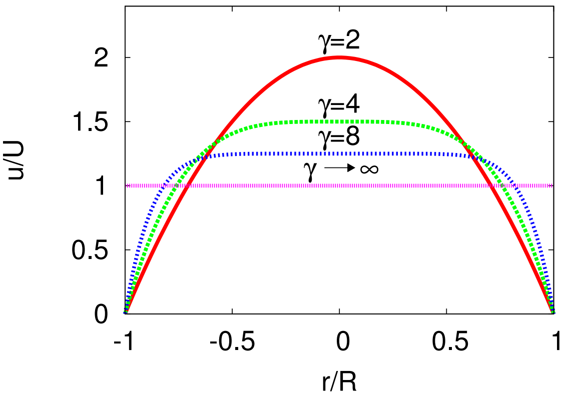

Figure 3.3.: A radial cut through a normalized velocity profile showing the influence of γ on the profile shape.

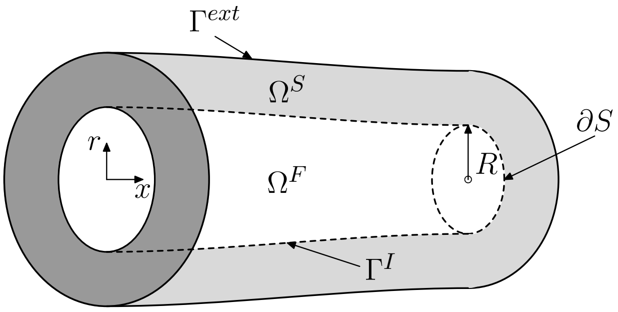

Figure 3.4.: Illustration of the various domains within the compliant pipe. Ω^{F}= fluid domain; Ω^{S}= structure domain; Γ^{I}= fluid-structure interface; Γ^{ext} = external pipe surface; ∂S = perimeter of a fluid cross-sectional surface S.

Figure 3.4 illustrates the various domains in a compliant pipe. The dimension reduction is achieved in the following section by applying the Reynolds transport theorem to mass and momentum conservation of the 3D controlled volume. Furthermore, wall models, compatibility conditions and various boundary conditions are also covered in the following sections. The state variables used for reducing problems dimension are defined as:

$$\begin{aligned} A &= \int_{S(t,x)} \mathrm{d}\sigma \\ Q &= \int_{S(t,x)} u\left(t,x\right)\mathrm{d}\sigma = UA \\ P &= \frac{1}{A}\int_{S(t,x)} p\left(t,x\right)\mathrm{d}\sigma, \end{aligned}$$

where A is the area of a cross-section S, Q the total flow rate at cross section σ, p the pressure inside the pipe and P the average pressure on S.

3.2.1. Conservation of mass

Applying the Reynolds' transport theorem for the mass inside the control volume of the 1D fluid domain (Ω^{F} in Figure 3.4), the mass conservation is

$$\rho\frac{\mathrm{d}V}{\mathrm{d}t} + \rho Q\left(l,t\right) - \rho Q\left(0,t\right) = 0,$$

where V is the volume of a pipe, l the length of a pipe and ρ is the density of the fluid. Knowing that

$$\int_0^l \frac{\partial Q\left(t\right)}{\partial x}\mathrm{d}x = Q\left(l,t\right) - \rho Q\left(0,t\right),$$

the mass conservation of the incompressible fluid in Ω^{F} is

$$\frac{\partial A}{\partial t} + \frac{\partial Q}{\partial x} = 0. \tag{3.6}$$

3.2.2. Balance of momentum

Applying the Reynolds transport theorem the momentum of the controlled volume Ω^{F}, the balance of momentum is

$$\frac{\mathrm{d}}{\mathrm{d}t}\int_0^l \rho Q \mathrm{d}x + (\alpha\rho Q u)_l - (\alpha\rho Q u)_0 = F, \tag{3.7}$$

where F is the total external force applied onto the control volume and α is the momentum correction factor defined as

$$\alpha = \frac{\int_S \rho u^2 \mathrm{d}\sigma}{\rho U^2 A} = \frac{2+\gamma}{1+\gamma}.$$

The balance of forces on Ω^{F} yields

$$F = (PA)_0 - (PA)_l + \int_0^l \int_{\partial s} p \mathrm{d}s\mathrm{d}x + \int_0^l f \mathrm{d}x,$$

where f is the shear force acting on ∂S. The wall shear stress is defined as

$$\tau_{\mathrm{w}} = \mu \left.\frac{\partial u}{\partial r}\right|_{r=R} = \mu\left(\gamma+2\right)\frac{U}{R},$$

where μ is the fluid dynamic viscosity. Thus, the wall shear force f is

$$f = \int_{\partial S} \tau_{\mathrm{w}} \mathrm{d}s = 2\pi\mu\left(\gamma+2\right)\frac{Q}{A}.$$

Due to plain strain assumption, x and t are independent variables, thus eq (3.7) can be rewritten as

$$\int_0^l \left(\rho\frac{\partial Q}{\partial t} + \rho\frac{\partial \alpha Q U}{\partial x}\right)\mathrm{d}x = \int_0^l \left(-\frac{\partial PA}{\partial x} + p\frac{\partial A}{\partial x} + f\right)\mathrm{d}x.$$

Finally, after some mathematical manipulations, the balance of momentum in a compliant pipe is described as following

$$\frac{\partial Q}{\partial t} + \frac{\partial \alpha Q^2/A}{\partial x} = -\frac{A}{\rho}\frac{\partial P}{\partial x} + 2\pi\frac{\mu}{\rho}\left(\gamma+2\right)\frac{Q}{A}. \tag{3.8}$$

3.2.3. Wall mechanics

To close the problem defined by eq (3.6) and eq (3.8), a pressure to area relationship is required. Such a relationship has been earlier found by Formaggia et al. [38] such that it accounted for several phenomena, such as inertial and visco-elastic effects. The visco-elastic behavior of the one dimensional pipe wall is

$$P = P_{\text{ext}} + \psi^{\text{e}} + \psi^{\text{v}}, \tag{3.9}$$

where

$$\psi^{\text{e}} = \beta_{\text{s}} \frac{\sqrt{A} - \sqrt{A_0}}{A_0}, \ \psi^{\text{v}} = \frac{\gamma_{\text{s}}}{A\sqrt{A}} \frac{\partial A}{\partial t},$$

with

$$\beta_{\text{s}} = \sqrt{\pi} \frac{h_{\text{s}} E_{\text{s}}}{1 - \nu_{\text{s}}^2},$$

where A_0 is the reference area, h_{s} the wall thickness, ν_{s} the wall Poisson ratio, E_{s} the wall elastic Young's modulus and γ_s is a viscous variable that will defined later in Chapter 4 explicitly for blood vessels and for airways. The wall inertial effects are neglected due to their negligible contribution [38].

3.2.4. Compatibility conditions (characteristic variables)

Combining equations (3.6), (3.8), and (3.9), a 1D viscoelastic pipe is described by the set of equation given in the following

$$\begin{cases} \frac{\partial A}{\partial t} + \frac{\partial Q}{\partial x} = 0 & \text{in } (0, l) \times (0, T_{\text{fin}}), \\ \frac{\partial Q}{\partial t} + \frac{\partial \alpha Q^2/A}{\partial x} + \frac{A}{\rho}\frac{\partial P}{\partial x} - 2\pi\frac{\mu}{\rho}(\gamma + 2)\frac{Q}{A} = 0 & \text{in } (0, l) \times (0, T_{\text{fin}}), \\ P = P_{\text{ext}} + \psi^{\text{e}} + \psi^{\text{v}} & \text{in } (0, l) \times (0, T_{\text{fin}}), \\ A = A_0, \ Q = 0 & \text{in } (0, l) \times \{0\}, \end{cases} \tag{3.10}$$

where T_{fin} is the final simulation time. The problem of eq (3.10) requires the knowledge of two physical variables at each boundary. However, in practice only one physical variable is available. To solve this problem, the viscous effects at the boundary are initially neglected and an eigenvalue analysis is performed by firstly rewriting eq (3.10) in the following compact form

$$\frac{\partial \mathbf{U}}{\partial t} + \mathbf{H}\frac{\partial \mathbf{U}}{\partial x} = \mathbf{S} \tag{3.11}$$

or as

$$\frac{\partial \mathbf{U}}{\partial t} + \frac{\partial \mathbf{F}}{\partial x} = \mathbf{S}, \tag{3.12}$$

where

$$\mathbf{U} = \begin{bmatrix} A \\ Q \end{bmatrix}, \ \mathbf{H} = \frac{\partial \mathbf{F}}{\partial x}, \ \mathbf{F} = \begin{bmatrix} Q \\ F_2 \end{bmatrix}, \ \mathbf{S} = \begin{bmatrix} 0 \\ S_2 \end{bmatrix},$$

and

$$\begin{aligned}
F_2 &= \int_{A_0}^{A} \frac{A}{\rho}\frac{\partial \psi^{\mathrm{e}}}{\partial A}\mathrm{d}A + \alpha\frac{Q^2}{A}, \\
S_2 &= K_{\mathrm{R}}\frac{Q}{A} + \frac{A}{\rho}\left(\frac{\partial \psi^{\mathrm{e}}}{\partial A_0}\frac{\partial A_0}{\partial x} + \frac{\partial \psi^{\mathrm{e}}}{\partial \beta_{\mathrm{s}}}\frac{\partial \beta_{\mathrm{s}}}{\partial z}\right), \\
K_{\mathrm{R}} &= -2\pi\frac{\mu}{\rho}\left(\gamma+2\right).
\end{aligned}$$

The motivation behind performing an eigenvalue analysis on eq (3.11) is the pulsating nature of blood flow [43; 159]. This is achieved by taking Λ and $\mathbf{L}$, the eigenvalue and eigenvalue vector matrices of $\mathbf{H}$, such that $\mathbf{LHL}^{-1} = \Lambda$. Thus

$$\Lambda = \left[\begin{array}{cc} \lambda_1 & 0 \\ 0 & \lambda_2 \end{array}\right], \ \mathbf{L} = \chi\left[\begin{array}{cc} \lambda_1 & 1 \\ \lambda_2 & 1 \end{array}\right],$$

where

$$\lambda_{1,2} = \alpha\frac{Q}{A} \pm \underbrace{\sqrt{c^2 + \alpha\left(\alpha-1\right)\left(\frac{Q}{A}\right)^2}}_{c_\alpha}$$

and χ is a random non-zero number taken to be 1. c is the characteristic wave speed and found to be

$$c^2 = \left(\frac{\beta}{2A_0\rho}\right)A^{1/2}$$

Under physiological conditions $A\left(t,x\right) > 0$ and eq (3.9) results in $\partial\psi^{\mathrm{e}}/\partial A > 0$. This means that $\lambda_1 \geq 0$ and $\lambda_1 \leq 0$, which means that eq (3.11) is a hyperbolic problem. In other words, the flow within a 1D pipe is expressed via two pseudo-characteristic waves traveling in opposite directions. These pseudo-characteristics waves are called Riemann variables $\mathbf{W}$ and defined such that $\partial\mathbf{W}/\partial\mathbf{U} = \mathbf{L}$. Thus, eq (3.11) is reformulated as:

$$\frac{\partial \mathbf{W}}{\partial t} + \Lambda\frac{\partial \mathbf{W}}{\partial x} = \mathbf{LS}, \ \mathbf{W} = \left[W_1 \ W_2\right]^{\mathrm{T}}. \tag{3.13}$$

Solving eq (3.13) analytically results to

$$W_{1,2} = \frac{Q}{A} \pm 4c.$$

In other words

$$Q = A\frac{W_1+W_2}{2}$$

and

$$A = \left(\frac{W_1-W_2}{8}\right)^4\left(\frac{2\rho}{\beta}\right)^2.$$

Numerically, from eq (3.13) the resulting values of W are

$$\begin{aligned} W_1^{n+1}|_{x=L} &= W_1^n|_{x=L-\lambda_1\Delta t} \\ W_2^{n+1}|_{x=0} &= W_2^n|_{x=-\lambda_2\Delta t}. \end{aligned}$$

3.2.5. Boundary conditions

To close the 1D pipe problem boundary conditions prescribing inlet, outlet, and junction boundaries are derived in what follows

Inlet and terminal boundary conditions

The inlet and the terminal boundary conditions are either strongly enforced or weakly enforced. The strongly enforced boundary conditions are obtained by prescribing the exact boundary value without any further consideration of the waves traveling inside the system. The weakly enforced boundaries are obtained by prescribing the nearest value to the desired one which would not disturb the waves traveling out of the system. This is achieved via describing a reflection factor $R_\mathrm{f} \in [0,1]$ such that the boundary conditions in the following section became strongly enforced when $R_\mathrm{f} = 1$ and weakly enforced (wave absorbing) when $R_\mathrm{f} = 0$ [100; 101].

Reflective boundary condition

The reflective boundary condition determines whether a wave approaching a boundary should be reflected back into the system or absorbed out the system. At an inlet the reflected/absorbed wave is

$$W_2 = -R_\mathrm{f}\left(W_1 - W_1^0\right) + W_2^0.$$

At an outlet the reflective boundary condition is

$$W_1 = -R_\mathrm{f}\left(W_2 - W_2^0\right) + W_1^0.$$

Once the reflected/absorbed wave is evaluated, the boundary degrees of freedom are evaluated as following

$$\begin{aligned} A_{\mathrm{in/out}} &= \left(\frac{W_1 - W_2}{8}\right)^4 \left(\frac{2\rho}{\beta}\right)^2, \\ Q_{\mathrm{in/out}} &= A\frac{W_1 + W_2}{2}. \end{aligned}$$

Prescribed cross-sectional area condition

The cross-sectional area boundary condition $\bar{A}_{\mathrm{in/out}}$ is derived as following:

$$\begin{aligned}
A_{\mathrm{in/out}} &= \bar{A}_{\mathrm{in/out}}, \\
U_{\mathrm{in/out}} &= \left(R_{\mathrm{f}} W^0_{2/1} - (1 - R_{\mathrm{f}})\, W_{2/1}\right) \pm 4 \left(\bar{A}\right)^{1/4} \sqrt{\frac{\beta}{2\rho A_0}}, \\
Q_{\mathrm{in/out}} &= U_{\mathrm{in/out}} A_{\mathrm{in/out}}.
\end{aligned}$$

Prescribed pressure condition

The pressure boundary condition $\bar{P}_{\mathrm{in/out}}$ is derived as following:

$$\begin{aligned}
A_{\mathrm{in/out}} &= \left(\frac{\bar{P} - P_{ext}}{\beta} + \sqrt{A_0}\right)^2, \\
U_{\mathrm{in/out}} &= \left(R_{\mathrm{f}} W^0_{2/1} - (1 - R_{\mathrm{f}})\, W_{2/1}\right) \pm 4 \left(A\right)^{1/4} \sqrt{\frac{\beta}{2\rho A_0}}, \\
Q_{\mathrm{in/out}} &= U_{\mathrm{in/out}} A_{\mathrm{in/out}}.
\end{aligned}$$

Prescribed velocity condition

The velocity boundary condition $\bar{U}_{\mathrm{in/out}}$ is derived as following:

$$\begin{aligned}
A_{\mathrm{in/out}} &= \frac{\left(\bar{U}_{\mathrm{in/out}} \mp \left(R_{\mathrm{f}} W^0_{2/1} - (1 - R_{\mathrm{f}})\, W_{2/1}\right)\right)^4}{64} \left(\frac{\rho A_0}{\beta}\right)^2, \\
U_{\mathrm{in/out}} &= \bar{U}_{\mathrm{in/out}}, \\
Q_{\mathrm{in/out}} &= U_{\mathrm{in/out}} A_{\mathrm{in/out}}.
\end{aligned}$$

Prescribed volumetric flow rate

The flow rate boundary condition $\bar{Q}_{\mathrm{in/out}}$ is derived by iteratively solving the following nonlinear problem for $A_{\mathrm{in/out}}$:

$$\begin{aligned}
Q_{\mathrm{in/out}} &= \bar{Q}_{\mathrm{in/out}}, \\
\mathcal{F}_Q &= \left(R_{\mathrm{f}} W^0_{2/1} - (1 - R_{\mathrm{f}})\, W_{2/1}\right) A_{\mathrm{in/out}} \left(1 \pm 4 \sqrt{\frac{\beta}{2\rho A_0}} \left(A_{\mathrm{in/out}}\right)^{1/4}\right) - \bar{Q}_{\mathrm{in/out}} = 0.
\end{aligned}$$

Windkessel boundary conditions

Windkessel boundary conditions are used to reduce the trimmed terminal sections into a one point boundary condition. They are known to well mimic the behavior of downstream trees, especially in blood vessels [156]. They can be tricky to calibrate, however recently developed tuning techniques facilitated their use [12; 67; 127; 163]. Figure 3.5 shows a three element

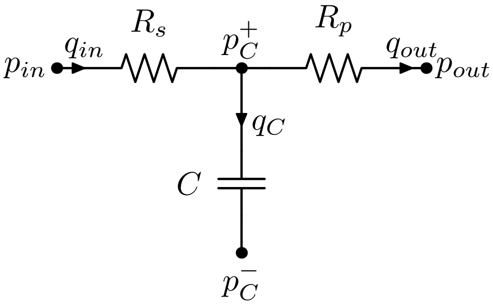

Figure 3.5.: A three element windkessel model

windkessel model with two resistances and a capacitor. The systemic resistance R_s is nothing other than the reflective factor R_f defined as [3]

$$R_\mathrm{f} = \frac{R_\mathrm{s} - \frac{c_0}{A_0}\rho}{R_\mathrm{s} + \frac{c_0}{A_0}\rho}.$$

Another way to interpret R_s, is that it defines the size or filters out the high frequency waves. Westerhof et al. [156] and Alastruey et al. [3] showed that taking $R_\mathrm{s} = \frac{c_0}{A_0}\rho$, i.e. $R_\mathrm{f} = 0$, filtered out unphysiological high frequency waves. The peripheral resistance R_p defines the entire resistance of the downstream bed and is evaluated as

$$\tilde{P}_\mathrm{in} = \left(R_\mathrm{p} + R_\mathrm{s}\right)\tilde{Q}_\mathrm{in},$$

where $\tilde{P}_\mathrm{in}$ and $\tilde{Q}_\mathrm{in}$ are the time averaged inlet pressure and flow rate, respectively. Finally, C is the downstream tree compliance. Mathematically, the windkessel element is modeled as

$$\begin{cases} C\frac{d\left(P_c - P_c^-\right)}{dt} + Q_\mathrm{out} - Q_\mathrm{in} = 0 \\ R_\mathrm{p}Q_\mathrm{out} + P_\mathrm{out} - P_\mathrm{C} = 0 \end{cases}.$$

Knowing that at an outlet the forward characteristic wave is known, then the following nonlinear equation is solved for A

$$\mathcal{F}\left(A\right) = R_\mathrm{s}W_1A - 4R_\mathrm{s}\sqrt{\frac{\beta}{2\rho A_0}}A^{\frac{5}{4}} - P_0 - \frac{\beta}{A_0}\left(\sqrt{A} - \sqrt{A_0}\right) + P_C = 0. \tag{3.14}$$

P_c^- is usually set to be zero and P_out is set to a constant value, P_C^{n+1} is estimated as $P_\mathrm{C}^{n+1} = P_\mathrm{C}^n + \frac{\Delta t}{C}\left(Q_\mathrm{in}^n - Q_\mathrm{out}^n\right)$, Q_out^n is estimated as $Q_\mathrm{out}^n = \frac{P_\mathrm{C}^n - P_\mathrm{out}}{R_\mathrm{p}}$ and $P_\mathrm{C}^{n-1} = 0$ for $n = 0$.

Junction boundary condition

The junctions are formulated using the approach of [15]. The current work considers a junction as any form of summation, bifurcation or a combination of summation and bifurcation nodes (see Figure 3.6). A junction connecting N_j number of pipes has $2N_\mathrm{j}$ unknown degrees of freedom. To find the unknown degrees of freedom a system of $2N_\mathrm{j}$ equations must be constructed. The

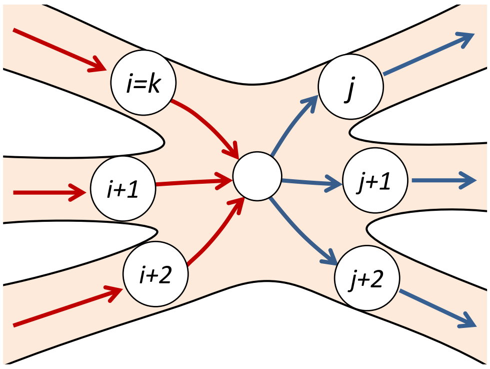

Figure 3.6.: A general representation of a 1D junction. Terminals numbered by i are outlets. Terminal numbered by j are inlets.

conservation of mass and the conservation of pressure head (Bernoulli law) at a junction yield the following N_j equations:

$$\begin{aligned} \sum_i Q^i_\mathrm{out} &= \sum_j Q^j_\mathrm{in} \\ \frac{1}{\rho}P_k + \frac{1}{2}U_k^2 &= \frac{1}{\rho}P_l + \frac{1}{2}U_l^2;\ \forall\, l \neq k. \end{aligned} \tag{3.15}$$

The remaining N_j number of equations are found from the Riemann problem [125; 126]. At the various outlets, the forward characteristic waves are known whereas at the inlets the backward characteristic waves are known. Thus, the remaining N_j set of equations are represented in the following form

$$\begin{aligned} W_1^i = U_i + 4A_i^{1/4}\sqrt{\frac{\beta_i}{2\rho A_0^i}} \\ W_2^j = U_j - 4A_j^{1/4}\sqrt{\frac{\beta_j}{2\rho A_0^j}} \end{aligned} \tag{3.16}$$

Finally the nonlinear system of eq (3.15) and eq (3.16) is solved iteratively using a Newton-Raphson method.

3.3. 0D pipe flow domain

Solving the 1D pipe problem of eq (3.10) requires in each time step to solve the Riemann problem. In lungs, for example, solving the Riemann problem would be expensive. That is because the characteristic speeds can be up to two orders of magnitude larger that the speed of air. This means that very small time steps are required to solve the wave problem. To avoid the unnecessary computational costs the 1D problem is reduced into a 0D problem by integrating eq (3.10) along the length direction and by considering certain assumptions such as:

- $\partial A / \partial x = 0$.
- All geometric and material variables are constant along the x axis.

3.3.1. Conservation of mass

Integrating conservation of mass in eq (3.10) along the x axis

$$\int_{x_1}^{x_2} \left\{ \frac{\partial A}{\partial t} + \frac{\partial Q}{\partial x} \right\} \mathrm{d}x = 0$$

yields

$$l \frac{\partial A}{\partial t} = Q_{\text{in}} - Q_{\text{out}},$$

where the sub indices ”in” and ”out” stand for the values at x_1 and x_2 in Figure 3.2(b), respectively.

3.3.2. Wall mechanics

Integrating eq (3.9) along the x axis

$$\int_{x_1}^{x_2} P \mathrm{d}x = \int_{x_1}^{x_2} \left\{ \beta_{\text{s}} \left(\frac{\sqrt{A} - \sqrt{A_0}}{A_0} \right) + \gamma_{\text{s}} \left(\frac{1}{A\sqrt{A}} \frac{\partial A}{\partial t} \right) + P_{\text{ext}} \right\} \mathrm{d}x$$

yields

$$\tilde{P} = \beta_{\text{s}} \left(\frac{\sqrt{A} - \sqrt{A_0}}{A_0} \right) + \gamma_{\text{s}} \left(\frac{1}{A\sqrt{A}} \frac{\partial A}{\partial t} \right) + \tilde{P}_{\text{ext}}, \tag{3.17}$$

where

$$\tilde{P} = \frac{1}{(x_2 - x_1)} \int_{x_1}^{x_2} P \mathrm{d}x$$

and

$$\tilde{P}_{\text{ext}} = \frac{1}{(x_2 - x_1)} \int_{x_1}^{x_2} P_{\text{ext}} \mathrm{d}x.$$

After some mathematical manipulation, eq (3.17) is written as

$$\tilde{P} = \int \frac{1}{C} \left(Q_{\text{in}} - Q_{\text{out}} \right) \mathrm{d}t + R_{\text{vis}} \left(Q_{\text{in}} - Q_{\text{out}} \right) + \tilde{P}_{\text{ext}}, \tag{3.18}$$

where

$$C = \frac{2A_0\sqrt{A}}{\beta_{\text{s}}} l, \; R_{\text{vis}} = \frac{\gamma_{\text{s}}}{lA\sqrt{A}}.$$

3.3.3. Balance of momentum

Integrating conservation of momentum in eq (3.10) along the x and multiplying it by ρ/A

$$\frac{\rho}{A}\int_{x_1}^{x_2}\left\{\frac{\partial Q}{\partial t}+\frac{\partial}{\partial x}\left(\alpha\frac{Q^2}{A}\right)+\frac{A}{\rho}\left(\frac{\partial P}{\partial x}\right)+K_{\mathrm{R}}\frac{Q}{A}\right\}\mathrm{d}x=0$$

yields

$$\frac{\rho l}{A}\frac{\partial\tilde{Q}}{\partial t}+\frac{\alpha\rho}{A^2}\left(Q^2\right)_{x_1}^{x_2}+\left(P\right)_{x_1}^{x_2}+\frac{\rho l K_{\mathrm{R}}}{A^2}\tilde{Q}=0, \tag{3.19}$$

where

$$\tilde{Q}=\frac{1}{(x_2-x_1)}\int_{x_1}^{x_2}Q\mathrm{d}x.$$

After some mathematical manipulation, eq (3.19) is rewritten as

$$P_{\text{in}}-P_{\text{out}}=I\frac{\partial\tilde{Q}}{\partial t}+R_{\text{conv}}\left(\frac{Q_{\text{out}}+Q_{\text{in}}}{2}\right)+R_{\mu}\tilde{Q}, \tag{3.20}$$

where

$$I=\frac{\rho l}{A},\ R_{\text{conv}}=\frac{2\alpha\rho}{A^2}\left(Q_{\text{out}}-Q_{\text{in}}\right),\ R_{\mu}=\frac{\rho l K_{\mathrm{R}}}{A^2}.$$

By assuming that $\tilde{Q}=Q_{\text{in}}$, $\tilde{P}=P_{\text{in}}$ and $\tilde{P}_{\text{ext}}=\left(\tilde{P}_{\text{ext}}^{x_1}+\tilde{P}_{\text{ext}}^{x_2}\right)/2$, eq (3.20) and eq (3.18) are joined together to form the zero dimensional compliant pipe model:

$$\begin{cases} P_{\text{in}}-P_{\text{out}}=I\frac{\partial}{\partial t}\left(Q_{\text{out}}\right)+\left(R_{\text{conv}}+R_{\mu}\right)\left(Q_{\text{out}}\right)=0 \\ P_{\text{in}}=\int\frac{1}{C}\left(Q_{\text{in}}-Q_{\text{out}}\right)\mathrm{d}t+R_{\text{vis}}\left(Q_{\text{in}}-Q_{\text{out}}\right)+\tilde{P}_{\text{ext}}. \end{cases} \tag{3.21}$$

Figure 3.7 shows eq (3.21) using electrical components.

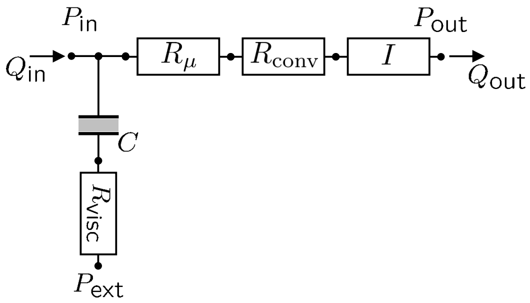

Figure 3.7.: Circuit representation of the 0D compliant pipe.

3.4. 0D alveolar domain

Following the earlier work of the author, the 0D alveolar domain is assumed to consist of acinar units [66]. Each acinus is assumed to consist of a tree of alveolar ducts, see Figure 3.8(b).

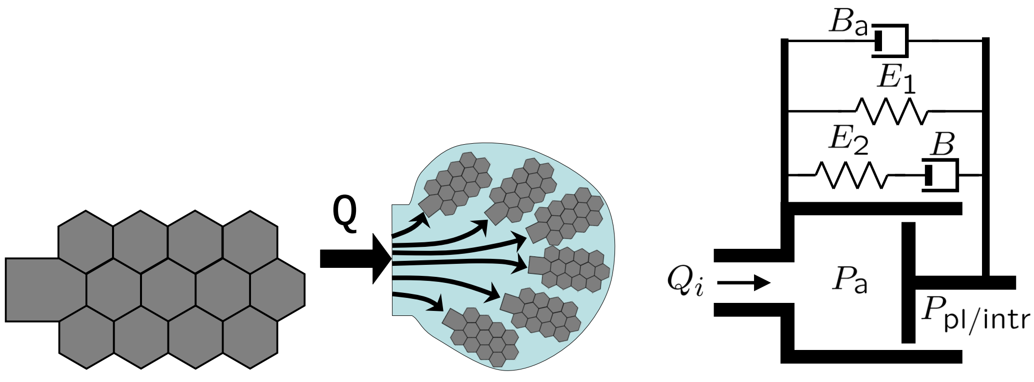

(a) (b) (c)

Figure 3.8.: A model of an acinus showing (a) schematic of an alveolar duct, (b) a four-element Maxwell model of an alveolar duct, showing the acinar pressure P_{a}, pleural/ inter-acinar pressure $P_{\mathrm{pl/intr}}$, and the flow Q_i and (c) an acinus filled with a tree of alveolar ducts [66].

The limited information about the parenchymal behavior of the human tissue has motivated the author to use the simulated behavior of the human alveolar ducts of Denny and Schroter [27; 28], shown in Figure 3.8(a). In this case, it is firstly assumed that an acinus is a volume filled with alveolar ducts (see Figure 3.8(b)). Secondly, a four-element nonlinear Maxwell model is developed such that it reproduces the pressure-volume behavior of an alveolar duct filled acinus (see Figure 3.8(c)). This approach allows the modeling of the whole acinus as a 0D element while maintaining its visco-elastic mechanical properties. In the following sections the 0D alveolar duct is first developed and then followed by the derivation of the 0D acinar element.

3.4.1. 0D alveolar duct

The four-element Maxwell model in Figure 3.8(b) reads as following

$$P_{\mathrm{tp}} + \frac{B}{E_2}\left(\frac{\mathrm{d}P_{\mathrm{tp}}}{\mathrm{d}t}\right) = \left(\frac{BB_{\mathrm{a}}}{E_2}\right)\left(\frac{\mathrm{d}^2V_i}{\mathrm{d}t^2}\right) + (B_{\mathrm{a}} + B)\left(\frac{\mathrm{d}V_i}{\mathrm{d}t}\right) + \frac{B}{E_2}\left(\frac{\mathrm{d}P_{\mathrm{E}_1}}{\mathrm{d}t}\right) + P_{\mathrm{E}_1}, \quad (3.22)$$

where

$$P_{\mathrm{E}_1} = E_1 \times (V_i - V_i^{\mathrm{o}})\,.$$

V_i is the volume of an alveolar duct, V_i^0 the stress free volume of an alveolar duct, B and B_{a} damping dashpots, E_1 and E_2 volumetric moduli of elasticity, and P_{tp} the trans-pulmonary pressure. The trans-pulmonary pressure P_{tp} is defined as

$$P = P_{\mathrm{a}} - P_{\mathrm{pl/intr}},$$

where P_{a} and $P_{\mathrm{pl/intr}}$ are the pressure values inside and outside the alveolar duct, respectively. In case of a linear 4-element Maxwell model, the eq (3.22) is described as:

$$B\frac{\mathrm{d}^2 P_{\mathrm{tp}}(t)}{\mathrm{d}t^2}+E_2\frac{\mathrm{d}P_{\mathrm{tp}}(t)}{\mathrm{d}t}=B_{\mathrm{a}}B\frac{\mathrm{d}^2 Q_i}{\mathrm{d}t^2}+\left(E_1B+E_2B+E_2B_{\mathrm{a}}\right)\frac{\mathrm{d}Q_i(t)}{\mathrm{d}t}+E_1E_2Q_i(t), \quad (3.23)$$

where $Q_i = \frac{\mathrm{d}V_i}{\mathrm{d}t}$ is the flow rate of air in and out of the alveolar duct. In case of a nonlinear 4-element Maxwell model, E_1 is modeled to represent the sigmoidal hyper elastic behavior of an alveolar duct [69] as following

$$\begin{aligned} E_1 &= E_1^{\mathrm{u}} + E_1^{\mathrm{l}}, \\ E_1^{\mathrm{u}} &= E_1^{\mathrm{o}} + b\left(V_i - V_i^{\mathrm{o}}\right) + \kappa^{\mathrm{u}} e^{\tau^{\mathrm{u}}\left(V_i - V_i^{\mathrm{o}}\right)}, \\ E_1^{\mathrm{l}} &= \kappa^{\mathrm{l}} e^{\tau^{\mathrm{l}}\left(V_i - V_i^{\mathrm{o}}\right)}, \end{aligned}$$

where E_1^{o}, b, κ^{u}, τ^{u},E_1^{l}, κ^{l}, τ^{l} are constants to be fitted to the human alveolar duct behavior later in Chapter 4. The reason the sigmoidal behavior of E_1 is fitted with eq (3.24) is because the classical sigmoidal functions resulted in numerical singularities.

3.4.2. 0D acinus

This work assumes that each acinus had an N_{ad} number of alveolar ducts. Thus a 0D acinar model is evaluated from eq (3.22) and eq (3.23) by substituting the following

$$\begin{aligned} Q_i &= \frac{Q}{N_{\mathrm{ad}}}, \\ V_i &= \frac{V}{N_{\mathrm{ad}}}, \end{aligned}$$

where Q is the flow rate of air flowing in and out of an acinus and V the volume of an acinus. Thus a linear 0D acinar model yields

$$N_{\mathrm{ad}}B\frac{\mathrm{d}^2 P_{\mathrm{tp}}(t)}{\mathrm{d}t^2}+N_{\mathrm{ad}}E_2\frac{\mathrm{d}P_{\mathrm{tp}}(t)}{\mathrm{d}t}=B_{\mathrm{a}}B\frac{\mathrm{d}^2 Q}{\mathrm{d}t^2}+\left(E_1B+E_2B+E_2B_{\mathrm{a}}\right)\frac{\mathrm{d}Q(t)}{\mathrm{d}t}+E_1E_2Q(t), \quad (3.25)$$

and the nonlinear 0D acinar model yields

$$N_{\mathrm{ad}}P_{\mathrm{tp}}+N_{\mathrm{ad}}\frac{B}{E_2}\left(\frac{\mathrm{d}P_{\mathrm{tp}}}{\mathrm{d}t}\right)=\left(\frac{BB_{\mathrm{a}}}{E_2}\right)\left(\frac{\mathrm{d}Q}{\mathrm{d}t}\right)+\left(B_{\mathrm{a}}+B\right)Q+N_{\mathrm{ad}}\frac{B}{E_2}\left(\frac{\mathrm{d}P_{\mathrm{E_1}}}{\mathrm{d}t}\right)+N_{\mathrm{ad}}P_{\mathrm{E_1}}. \quad (3.26)$$

3.5. 0D inter-acinar tissue

In physiology, neighboring alveoli and thus neighboring acini share a common wall. This is interpreted as if each acinus is glued to its neighboring acinus via an inter-acinar linker. The linker carries information about the neighboring acinus, such as when two neighboring acini compete for the same volume during their expansion. Thus, inflating one acinus might be hindered or facilitated by a neighboring acinus, depending on whether the neighbor is growing or shrinking. To illustrate the physics behind inter-acinar dependencies, the four acini in Figure 3.9 are assumed. Furthermore, the acinar wall is considered to be a thin structure and to deform uniformly. Taking

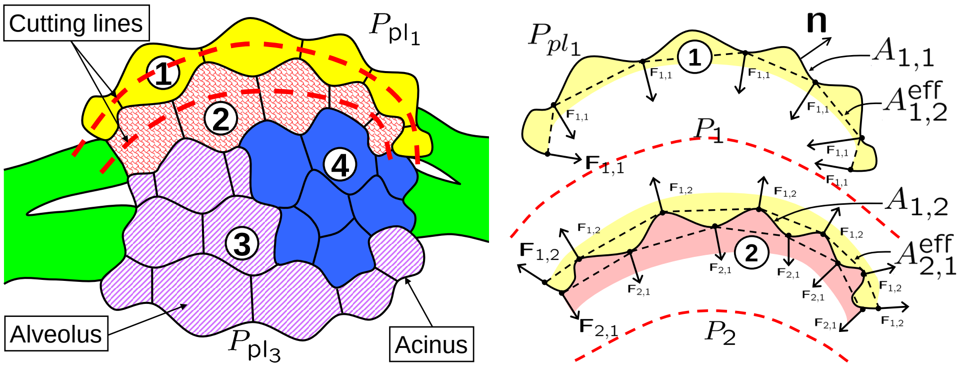

(a) (b)

Figure 3.9.: A cartoon schematic showing (a) four acini with two cuts and (b) the balance of forces inside acinus 1 and part of acinus two.

the balance of forces within the first acinus, labeled as ① in Figure 3.9, two surface areas are distinguished: the first is labeled as $A_{1,1}$ in Figure 3.9(b) and is on the side of acinus Ac_1 that is subjected to the pleural space. The second, is labeled as $A_{1,2}$ in Figure 3.9(b) and is on the side of acinus Ac_1 that is interacting with acinus Ac_2. Following the work of [95], the balance of forces on the first side read as

$$\int_{A_{1,1}} P_1 \mathbf{n} dA - \int_{A_{1,1}} P_{\mathrm{pl}_1} \mathbf{n} dA - \sum \mathbf{F}_{1,1} = 0, \tag{3.27}$$

where P_1 is the alveolar pressure in acinus Ac_1, P_{pl_1} the pleural pressure outside acinus Ac_1, $A_{1,1}$ the connecting surface area between acinus Ac_1 and the pleural space and $\mathbf{n}$ the surface normal (see Figure 3.9). $\sum \mathbf{F}_{1,1}$ denotes the forces resulted from straining the acinus by a transpulmonary pressure $P_{\mathrm{tp}_1} = K_{\mathrm{ac}_1} V_{\mathrm{ac}_1}$, where K_{ac_1} is the volumetric stiffness of acinus Ac_1. Thus eq (3.27) became

$$P_1 A^{\mathrm{eff}}_{1,1} - P_{\mathrm{pl}_1} A^{\mathrm{eff}}_{1,1} - K_{\mathrm{ac}_1} V_{\mathrm{ac}_1} A^{\mathrm{eff}}_{1,1} = 0, \tag{3.28}$$

which also incorporated the correct assumption that pressure values are evenly distributed around an acinus wall. Following the same procedure for balance of forces at the second side of acinus Ac_1 yields

$$\int_{A_{1,2}} P_1 \mathbf{n} dA - \int_{A_{2,1}} P_2 \mathbf{n} dA - \sum \mathbf{F}_{1,2} + \sum \mathbf{F}_{2,1} = 0, \tag{3.29}$$

where $\sum \mathbf{F}_{1,2}$ and $\sum \mathbf{F}_{2,1}$ resulted from trans-pulmonary pressures $P_{\mathrm{tp}_1} = K_{\mathrm{ac}_1} V_{\mathrm{ac}_1}$ and $P_{\mathrm{tp}_2} = K_{\mathrm{ac}_2} V_{\mathrm{ac}_2}$, respectively. K_{ac_1} and K_{ac_2} are the volumetric stiffnesses of acinus Ac_1 and Ac_2, respectively. Eq (3.29) thus yields

$$P_1 A^{\mathrm{eff}}_{1,2} - K_{\mathrm{ac}_1} V_{\mathrm{ac}_1} A^{\mathrm{eff}}_{1,2} - P_2 A^{\mathrm{eff}}_{2,1} + K_{\mathrm{ac}_2} V_{\mathrm{ac}_2} A^{\mathrm{eff}}_{2,1} = 0. \tag{3.30}$$

Knowing that acinus Ac_1 is surrounded by the pleural space and part of acinus Ac_2 (as shown in Figure 3.9(a)), the total balance of forces in acinus Ac_1 resulted from summing eq (3.28) and eq (3.30) to yield the following

$$P_1 A^{\mathrm{eff}}_{1} - K_{\mathrm{ac}_1} V_{\mathrm{ac}_1} A^{\mathrm{eff}}_{1} - P_{\mathrm{pl}_1} A^{\mathrm{eff}}_{1,1} - P_2 A^{\mathrm{eff}}_{2,1} + K_{\mathrm{ac}_2} V_{\mathrm{ac}_2} A^{\mathrm{eff}}_{2,1} = 0. \tag{3.31}$$

In the general case that a acinus Ac_i is surrounded by several acini Ac_j, eq (3.31) yields the following balance of forces

$$P_i A^{\mathrm{eff}}_{i} - K_{\mathrm{ac}_i} V_{\mathrm{ac}_i} A^{\mathrm{eff}}_{i} - P_{\mathrm{pl}_i} A^{\mathrm{eff}}_{i,i} - \sum_{j \neq i} P_j A^{\mathrm{eff}}_{j,i} + \sum_{j \neq i} K_{\mathrm{ac}_j} V_{\mathrm{ac}_j} A^{\mathrm{eff}}_{j,i} = 0.$$

Dividing this equation by A^{eff}_i

$$P_i - K_{\mathrm{ac}_i} V_{\mathrm{ac}_i} - P_{\mathrm{pl}_i} \frac{A^{\mathrm{eff}}_{i,i}}{A^{\mathrm{eff}}_{i}} - \sum_{j \neq i} P_j \frac{A^{\mathrm{eff}}_{j,i}}{A^{\mathrm{eff}}_{i}} + \sum_{j \neq i} K_{\mathrm{ac}_j} V_{\mathrm{ac}_j} \frac{A^{\mathrm{eff}}_{j,i}}{A^{\mathrm{eff}}_{i}} = 0. \tag{3.32}$$

By defining a fictitious pressure that can replace the forces generated by a neighboring acinus onto an acinus Ac_i, the acinar recoil is represented as

$$P_i - P_{\mathrm{intr}_i} = K_{\mathrm{ac}_i} V_{\mathrm{ac}_i},$$

where the fictitious pressure P_{intr} is named as the inter-acinar pressure. Thus eq (3.32) results

$$P_{\mathrm{intr}_i} - P_{\mathrm{pl}_i} \frac{A^{\mathrm{eff}}_{i,i}}{A^{\mathrm{eff}}_{i}} - \sum_{j \neq i} P_{\mathrm{intr}_j} \frac{A^{\mathrm{eff}}_{j,i}}{A^{\mathrm{eff}}_{i}} = 0. \tag{3.33}$$

3.6. 1D scalar transport

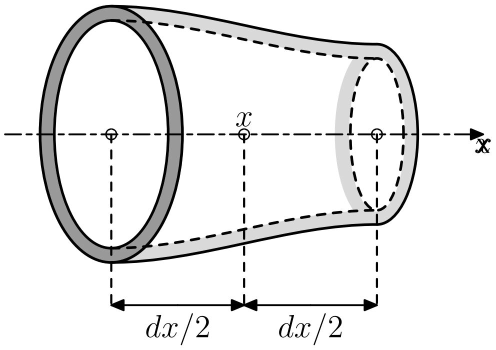

Figure 3.10.: An infinitesimal one dimensional pipe element

The one dimensional transport of O_2 is found from the conservation of O_2 molecules. For this purpose, the infinitesimal 1D pipe element in Figure 3.10 is assumed. To formulated the conservation of O_2, it is assumed that O_2 is mixed fully within a cross-sectional area and that O_2 is neither deposited nor is generated except at the O_2 exchange interface. The balance of O_2 molecules read

$$\frac{\partial\left(c_{\mathrm{s}} V\right)}{\partial t}=J\left(x-\frac{\mathrm{d} x}{2}\right)-J\left(x+\frac{\mathrm{d} x}{2}\right), \tag{3.34}$$

where c_{s} is the concentration of O_2, V the volume of the pipe element and J the flux of O_2 molecules. The O_2 flux J included the convective and diffusive transport and is written as

$$J(x)=Q c_{\mathrm{s}}-D_{\mathrm{O}_2} A \frac{\partial c_{\mathrm{s}}}{x},$$

where Q is the flow rate of the fluid carrying O_2, D_{O_2} the O_2 diffusion coefficient and A the cross-sectional area of a pipe. Using Taylor's truncated series in eq (3.34) yields

$$\begin{aligned} J\left(x-\frac{\mathrm{d} x}{2}\right)-J\left(x+\frac{\mathrm{d} x}{2}\right) = & \left(Q(x)-\frac{\mathrm{d} x}{2} \frac{\partial Q(x)}{\partial x}\right)\left(c_{\mathrm{s}}(x)-\frac{\mathrm{d} x}{2} \frac{\partial c_{\mathrm{s}}(x)}{\partial x}\right) \\ & -D_{\mathrm{O}_2}\left(A(x)-\frac{\mathrm{d} x}{2} \frac{\partial A}{\partial x}\right)\left(\frac{\partial c_{\mathrm{s}}(x)}{\partial x}-\frac{\mathrm{d} x}{2} \frac{\partial^2 c_{\mathrm{s}}}{\partial x^2}\right) \\ & -\left(Q(x)+\frac{\mathrm{d} x}{2} \frac{\partial Q(x)}{\partial x}\right)\left(c_{\mathrm{s}}(x)+\frac{\mathrm{d} x}{2} \frac{\partial c_{\mathrm{s}}(x)}{\partial x}\right) \\ & +D_{\mathrm{O}_2}\left(A(x)+\frac{\mathrm{d} x}{2} \frac{\partial A}{\partial x}\right)\left(\frac{\partial c_{\mathrm{s}}(x)}{\partial x}+\frac{\mathrm{d} x}{2} \frac{\partial^2 c_{\mathrm{s}}}{\partial x^2}\right) . \end{aligned} \tag{3.35}$$

by eliminating the negligible nonlinear terms, eq 3.35 became

$$V \frac{\partial c_{\mathrm{s}}}{\partial t}+c_{\mathrm{s}} \frac{\partial V}{\partial t}=-Q \frac{\partial c_{\mathrm{s}}}{\partial x} \mathrm{d} x-c_{\mathrm{s}} \frac{\partial Q}{\partial x} \mathrm{d} x+D_{\mathrm{O}_2} A \frac{\partial^2 c_{\mathrm{s}}}{\partial x^2} \mathrm{d} x+D_{\mathrm{O}_2} \frac{\partial A}{\partial x} \frac{\partial c_{\mathrm{s}}}{\partial x} \mathrm{d} x .$$

Taking into account the plain strain assumption and the mass conservation equation from Section 3.2

$$\frac{\partial Q}{\partial x}=-\frac{\partial A}{\partial t},$$

the 1D transport of O_2 is is found as

$$\frac{\partial c_{\mathrm{s}}}{\partial t}+\frac{Q}{A} \frac{\partial c_{\mathrm{s}}}{\partial x}=D_{\mathrm{O}_2} \frac{\partial^2 c_{\mathrm{s}}}{\partial x^2}+D_{\mathrm{O}_2} \frac{1}{A} \frac{\partial A}{\partial x} \frac{\partial c_{\mathrm{s}}}{\partial x} . \tag{3.36}$$

3.6.1. Boundary conditions and junctions

The transport of O_2 is solve explicitly in time using upwind forward Euler. This means that O_2 concentration is only prescribed at an inflow boundary. At a junction the O_2 is assumed to fully mix and the volume of the junction is negligible (see Figure 3.11). Thus, all fluid flowing out of the junction has the same concentration.

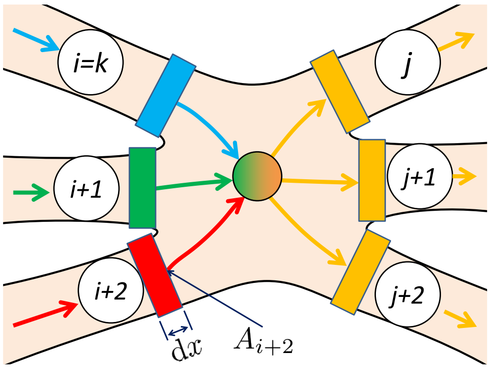

Figure 3.11.: A generalized junction of a 1D transport model.

Looking at Figure 3.11, i defines the terminal numbers through which fluid flows into the junction and j the terminal numbers through which fluid flows out of the junction. Applying the balance of mass yields

$$\sum \dot{n}_i^{\mathrm{O}_2} = \sum \dot{n}_j^{\mathrm{O}_2}, \tag{3.37}$$

where $\dot{n}^{\mathrm{O}_2}$ is the molecule flow rate of O_2. Eq (3.37) is rewritten as

$$\sum c_i Q_i = \sum c_j Q_j, \tag{3.38}$$

where C is the O_2 concentration and Q the fluid flow rate. Since O_2 is assumed to fully mix, then fluid flowing out of the junction has the same concentration, i.e.

$$c_j = \frac{\sum c_i Q_i}{\sum Q_j} = \frac{\sum c_i Q_i}{\sum Q_i}. \tag{3.39}$$

However due to the singularities at zero flow rate eq (3.39) is approximated for low Reynolds numbers $\mathrm{Re} < 10^{-6}$ as

$$c_j = \frac{\sum c_i A_i}{A_\mathrm{J}}, \ A_\mathrm{J} = \sum A_i, \tag{3.40}$$

where

$$\mathrm{Re} = \arg\max_{\forall i} \mathrm{Re}_i$$

and Re_i is the Reynolds number at a terminal i of a junction (see Figure 3.11).

3.7. Oxygen exchange interface

The exchange of O_2 between air and blood happens at the alveolar level. In this case, O_2 defuses from a high O_2 concentration medium (alveolus) to a low O_2 concentration medium (blood capillary); see Figure 3.12. Mathematically, such a phenomenon is modeled using Fick's law [152; 155]

$$Q_{\mathrm{O}_2} = D_\mathrm{T}^\mathrm{I} \left(P_{\mathrm{O}_2}^{\mathrm{air}} - P_{\mathrm{O}_2}^{\mathrm{Hb}} \right), \tag{3.41}$$

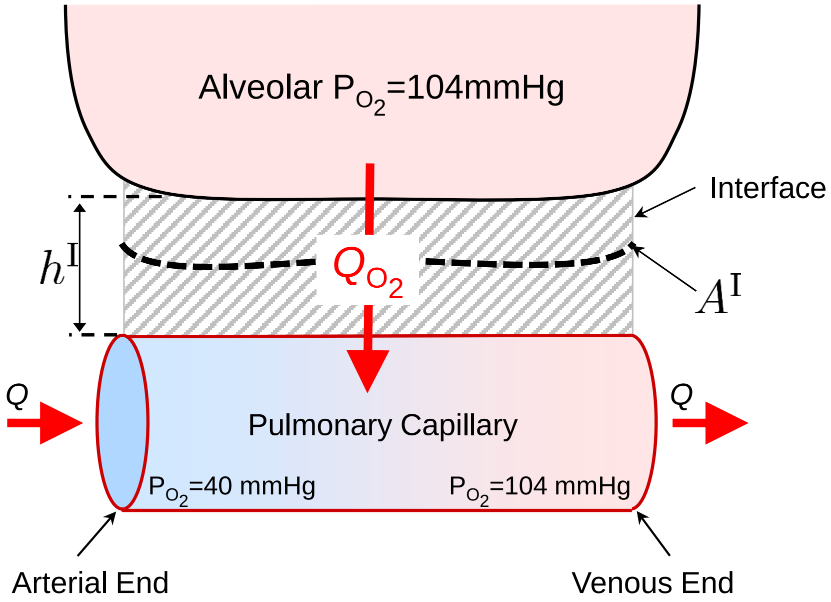

Figure 3.12.: Schematic of the O_2 exchange interface between an alveolus and a blood capillary

where Q_{O_2} is the volumetric flow rate of the O_2 molecules at the interface, $D_{\mathrm{T}}^{\mathrm{I}}$ an interface diffusion constant, $P_{\mathrm{O}_2}^{\mathrm{air}}$ the partial pressure of O_2 in air and $P_{\mathrm{O}_2}^{\mathrm{Hb}}$ is the partial pressure of O_2 in blood. The interface diffusion constant is defined as

$$D_{\mathrm{T}}^{\mathrm{I}} = \left(\frac{A_{\mathrm{O}_2}^{\mathrm{I}}}{h_{\mathrm{O}_2}^{\mathrm{I}}} \right) D_{\mathrm{O}_2}^{\mathrm{I}},$$

where $A_{\mathrm{O}_2}^{\mathrm{I}}$ is the total common surface between the alveoli and the blood capillaries, $h_{\mathrm{O}_2}^{\mathrm{I}}$ the O_2 interface thickness and $D_{\mathrm{O}_2}^{\mathrm{I}}$ an O_2 diffusion constant.

3.8. Coupling of multi-dimensional fluid domains

Reproducing the correct flow behavior within 3D biofluid networks required the correct modeling of the trimmed boundaries [66]. In pulmonary problems, various types of boundary conditions are applied in literature at outlets, such as zero-traction or (non-)uniform pressure boundary conditions [42; 54; 71; 104; 128; 162; 166] and velocity or flow rate boundary conditions [17; 104]. However, recently the author et al. [66] showed that treating the boundaries with such conditions produced wrong flow distribution in a 5 outlet tracheobronchial geometry. At inlets, the velocity or flow rate is usually prescribed in the form of Dirichlet boundary conditions [17; 42; 54; 71; 86; 104; 162; 166]. However, sometimes flow is not *a priori* known. As such, coupling the 3D trimmed boundary with reduced-D representation is essential and finding alternative inlet conditions, such as pressure condition, became a necessity [53; 66; 73].

Many works are dedicated for coupling 3D flow domains with reduced-D problems. One of the earliest approaches are proposed by Formaggia et al. [37; 41]. Alternative approaches are proposed later by [13; 73; 79; 148]. A general implicit coupling approach between various domains is recently presented by Malossi et al. [93] and tested on coupled 3D/Reduced-D fluid domains. Detailed stability analyses of the various couplings are formulated by Formaggia et al. [37]. A brief overview over the various coupling approaches showed that the Dirichlet-to-Neumann coupling developed by Vignon-Clementel et al. [148] yields the most flexible framework. That is because the Dirichlet-to-Neumann coupling is implemented within the Neumann boundary conditions with no modifications to the 3D flow problem. In brief, the Dirichlet-to-Neumann coupling read as following: First the flow rate is calculated on the 3D side of the coupled interface and passed to the reduced-D side of the coupled interface. Then the reduced-D problem is solved for the 3D calculated flow rate and the pressure on the 0D side of the coupled interface is evaluated. Finally, the reduced-D pressure is passed back to the 3D side of the coupling interface as a Neumann boundary condition. Another advantage of such a coupling approach is that it bounded the 3D problem in a weak manner. Thus prevented any ill-conditioning of the 3D boundary value problem.

The problems with the Dirichlet-to-Neumann coupling are reported only recently, when instabilities associated with reversed flow on Neumann boundaries are observed in [10; 11; 96]. Such instabilities arose from introducing artificial in- and outflow boundaries, which are not only required for the coupling of reduced-D models to 3D domains. But also for the correct definition of physiologically reasonable flow and/or pressure conditions at these boundary sections. The reason behind that is that unlike what is done in eq (3.5), the Neumann boundary condition is implemented in an inconsistent manner, by simply ignoring the inflow term $u_{\mathrm{n}}^{\mathrm{in}}\mathbf{u}$. This inconsistency made the coupling unstable during reversed flow [53; 73; 96]. Recent works such as [10; 73] have successfully substituted the natural inflow term by a stabilizing term. However, these are either inconsistent approaches or required extra coding and modification to the 3D framework, thus are avoided in this work. The same problem is encountered at Neumann outlets whenever flow partially or completely reversed, that is, outlets became (partial) inlets. Partial retrograde flow usually arose due to flow recirculation induced by the bifurcating nature of the geometry. Complete reversal of the flow direction occurred in airflow simulations during the expiratory phase. Interesting enough, despite the potential existence of these instabilities, several examples are found in the literature using an standard Neumann boundary conditions (without $u_{\mathrm{n}}^{\mathrm{in}}\mathbf{u}$ term) although the flow entered the domain [71; 162; 166]. However, stable solutions sometimes are simply considered as a ”lucky strikes”, or their ”stability” is due to undesirable artificial numerical effects, and it is unlikely that such a boundary condition set-up works properly for all scenarios [53]. Furthermore, three alternative inflow stabilization approaches are detailed by Moghadam et al. [96]. The fist method, ”outlet stabilization”, is achieved by resolving the Neumann boundary condition using an additional term which arose naturally from integration by parts. Indeed, the proposed term can guarantee stability and is consistent when $\beta = 1.0$, as is earlier shown by Hughes et al. [63; 64] and later used for biomechanical problems by Bazilevs et al. [9]. The second method covered by Moghadam et al. [96] constrained the normal velocities by eliminating the tangential flow via Dirichlet boundary conditions. However, that method failed at higher Reynolds numbers and showed sever oscillations among the boundary velocities. The third method proposed by Moghadam et al. [96], is originally developed by Kim et al. [73] and aimed to weakly constrain the velocity profiles at the Neumann boundary using Lagrange multipliers. However the implementation of such a method is not straight forward and can be very invasive to the 3D flow framework.

As such, this work considered the Dirichlet-to-Neumann coupling where the pressure from the reduced-D problem is applied onto the 3D boundary as a total momentum flux (see eq (3.5)). Furthermore, the coupling is implemented in two manners. In the first, the coupling is assumed to be weak and explicit and is detailed in Figure 3.13(a). In the second, the coupling is assumed to be strong and implicit and is detailed in Figure 3.13(b). Furthermore, the coupling is implemented within the Newton iteration steps of the fluid problem. This allowed the 3D and Reduced-D domains to converge in parallel and faster manner [68; 97]. The algorithm in Figure 3.14 details the 3D/Reduced-D Neumann-to-Dirichlet coupling approach implemented in this work.

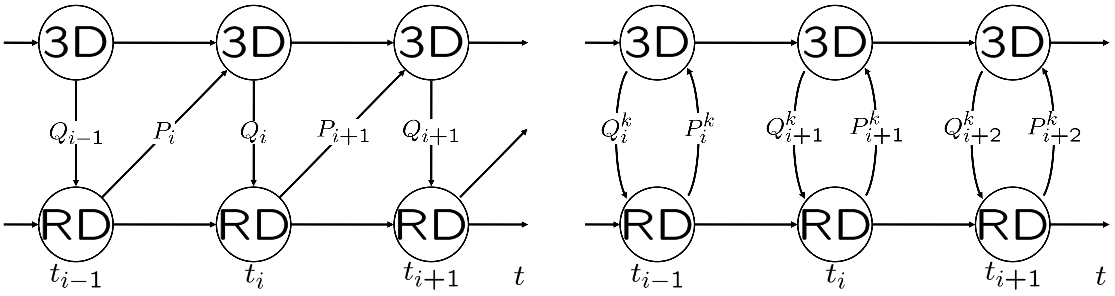

(a) (b)

Figure 3.13.: Two 3D/reduced-D coupling types showing (a) weak coupling and (b) strong coupling; RD: Reduced-D.

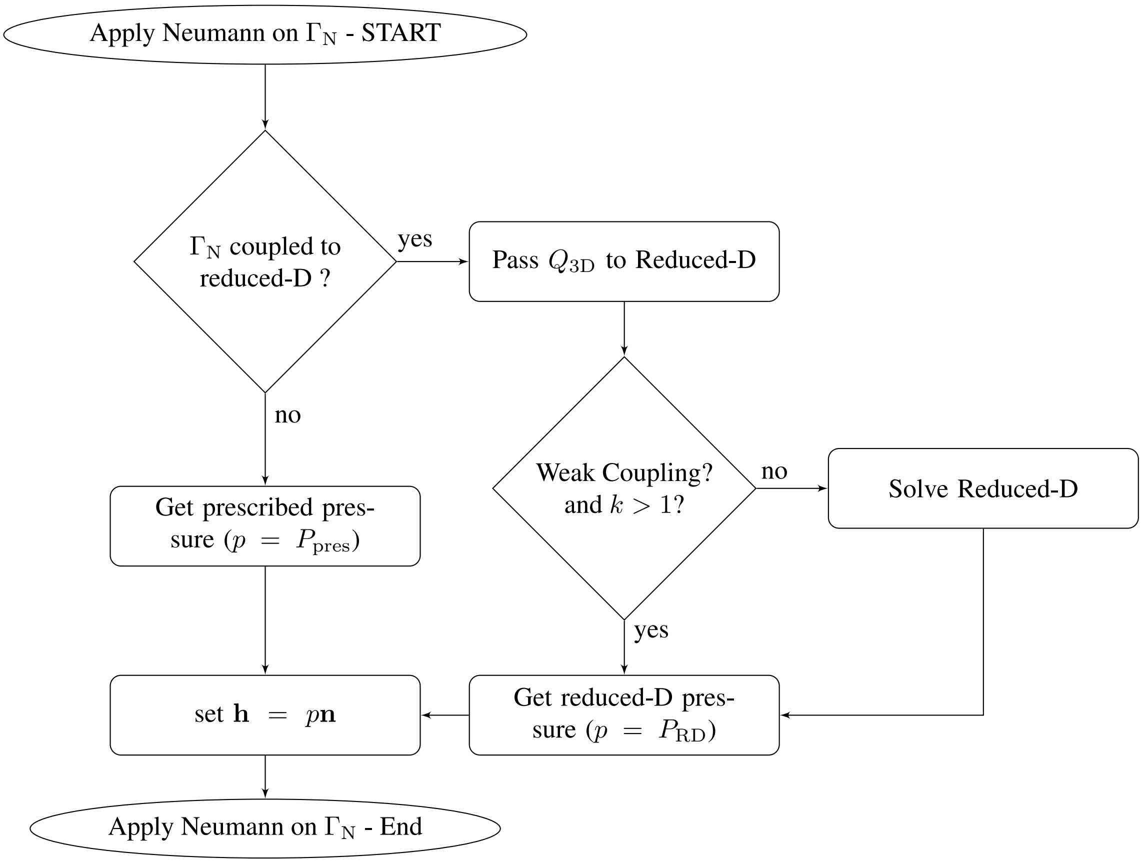
Apply Neumann on Γ_N - START
Γ_N coupled to reduced-D ?
yes
Pass Q_3D to Reduced-D
no
Weak Coupling? and $k > 1$?
no
Solve Reduced-D
Get prescribed pressure ($p = P_\text{pres}$)
yes
set $\mathbf{h} = p\mathbf{n}$
Get reduced-D pressure ($p = P_\text{RD}$)
Apply Neumann on Γ_N - End

Figure 3.14.: A flow chart of the Dirichlet-to-Neumann coupling developed and used in this work.

4. Parameter identification

> ". . . good function is assured by good engineering in all parts of complex organisms."
>
> - Ewald R. Wiebel, *Symmorphosis On Form and Function in Shaping Life*

This chapter is dedicated to identify the various material and physical parameters of the lung's different components. For this purpose the lung is divided into three different sections - the ventilatory/respiratory system, the circulatory system and the oxygen transport. The ventilatory system is the region of the lung that facilitates air transport and is build of the conducting airways, respiratory airways, and lung tissue. The pulmonary circulatory system is the region through which blood flows and is composed of the pulmonary arteries, pulmonary veins, and pulmonary capillaries. The oxygen transport details the transport of oxygen through air, through blood and from air to blood.

4.1. Ventilatory system

The ventilator system is modeled using the 0D models of Chapter 3. In the following subsection, a detailed parameter identification of the airway resistances, airway compliance, airway visco-elasticity, acinar stiffness, acinar visco-elasticity, and inter-acinar dependencies is presented.

4.1.1. Conductive airways

Air enters the upper tract at very high speeds and reaches its peak velocity at the level of the glottis [23]. Even at rest conditions and relaxed breathing rates ($7.5\,\mathrm{l/min}$) air in the trachea reaches velocities higher than $4\,\mathrm{m/s}$ [66]. However due to the bifurcating structure of the bronchial tree and the increased total cross-sectional area with each generation, air looses its velocity quickly the closer it approaches the periphery. In other words, the flow of air is conductive dominant in the lower generations and diffusive dominant in the upper generations. The elevated Reynolds numbers in the lower airway generations showed that they experience turbulent flows. Thus previous attempts to model airway resistance using a simple Poiseuille law led to a large under estimation of the bronchial pressure drop. This is shown earlier by Pedley et al. [111], who performed extensive experiments on casts of human airways and has indeed observed that the pressure drop across the lower generation airways is up to 9 times higher than when estimated with laminar models (Hagen-Poiseuille resistances). Since the experiments in [111] are performed on a hard casts of a human bronchial trees and at constant inlet flow rate, these results are used to tune the resistance of the 0D pipe model (defined in eq (3.21)). In other words, tuning the airway resistance is achieved while neglecting the compliant wall effects and fluid inertial effects. As such, the 0D pipe model is simplified to

$$P_{\text{in}} - P_{\text{out}} = R_\mu Q,$$

where R_μ is the airway resistance to flow. In case of laminar flows, i.e. low Reynolds numbers ($\mathrm{Re} < 2000$), the airway resistance (R_μ) is approximated using Hagen-Poiseuille equation for laminar flows (parabolic velocity profile, i.e. $\gamma = 2$) in circular pipe as

$$R_\mathrm{p} = \frac{8\mu l_\mathrm{aw}}{\pi R_\mathrm{aw}^4}, \tag{4.1}$$

where l_aw denotes the length of an airway, R_aw the radius of an airway and μ the dynamic viscosity of air. In case of turbulent flows, i.e. high Reynolds numbers ($\mathrm{Re} > 2000$), the models of [81; 110; 111; 122; 123; 147] are used to estimate the airway resistance. The earliest known resistive model that captured airway resistances at higher Reynolds numbers is Rohrer's model (named after Rohrer [123]). Rohrer's model is based on an empirical model for flow and pressure and stated that

$$P_\mathrm{in} - P_\mathrm{out} = K_1 Q + K_2 Q^2,$$

where K_1 and K_2 are two constants. While Rohrer's model could well describe the relationship between pressure drop and flow rate relationship in turbulent pipe flows, it could not tell anything about the physics. Thus, every time the geometric dimensions or the material parameters changed, new values for K_1 and K_2 are required to be experimentally evaluated. The first airway resistive model that contained physical and geometric information is developed by Pedley et al. [111] and stated that

$$R = \gamma_\mathrm{p} \left(\mathrm{Re} \frac{D_\mathrm{aw}}{l_\mathrm{aw}} \right)^{1/2} R_\mathrm{p}, \tag{4.2}$$

where R_p is the Poiseuille resistance defined in eq (4.1), D_aw the diameter of an airway, Re the Reynolds number and $\gamma_\mathrm{p} = 0.327$. The Reynolds number is defined as:

$$\mathrm{Re} = \frac{4\rho\,|Q|}{\mu \pi D_\mathrm{aw}},$$

where ρ is the density of air. To avoid singularities at zero flow rate, eq (4.2) is rewritten as

$$R = \begin{cases} \gamma_\mathrm{p} \left(Re\frac{D}{L}\right)^{1/2} R_\mathrm{p} & \gamma_\mathrm{p} \left(Re\frac{D}{L}\right)^{1/2} > 1 \\ R_\mathrm{p} & \gamma_\mathrm{p} \left(Re\frac{D}{L}\right)^{1/2} \leq 1 \end{cases}. \tag{4.3}$$

Such a modification includes a physical constraint, which states that the minimum resistance may not fall below Poiseuille resistance because no resistance is less dissipative than Poiseuille resistance.

Another physically meaningful resistive model was later developed by Reynolds and Lee [122], which is based on Rohrer's equation. However, unlike Rohrer's model, Reynolds managed to include the geometric and material information into the variables K_1 and K_2. The Reynolds resistive model states

$$R = R_\mathrm{p} \left(3.4 + 2.1 \times 10^{-3}\mathrm{Re}\right). \tag{4.4}$$

Lambert et al. [81] showed that the Reynolds resistive model fits well the resistance of expiration. Looking at eq (4.4), two terms are observed. The first term in eq (4.4) is a constant term. The second term in eq (4.4) is dependent on the Reynolds number, thus adds a nonlinearity to the pressure/flow rate relationship. It is also observed, in eq (4.4), that during low Reynolds number flows, the resistance is equal to 3.4 times that of the Poiseuille resistance. Which means that the first term in eq (4.4) is a laminar term. Reynolds et al. [122] argued that the 3.4 term is the geometric contribution of summing trees. The second (nonlinear) term in eq (4.4) becomes dominant at high Reynolds number flows, thus models the contribution of turbulence. The advantage of the Reynolds' model to that of Pedley's is that it is differentiable at all time. However, it is recently noted by the author in [66] that Reynolds' model can over estimate the resistance in the upper airway generations and that the 3.4 factor must be reduced to 1.0, thus

$$R = R_{\mathrm{p}} \left(1.0 + 2.1 \times 10^{-3} Re\right). \tag{4.5}$$

Recent investigations of van Ertbruggen et al. [147] observed that the assumption of constant γ_{p} in Pedley's model lead to overestimation of the bronchial resistance. They thus extended the model in eq (4.3) by assuming different γ_{p} values for different generation numbers. This is achieved by performing *in silico* experiments on 3D tracheobronchial tree of more that 7 generations. The results are shown in Table 4.1.

Table 4.1.: Evaluated γ_{p} for the first seven lung generations according to [147].

Generation	0	1	2	3	4	5	6	7	>7
γ_{p}	0.162	0.239	0.244	0.295	0.175	0.303	0.356	0.566	0.327

To validate the proper choice of airway resistive component, three sets of *in silico* total bronchial pressure drop (TBPD) experiments are performed. In each set of experiment one of the presented resistive models (Pedley, Reynolds and van Ertbruggen) is tested on two geometries. The first geometry is a tree of 0D airways of the entire conducting zone (see Figure 4.1(a)). The second geometry is a 3D tracheobronchial tree coupled to a tree of 0D airways of the lobar conducting zone (see Figure 4.1(b)). The 3D tracheobronchial tree started at the tracheal inlet and ended just at the inlets of the lung lobes. The terminal airways in both geometries are subjected to a zero pressure, whereas the inlet of the trachea is subjected to a flow rate of

$$Q_{\mathrm{t}} = 120 \left|\sin\left(2 \cdot \pi t/4\right)\right| \mathrm{l/min}.$$

The 3D tracheobronchial geometry is modeled using the 3D Navier-Stokes of Section 3.1. The 3D and the 0D models are coupled using the Dirichlet-to-Neumann coupling detailed in Section 3.8. Numerically, the 3D domain is discretized using a stabilized implicit finite-element model and the 0D using implicit finite difference (See the Appendix). In time, both of the domains are discretized with a time step of 1 ms. No mesh refinement study is performed in this work. However, the same 3D geometry is analyzed in [23], who showed that the selected mesh size and time step are in a very good agreement with a finer turbulent model. The results of TBPD for the different resistive models are presented in Figure 4.2. The first TBPD comparison using Pedley's model is shown in Figure 4.2(a). It is observed that the TBPD is overestimated by a maximum of $\sim 20\%$. The second comparison shown in Figure 4.2(b) is performed using the van Ertbruggen model, i.e. the same model as the first one but the γ_{p} values are taken from

Table 4.1. The results showed that the van Ertbruggen model matched the coupled 3D-0D much better and the overestimation of TBPD is reduced to only $\sim 4\%$. The third comparison is performed for the Reynolds' modified model in eq (4.5). This model showed a maximum of $\sim 20\%$ over estimation of the TBPD at $\sim 60\,\mathrm{l/min}$ (see Figure 4.2(c)). Despite the differences between the coupled 3D-0D model and the fully 0D model, it is important to point out that all of the three aforementioned 0D models are suitable for modeling airways. This can be clearly seen in Figures 4.2(a-c) where, firstly, the nonlinear pressure flow rate relationship is well represented. Secondly, all of the aforementioned 0D models reproduced TBPD that are close to that recorded in physiology (see [111]). However, from here on this work will use the van Ertbruggen model as the resistance model of the 0D airways.

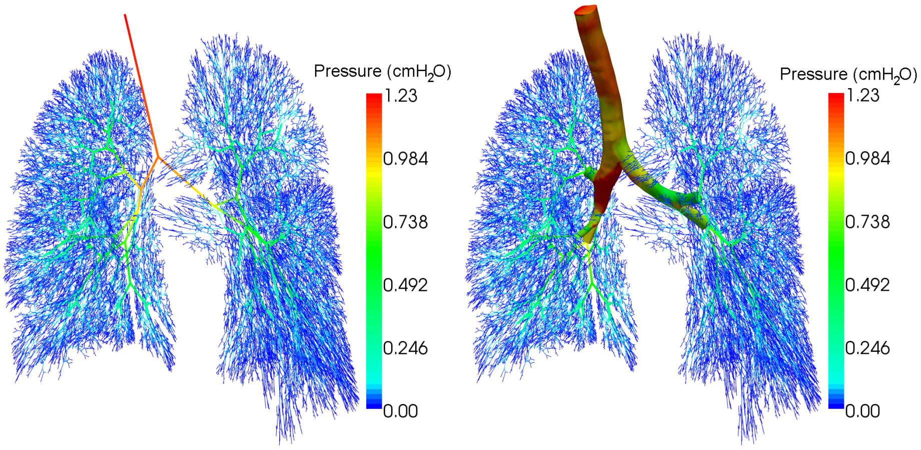

(a) (b)

Figure 4.1.: Pressure values at $Q_{\mathrm{in}} = 120\,\mathrm{l/min}$ in (a) tree of 0D airway modeled using γ from Table 4.1 and (b) the coupled 3D-0D corresponding model.

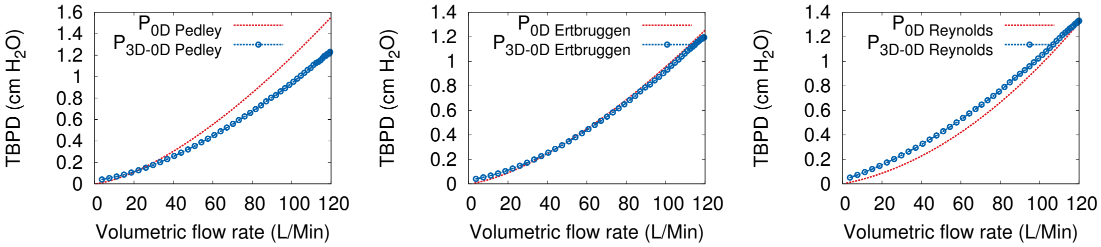

(a) (b) (c)

Figure 4.2.: Comparison of total bronchial pressure drop (TBPD) versus flow rate for the different coupled 3D-0D models and fully 0D models: (a) Pedley's model, (b) van Ertbruggen's model and (c) modified Reynolds' model.

Airway compliance

The airway compliance comes from the airway wall elasticity. In humans, the lower the airway generations are the stiffer the airways are. That is because the lower the airway generations are the more cartilage the airways have. In Section 3.3, the compliance of an airway is found to be

$$C = l_{\mathrm{aw}} \frac{\partial A_{\mathrm{aw}}}{\partial P} = \frac{2A_0\sqrt{A_{\mathrm{aw}}}}{\beta_{\mathrm{s}}} l_{\mathrm{aw}},$$

where

$$\beta_{\mathrm{s}} = \sqrt{\pi} \frac{h_{\mathrm{aw}} E_{\mathrm{aw}}}{1 - \nu_{\mathrm{s}}^2}.$$

While airway area (A_{aw}) and airway length (l_{aw}) are obtained from the geometry in Section 2, A_0, h_{aw} and E_{aw} are unknown. The airway wall thickness is found from morphological measurements of [98], who found a radius-to-thickness ratio for different generation numbers (see Table 4.2). The wall modulus of elasticity is fitted to the measurements reported in [81]. This is done by fitting the wall model used in this work to the generation dependent trumpet model of the human respiratory system, shown in Figure 4.3. The wall model of [81] consists of two parts and included only the conducting zone of the lower respiratory tract. The first part modeled airways under compression and the second part modeled airways under distension. Mathematically, the airway compression is modeled as

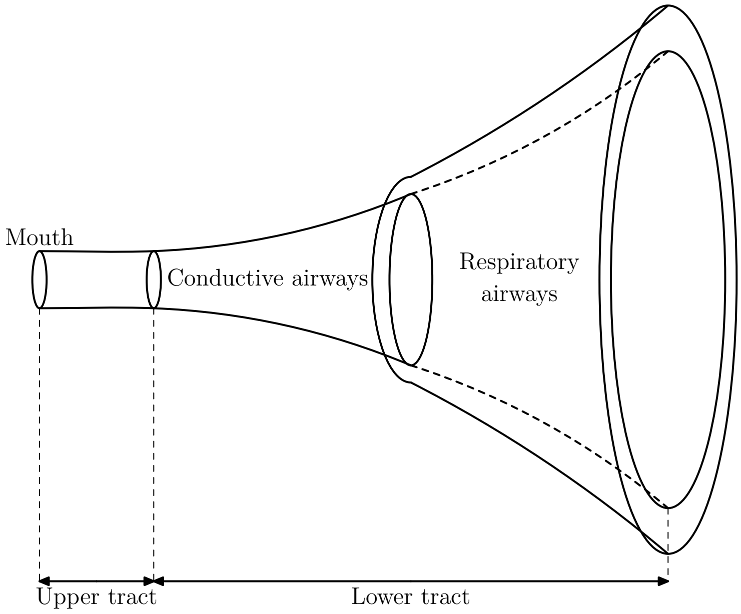

Figure 4.3.: Trumpet model of a human respiratory system as presented in [133].

$$A_{\mathrm{aw}} = A_0 \left(1 - \frac{P_{\mathrm{tm}}}{P_{\mathrm{c}}}\right)^{-n_{\mathrm{c}}} \tag{4.6}$$

where P_{tm} is the trans-mural pressure. The airway distention

$$\frac{A_{\mathrm{aw}}}{A_{\mathrm{m}}} = 1 - \left(1 - \frac{A_0}{A_{\mathrm{m}}}\right)\left(1 - \frac{P_{\mathrm{tm}}}{P_{\mathrm{d}}}\right)^{-n_{\mathrm{d}}}, \tag{4.7}$$

where A_{m} is the airways cross-sectional area at maximum trans-mural pressure and

$$P_{\mathrm{c}} = \frac{A_0}{A_{\mathrm{m}}} n_{\mathrm{c}} E';\; P_{\mathrm{d}} = -n_{\mathrm{d}}\left(1 - \frac{A_0}{A_{\mathrm{m}}}\right) E'.$$

n_{c}, n_{d}, A_0/A_{m} and E' shown in Table 4.2. The airway moduli of elasticity in this work are fitted by setting the compliance of in this work equal to the compliance of Lambert et al. [81]. Since the geometry in Section 2 is extracted at end expiration, all airways are considered to be subjected to a trans-mural pressure of $P_{\mathrm{tm}} = -5.3\,\mathrm{cmH_2O}$. Thus, the compliance in this work is set equal to the compliant of eq (4.7) at $P = -5.3\,\mathrm{cmH_2O}$. The compliance of eq (4.7) read as:

Table 4.2.: Airway wall parameters taken from [81]. The radius-to-thickness ratio ($R_{\mathrm{aw}}/h_{\mathrm{aw}}$) is is taken from [98]. * is the average value between all generations from 10 to 14.

Generation	$R_{\mathrm{aw}}/h_{\mathrm{aw}}$	n_{d}	n_{c}	A_0/A_{m}	E' (kPa)
0	6.745	10	0.5	0.882	9.09
1	5.135	10	0.5	0.882	9.09
2	3.930	10	0.6	0.686	1.96
3	2.660	10	0.6	0.546	1.25
4	2.090	10	0.7	0.450	1.00
5	1.675	10	0.8	0.370	0.80
6	1.445	10	0.9	0.310	0.70
7	1.375	10	1.0	0.255	0.62
8	1.355	10	1.0	0.213	0.57
9	1.350	10	1.0	0.184	0.54
10	1.355	10	1.0	0.153	0.51
11	1.370	9	1.0	0.125	0.48
12	1.335	8	1.0	0.100	0.45
13	1.505	8	1.0	0.075	0.44
14	1.175	8	1.0	0.057	0.42
15	1.348*	7	1.0	0.045	0.41
16	1.348*	7	1.0	0.039	0.41

$$\frac{C_{\mathrm{lam}}}{l_{\mathrm{aw}}} = A_{\mathrm{m}} n_{\mathrm{d}}\left(1 - \frac{A_0}{A_{\mathrm{m}}}\right)\left(\frac{-1}{P_{\mathrm{d}}}\right)\left(1 - \frac{P}{P_{\mathrm{d}}}\right)^{-n_{\mathrm{d}}-1} \tag{4.8}$$

Setting the compliance of the eq (3.9) equal to that of eq (4.8)

$$\frac{2A_0\sqrt{A_{\mathrm{aw}}}}{\beta_{\mathrm{s}}} l_{\mathrm{aw}} = C_{\mathrm{lam}},$$

resulted in

$$E_{\mathrm{aw}} = \left(\frac{2A_0\sqrt{A_{\mathrm{aw}}}}{\pi h_{\mathrm{aw}}}\right)\left(\frac{l_{\mathrm{aw}}}{C_{\mathrm{lam}}}\right).$$

Table 4.3 shows the variation in material properties for some airways at different generations. The effect of compliance is investigated under severe ventilation conditions on the conductive bronchial tree, described in Section 2. For this purpose, two sets of simulation are performed. The first set of simulations is tested on a complaint bronchial tree (RC model), whereas the second set of simulations is performed on a rigid bronchial tree (R model). For both models 9 combinations of tidal volumes and ventilation frequencies are tested. Such that the tidal volumes (V_{TD}) are $0.25\,\mathrm{l}$, $0.5\,\mathrm{l}$ and $1.0\,\mathrm{l}$ per inspiration cycle. The ventilation frequencies (f_{v}) are chosen to be 0.25 Hz, 1 Hz and 4 Hz. As such the tracheal enforced flow rate is of the form

Table 4.3.: Geometric and physical values for some of the airways in different generations.

Generation	A_{aw} (mm^2)	A_0 (mm^2)	h_{aw} (mm)	E_{aw} (kPa)	c (m/s)
0	194.80000	185.314166	1.167	183.853	110.4
1	136.44000	129.789741	1.283	139.968	110.4
2	57.05908	45.382604	1.084	26.222	59.7
3	28.17046	18.893515	1.126	9.695	48.1
4	13.25691	7.640260	0.983	5.175	42.7
5	6.23865	3.004775	0.841	2.979	39.6
6	2.93588	1.205537	0.669	1.970	37.6
7	1.38161	0.472983	0.482	1.434	36.0
8	0.65018	0.187113	0.336	1.122	35.0
9	0.30597	0.076481	0.231	0.935	34.3
10	0.14399	0.030152	0.158	0.754	33.6
11	0.06776	0.011634	0.107	0.609	33.2
12	0.03189	0.004390	0.075	0.467	32.9
13	0.01501	0.001560	0.046	0.385	32.4
14	0.00706	0.000559	0.040	0.225	32.1
15	0.00332	0.000209	0.024	0.203	32.0
16	0.00156	0.000085	0.017	0.176	31.9

$$Q_{\mathrm{t}} = \frac{V_{\mathrm{TD}} f_{\mathrm{v}}}{2}\left(1 - \cos\left(2t\pi f_{\mathrm{v}}\right)\right).$$

At the terminal airways a pressure condition is enforced of the form

$$P_{\text{term}} = \left(\frac{P_{\text{tp}}^{\max}}{2}\right)\left(1 - \cos\left(2t\pi f_{\text{v}}\right)\right),$$

where $P_{\text{tp}}^{\max} = 15\,\text{cmH}_2\text{O}$ imitates the extreme mechanical ventilation conditions. The results are presented in Figure 4.4. The increase in ventilation frequency led to a negligible phase shift between the R and the RC model. Thus showing that under mechanical ventilation the complaint effects are negligible. However, the increase in the cross-sectional area led to a lower total bronchial pressure drop. Thus suggesting that airway compliant effects may not be ignored.

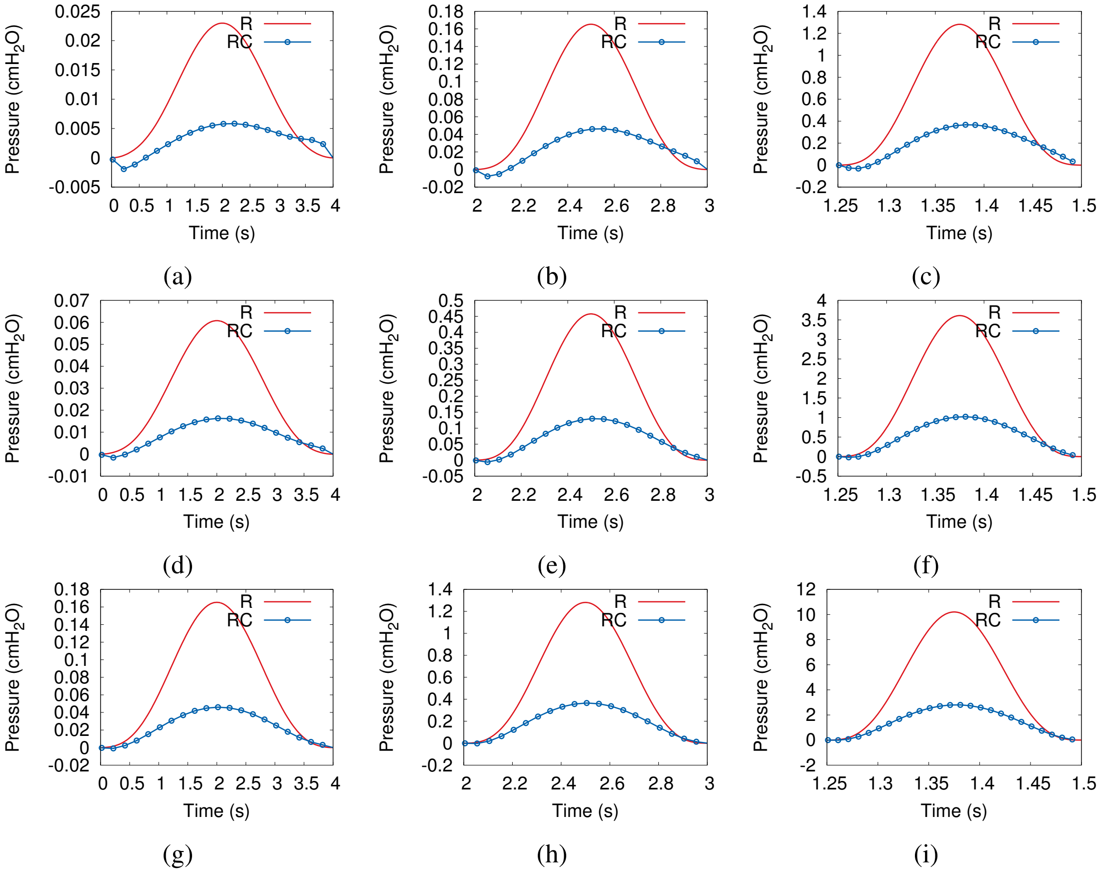

Figure 4.4.: Total bronchial pressure drop of the RC bronchial tree compared to R bronchial tree for (a) TV=$0.25\,\text{l}$ and $f = 0.25\,\text{Hz}$, (b) TV=$0.25\,\text{l}$ and $f = 1\,\text{Hz}$, (c) TV=$0.25\,\text{l}$ and $f = 4\,\text{Hz}$, (d) TV=$0.5\,\text{l}$ and $f = 0.25\,\text{Hz}$, (e) TV=$0.5\,\text{l}$ and $f = 1\,\text{Hz}$, (f) TV=$0.5\,\text{l}$ and $f = 4\,\text{Hz}$, (g) TV=$1\,\text{l}$ and $f = 0.25\,\text{Hz}$, (h) TV=$1\,\text{l}$ and $f = 1\,\text{Hz}$, and (i) TV=$1\,\text{l}$ and $f = 4\,\text{Hz}$.

Inertial Effects

It is known that in airways, inertial effects are observed during high frequencies and can totally be ignored in low frequencies [8]. To validate that, inertial effects are investigated in the same manner as the compliant effects, i.e. under extreme ventilation conditions, on the bronchial tree described in Section 2. Again, two sets of simulation are performed. The first set of simulations is tested on a complaint-inertial bronchial tree (RLC model), whereas the second set of trees are performed on a rigid bronchial tree (R model). For both models 9 combinations of tidal volumes and ventilation frequencies are tested. Such that the tidal volumes (V_{TD}) are $0.25\,\mathrm{l}$, $0.5\,\mathrm{l}$ and $1.0\,\mathrm{l}$ per inspiration cycle. The ventilation frequencies (f_{v}) are chosen to be $0.25\,\mathrm{Hz}$, $1\,\mathrm{Hz}$ and $4\,\mathrm{Hz}$. As such the tracheal enforced flow rate is of the form

$$Q_{\mathrm{t}} = \frac{V_{\mathrm{TD}} f_{\mathrm{v}}}{2} \left(1 - \cos\left(2t\pi f_{\mathrm{v}}\right)\right).$$

At the terminal airways a pressure condition is enforced of the form

$$P_{\mathrm{term}} = \left(\frac{P_{\mathrm{tp}}^{\mathrm{max}}}{2}\right) \left(1 - \cos\left(2t\pi f_{\mathrm{v}}\right)\right),$$

where $P_{\mathrm{tp}}^{\mathrm{max}} = 15\,\mathrm{cmH_2O}$ imitates the extreme mechanical ventilation conditions. The results are presented in Figure 4.5. The increase in ventilation frequency led to a significant phase shift between the R and the RLC model. Thus showing that under mechanical ventilation the inertial effects are not negligible. However, the peak tracheal pressure is similar to the one observed in Figure 4.4.

Viscous effects

The viscous effects of airway wall, represented by R_{vis}, are fitted to the measurements of [70], who fitted the airway wall material using complex modulus spectra $G^{*}\left(\omega\right) = G'_{\mathrm{aw}}\left(\omega\right) + iG''_{\mathrm{vis}}\left(\omega\right)$, where $\left(\omega\right) = 2\pi f$ is the angular frequency and f stands for frequency. As such, the wall model used in this work, i.e. of eq (3.9) is rewritten as

$$P\left(\omega\right) - P_{\mathrm{ext}}\left(\omega\right) = \frac{\sqrt{\pi} h_{\mathrm{aw}}}{\left(1 - \nu^{2}\right)\sqrt{A_0}} \left[G'\left(\omega\right) + jG''\left(\omega\right)\right] \epsilon\left(\omega\right)$$

where ϵ is the circumferential strain defined as

$$\epsilon = \frac{\sqrt{A_{\mathrm{aw}}} - \sqrt{A_0}}{\sqrt{A_0}}.$$

From the results of G' and G'' in [70], it is observed that G' is almost constant for all frequencies whereas G'' is a linear function of the frequency. As such is $G' = E_{\mathrm{aw}}$ and $G'' = \left(\omega/2\pi\right) R''$, where $G'\left(\omega\right)/R''\left(\omega\right) = 8$ [66]. This means that eq (3.9) can again be rewritten in frequency domain as

$$P\left(\omega\right) - P_{\mathrm{ext}}\left(\omega\right) = \frac{\beta_{\mathrm{s}}}{\sqrt{A_0}} \left(1 + j\omega\frac{1}{16\pi}\right) \epsilon\left(\omega\right)$$

and in time domain as

$$P - P_{\mathrm{ext}} = \frac{\beta_{\mathrm{s}}}{\sqrt{A_0}} \left(\epsilon + \frac{1}{16\pi}\frac{\partial\epsilon}{\partial t}\right).$$

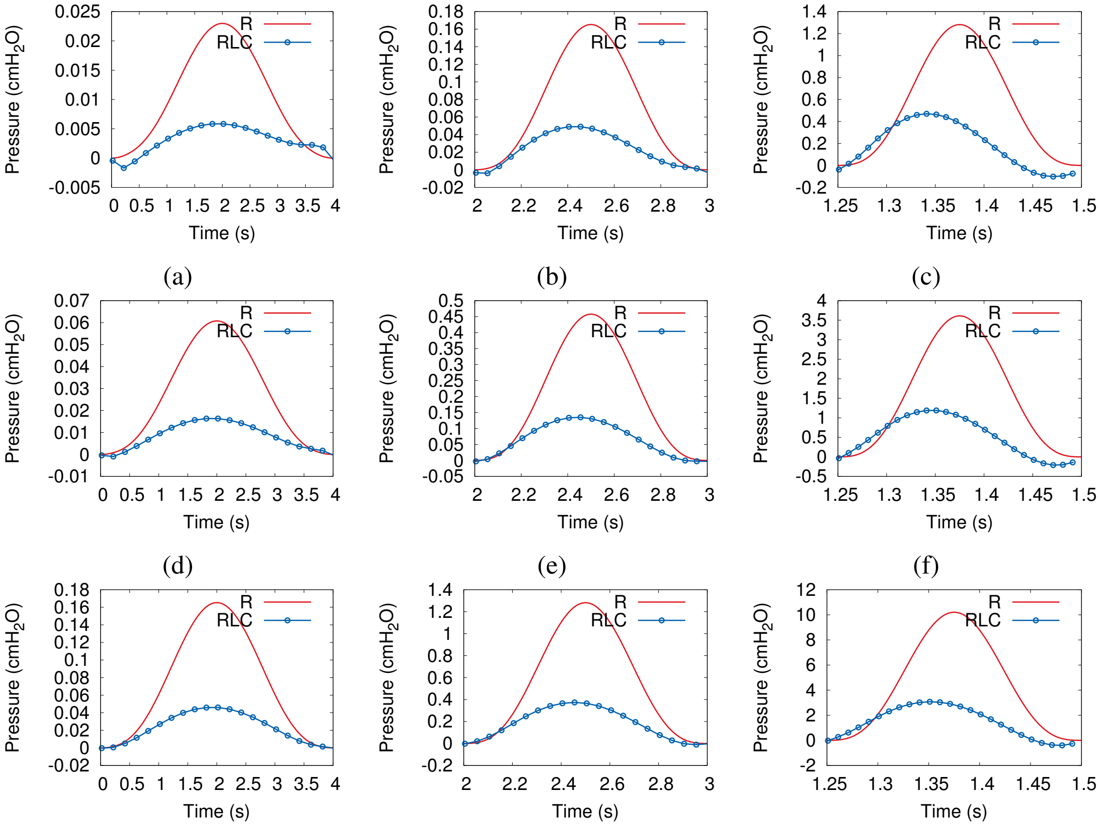

(a) (b) (c)

(d) (e) (f)

(g) (h) (i)

Figure 4.5.: Total bronchial pressure drop of the RLC bronchial tree compared to R bronchial tree for (a) TV=$0.25\,\mathrm{l}$ and $f = 0.25\,\mathrm{Hz}$, (b) TV=$0.25\,\mathrm{l}$ and $f = 1\,\mathrm{Hz}$, (c) TV=$0.25\,\mathrm{l}$ and $f = 4\,\mathrm{Hz}$, (d) TV=$0.5\,\mathrm{l}$ and $f = 0.25\,\mathrm{Hz}$, (e) TV=$0.5\,\mathrm{l}$ and $f = 1\,\mathrm{Hz}$, (f) TV=$0.5\,\mathrm{l}$ and $f = 4\,\mathrm{Hz}$, (g) TV=$1\,\mathrm{l}$ and $f = 0.25\,\mathrm{Hz}$, (h) TV=$1\,\mathrm{l}$ and $f = 1\,\mathrm{Hz}$, and (i) TV=$1\,\mathrm{l}$ and $f = 4\,\mathrm{Hz}$.

Finally, further mathematical manipulation yields the following viscous resistance

$$R_{\mathrm{visc}} = \frac{1}{16\pi l}\left(\frac{\beta_{\mathrm{s}}}{A_0\sqrt{A_{\mathrm{aw}}}}\right).$$

The airway wall viscous effects are investigated in a similar manner to the compliant effects on the bronchial tree described in Section 2, i.e. under extreme ventilation conditions. Again, two sets of simulation are performed. The first set of simulations is tested on a visco-elastic-inertial bronchial tree (RLC-visc model), whereas the second set of trees are performed of a rigid bronchial tree (R model). For both models 9 combinations of tidal volumes and ventilation frequencies are tested. Such that the tidal volumes (V_{TD}) are $0.25\,\mathrm{l}$, $0.5\,\mathrm{l}$ and $1.0\,\mathrm{l}$ per inspiration cycle. The ventilation frequencies (f_{v}) are chosen to be $0.25\,\mathrm{Hz}$, $1\,\mathrm{Hz}$ and $4\,\mathrm{Hz}$. As such the tracheal enforced flow rate is of the form

$$Q_{\mathrm{t}} = \frac{V_{\mathrm{TD}} f_{\mathrm{v}}}{2}\left(1 - \cos\left(2t\pi f_{\mathrm{v}}\right)\right).$$

At the terminal airways a pressure condition is enforced of the form

$$P_{\mathrm{term}} = \left(\frac{P_{\mathrm{tp}}^{\mathrm{max}}}{2}\right)\left(1 - \cos\left(2t\pi f_{\mathrm{v}}\right)\right),$$

where $P_{\mathrm{tp}}^{\mathrm{max}} = 15\,\mathrm{cmH_2O}$ imitates the extreme mechanical ventilation conditions. The results in

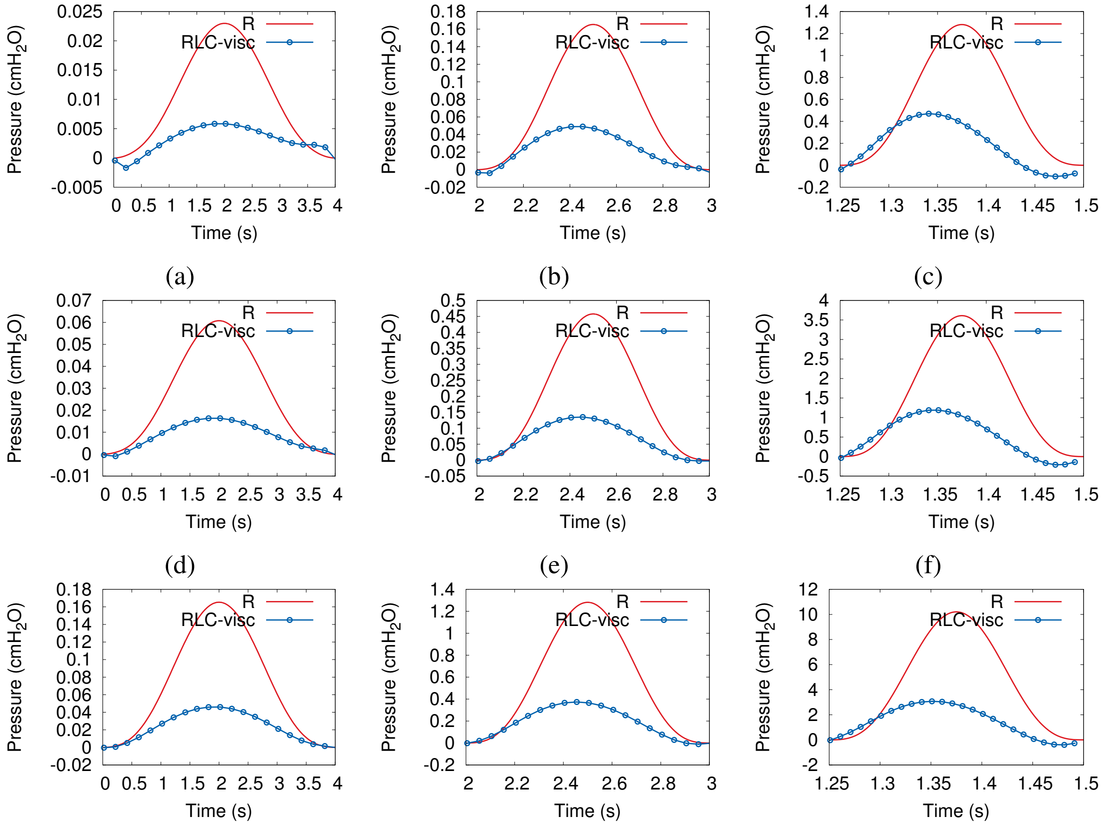

(a) (b) (c)

(d) (e) (f)

(g) (h) (i)

Figure 4.6.: Total bronchial pressure drop of the visco-elastic RLC bronchial tree compared to R bronchial tree for (a) TV=$0.25\,\mathrm{l}$ and $f = 0.25\,\mathrm{Hz}$, (b) TV=$0.25\,\mathrm{l}$ and $f = 1\,\mathrm{Hz}$, (c) TV=$0.25\,\mathrm{l}$ and $f = 4\,\mathrm{Hz}$, (d) TV=$0.5\,\mathrm{l}$ and $f = 0.25\,\mathrm{Hz}$, (e) TV=$0.5\,\mathrm{l}$ and $f = 1\,\mathrm{Hz}$, (f) TV=$0.5\,\mathrm{l}$ and $f = 4\,\mathrm{Hz}$, (g) TV=$1\,\mathrm{l}$ and $f = 0.25\,\mathrm{Hz}$, (h) TV=$1\,\mathrm{l}$ and $f = 1\,\mathrm{Hz}$, and (i) TV=$1\,\mathrm{l}$ and $f = 4\,\mathrm{Hz}$.

Figure 4.6 show no difference to the results of Figure 4.5. Thus suggesting that the airway wall viscous effects are negligible.

4.1.2. Respiratory airways (0D acinar model)

Due to lack of information about human lung tissue, the acinar models are tuned to the PV-curves of the *in silico* model of Denny and Schroter [29]. This is performed through two steps. Firstly, the Maxwell components of the linear 0D alveolar duct model in eq (3.23) are fitted to reproduce the tidal breathing tissue elasticity (E_{dyn}) and tissue resistance (R_{dyn}) curves of [29]. The tissue elasticity (E_{dyn}) and resistance (R_{dyn}) of the alveolar duct model are defined as

$$P_{\mathrm{tp}}(\omega) = \left(E_{\mathrm{dyn}} + j\omega R_{\mathrm{dyn}}\right)\Delta V_i(\omega),$$

where P_{tp} is the trans-pulmonary pressure, ΔV_i the change in alveolar duct volume and ω the angular frequency. A simple mathematical manipulation of Maxwell model in eq (3.23) leads to

$$\begin{aligned} E_{\mathrm{dyn}} &= \frac{\omega^2 B^2 (E_1 + E_2) + E_1 E_2^2}{E_2^2 + \omega^2 B^2} \\ R_{\mathrm{dyn}} &= \frac{E_2^2 (B + B_a) + \omega^2 B_a B^2}{E_2^2 + \omega^2 B^2}. \end{aligned}$$

The fitted Maxwell E_{dyn} and R_{dyn} resulted in Maxwell components presented Table 4.4. The results in Figure 4.7 show a very good agreement between the fitted 0D alveolar duct Maxwell model and the *in silico* model of Denny and Schroter [29].

Table 4.4.: Maxwell elements calibrated to E_{dyn} and R_{dyn} of [29]

$\mathrm{E_1}$	1.46×10^5	$\mathrm{cmH_2O \cdot ml^{-1}}$
$\mathrm{E_2}$	0.53×10^5	$\mathrm{cmH_2O \cdot ml^{-1}}$
B	32.85×10^3	$\mathrm{cmH_2O \cdot s \cdot ml^{-1}}$
B_a	1.88×10^3	$\mathrm{cmH_2O \cdot s \cdot ml^{-1}}$

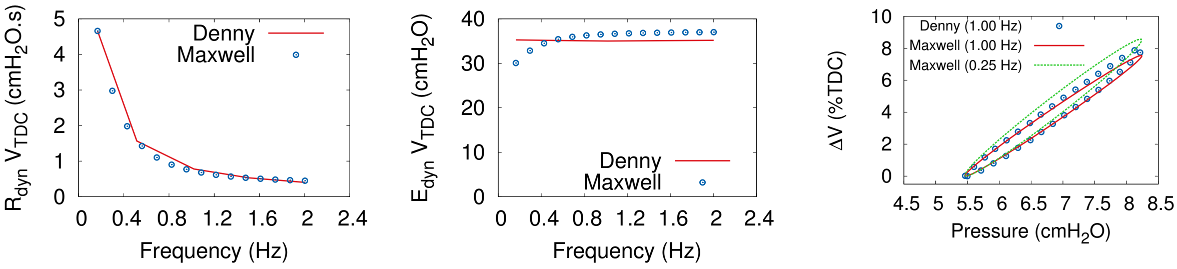

(a) (b) (c)

Figure 4.7.: Fitted 0D alveolar duct showing (a) tissue resistance (R_{dyn}) multiplied by V_{TDC}, (b) tissue elastance (E_{dyn}) multiplied by V_{TDC} and (c) PV-curves at cyclic loading of $1.0\,\mathrm{Hz}$ and $0.25\,\mathrm{Hz}$. V_{TDC} is the duct total capacitance defined as the alveolar duct's volume at a trans-pulmonary pressure $P_{\mathrm{tp}} = 30\,\mathrm{cmH_2O}$.

The nonlinear 0D alveolar duct is tuned also using the *in silico* model of Denny and Schroter [29]. In this case E_2, B and B_{a} are kept the same as in Table 4.4. However, the hyper-elastic E_1, defined in eq (3.24), is fitted to the quasi-static PV-curve of the saline filled alveolar duct under full pressure span in [29]. Thus, yielding the following terms

$$\begin{aligned}
E_1^{\mathrm{o}} &= 6.510\times 10^{6}\,\mathrm{Pa}\cdot\mathrm{ml}^{-1}\\
b &= 35.23\times 10^{9}\,\mathrm{Pa}\cdot\mathrm{ml}^{-2}\\
\kappa^{\mathrm{u}} &= 6.971\times 10^{-3}\,\mathrm{Pa}\cdot\mathrm{ml}^{-1}\\
\tau^{\mathrm{u}} &= 14.47\,\mathrm{cm}\cdot\mathrm{s}^{-1}\\
\kappa^{\mathrm{l}} &= 5.320\times 10^{7}\,\mathrm{Pa}\cdot\mathrm{ml}^{-1}\\
\tau^{\mathrm{l}} &= -9.0\,\mathrm{cm}\cdot\mathrm{s}^{-1}.
\end{aligned}$$

Figure 4.8(a) shows E_1 as a function of the alveolar volume, where V_a^{TDC} is the volume of an alveolar duct at total duct capacitance (TDC). TDC is defined as the state when the trans-pulmonary pressure (P_{tp}) is equal to $30\,\mathrm{cmH_2O}$. Figure 4.8(b) shows a very good agreement between the quasi-static PV-curve of the nonlinear Maxwell alveolar duct and the saline filled alveolar duct of [29]. Figure 4.8(c) shows again an excellent match between the tidal volume results of the nonlinear Maxwell alveolar duct and the *in silico* model of [29].

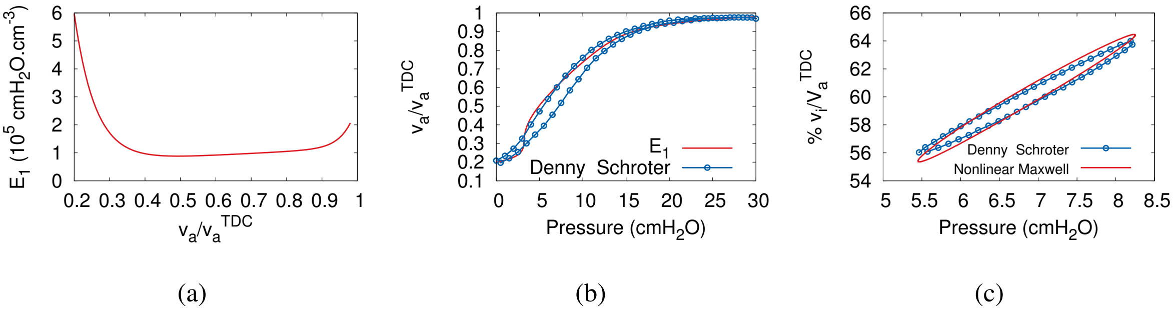

(a) (b) (c)

Figure 4.8.: Nonlinear 0D alveolar Maxwell model showing (a) Fitted E_1 stiffness for different alveolar duct volumes; (b) quasi-static PV curves of the 4-element Maxwell alveolar duct versus the saline filled alveolar duct of [29]; (c) cyclic tidal PV curves of the 4-element Maxwell alveolar duct versus the results of [29].

To validate the Maxwell alveolar duct, the model is tested for the full trans-pulmonary pressure span on the entire respiratory system shown in Figure 2.6. For this purpose, the respiratory zone is first evaluated at the stress free state, i.e. $P_{\mathrm{tp}} = 0\,\mathrm{cmH_2O}$. This is simply achieved by scaling all the acini in Figure 2.6 by a factor of $\varrho = 0.35$. This factor is simply evaluated from Table 2.2 as

$$\varrho = \frac{V_{\mathrm{ad}}\big|_{P_{\mathrm{tp}}=0\mathrm{cmH_2O}}}{V_{\mathrm{ad}}\big|_{P_{\mathrm{tp}}=5.3\mathrm{cmH_2O}}}.$$

The full trans-pulmonary pressure span is tested under spontaneous breathing. This means that the flow of air into the lung is driven by the negative pleural pressure generated from the deformations of the diaphragm and the rib cage. The author considers, based on data reported in physiology, that a healthy adult human being should have a pleural pressure of -2 to $0\,\mathrm{cmH_2O}$ at residual volume [78], a $-5.3\,\mathrm{cmH_2O}$ at functional residual volume [43; 155], a $-8.3\,\mathrm{cmH_2O}$ at peak relaxed tidal volume [43; 155] and $-30\,\mathrm{cmH_2O}$ at the total lung capacitance [56]. These pleural pressure values are combined together into the following form

$$P_{\mathrm{pl}} = 0.5\left(P_{\max} - P_{\min}\right)\left[\cos\left(2t\pi/T + \phi\right) + 1\right] + P_{\min} + P_{\mathrm{pl}}^{\mathrm{g}}, \tag{4.9}$$

where $P_{\max}$, $P_{\min}$, T and ϕ are defined in Table 4.5. Furthermore, the respiratory system is tested under spatially heterogeneous pleural pressure by subjecting it to gravitational forces. The gravitational pleural $P_{\mathrm{pl}}^{\mathrm{g}}$ is defined as

Table 4.5.: Assumed pleural pressure variables, for eq (4.9), during a spirometry simulation.

time (s)	P_{min} (cmH$_2$O)	P_{max} (cmH$_2$O)	ϕ (rad)	T (s)
$t \leq 16$	-8.3	-5.3	0	4
$16 < t \leq 18$	-30	-5.3	0	4
$18 < t \leq 28$	-30	0.0	$6\pi/5$	20
$28 < t \leq 30$	-5.3	0.0	0	4
$t > 30$	-8.3	-5.3	0	4

$$P_{\mathrm{pl}}^{\mathrm{g}} = \left(\mathbf{N}_1 P_{\min}^{\mathrm{g}} + \mathbf{N}_2 P_{\max}^{\mathrm{g}}\right)^{\mathrm{T}} \cdot \mathbf{n}_{\mathrm{g}}, \tag{4.10}$$

where $\mathbf{n}_{\mathrm{g}}$ is the direction of gravity. $P_{\max}^{\mathrm{g}} = 3.75\,\mathrm{cmH_2O}$ and $P_{\min}^{\mathrm{g}} = -3.75\,\mathrm{cmH_2O}$ are taken from [155]. $\mathbf{N}_1$ and $\mathbf{N}_2$ are defined as:

$$\mathbf{N}_1 = -\frac{\mathbf{x} - \mathbf{x}_{\min}}{L_{\mathrm{u}}}, \quad \mathbf{N}_2 = -\frac{\mathbf{x}_{\max} - \mathbf{x}}{L_{\mathrm{u}}},$$

where L_{u} is the height of the lung in the upright position, $\mathbf{x}$ is the spatial coordinate of any point within the lung and $\mathbf{x}_{\mathrm{min,max}}$ defined as

$$\mathbf{x}_{\mathrm{min,max}} = \mathbf{x}_{\mathrm{c}} \pm \frac{L_{\mathrm{u}}}{2}\mathbf{n}_{\mathrm{g}}.$$

$\mathbf{x}_{\mathrm{c}}$ is the midpoint between the furthest two points in the lung, along the direction vector $\mathbf{n}_{\mathrm{g}}$, i.e. $\mathbf{x}_{\mathrm{c}}$ is defined as

$$\mathbf{x}_{\mathrm{c}} = \frac{\mathbf{x}_{i^*} + \mathbf{x}_{j^*}}{2}$$

such that

$$\left(i^*, j^*\right) = \arg \max_{(i,j)\in\mathcal{I}\times\mathcal{I}} d^2\left(\mathbf{x}_i, \mathbf{x}_j\right),$$

where $d^2\left(\mathbf{x}_i, \mathbf{x}_j\right) = \left(\mathbf{x}_i \cdot \mathbf{n}_{\mathrm{g}} - \mathbf{x}_j \cdot \mathbf{n}_{\mathrm{g}}\right)^2, \mathcal{I} = \{1, \cdots, n_p\}$ and n_p the total number of points inside the lung geometry. Figure 4.9 shows how $P_{\mathrm{pl}}^{\mathrm{g}}$ looks for different lung positions, i.e. different $\mathbf{n}_{\mathrm{g}}$. The center line in Figure 4.9, where $P_{\mathrm{pl}}^{\mathrm{g}} = 0$, denoted the set of points where $\mathbf{x}_{\mathrm{c}}$ is located for the presented different positions. Figure 4.9 shows that the assumed gravitational pleural pressure is linear. This assumption is true for lungs that deform only in the direction of the gravity and is observed in the finite-element (FE) simulation results of [136]. At the trachea, the respiratory system is simply subjected to zero pressure. The pleural pressures of eq (4.9) and eq (4.10) are

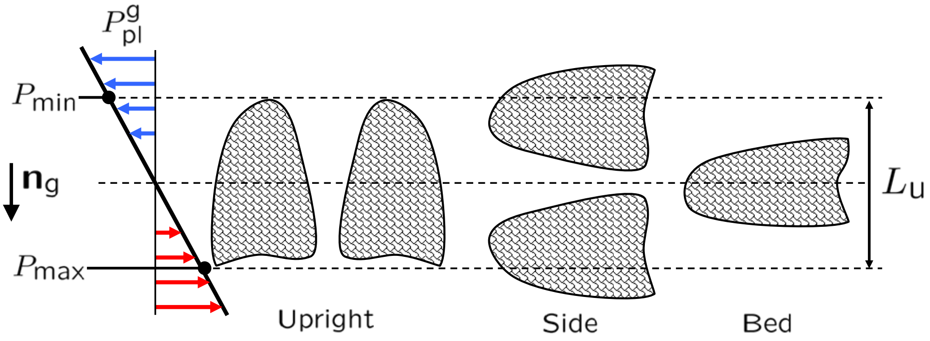

Figure 4.9.: Representation of gravitational effects, P_{pl}^{g}, for different lung positions

added together and enforced onto all of the acini. The subject is assume in upright position. The simulations are performed for a time step of $1\,\text{ms}$. The simulation results are shown in

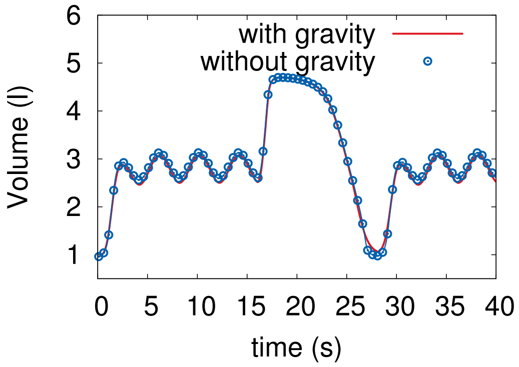

Figure 4.10.: Results of the lung volume variation during of spontaneous breathing.

Figure 4.10 and Figure 4.11. The lung volumes in Figure 4.10 show that the 0D acinar model reproduced physiological results. The acinar volumetric strains in Figure 4.11 shows that the 0D model performs well under various conditions. Furthermore, it is clear that the model gives a deeper insight into the lung state. That is observed after noticing that while lung volumes did not change after adding the contribution of gravity, the local acinar state significantly changed.

4.1.3. Inter-acinar dependencies

Throughout this work, each acinus is assumed to share its surface area equally among its neighboring acini. This implied that, in eq (3.33), $A_{i,k}^{\text{eff}} = A_{i,j}^{\text{eff}} = A_i^{\text{eff}}/N_i$, where N_i is the number of neighborhoods of acinus Ac_i. This leads to the following interdependence model

$$P_{\text{intr}_i} - \frac{P_{\text{pl}_i}}{N_i} - \sum_{j \neq i} \frac{P_{\text{intr}_j}}{N_i} = 0. \tag{4.11}$$

To illustrate how acini can compete for the same volume, the two examples in Figure 4.12 are assumed. In both of the sketched examples the two acini are interconnected via an incompress-

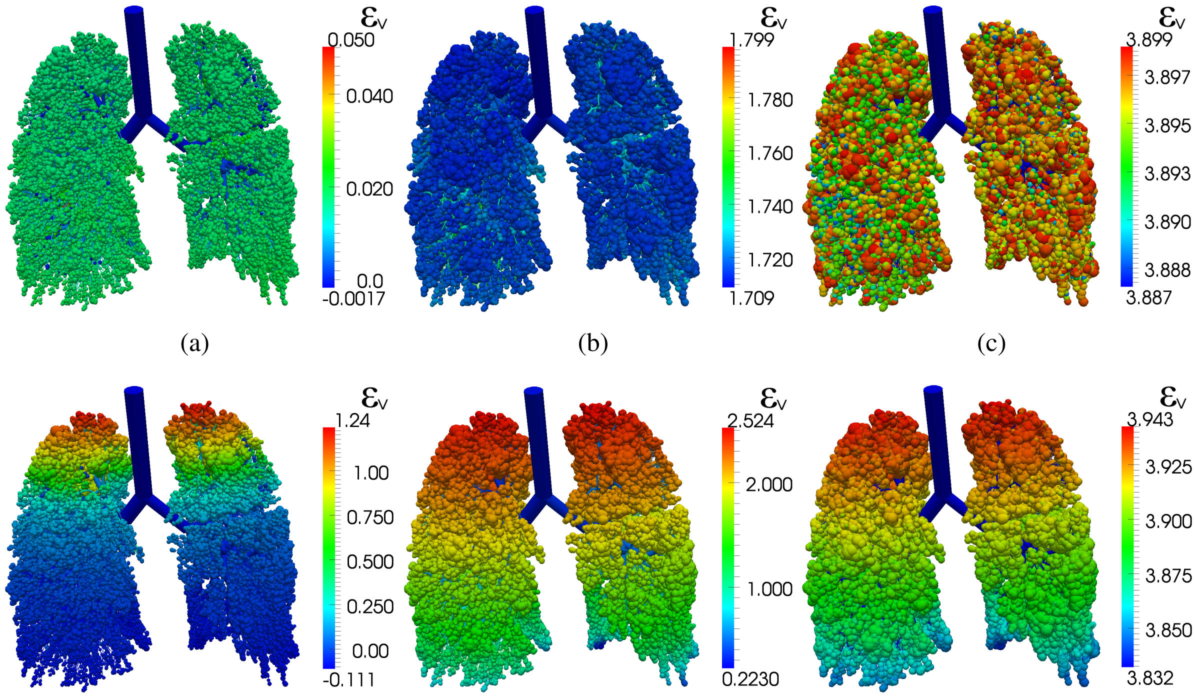

(a) (b) (c)

(d) (e) (f)

Figure 4.11.: Acinar volumetric strain of a spontaneously breathing lung at (a) residual volume without gravitational effects; (b) functional residual volume without gravitational effects; (c) total lung capacitance without gravitational effects; (d) residual volume with gravitational effects; (e) functional residual volume with gravitational effects; (f) total lung capacitance with gravitational effects.

ible tissue. However, the tissue in Figure 4.12(a) is surrounded by a rigid wall, whereas the tissue in Figure 4.12(b) is not. This means that, in Figure 4.12(a) the sum of both acinar volumes is expected to remain constant, whereas in Figure 4.12(b) the sum of both acinar volumes is allowed to change. The volume competition is observed after the acini are subjected to internal pressure. In both of the cases of Figure 4.12 each acinus is assumed to have a volume of 1.0 units of volume (i.e. $V_1^0 = V_2^0 = V^0 1.0$) and a constant volumetric stiffness of 1.0 units of volumetric stiffness (i.e. $K_{\mathrm{ac}_1} = K_{\mathrm{ac}_2} = K_{\mathrm{ac}} = 1.0$). The wall in Figure 4.12(a) is modeled as a resistance pressure P_{w}, such that the sum of both acini may not exceed 2.0 units-of-volume (see Figure 4.13(a)). The pleural pressure in Figure 4.12(b) is considered to be zero ($P_{\mathrm{pl}_1} = P_{\mathrm{pl}_2} = 0$). The first acinus is assumed to have a zero pressure ($P_1 = 0$) and the second acinus is subjected to

$$P_2 = \frac{1}{2}\left(1 + \cos\left(\pi t / T\right)\right),$$

where t is time and T is equal to 1.0 units of time. The 0D representations of the examples in Figure 4.12 are shown in Figure 4.13. The simulations are performed for a time period of T. The results are shown in Figure 4.14. The balance of forces between the two acini in Figure 4.13(a)

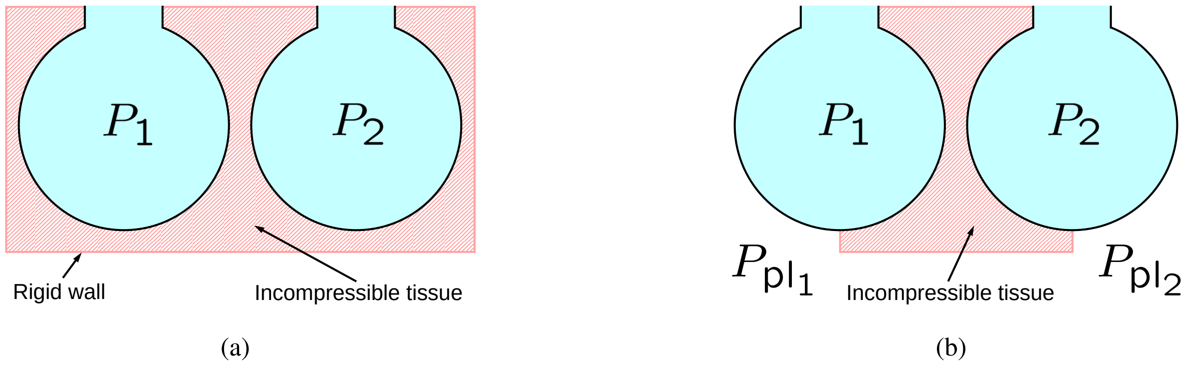
P_1
P_2
Rigid wall
Incompressible tissue
(a)
P_1
P_2
P_{pl_1}
Incompressible tissue
P_{pl_2}
(b)

Figure 4.12.: A cartoon sketch of two acini trapped inside an incompressible tissue. The tissue is surrounded by (a) rigid wall and (b) flexible wall.

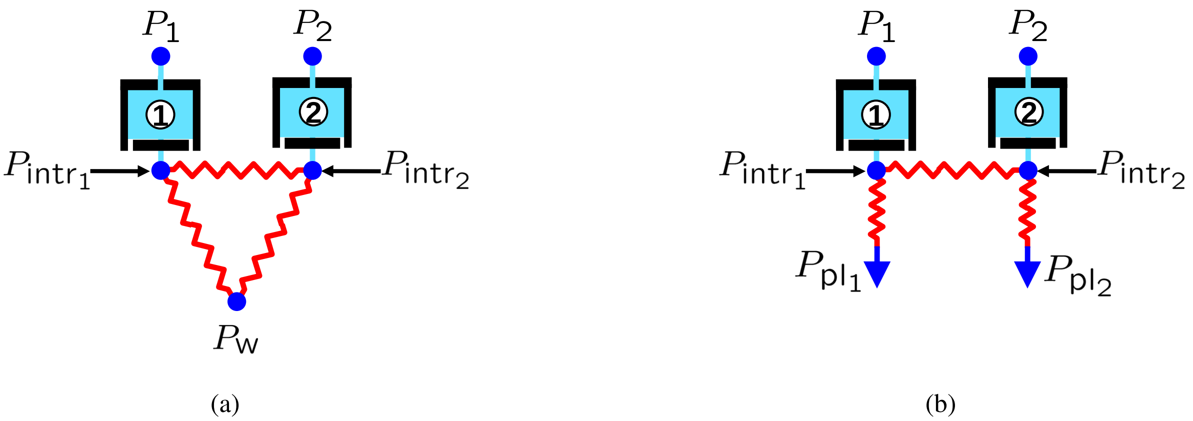
P_1
P_2
①
②
P_{intr_1}
P_{intr_2}
P_{w}
(a)
P_1
P_2
①
②
P_{intr_1}
P_{intr_2}
P_{pl_1}
P_{pl_2}
(b)

Figure 4.13.: A cartoon sketch of two acini trapped inside an incompressible tissue. The tissue is surrounded by (a) rigid wall and (b) flexible wall.

read

$$\begin{aligned} P_{\mathrm{intr}_1} - \frac{1}{2}P_{\mathrm{w}} - \frac{1}{2}P_{\mathrm{intr}_2} &= 0, \\ P_{\mathrm{intr}_2} - \frac{1}{2}P_{\mathrm{w}} - \frac{1}{2}P_{\mathrm{intr}_1} &= 0. \end{aligned}$$

The balance of forces between the two acini in Figure 4.13(b) read

$$\begin{aligned} P_{\mathrm{intr}_1} - \frac{1}{2}P_{\mathrm{pl}_1} - \frac{1}{2}P_{\mathrm{intr}_2} &= 0, \\ P_{\mathrm{intr}_2} - \frac{1}{2}P_{\mathrm{pl}_2} - \frac{1}{2}P_{\mathrm{intr}_1} &= 0. \end{aligned}$$

The examples of Figure 4.12 are expected to perform as following:

- In Figure 4.12(a), only acinus Ac_2 is subjected to an internal pressure. This means that, acinus Ac_2 must expand, whereas acinus Ac_1 must shrink. This also means that, the expansion in acinus Ac_2 must be resisted by the stiffness of acinus Ac_1. Since the volume of both acini may not exceed 2.0 units-of-volume, acinus Ac_2 should increase its volume by $V_2 = V_2^0 + (P_2 - P_1)/(2K_{\mathrm{ac}})$, i.e. $V_2 = 1.0 + (P_2 - P_1)/2$ and $V_1 = 1.0 - (P_2 - P_1)/2$.
- In Figure 4.12(b), both acini are subjected to a flexible wall, then both acini should behave independently from each other. Therefore, acinus Ac_1 and acinus Ac_2 should increase their volume by $V_1 = V_1^0 + (P_1 - P_{\mathrm{pl}_1})/(K_{\mathrm{ac}})$ and $V_2 = V_2^0 + (P_2 - P_{\mathrm{pl}_2})/(K_{\mathrm{ac}})$, respectively, i.e. $V_1 = 1.0 + P_2$ and $V_1 = 1.0 + P_1$.

Looking at the results in Figure 4.14, the inter-acinar linkers successfully captured the scenarios presented in Figure 4.12. Thus, the results of Figure 4.14 matched the analytic solutions.

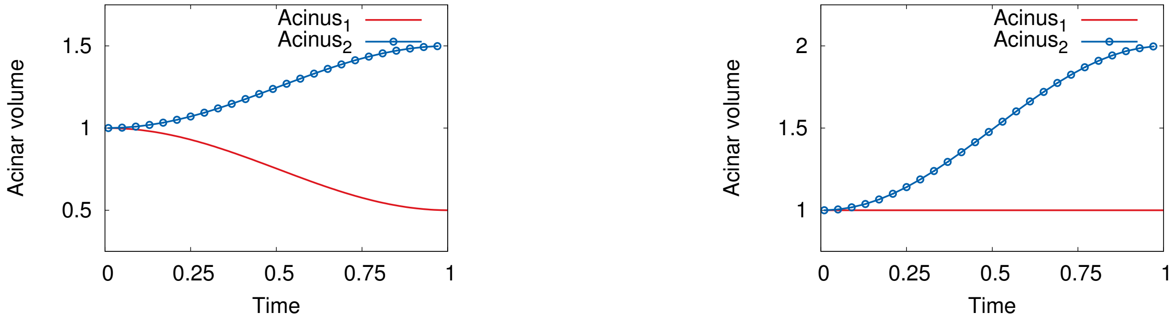

(a)

(b)

Figure 4.14.: Volume of the two interconnected 0D acini for (a) the rigid wall case in Figure 4.12(a) and (b) for the flexible wall case in Figure 4.12(b).

Further investigation of the examples of Figure 4.12 shows that the inter-acinar linkers can simply be replaced by the wall pressure (P_{w}). This is indeed the case, since both acini are subjected to a homogeneous wall forces. To illustrate the importance of the inter-acinar linkers, presented by eq (4.11), on problems with heterogeneous wall forces, the four-acini in Figure 3.9(a) are investigated. The 0D representation of Figure 3.9(a) is presented in Figure 4.15. The balance of forces between the different acini reads as

$$\begin{aligned}
P_{\mathrm{intr}_1} - \frac{1}{2}P_{\mathrm{pl}_1} - \frac{1}{2}P_{\mathrm{intr}_2} &= 0,\\
P_{\mathrm{intr}_2} - \frac{1}{3}P_{\mathrm{intr}_1} - \frac{1}{3}P_{\mathrm{intr}_3} - \frac{1}{3}P_{\mathrm{intr}_4} &= 0,\\
P_{\mathrm{intr}_3} - \frac{1}{3}P_{\mathrm{pl}_3} - \frac{1}{3}P_{\mathrm{intr}_2} - \frac{1}{3}P_{\mathrm{intr}_4} &= 0,\\
P_{\mathrm{intr}_4} - \frac{1}{2}P_{\mathrm{intr}_2} - \frac{1}{2}P_{\mathrm{intr}_3} &= 0.
\end{aligned}$$

All acini are assumed to have the same volume and are modeled using the nonlinear acinar model of Section 3.4. The first test is performed by applying a homogeneous pleural pressure as shown

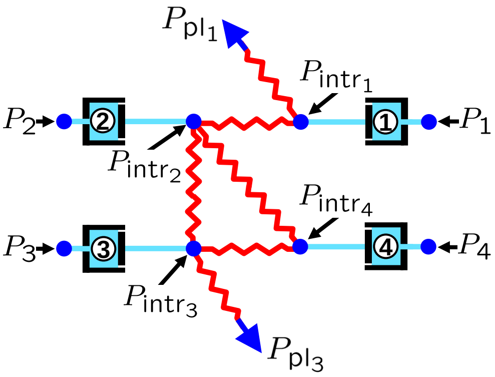

(a)

Figure 4.15.: 0D model of Figure 3.9(a)

in Figure 4.16(a). The second test is performed by applying a heterogeneous pleural pressure as shown in Figure 4.16(b). The results of the homogeneous and heterogeneous pleural pressure

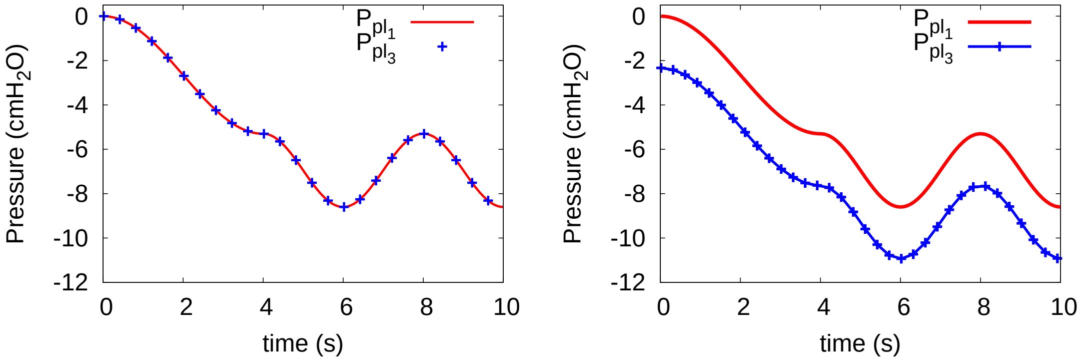

(a) (b)

Figure 4.16.: Pleural pressures used in two different simulations; (a) $P_{\mathrm{pl}_1} = P_{\mathrm{pl}_3}$; (b) $P_{\mathrm{pl}_1} = P_{\mathrm{pl}_3} + 2\,\mathrm{cmH_2O}$

simulations are shown in Figure 4.17 and Figure 4.18, respectively. The results in Figure 4.17 show that the homogeneous pleural pressure led to a homogeneous distribution of inter-acinar pressure, i.e. a homogeneous distribution of the acinar volumetric strain. However, the results in Figure 4.18 show that the heterogeneous pleural pressure led to a heterogeneous distribution of inter-acinar pressure and a heterogeneous volumetric straining of the acini. Thus showing the necessity of using inter-acinar linkers when the acini are subjected to heterogeneous forces.

Further validation of inter-acinar linkers is preformed by testing the model on the same respirator system setup of Section 4.1.2. However, the inter-acinar linkers of Figure 2.9 are included. The spontaneous breathing pressure of eq (4.9) and eq (4.10) are applied only onto the pleural acini. The tracheal inlet is again assumed to have a zero pressure at all time and a time step of $1\,\mathrm{ms}$ is used to discretize the problem in time. Figure 4.19 shows simulated results of spontaneous breathing with inter-acinar dependencies included. Table 4.6 details the effect

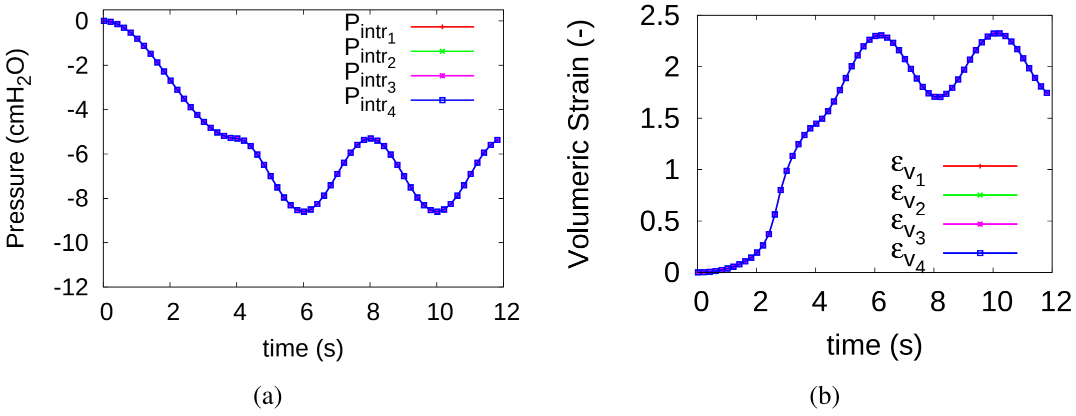

(a) (b)

Figure 4.17.: Results of simulating the 4 acini in Figure 4.15 with homogeneous pleural pressure showing (a) the different inter-acinar pressures and (b) the volumetric strain of the different acini.

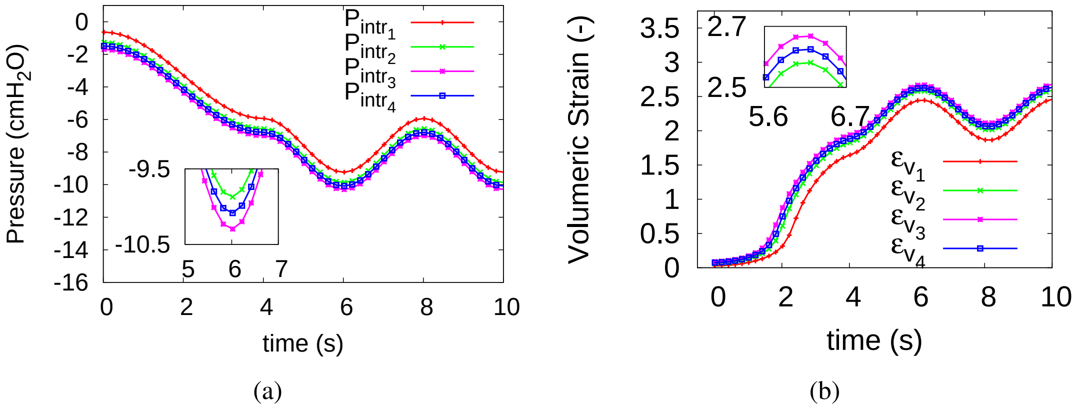

(a) (b)

Figure 4.18.: Results of simulating the 4 acini in Figure 4.15 with heterogeneous pleural pressure showing (a) the different inter-acinar pressures and (b) the volumetric strain of the different acini.

of inter-acinar dependencies on lung volumes. It can be noticed from Table 4.6 that the inter-acinar dependencies have almost no effect on the lung volumes. However, looking deeper into Table 4.6 two important things are observable: Firstly, inter-acinar linkers have no effect on the lung volume when gravity is ignored. This can indeed be proven analytically [95], and thus further validates the correctness of the inter-acinar linkers. Secondly, the inter-acinar linkers slightly effect the lung volumes when gravity is accounted for. This can indeed be noticed from the results of Figure 4.20, where the inter-acinar linkers allowed for an interaction between the neighboring acini which lei within different gravitational levels. Thus, increasing the heterogeneity of acinar strain and the heterogeneous ventilation of the human lung (see Figure 4.21).

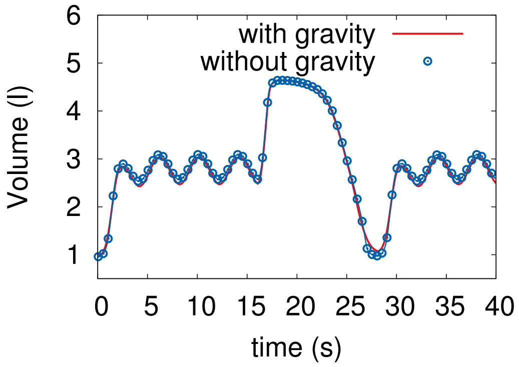

Figure 4.19.: Results of the lung volume variation during of spontaneous breathing when inter-acinar linkers are taken into consideration.

Table 4.6.: Lung volumes during simulated spontaneous breathing.

	Without inter-acinar linkers		With inter-acinar linkers	
Lung volumes (l)	no gravity	gravity	no gravity	gravity
Functional residual capacity (FRC)	2.59	2.50	2.59	2.47
Tidal volume (TV)	0.54	0.57	0.54	0.57
Total lung capacity (TLC)	4.70	4.70	4.70	4.64
Residual volume (RV)	0.98	1.07	0.98	1.08

Super-syringe

In this section the entire respiratory system and the inter-acinar linker tree are pushed to their limits by performing a super-syringe test. For this purpose, the patient is assumed in supine position. Hence, the gravitational vector is pointing from the chest to the back. 30% of the acini that are closest to the back are de-recruited by occluding all peripheral conducting airways within a region of $5\,\mathrm{cm}$ away from the back (see Figure 4.22). The super-syringe technique is used to measure the quasi-static PV curve of a lung. This is achieved through gradually inflating the lung with a volume of 50 to $100\,\mathrm{ml}$ using a syringe. Each time the lung is inflated with a syringe, the pressure decay curve is observed for few seconds. Once the pressure curve relaxes, another 50 to $100\,\mathrm{ml}$ of air is forced in. This process is repeated until an elevated tracheal pressure is observed. Once the inflation process is done, the lung is deflated using the syringe with volumes of 50 to $100\,\mathrm{ml}$ each step. Finally, lung volume is plotted versus the airway pressure. Following the curves in [57], the diseased lung is inflated in 10 steps by $100\,\mathrm{ml}$ per step. The whole inflation process is set to be $27\,\mathrm{s}$, i.e. $2.7\,\mathrm{s}$ per step. The deflation process is also set to $27\,\mathrm{s}$ with 10 deflation steps. Each deflation step is performed by sucking out $100\,\mathrm{ml}$ of air. The syringe is as

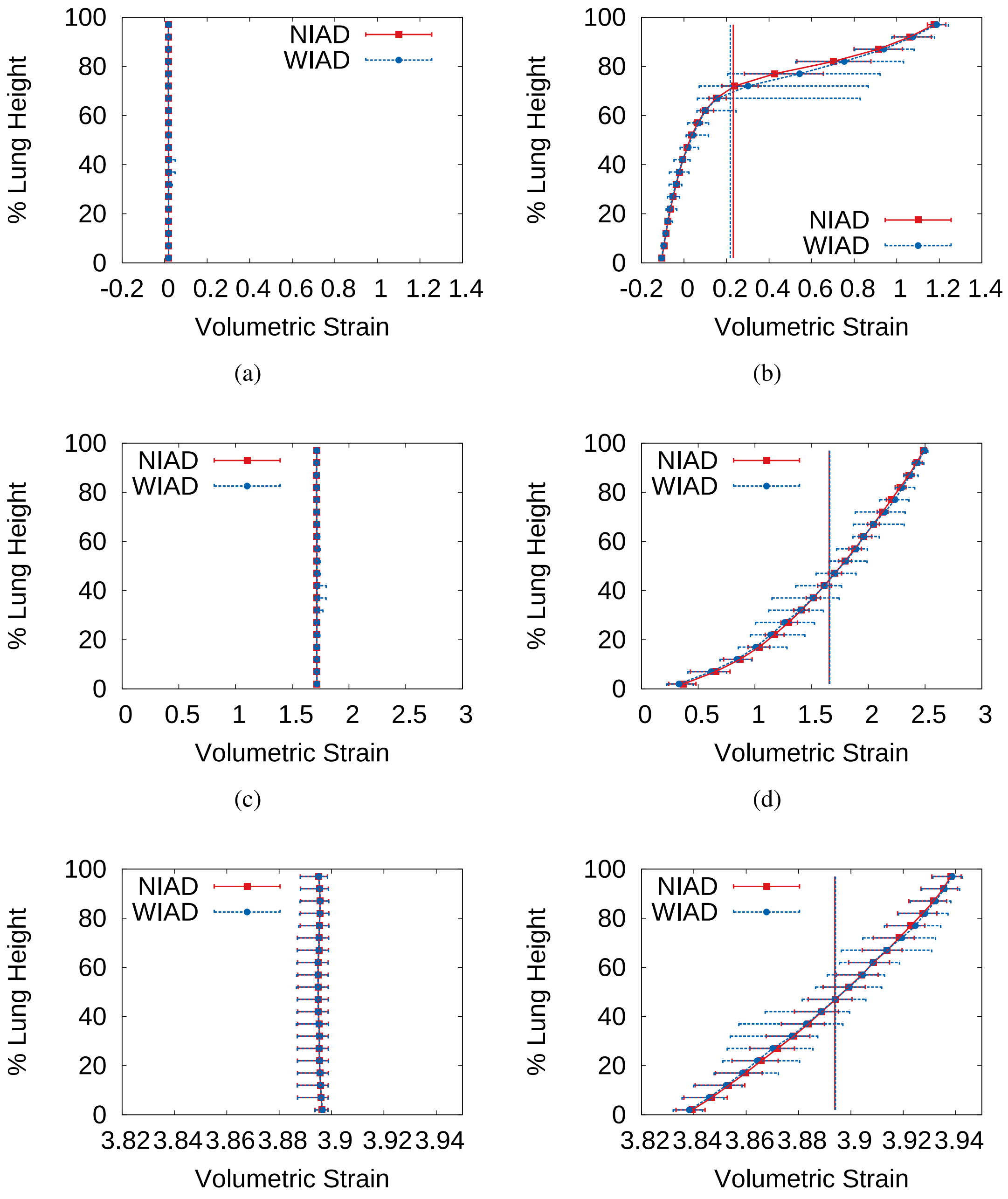

(a) (b) (c) (d) (e) (f)

Figure 4.20.: Acinar volumetric strain for different lung height percentage in simulated upright lungs during spontaneous breathing showing (a) residual volume without gravitational effects; (b) residual volume with gravitational effects; (c) functional residual volume without gravitational effects; (d) functional residual volume with gravitational effects; (e) total lung capacitance without gravitational effects; (f) total lung capacitance with gravitational effects. NIAD = No inter-acinar dependencies; WIAD = With inter-acinar dependencies.

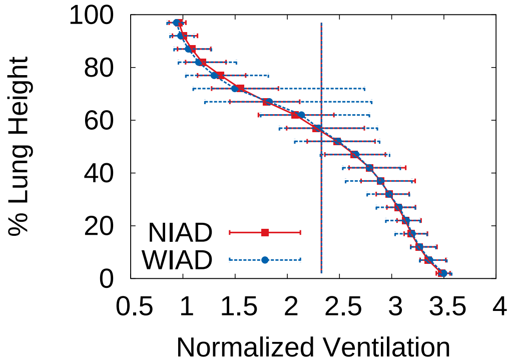

Figure 4.21.: Normalized ventilation in an upright healthy lung at peak tidal inspiratory flow rate (t=17 s). NIAD = No inter-acinar dependencies; WIAD = With inter-acinar dependencies.

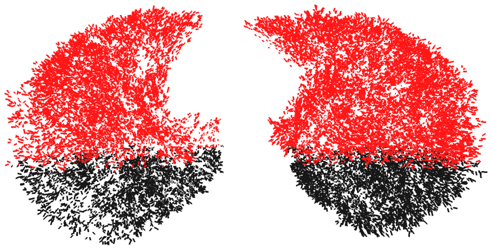

Figure 4.22.: Lung with 30% de-recruited acini close to the spine. The de-recruited acini are colored in black

such modeled as a flow rate condition at the inlet of the trachea and read as following

$$Q_{\mathrm{t}} = \begin{cases} K_{\mathrm{in/de}} \times (100\,\mathrm{ml})\,/T_{\mathrm{syr}} & (N_{\mathrm{cyc}}-1)\,T \le t < (N_{\mathrm{cyc}}-1)\,T + T_{\mathrm{syr}} \\ 0.0\,\mathrm{ml/s} & (N_{\mathrm{cyc}}-1)\,T + T_{\mathrm{syr}} \le t < (N_{\mathrm{cyc}})\,T \end{cases},$$

where $T_{\mathrm{syr}} = 0.3\,\mathrm{s}$ is the inflation/deflation time, $K_{\mathrm{in/de}} = +1$ during inflation and -1 during deflation, $T = 2.7\,\mathrm{s}$ and N_{cyc} the cycle or step number.

As for pleural pressure: During super-syringe maneuver, the patient are unconscious or unable to breathe spontaneously. Thus, the diaphragm and the rib cage act as a burden that prevents air from being pushed into the lung. This means that, opposite to spontaneous breathing, during mechanical ventilation pleural pressure increases every time the lung volume increases. Hence, for high lung volumes, a positive pleural pressure can be observed. Such a behavior is modeled as

$$P_{\mathrm{pl}}^{\mathrm{dyn}} = P_{\mathrm{pl}}^{0} + b_{\mathrm{p}} V_{\mathrm{VC_p}} + c_{\mathrm{p}} e^{\left(d_{\mathrm{p}} V_{\mathrm{VC_p}}\right)}, \tag{4.12}$$

where $V_{\mathrm{VC_p}} = (V - V_{\mathrm{R}})\,/\,(V_{\mathrm{TLC}} - V_{\mathrm{R}})$ is the percentile vital capacitance, V_{TLC} the total lung capacitance, V_{R} is the residual volume. All volumes in eq (4.12) are considered for the baby lung only[6]. The wall model of the pleural space is fitted to the measurements reported by [57] and yielded the following parameters

---

[6] *Baby lung* is a term used to define the inflatable part of the lung.

$$\begin{aligned} P_{\mathrm{pl}}^{0} &= -9.772\,\mathrm{cmH_2O}, \\ b_{\mathrm{p}} &= 20.344\,\mathrm{cmH_2O}, \\ c_{\mathrm{p}} &= -33.382\,\mathrm{cmH_2O}, \\ d_{\mathrm{p}} &= -7.686. \end{aligned}$$

The resulting simulated pressure curves at the trachea during inflation and deflation are shown in Figure 4.23. The corresponding quasi-static PV curve is shown in Figure 4.24. It is important to point out that the results in Figure 4.23 and Figure 4.24 are both qualitatively and quantitatively in good agreement with those reported in [57]. The hysteresis in Figure 4.24 is smaller than

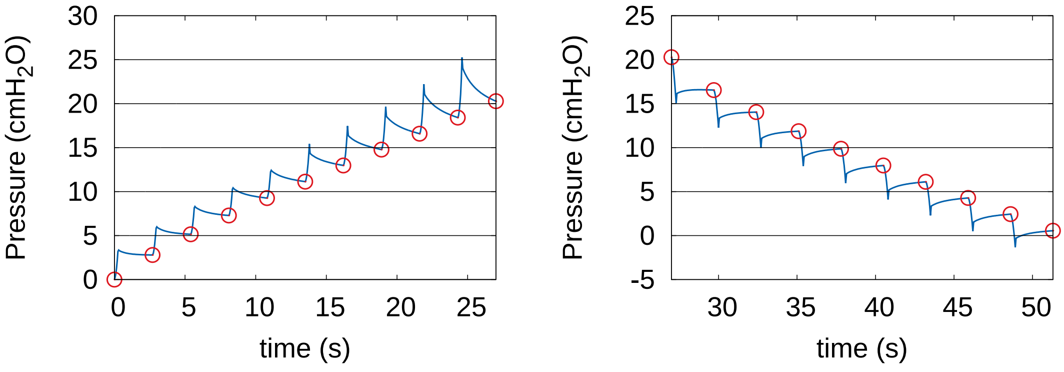

(a) (b)

Figure 4.23.: Simulated tracheal pressure during (a) super-syringe inflation and (b) super-syringe deflation. The point marked with an open circles represent the pressure values that would be chosen to construct a quasi-static pressure-volume curve.

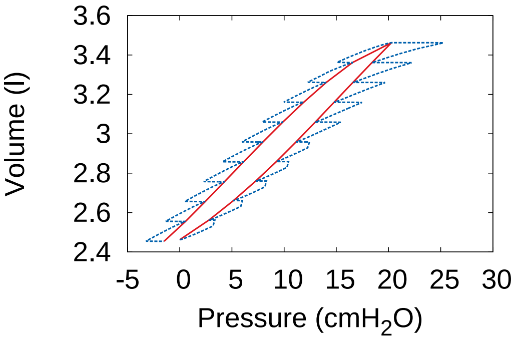

Figure 4.24.: Simulated quasi-static PV curve generated using the super-syringe maneuver. The dotted line stands for the bold line in Figure 4.23. The bold line stands for connecting large open circles in Figure 4.23 together.

the one reported in [57]. That is because, in [57] acinar recruitment and leakage of air at the intubation point are observed, which are not accounted for in this work.

4.2. Pulmonary circulatory system

In the following sections, the resistance of the pulmonary capillaries is firstly evaluated. Then the Young's moduli of elasticity of the pulmonary blood vessels are tuned to generate the correct systolic and diastolic pressure.

4.2.1. Pulmonary capillary networks

The pulmonary capillaries include a network of arteriole and venules as is presented in Figure 2.15. What makes the capillaries special is that they make up most of the resistance and least of the compliance [16]. This means that the capillaries can be assumed as stiff resistive trees. Due to large bifurcation of the capillary blood vessels, the effects of the very small blood vessels disappear [153]. Thus, the resistance of the capillaries is mostly within the larger vessels. For this purpose, the resistance of a tree of blood capillaries is calculated only for generations with radius greater or equal to $r_{\mathrm{res}} = 0.15\,\mathrm{mm}$ [109]. Following the definitions in Section 2.4, a capillary network can be simplified down to a resistance

$$R_{\mathrm{cap}_T} = R_{\mathrm{artl}_\mathrm{T}} + R_{\mathrm{venl}_\mathrm{T}},$$

where $R_{\mathrm{artl}_\mathrm{T}}$ and $R_{\mathrm{venl}_\mathrm{T}}$ are the total resistances of arteriole and venule trees. Thus the total resistance of a capillary network is

$$R_{\mathrm{cap}_T} = \sum_{n=0}^{N_{\mathrm{res}}} \left(\frac{8\mu_{\mathrm{bld}} L_{\mathrm{a}_0}}{2^n \pi \alpha_{\mathrm{dp}}^{3n} \left(r_{\mathrm{a}_0}\right)^4} \right) + \sum_{n=0}^{N_{\mathrm{res}}} \left(\frac{8\mu_{\mathrm{bld}} L_{\mathrm{v}_0}}{2^n \pi \alpha_{\mathrm{dp}}^{3n} \left(r_{\mathrm{v}_0}\right)^4} \right),$$

where L_{a_0} is the initial arteriole length, L_{v_0} initial venule length, μ_{bld} blood viscosity, α_{dp} defined in Section 2.4 and N_{res} is found from

$$r_{\mathrm{res}} = \alpha_{\mathrm{dp}}^{N_{\mathrm{res}}} r_{\mathrm{a}_0}.$$

4.2.2. Pulmonary arteries and veins

Due to the limited information on the wall material of the pulmonary blood vessels, constant arterial and venous stiffnesses are assumed. Since in healthy adult humans veins are four times more compliant, the venous stiffness (E_{ven}) is set to one-fourth of the arterial stiffness (E_{art}) [56].

The arterial stiffness is then found iteratively by solving the following problem

$$\begin{aligned} &\underset{f_\mathrm{p}}{\text{minimize}} && f_\mathrm{p} = \left|P^{\mathrm{PV}}_{\max} - P_{\mathrm{systolic}}\right| + \left|P^{\mathrm{PV}}_{\min} - P_{\mathrm{diatolic}}\right| \\ &\text{subject to} && Q_{\mathrm{PV}}(t) = \begin{cases} Q_{\max}\left[1+\cos\left(2\pi t/T_{\mathrm{sys}}\right)\right] & 0 \leq t_{\mathrm{cyc}} \leq T_{\mathrm{sys}} \\ 0 & T_{\mathrm{sys}} < t_{\mathrm{cyc}} < T_{\mathrm{dia}} \end{cases}, \\ & E_{\mathrm{ven}} = \frac{E_{\mathrm{art}}}{4} \end{aligned}$$

where $Q_{\mathrm{PV}}(t)$ is the blood flow rate at the pulmonary valve, $Q_{\max}$ peak pulmonary valve flow rate, $t_{\mathrm{cyc}} = t - n_{\mathrm{cyc}}T$, n_{cyc} cardiac cycle number, T period of a cardiac cycle and T_{sys} the period of systolic phase. $p^{\mathrm{PV}}_{\max}$ and $p^{\mathrm{PV}}_{\min}$ are the peak and minimum pulmonary valve blood pressure, respectively. $p_{\mathrm{systolic}} = 23\,\mathrm{mmHg}$ and $p_{\mathrm{diatolic}} = 4\,\mathrm{mmHg}$ are the systolic and diastolic blood pressure, respectively. The cardiac output is taken to be $5\,\mathrm{l/min}$, i.e.$\frac{1}{T}\int_0^T Q_{\mathrm{LV}}\mathrm{d}t = 5\,\mathrm{l/min}$, $T = 1\,\mathrm{s}$ and $T_{\mathrm{sys}} = 0.3\,\mathrm{s}$. The blood pressure at the atrium side is taken to be $0\,\mathrm{mmHg}$. The viscous constant of the blood vessel wall γ_s is taken as

$$\gamma_\mathrm{s} = \frac{T_\mathrm{s}\tan\left(\phi_\mathrm{s}\right)\beta_\mathrm{s}}{4\pi},$$

where β_s is taken from Section 3.2, $\phi_\mathrm{s} = 11°$ and $T_\mathrm{s} = T_{\mathrm{sys}}$ [92]. The optimization problem resulted in an arterial stiffness of $E_{\mathrm{art}} = 250\,\mathrm{kPa}$. The resulted arterial stiffness successfully reproduced the systolic and diastolic blood pressures (see Figure 4.25). The mean pulmonary pressure fell within the measurable data of [19].

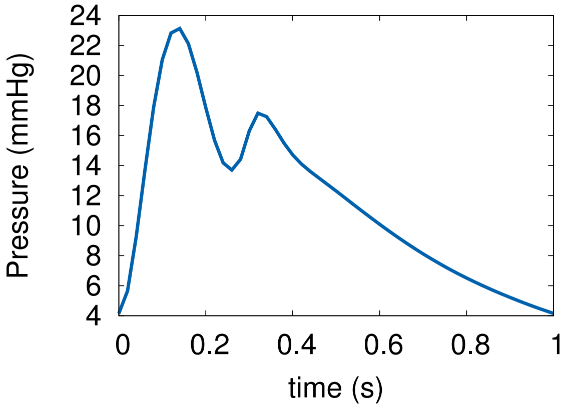

Figure 4.25.: Simulated blood pressure at the arterial side of the pulmonary valve.

4.3. Oxygen transport

In this section all parameters associated with blood transport and blood diffusion are found from preexisting literature. For the one dimensional O_2 flow model, presented in section 3.6, the only missing term is the diffusion coefficient (D_{O_2}). The oxygen diffusion of oxygen in air is found to be $D^{air}_{O_2} = 22.34\,\mathrm{mm}^2 \cdot \mathrm{s}^{-1}$ [30]. The diffusion of oxygen in blood is found to be $D^{bld}_{O_2} = 2 \times 10^{-3}\,\mathrm{mm}^2 \cdot \mathrm{s}^{-1}$ [139]. Furthermore, the diffusion coefficient of the alveolar interface separating air from blood is found to be $D^{\mathrm{I}}_{O_2} = 3.0 \times 10^{-9}\,\mathrm{mm}^2 \cdot \mathrm{s}^{-1} \cdot \mathrm{mmHg}^{-1}$ [155]. The concentration of oxygen in a fluid is defined as

$$c_{\mathrm{s}} = \frac{n_{\mathrm{O}_2}}{V_{\mathrm{f}}}.$$

where n_{O_2} is the number of moles of oxygen and V_{f} the volume of a solute (air or blood) in which O_2 is being dissolved. In pulmonary mechanics oxygen concentration is measured by PO_2, i.e. O_2 partial pressure. However, PO_2 is defined in air differently than in blood. As such, in the following sections a relationship between air and blood PO_2 and their corresponding O_2 concentrations is derived.

4.3.1. O_2 concentration in air

The oxygen partial pressure is the amount of pressure O_2 contributes to the atmospheric pressure. This means that the atmospheric pressure P_{atm} is the sum of partial pressures of nitrogen, oxygen, carbon dioxide, etc... Under normal conditions, air in lungs behaves as an incompressible ideal gas. Thus, number of moles of oxygen in air is deduced from the ideal gas law as

$$\frac{P_{\mathrm{O}_2}}{n_{\mathrm{O}_2}} = \frac{P_{\mathrm{atm}}}{n_{\mathrm{tot}}},$$

where n_{O_2} is the number of O_2 molecules and n_{tot} the total amount of moles in air. This also means that

$$n_{\mathrm{O}_2} = P_{\mathrm{O}_2} \frac{V_{\mathrm{air}}}{RT},$$

where $R = 8.314\,\mathrm{J} \cdot \mathrm{mol}^{-1} \cdot \mathrm{K}^{-1}$ and T the temperature in degrees Kelvin. This implies that the concentration of O_2 in in a volume of air is

$$c^{\mathrm{air}}_{\mathrm{s}} = \frac{n_{\mathrm{O}_2}}{V_{\mathrm{air}}} = \frac{P_{\mathrm{O}_2}}{RT}.$$

4.3.2. O_2 concentration in blood

In blood, PO_2 is defined via a saturation curve as the volume of oxygen that is absorbed by hemoglobin when exposed to an air with a certain PO_2. The oxygen saturation curve is defined by Keener and Sneyd [72] as

$$V^{\mathrm{bld}}_{\mathrm{O}_2} = \left(\frac{\left(P^{\mathrm{b}}_{\mathrm{O}_2}\right)^{\xi}}{\left(P^{\mathrm{bld}}_{\mathrm{O}_2}\right)^{\xi} + \left(\tilde{P}_{\mathrm{O}_2}\right)^{\xi}} \right) V^{\mathrm{sat}}_{\mathrm{O}_2}, \tag{4.13}$$

where $P^{bld}_{O_2}$ is the oxygen partial pressure in blood, $\tilde{P}_{\mathrm{O}_2} = 26\,\mathrm{mmHg}$ the oxygen partial pressure at 50% oxygen saturation, $\xi = 2.5$ and $V^{\mathrm{sat}}_{\mathrm{O}_2}$ the 100% saturation volume of oxygen in blood.

Under healthy conditions, a $100\,\mathrm{ml}$ of human blood fully saturates with $20.8\,\mathrm{ml}$ of O_2 [155]. As such $V^{\mathrm{sat}}_{\mathrm{O_2}}$ is defined as

$$V^{\mathrm{sat}}_{\mathrm{O_2}} = \left(\frac{20.8}{100}\right) V_{\mathrm{bld}},$$

where V_{bld} is the volume of blood. The molar volume of any gas at standard temperature and pressure is $V_{\mathrm{m}} = 22.4\,\mathrm{l/mol}$ i.e.

$$n^{\mathrm{bld}}_{\mathrm{O_2}} = \frac{V^{\mathrm{bld}}_{\mathrm{O_2}}}{V_{\mathrm{m}}}. \tag{4.14}$$

thus the concentration of oxygen in blood is

$$c^{\mathrm{bld}}_{\mathrm{s}} = \frac{n^{\mathrm{bld}}_{\mathrm{O_2}}}{V_{\mathrm{bld}}} = \frac{V^{\mathrm{bld}}_{\mathrm{O_2}}}{V_{\mathrm{m}} V_{\mathrm{bld}}} = \frac{0.208}{V_{\mathrm{m}}} \left(\frac{\left(P^{\mathrm{b}}_{\mathrm{O_2}}\right)^{\xi}}{\left(P^{\mathrm{bld}}_{\mathrm{O_2}}\right)^{\xi} + \left(\tilde{P}_{\mathrm{O_2}}\right)^{\xi}} \right). \tag{4.15}$$

4.3.3. Model validation of the oxygen transport

To validate the O_2 transport model parameters, two experiments are performed. The first consisted of a two chamber lung model whereas the second is a five chamber lung model. Both models we constructed as following:

1. The conducting airways are taken from Section 2.2. For the two chamber model the conducting airways are trimmed just before the primary bronchi's bifurcation. Whereas for the five chamber model the airways are trimmed just before the lobar inlets.
2. Alveolar trees are grown inside the chambers of the lung models.
3. Pulmonary circulatory trees are generated using the respiratory systems constructed in step 1 and step 2 and the algorithms of Section 2.4.

In total the two chamber lung consisted of 3 airways, 2 acinar trees, 2 arteries, 2 veins and 2 capillary trees. The total volume of blood is $7.077\,\mathrm{ml}$, $80.0\,\mathrm{ml}$ and $12.02\,\mathrm{ml}$ for arteries, capillaries and veins, respectively. The five chamber model consisted of 9 airways, 8 arteries, 8 veins, 5 acinar trees and 5 capillary trees. The total volume of blood is $20.0\,\mathrm{ml}$, $80.0\,\mathrm{ml}$ and $36.0\,\mathrm{ml}$ for arteries, capillaries and veins, respectively. The two chamber and five chamber models are shown in Figure 4.28 and Figure 4.28, respectively.

At the trachea inlet a zero pressure is enforced and a $P^{air}_{\mathrm{O_2}} = 150\,\mathrm{mmHg}$ is assumed. The pleural space is subjected to a pressure of

$$P_{\mathrm{pl}} = 0.5\left(P_{\max} - P_{\min}\right)\left[\cos\left(2t\pi/T + \phi\right) + 1\right] + P_{\min},$$

where $\phi = 0$, $T = 4\,\mathrm{s}$, $P_{\max} = -530\,\mathrm{cmH_2O}$ and $P_{\min} = -830\,\mathrm{cmH_2O}$. At the pulmonary ventricle the following cardiac output is prescribed

$$Q_{\mathrm{PV}}(t) = \begin{cases} Q_{\max}\left[1 + \cos\left(2\pi t/T_{\mathrm{sys}}\right)\right] & 0 \le t_{\mathrm{cyc}} \le T_{\mathrm{sys}} \\ 0 & T_{\mathrm{sys}} < t_{\mathrm{cyc}} < T_{\mathrm{dia}} \end{cases}$$

where $t_{\mathrm{cyc}} = t - n_{\mathrm{cyc}}T$ and n_{cyc} cardiac cycle number. The constants in the prescribed cardiac output are defined as $T = 1\,\mathrm{s}$, $T_{\mathrm{sys}} =$, $T_{\mathrm{sys}} = 0.3\,\mathrm{s}$ and $\frac{1}{T}\int_0^T Q_{\mathrm{PV}}\mathrm{d}t = 5\,\mathrm{l/min}$. The oxygen partial pressure at the pulmonary valve is assumed to be $40\,\mathrm{mmHg}$. At the left atrium a zero blood pressure is prescribed. Both models are discretized with a time step of $1\,\mathrm{ms}$ and computed for $200\,\mathrm{s}$. The flow within the respiratory system converged to a periodic steady-state after the second respirator cycle. The flow within the pulmonary circulation converged to a periodic steady-state after the third cardiac cycle. The oxygen levels within the two chamber lung converged to a periodic steady-state only after $120\,\mathrm{s}$, i.e. 30 breathes. The tidal volume is $\approx 0.5\,\mathrm{l}$ per breath in each of the examples.

Oxygen transport in a two chamber lung model

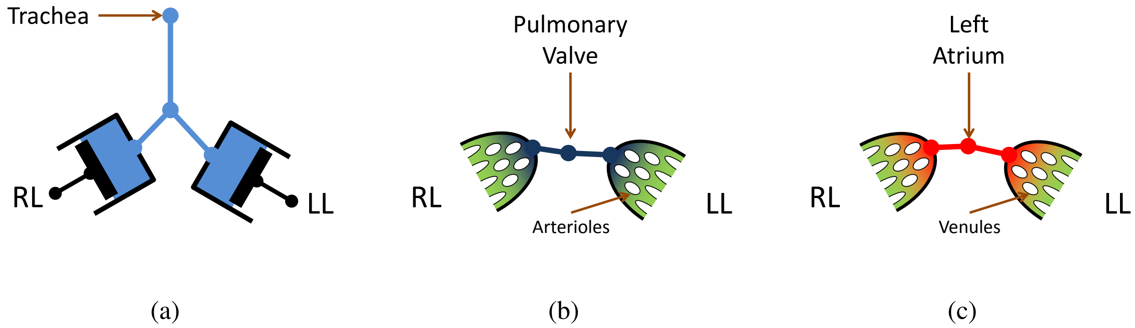

(a) (b) (c)

Figure 4.26.: Simplified two chamber lung model showing (a) respiratory system, (b) pulmonary arteries and (c) pulmonary veins. LL= left lung; RL= right lung; LT= left top; LB= left bottom; RT= right top; RM= right middle; RB= right bottom.

The P_{O_2} results of the two chamber model are detailed in Figure 4.27 over 4 converged physical seconds. It is observed that the blood coming back to heart had an average $P_{\mathrm{O}_2}^{\mathrm{bld}} = 128.82\,\mathrm{mmHg}$ fluctuating between $[125, 131]\,\mathrm{mmHg}$. Similar healthy P_{O_2} levels are observed at the exit of the capillary trees (see Figure 4.27). The oxygen partial pressure in the respiratory system dropped from $150\,\mathrm{mmHg}$ at the trachea to $\approx 136\,\mathrm{mmHg}$ at the respiratory zone. In other words, the low oxygenated blood coming from the right ventricle is properly saturated inside the capillaries. Thus properly validating the O_2 transport model.

Oxygen transport in a five chamber lung model

The P_{O_2} results of the five chamber model are detailed in Figure 4.29 over 4 converged physical seconds. It is observed that the blood coming back to heart had an average $P_{\mathrm{O}_2}^{\mathrm{bld}} = 129.51\,\mathrm{mmHg}$ fluctuating between $[127.8, 131]\,\mathrm{mmHg}$. Similar healthy P_{O_2} levels are observed at the exit of the capillary trees (see Figure 4.27). The oxygen partial pressure in the respiratory system dropped from $150\,\mathrm{mmHg}$ at the trachea to $\approx 136\,\mathrm{mmHg}$ at the respiratory zone. In other words, the low oxygenated blood coming from the right ventricle is properly saturated inside the capillaries. Thus, again properly validating the O_2 transport model.

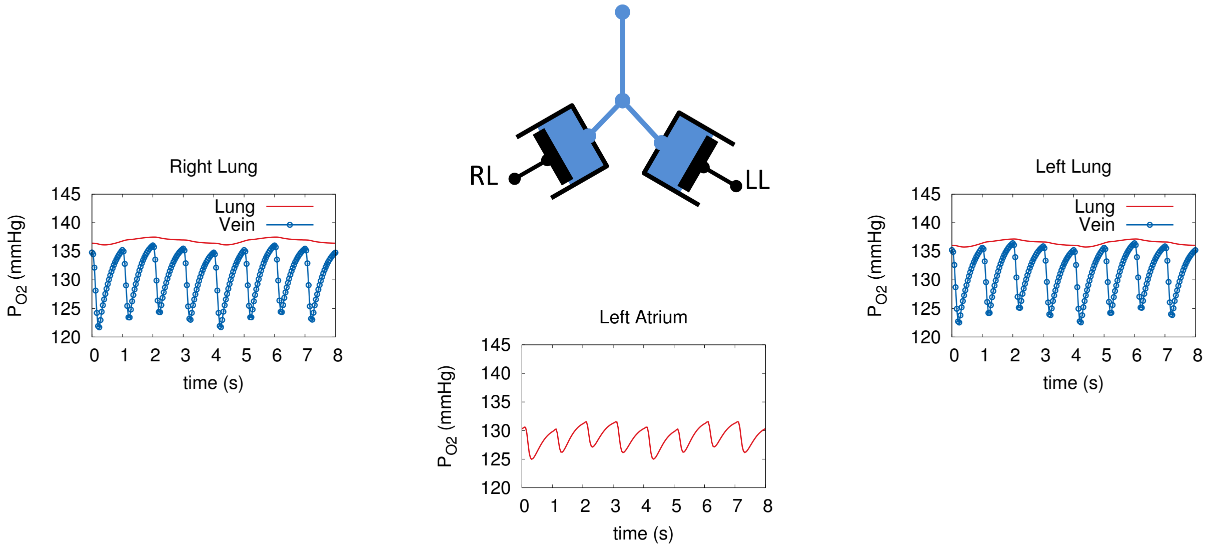

Figure 4.27.: PO_2 results of the two chamber lung model during two spontaneous breathing cycles. Lung= results inside the respiratory zone; Vein= results at the exist of the capillary network; LL= left lung; RL= right lung.

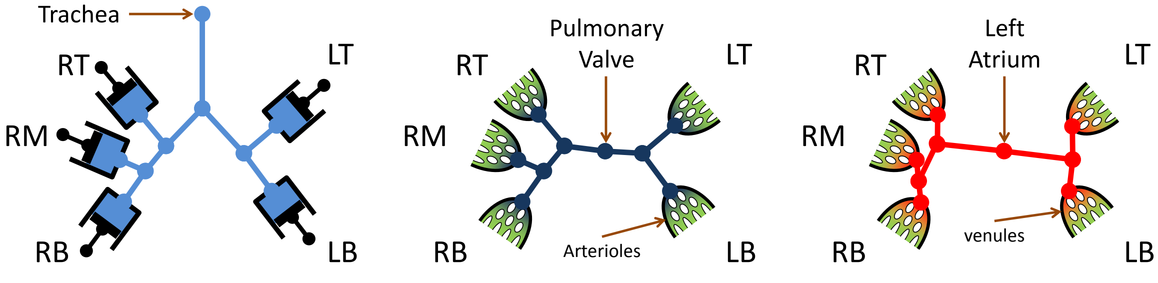

(a) (b) (c)

Figure 4.28.: Simplified five chamber lung model showing (a) respiratory system, (b) pulmonary arteries and (c) pulmonary veins. LL= left lung; RL= right lung; LT= left top; LB= left bottom; RT= right top; RM= right middle; RB= right bottom.

4.4. Coupling 3D and reduced-D domains

To test the coupling approach described in Section 3.8, a 3D tracheobronchial geometry (Figure 4.4(c)) is coupled to a tree of 0D airways representing the lung lobes (Figure 4.4(b)). The trees of 0D airways are in turn coupled to trees of 0D acini (Figure 4.4(a)). For the boundary conditions, a homogeneous pleural pressure is prescribed to all of the acini in form of

$$P_{\mathrm{pl}} = P_{\mathrm{pl}_{\mathrm{max}}} + \frac{\Delta P_{\mathrm{pl}}}{2} \left(1 - \cos\left(2\pi t/T + \phi\right)\right) \tag{4.16}$$

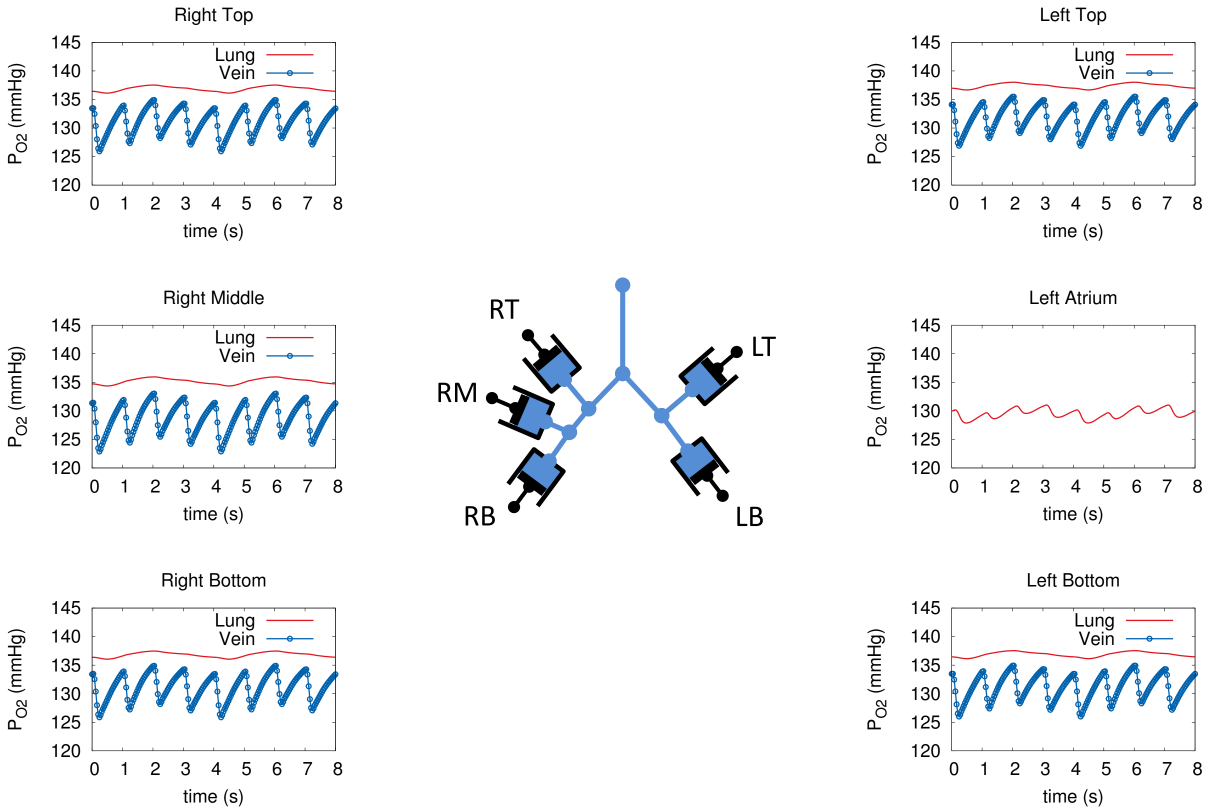

Figure 4.29.: PO_2 results of the five chamber lung model during two spontaneous breathing cycles. Lung= results inside the respiratory zone; Vein= results at the exist of the capillary network; LT= left top; LB= left bottom; RT= right top; RM= right middle; RB= right bottom.

where $P_{\mathrm{pl}_{\max}} = -5.3\,\mathrm{cmH_2O}$, $\Delta P_{\mathrm{pl}} = -3.3\,\mathrm{cmH_2O}$ and $\phi = \pi/11$. At the tracheal inlet, a zero pressure is prescribed in form of no traction (do-nothing) boundary condition. The coupled problem is solved iteratively until pressure and velocity norms converge to $10^{-6}\,\mathrm{Pa}$ and to $10^{-6}\,\mathrm{mm/s}$. The results in Figure 4.31 show the surface averaged pressure values on the coupling boundaries. A pressure mismatch is observed at the 3D boundaries, which behaved as inlets; see boundaries labeled B, C, D, E and F during the expiratory phase and boundary labeled A during the inspiratory phase. Such a boundary mismatch is never reported before the work of Gravemeier et al. [53] and the author et al. [68]. That is because the inflow term $(u_n^{\mathrm{in}}\mathbf{u})$ in the Neumann boundary condition is only dominant in airway flow [68] and is of a minor influence on the boundary pressure in hemodynamic problems. To validate this, the coupling approach is tested on a coupled 3D-1D-0D network of systemic arteries. The geometry of the 1D arterial network in Figure 4.32(a) is taken from [3]. The 3D healthy abdominal aorta is segmented from a patient suffering from a thoracic aneurysm[7]. The inlet of the 3D abdominal aorta is coupled to the outlet of the 1D abdominal aorta. The 3D common iliac arteries are coupled to 0D 3-

---

[7] The CT-DICOM images of the abdominal aorta are supplied by Prof. Dr. Hans-H. Eckstein, Department for Vascular Surgery, Klinikum rechts der Isar, Munich.

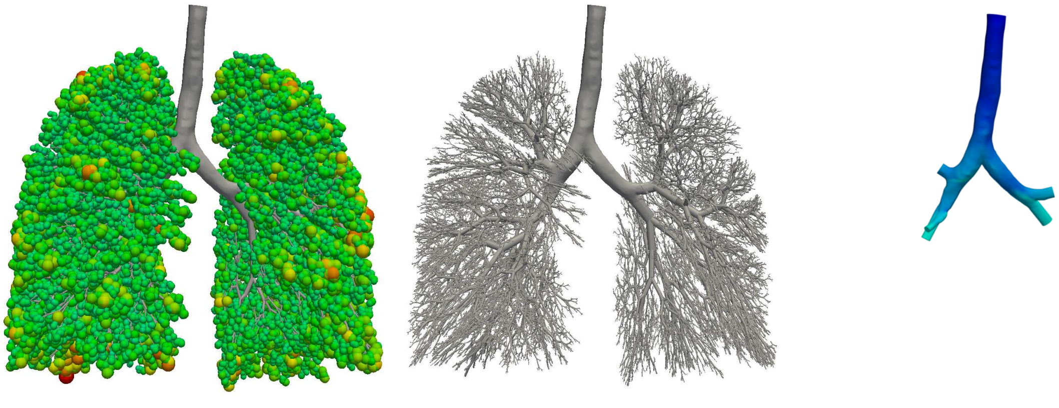

(a) (b) (c)

Figure 4.30.: The coupled 3D/reduced-D respiratory system showing (a) the entire respiratory system, (b) only the convective airways and (c) only the 3D tracheobronchial tree.

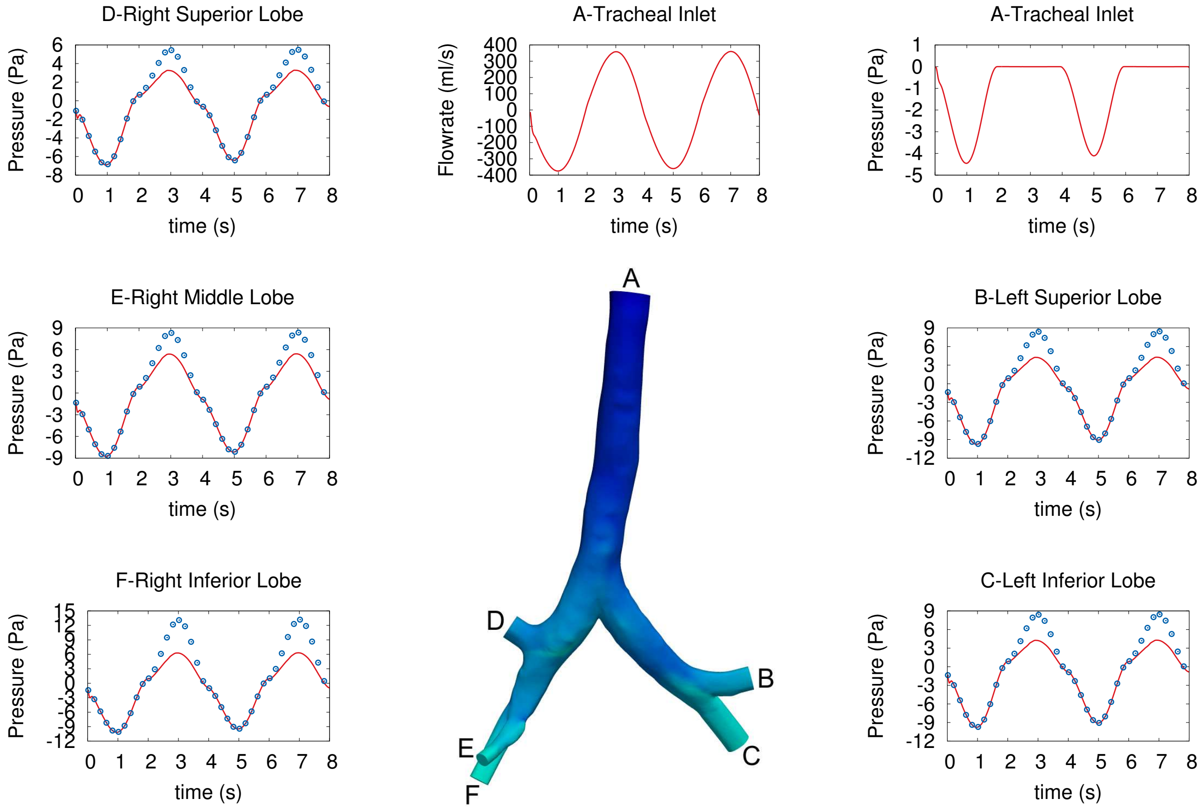

Figure 4.31.: Natural respiration results for the case where Neumann conditions are approximated by pressure (line values: pressure and flow rate values on 3D boundary, dotted values: pressure values on the 0D boundary).

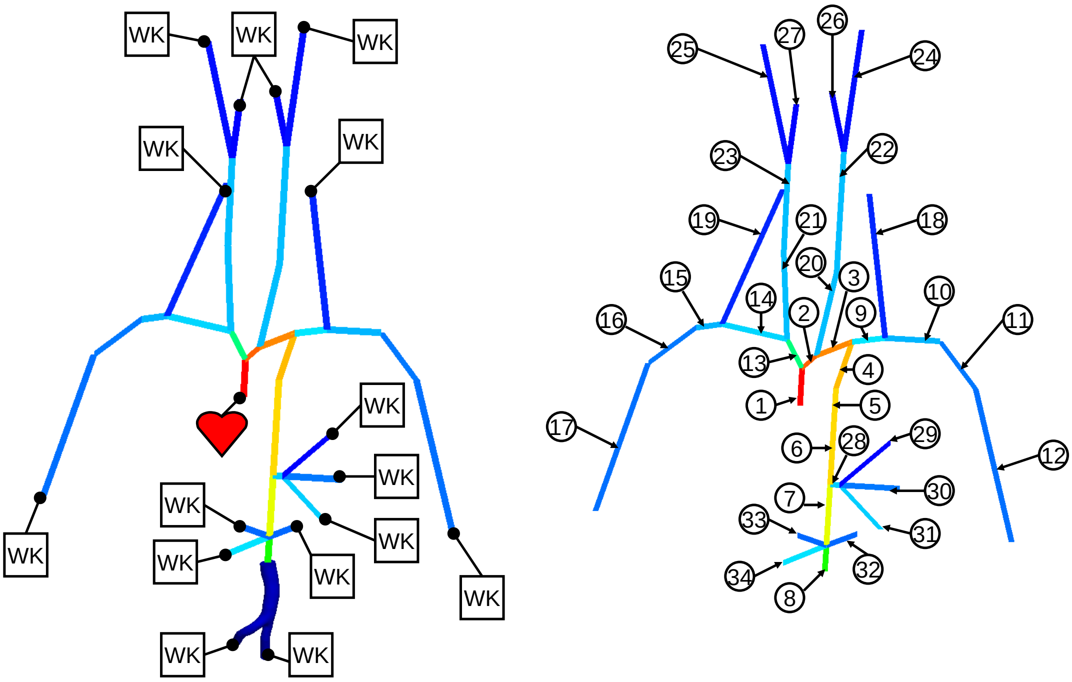
WK
WK
WK
WK
WK
WK
WK
WK
WK
WK
WK
WK
WK
WK
WK
26
25
27
24
23
22
19
21
18
20
15
3
14
2
9
10
16
11
13
4
1
5
17
29
12
6
28
30
7
33
31
34
32
8

(a) (b)

Figure 4.32.: Multi-dimensional human arterial network showing (a) coupled 3D abdominal aorta, 1D arterial tree and 0D windkessel boundary condition. The 1D arteries are labeled (b) with numbers in circle. The 0D windkessel boundary conditions are labeled (a) with WK.

element windkessel elements. The remaining terminal outlets of the 1D arteries are coupled to 0D 3-element windkessel elements. The physical parameters of the 1D arteries are presented in Table 4.7. The parameters of the 0D windkessel elements are presented in Table 4.8. As for boundary conditions, the venous pressure is assumed to be zero. A flow rate boundary condition is enforced at the ascending Aorta of the form

$$Q_{\mathrm{H}}(t) = \begin{cases} Q_{\mathrm{p}} \sin\left(\pi t / T_{\mathrm{sys}}\right) & 0 \leq t_{\mathrm{cyc}} \leq T_{\mathrm{sys}} \\ 0 & T_{\mathrm{sys}} < t_{\mathrm{cyc}} < T_{\mathrm{dia}} \end{cases},$$

where $Q_{\mathrm{H}}(t)$ is the output cardiac flow rate, Q_{p} the peak output cardiac flow rate, $t_{\mathrm{cyc}} = t - n_{\mathrm{cyc}}T$, n_{cyc} cardiac cycle number, T period of a cardiac cycle and T_{sys} the period of systolic phase. The cardiac output is taken to be $5\,\mathrm{l/min}$, i.e.$\frac{1}{T}\int_0^T Q_{\mathrm{H}}\mathrm{d}t = 5\,\mathrm{l/min}$, $T = 1\,\mathrm{s}$ and $T_{\mathrm{sys}} = 0.3\,\mathrm{s}$. In time, the 3D problem is discretized with a time step of $1\,\mathrm{ms}$ whereas the 1D problem is discretized with a time step of $0.1\,\mathrm{ms}$. The 0D windkesel elements coupled to the 3D problem are solved using periodic Fourier transformation, whereas the ones coupled to the 1D arteries are solved monolithically with the 1D problem. The results of the 3D-1D coupling interface are shown in Figure 4.33. Indeed, it is observable that in hemodynamics the inflow term ($u_n^{\mathrm{in}}\mathbf{u}$) in the Neumann boundary condition did not lead to a mismatch of pressure at the abdominal aortic 3D inlet boundary. This is because, compared to airway flow, blood has lower speed and is subjected to higher pressure values. Thus, pressure match on an inflow Neumann boundary did not require extra treatment of the inertial effects.

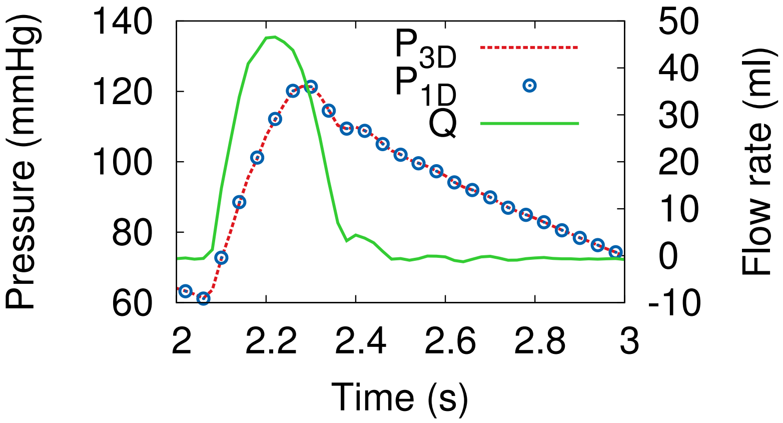

Figure 4.33.: Results of the coupled 3D-1D-0D arterial network showing the flow rate at the abdominal aortic coupling interface (Q), the pressure at the 3D side of the abdominal aortic inlet ($P_{3\mathrm{D}}$) and the pressure at the 1D side of abdominal aortic inlet ($P_{1\mathrm{D}}$).

4.4.1. Treatment of inertial effects in airflow (towards a matching boundary pressure)

The Neumann boundary condition as defined in eq (3.5) guaranties a stable boundary condition during reversed flows. However, to obtain pressure match at an inflow Neumann boundary,

Table 4.7.: Physical parameters and geometric details of 1D arterial systemic circulation taken from [3; 121].

ID	Name	E_{art} (kPa)	ν_{s}	D_{art} (mm)	h_{art} (mm)	L_{art} (mm)
1	Ascending Aorta	400.0	0.5	29.0	1.63	40.0
2	Aortic Arch I	400.0	0.5	26.4	1.32	20.0
3	Aortic Arch II	400.0	0.5	25.4	1.27	38.9
4	Thoracic Aorta I	400.0	0.5	24.0	1.20	52.0
5	Thoracic Aorta II	400.0	0.5	23.2	1.16	52.0
6	Thoracic Aorta III	400.0	0.5	23.2	1.16	52.0
7	Abdominal Aorta I	400.0	0.5	21.6	1.08	68.0
8	Abdominal Aorta II	400.0	0.5	16.0	0.80	29.8
9	Left Subclavian	400.0	0.5	8.4	0.67	34.0
10	Left Axilliary	400.0	0.5	7.2	0.62	56.0
11	Left Brachial I	400.0	0.5	5.6	0.55	63.0
12	Left Brachail II	400.0	0.5	5.4	0.53	172.0
13	Brachiocephalic	400.0	0.5	12.4	0.86	34.0
14	Right Subclavian	400.0	0.5	8.0	0.66	68.0
15	Right Axilliary	400.0	0.5	7.2	0.62	27.0
16	Right Brachial I	400.0	0.5	5.6	0.55	63.0
17	Right Brachial II	400.0	0.5	5.4	0.53	172.0
18	Left Vertebral	800.0	0.5	3.6	0.45	148.0
19	Right Vertebral	800.0	0.5	3.6	0.45	51.0
20	Left Common Carotid I	400.0	0.5	7.4	0.63	89.0
21	Left Common Carotid II	400.0	0.5	7.4	0.63	89.0
22	Right Common Carotid I	400.0	0.5	7.4	0.63	89.0
23	Right Common Carotid II	400.0	0.5	7.4	0.63	89.0
24	Left External Carotid	800.0	0.5	3.0	0.42	118.0
25	Right External Carotid	800.0	0.5	3.0	0.42	118.0
26	Left Internal Carotid	800.0	0.5	2.6	0.39	59.0
27	Right Internal Carotid	800.0	0.5	2.6	0.39	59.0
28	Coeliac	400.0	0.5	7.8	0.64	10.0
29	Gastric	400.0	0.5	2.6	0.45	71.0
30	Splenic	400.0	0.5	7.8	0.49	63.0
31	Hepatic	400.0	0.5	5.6	0.54	66.0
32	Left Renal Artery	400.0	0.5	5.2	0.53	35.3
33	Right Renal Artery	400.0	0.5	5.2	0.53	32.9
34	Superior mesenteric	400.0	0.5	8.3	0.69	50.6

the $u_n^{\text{in}}\mathbf{u}$ term in eq (3.5) should have been estimated, as is shown earlier by Gravemeier et al. [53]. To avoid such a pressure mismatch, Gravemeier et al. [53] suggested to add a correction term to the prescribed boundary pressure. They indeed succeeded in getting a pressure match at the coupling boundary, however this required the fore-knowledge of both the flow rate and

Table 4.8.: 0D windkessel boundary conditions of a systemic arterial circulation. All values are evaluated from [121]. All units are in [g,mm,s].

Name	R_s	C	R_p
Gastric	0.0844	0.0767	3.5555
Hepatic	0.1204	0.0767	3.5195
Splenic	0.2478	0.1200	2.0721
Renal	0.1291	0.2464	1.0042
Superior mesenteric	0.0864	0.2993	0.8469
Vertebral	0.2129	0.0018	5.0931
External Carotid	0.2511	0.0018	5.0549
Internal Carotid	0.2511	0.0018	5.0549
Brachial	0.1243	0.1087	2.4419

the velocity profile. Moghadam et al. [97] suggested to simply multiplied the $u_n^{\text{in}}\mathbf{u}$ term by a $0.0 < \beta < 1.0$. Without any further explanation, they chose $\beta = 0.2$ and performed an intensive study on patient-specific vascular examples and showed that their choice of β yielded stable results. However, as is noted by Gravemeier et al. [53], such stability cannot be extended to general problems. In addition to that even a choice of $\beta = 0.2$ would have still produced a pressure mismatch in the example of Figure 4.31 [68]. Furthermore, no further treatment of the β term yielded flattening of the velocity profile as could be observed in the numerical examples of Moghadam et al. [97] and will be shown later in this section.

To resolve this problem, the approach of [53] is chosen in a framework that only requires the foreknowledge of the velocity profile shape and is able to self evaluate the boundary flow rate [68]. This is achieved by modifying the coupling algorithm in Section 3.8 to the one presented in Figure 4.34. In current work, all airways and blood vessels are assumed to have cylindrical or semi-cylindrical shapes. Thus, the velocity profiles at the Neumann boundaries are boiled down to two types, generalized polynomial profile and Womersley profile. The generalized polynomial profile are used to model steady laminar flow or approximate averaged turbulent flows as following

$$u_n\left(r\right) = \frac{Q}{A}\left(\frac{\gamma+2}{\gamma}\right)\left[1+\left(\frac{r_i}{r_0}\right)^{\gamma}\right], \tag{4.17}$$

where Q is the volumetric flow rate, A the cross-sectional area, r_i the radial coordinate, r_0 the radius of the boundary surface and γ the polynomial order of the velocity profile. The Womersley profile is used to model a generalized flow profile of unsteady oscillating laminar pipe flow [161] and reads as following

$$u_n\left(r\right) = 2\frac{Q_0}{A}\left[1+\left(\frac{r_i}{r_0}\right)^{2}\right] + \sum_{k=1}^{N}\text{Real}\left\{\frac{Q_k}{A}\left[\frac{J_0\left(z\right)-J_0\left(\frac{r_i}{r_0}z\right)}{zJ_0\left(z\right)-2J_1\left(z\right)}\right]ze^{i\left(k\omega t-\phi_k\right)}\right\} \tag{4.18}$$

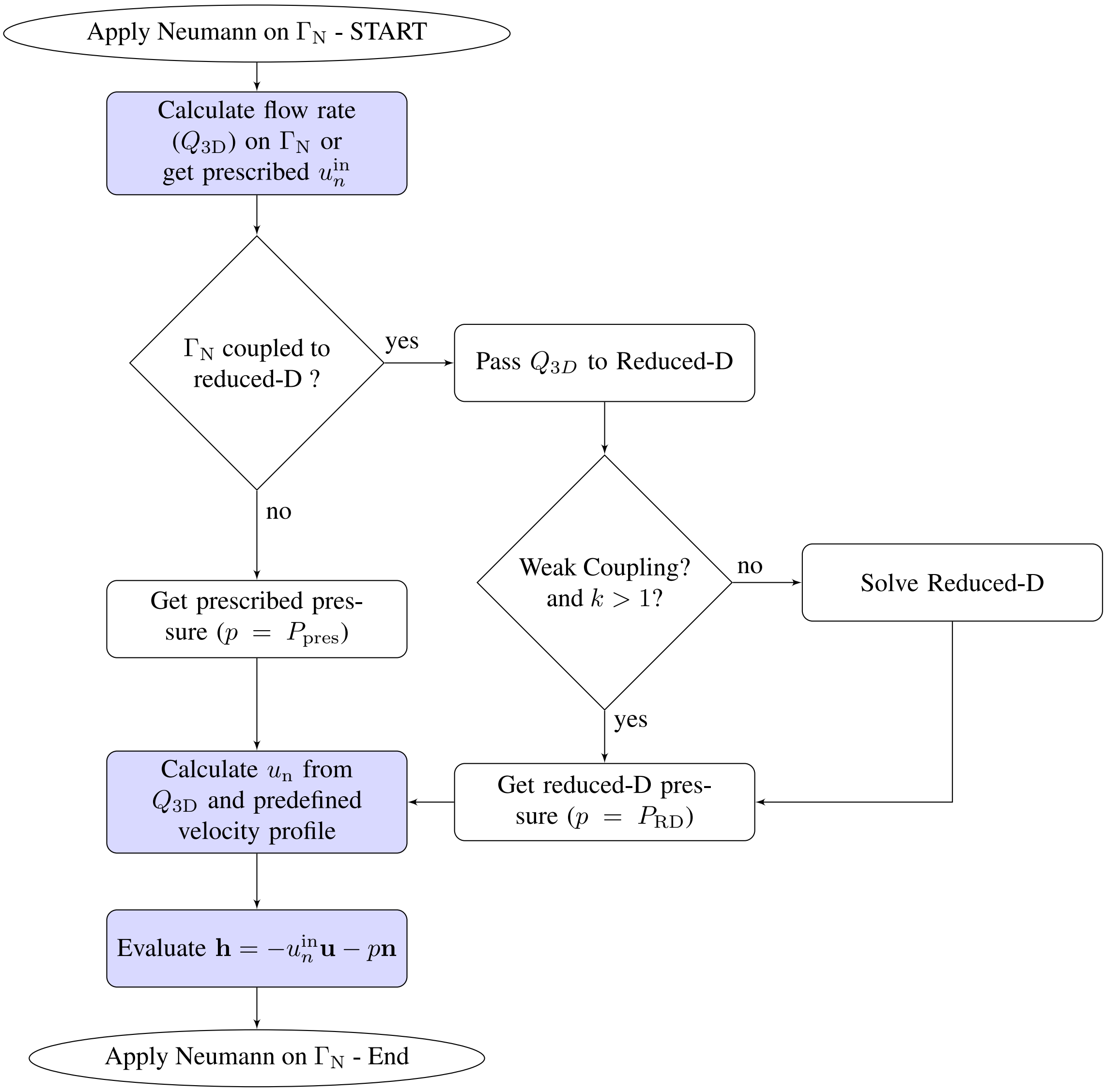
Apply Neumann on Γ_{N} - START
Calculate flow rate (Q_{3D}) on Γ_{N} or get prescribed u_n^{in}
Γ_{N} coupled to reduced-D ?
yes
Pass Q_{3D} to Reduced-D
no
Weak Coupling? and $k > 1$?
no
Solve Reduced-D
Get prescribed pressure ($p = P_{\text{pres}}$)
yes
Calculate u_{n} from Q_{3D} and predefined velocity profile
Get reduced-D pressure ($p = P_{\text{RD}}$)
Evaluate $\mathbf{h} = -u_n^{\text{in}}\mathbf{u} - p\mathbf{n}$
Apply Neumann on Γ_{N} - End

Figure 4.34.: Flow chart of the modified Dirichlet-to-Neumann algorithm that includes treatment of pressure mismatching during inflow. Blocks added and modified to the original algorithm are colored in light blue.

where $z = \alpha_{\mathrm{w}} i^{3/2}$, $\alpha_{\mathrm{w}} = r_0\sqrt{\frac{\omega}{\nu}}$ is the Womersley number, ω the angular frequency, ν the kinematic viscosity, and J_0 and J_1 Bessel functions of the first kind. Q_k and ϕ_k are evaluated from the Fourier fitting of the flow rate as

$$Q = Q_0 + \sum_{k=1}^{N} Q_k \cos\left(k\omega t - \phi_k\right).$$

The aforementioned two types of velocity profiles are defined only for circular cross-sectional areas. Thus, they are mapped onto semicircular cross-sectional areas using the method proposed in [101] (see Appendix F).

Two scenarios are investigated to validate of the Neumann's inertial term treatment against the analytic solution of an idealized tracheal geometry, approximated by a straight axi-symmetric tube, $15\,\mathrm{cm}$ long and $0.75\,\mathrm{cm}$ in radius. The motive behind using such a simplified geometry is the fact that the simulation results can be compared with the analytic solutions. The idealized tracheal tube is discretized using 28,944 elements resulting in 123,224 degrees of freedom. In time both 3D and reduced-D problems are discretized with 1 ms time step.

Case 1: Foreknown inflow velocities

In case velocities and pressure values on a Neumann inflow boundary are known then the full traction can be directly evaluated. For this purpose, the ideal tracheal geometry is assumed to have at the inlet a flow rate of

$$0.5\sin\left(\omega t\right)\ \mathrm{l/s},$$

where $\omega = 2\pi/T$, $T = 3\,\mathrm{s}$ and the Womersley number $\alpha = 2.73$. The outlet of the trachea is assumed to be connected to a 0D impedance tree of airways (For more detail on 0D impedance trees see Appendix E). The impedance tree is generated based on the ratios given by Comerford et al. [22]: $l_{\mathrm{r}} = 5.8$, $\beta_{\mathrm{l}} = 0.876$, $\beta_{\mathrm{r}} = 0.686$ and $r_{\mathrm{term}} = 0.15\,\mathrm{mm}$, where l_{r} is the airway length-to-radius ratio, β_{l} the radius ratio of left daughter airway to the parent airway, β_{r} the radius ratio of right daughter airway to the parent airway and r_{term} the terminating radius. The radius of the 3D pipe is taken to be the initial parent radius of the impedance tree. The stiffness E of the 0D airways is assumed to be constant an equal to $3.3\,\mathrm{kPa}$ [22]. The airway wall thickness is evaluated using the empirical model in [22] as following:

$$h = \zeta_1 r_{\mathrm{aw}}^2 + \zeta_2 r_{\mathrm{aw}} + \zeta_3$$

where r_{aw} is the airway radius, $\zeta_1 = -0.057\,\mathrm{mm}^{-1}$, $\zeta_2 = 0.2096$ and $\zeta_3 = 0.00904\,\mathrm{mm}$. Under the aforementioned flow rate, the flow inside the idealized trachea is found to be laminar. Thus, the analytic Womersley solution yielded the following pipe pressure drop across the tracheal boundaries:

$$\Delta P = 1.811\sin\left(\omega t + \pi/2\right)\ \mathrm{Pa}.$$

The outlet pressure is calculated from the impedance tree and the desired pipe flow rate and found to be

$$P_{\mathrm{out}} = 2.87\sin\left(\omega\left(t - 0.56\right) + \pi/2\right)\ \mathrm{Pa}.$$

Thus, the analytic inlet pressure (P_{in}) yielded

$$P_{\text{in}} = \Delta P + P_{\text{out}} = 1.811 \sin(\omega t + \pi/2) + 2.87 \sin(\omega(t - 0.56) + \pi/2) \text{ Pa}.$$

Two tests are performed. In the first the Neumann inflow inertial term is neglected whereas in the second the inertial term is treated. The simulation results of the first test are shown in Figures 4.35 and Figure 4.37. The simulation results of the second test are shown in Figure 4.36 and 4.38, respectively. The Neumann's inflow term treatment improved the convergence of the solver by reducing the number of Newton iteration steps from a maximum of 10 to a maximum of 4 steps. A clear comparison between Figures 4.35 and 4.36 shows that proper treatment of the Neumann boundary condition produced a perfect match between the analytic and numerical results. This is clearly seen in Figure 4.36 where the simulated inlet and outlet pressure and flow rate values perfectly matched the analytic results. A perfect matching between the 3D and 0D impedance boundaries is also observed in Figure 4.36(c). Furthermore, unlike Figure 4.37, Figure 4.38 shows that the flow is correctly developed by depicting the velocity profiles in the pipe at various points in time.

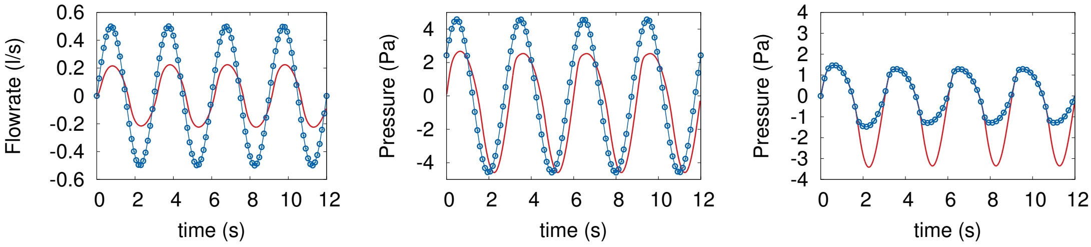

(a) (b) (c)

Figure 4.35.: Results of the traction-driven 3D air flow in a pipe coupled to an impedance tree with approximated pressure treatment of Neumann boundary condition: (a) flow rate, (b) average pressure at the inlet and (c) average pressure at the outlet (dotted values: analytic solution, solid line: values on 3D boundaries).

Case 2: Foreknown inflow velocity profile

In case only the velocity profiles at the inflow Neumann boundaries are known, then the velocities are evaluated from the flow rate on the 3D coupling boundary. To test treatment of the Neumann inflow inertial term, the ideal tracheal pipe inlet is subjected to a pressure of

$$P_{\text{in}} = 0.758 \sin(\omega t) \text{ Pa},$$

where the period T is taken to be $1.5\,\text{s}$ and the Womersley number is thus $\alpha = 3.87$. The tracheal outlet is subjected to zero pressure, i.e. do nothing boundary condition. The flow above configuration yields a lamina pipe flow, thus the analytic flow rate is calculated from Womersley's analytic solution as

$$Q = 0.1265 \sin(\omega t - \pi/2.8) \text{ l/s}.$$

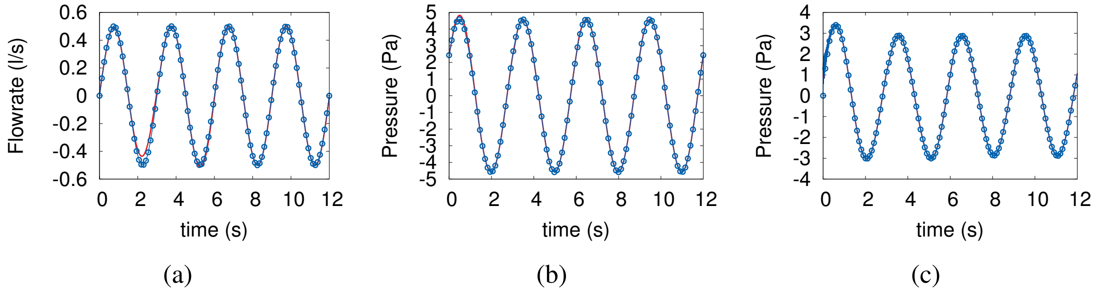

Figure 4.36.: Results of the traction-driven 3D air flow in a pipe coupled to an impedance tree with full Neumann treatment: (a) flow rate, (b) average pressure at the inlet and (c) average pressure at the outlet (dotted values: analytic solution, solid line: values on 3D boundaries). The pressure on the 0D tree side is plotted with a dashed line in (c). However, it is difficult to distinguish it from the dotted line.

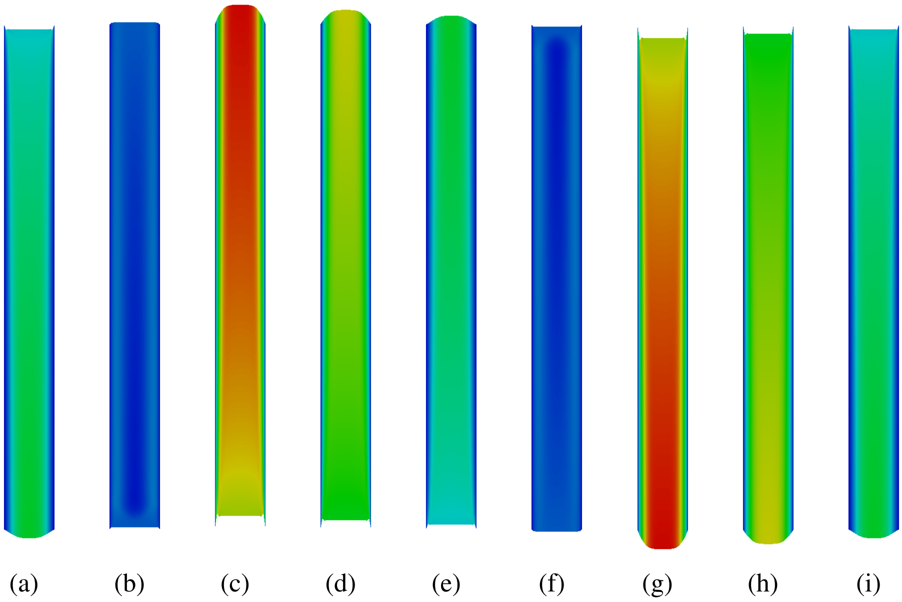

Figure 4.37.: A slice through the axis of a pipe showing the velocity profiles on colored velocity magnitude distribution for a traction-driven pipe flow coupled to an impedance tree with Neumann condition approximated by pressure (red color indicates high velocity, blue color low velocity); from right to left: $t = 6.0$, 6.2, 6.75, 7.3, 7.5, 7.7, 8.25, 8.8 and 9.0 s

Again two tests are performed. In the first the Neumann inflow inertial term is neglected whereas in the second is treated. The simulation results of the first test are presented in Figure 4.39 and Figure 4.41. The results of the second test are shown in Figure 4.40 and Figure 4.42. In this example, the full Neumann treatment slightly reduced the convergence of the solver by increasing the number of Newton iteration steps from a maximum of 4 to a maximum of 6 steps.

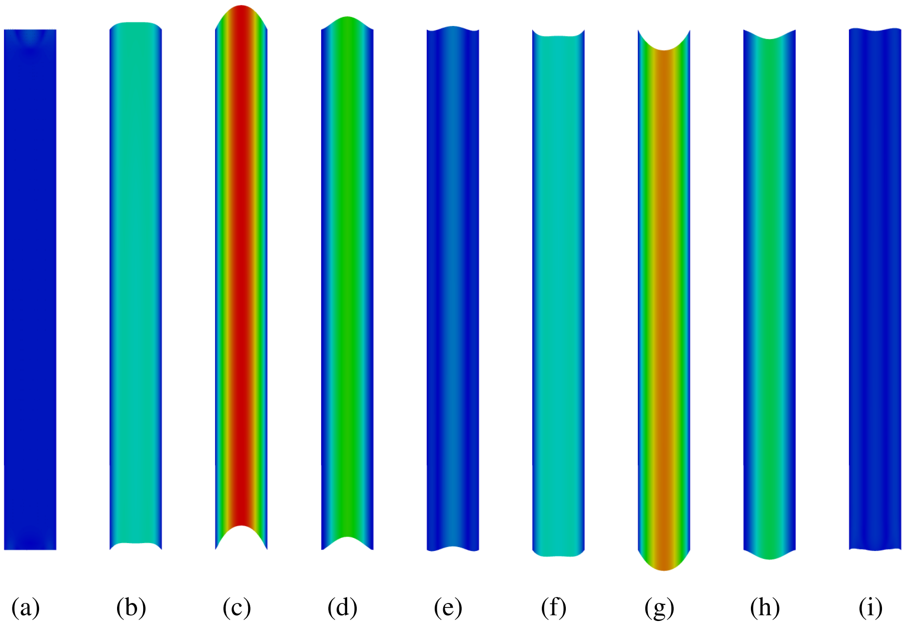

Figure 4.38.: A slice through the axis of a pipe showing the velocity profiles on colored velocity magnitude distribution for a traction-driven pipe flow coupled to an impedance tree with a fully treated Neumann condition (red color indicates high velocity, blue color low velocity); from right to left: $t = 6.0$, 6.2, 6.75, 7.3, 7.5, 7.7, 8.25, 8.8 and 9.0 s

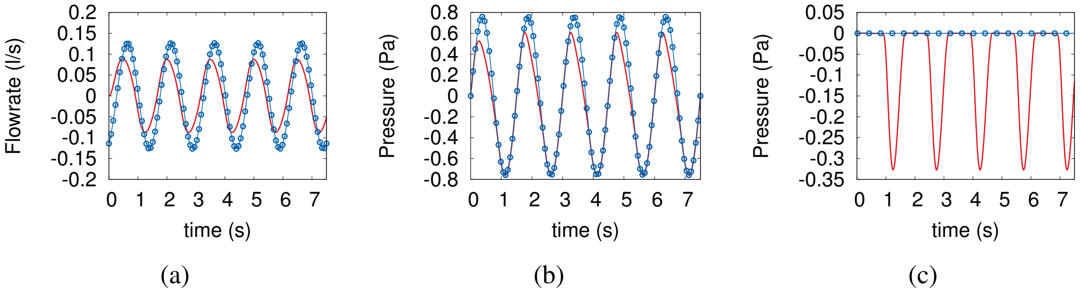

Figure 4.39.: Results of the pressure driven 3D air flow in a pipe with approximated pressure treatment of Neumann boundary condition: (a) flow rate, (b) average pressure at inlet, (c) average pressure at outlet (dotted values: analytic solution, solid line: values on 3D boundaries).

A comparison between Figures 4.39 and 4.40 showed that a proper treatment of the Neumann inertial term reproduced the correct pressure and flow rate values on the boundary. This is clearly noticed when comparing the numerical results to the analytic ones (see Figures 4.39 and 4.40). The mismatch in the first three cycles between the analytic and the numerical results in Figure 4.40 is due to the increased Womersley number. Such an increase in the Womersley

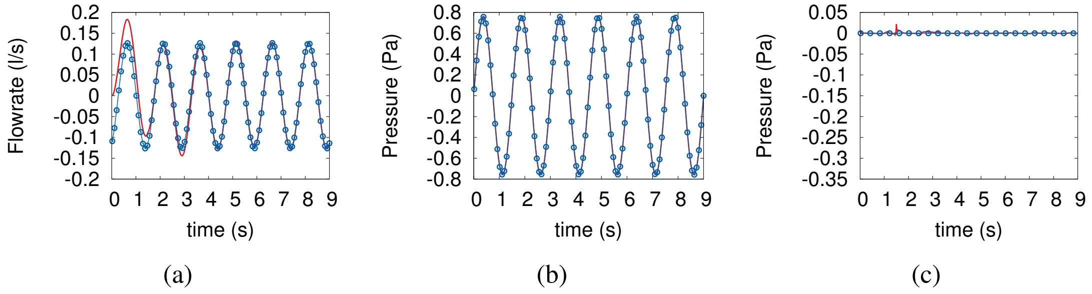

Figure 4.40.: Results of the pressure driven 3D air flow in a pipe with full Neumann treatment: (a) flow rate, (b) average pressure at inlet, (c) average pressure at outlet (dotted values: analytic solution, solid line: values on 3D boundaries).

number leads to an increase in the flow rate-pressure phase shift. In addition to that, all of the simulations started initially with zero velocity and pressure values, this in turn delayed the observation of periodic steady-state. The matching between inlet and outlet velocity profiles in Figure 4.42 indicated that the flow is correctly developed and that the boundary conditions are properly treated.

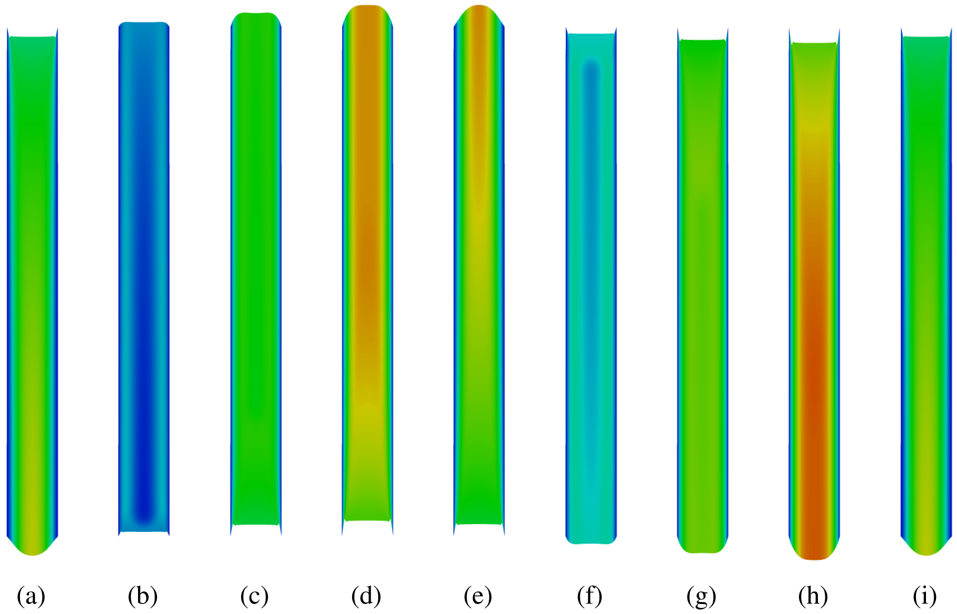

Figure 4.41.: A slice through the axis of a pipe showing the velocity profiles on colored velocity magnitude distribution for a pressure-driven pipe with Neumann condition approximated by pressure (red color indicates high velocity, blue color low velocity); from right to left: $t = 7.5, 7.72, 7.82, 7.92, 8.2, 8.5, 8.6, 8.7$ and 9.0 s

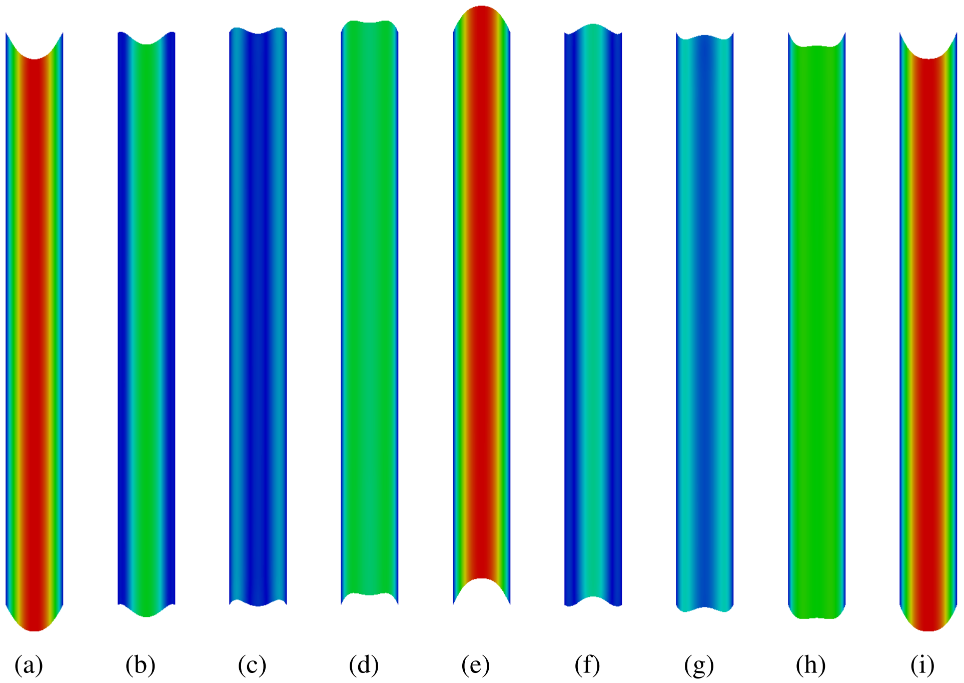

Figure 4.42.: A slice through the axis of a pipe showing the velocity profiles on colored velocity magnitude distribution for a pressure-driven pipe with fully treated Neumann condition (red color indicates high velocity, blue color low velocity); from right to left: t = 7.5, 7.72, 7.82, 7.92, 8.2, 8.5, 8.6, 8.7 and 9.0 s

Effects of Neumann inflow term treatment on hemodynamics

It is shown earlier in this section that, unlike airflow, in hemodynamics the inflow term of the Neumann condition does not need a full treatment. However, even though the inflow term is very small, it has a significant stabilizing effect. This opened a question, what is the influence of such a small term on the flow? For this purpose, a 3D compliant arterial pipe is constructed. The pipe length is taken to be $5\,\mathrm{cm}$ and the pipe diameter is assumed to be $1\,\mathrm{cm}$. The pipe thickness is taken to be $0.5\,\mathrm{mm}$. Each terminal of the 3D pipe is connected to a 1D pipe (see Figure 4.43). The blood is considered to be an incompressible Newtonian fluid with a kinematic viscosity $\nu = 4 \times 10^{-6}\,\mathrm{m^2/s}$ and a density $\rho = 1000\,\mathrm{kg/m^3}$. The 3D structure is modeled using Saint Venant-Kirchhoff material with first Lamé constant $\lambda_1 = 2.31\,\mathrm{MPa}$, second Lamé constant $\lambda_2 = 1.54\,\mathrm{MPa}$, Poisson's ratio $\nu_{\mathrm{3D}} = 0.3$ and density $\rho_{\mathrm{3D}} = 1200\,\mathrm{kg/m^3}$. The Structural part in the 1D model is considered as a linear elastic material with Young's modulus $E_{\mathrm{1D}} = 4\,\mathrm{MPa}$, Poisson's ration $\nu_{\mathrm{1D}} = 0.3$. The 1D pipes have the same geometric properties as the 3D one. Both terminal ends of the 3D structural domain are strictly fixed. Thus negative reflections at the boundaries coupling the 3D to the 1D domains are expected. The motive behind having reflections is to test the coupling under more complicated oscillatory conditions. A pressure wave $p\,(t) = 1\sin\left(\pi t/T_p\right)\,\mathrm{kPa}$ is forced at the inlet ($z = 0\,\mathrm{cm}$), where $T_p = 5\,\mathrm{ms}$. The outlet of the coupled 1D-3D-1D arterial setup ($z = 15\,\mathrm{cm}$) is defined as a nonreflective boundary. A time step $\Delta t = 10^{-5}\,\mathrm{s}$ is chosen for this simulation. The FSI frame work is solved monolithically [46; 80].

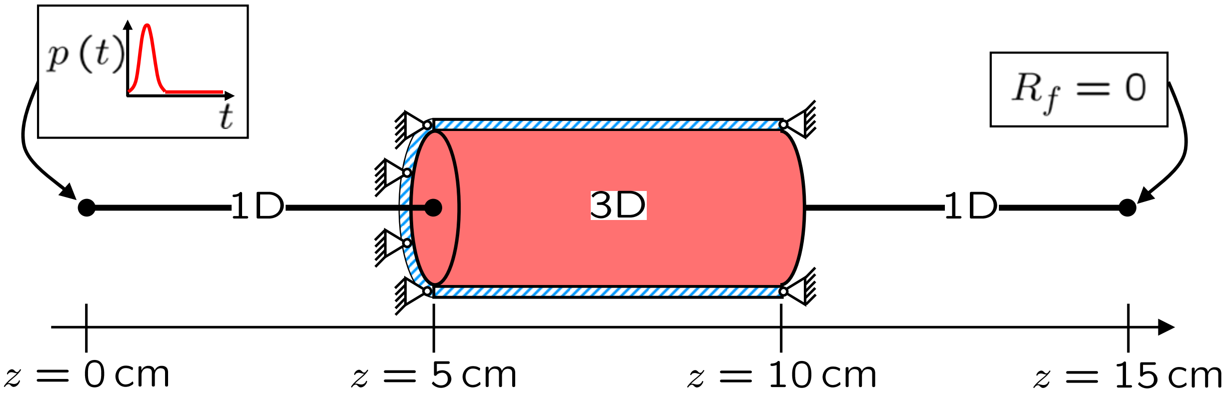

Figure 4.43.: Coupled 1D-3D-1D FSI artery having the 3D-1D coupling structural boundaries on the 3D side totally fixed.

Two tests are performed. In the first the Neumann inertial term is not treated whereas in the second the Neumann inertial term is properly treated by assuming a Womersley profile at the boundary. In the first test, a weak explicit coupling is assumed whereas for the second a strong implicit coupling is assumed. The results of the first test are detailed in Figure 4.44, where flow rate and pressure time curves results at the 3D-1D coupling interfaces are shown, i.e. at $z = 5\,\mathrm{cm}$ and $z = 10\,\mathrm{cm}$. The results of the second test at the coupled boundary are shown in Figure 4.45. First observation is that both tests had matching boundary pressures and that the treatment of the Neumann inertial term yielded no change in neither the coupled boundary pressure nor the coupled boundary flow rate. Furthermore, no change in the solver convergence is observed, i.e. the number of Newton iteration steps remained at a maximum of 4 steps. The almost identical results in Figures 4.44 and Figure 4.45 have again implied that in blood flow the Neumann inertial term treatment can be ignored. However, a deeper look into the velocity profiles at $z = 5\,\mathrm{cm}$ show that the Neumann inertial treatment resulted in Womersley velocity profiles; see Figure 4.46, and ignoring the Neumann inertial treatment again resulted in a flattened velocity profile.

In conclusion, the Neumann inertial treatment prevents nonphysical flattening of the velocity profile, enforces weakly the foreknown velocity profile and leads to a matching pressure at the coupling boundary.

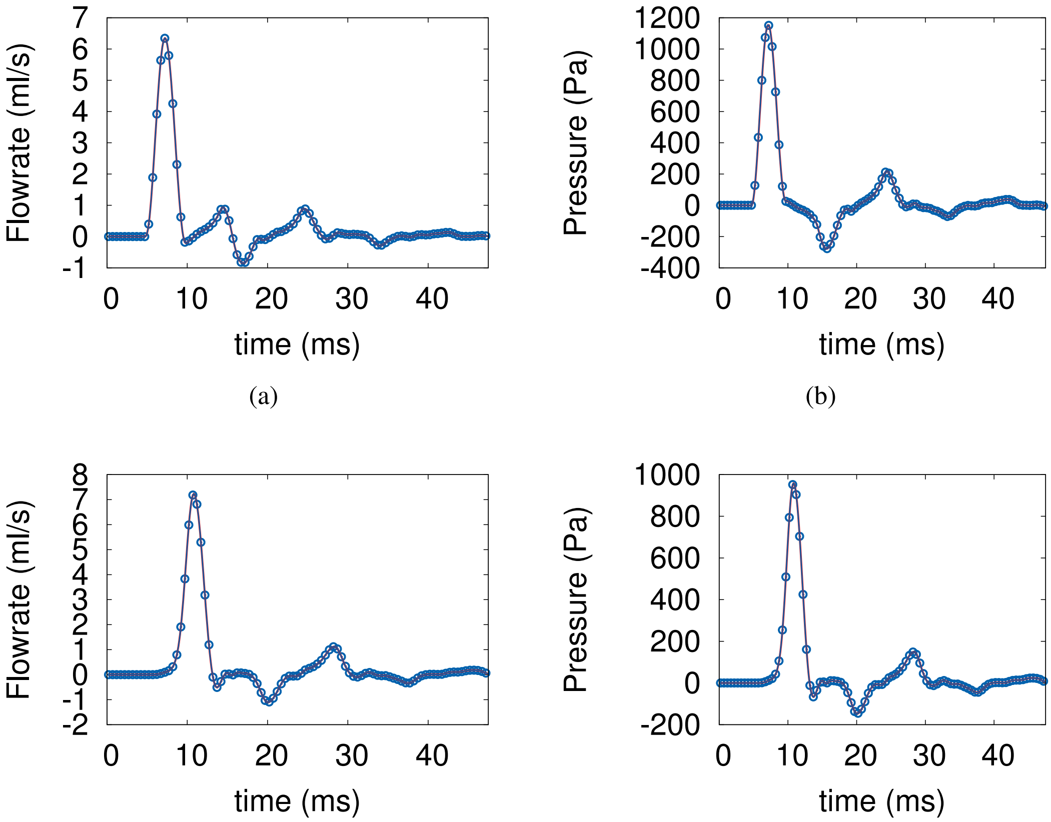

(a) (b)

(c) (d)

Figure 4.44.: Results of weakly coupled 1D-3D-1D FSI artery with traction approximated by pressure; (a) flow rate at $z = 5\,\mathrm{cm}$, (b) pressure at $z = 5\,\mathrm{cm}$, (c) flow rate at $z = 10\,\mathrm{cm}$ and (d) pressure at $z = 10\,\mathrm{cm}$. 3D values are presented by line, 1D values are presented by dots.

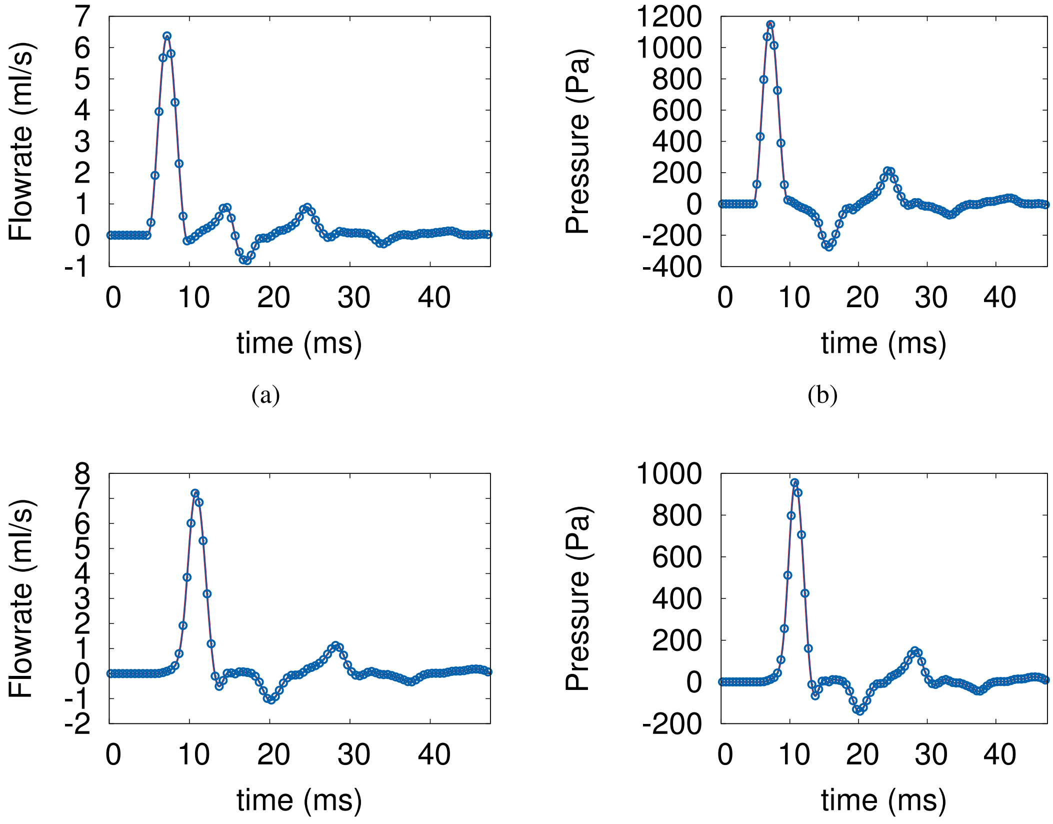

(a) (b)

(c) (d)

Figure 4.45.: Results of strongly coupled 1D-3D-1D FSI artery with traction fully treated; (a) flow rate at $z = 5\,\mathrm{cm}$, (b) pressure at $z = 5\,\mathrm{cm}$, (c) flow rate at $z = 10\,\mathrm{cm}$ and (d) pressure at $z = 10\,\mathrm{cm}$. 3D values are presented by line, 1D values are presented by dots.

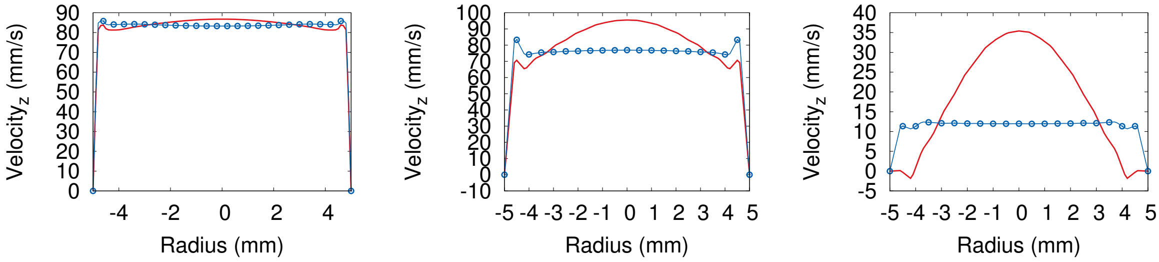

Figure 4.46.: Comparison between 3D velocity profiles at $z = 5\,\mathrm{cm}$ and (a) $t = 7\,\mathrm{ms}$, (b) $t = 7.8\,\mathrm{ms}$ and (c) $t = 24.3\,\mathrm{ms}$ for a fully treated traction (Line) and traction approximated by pressure (Dashed).

5. The Entire Lung Model

> ”However beautiful the strategy, you should occasionally look at the results.”
>
> - Sir Winston Churchill

The Entire lung model in Figure 1.6 is assembled from the respiratory system and the circulatory system using the geometries, the mathematical models and the parameters of Chapter 2, Chapter 3 and Chapter 4, respectively. In this chapter the entire lung model is experimented under three different states. The first state represents the lung of a relaxed subject in a zero gravitational field. The second state represents the lung of the same relaxed subject in an upright position at the sea level. The third state represents the lung of the same subject being mechanically ventilated in a supine position. The mechanically ventilated lung is tested on that same lung geometry twice, the first time the lung is assumed to be healthy whereas in the second time an illness is introduced into the lung. The illness is artificially added to the lung in form of an occlusion to 30% of the terminal conducting airways that are the closest to the spine (see Figure 4.22 in Section 4.1.3).

All of the entire lung examples are tested under relaxed conditions. Therefore, a fixed heart rate of 60 beats per minute and a cardiac output of 5 liters per minute are assumed at the pulmonary ventricle, which read as following

$$Q_{\mathrm{PV}}(t) = \begin{cases} Q_{\max}\left[1+\cos\left(2\pi t/T_{\mathrm{sys}}\right)\right] & 0 \leq t_{\mathrm{cyc}} \leq T_{\mathrm{sys}} \\ 0 & T_{\mathrm{sys}} < t_{\mathrm{cyc}} < T_{\mathrm{dia}} \end{cases}$$

where $t_{\mathrm{cyc}} = t - n_{\mathrm{cyc}}T$ and n_{cyc} is the cardiac cycle number. The constants in the prescribed cardiac output are found to be $T = 1\,\mathrm{s}$, $T_{\mathrm{sys}} =$, $T_{\mathrm{sys}} = 0.3\,\mathrm{s}$ and $Q_{\max} = \frac{1}{6T_{\mathrm{sys}}}\,\mathrm{l/min}$. The pleural gravitational effect are modeled in form of the pressure ($P^{\mathrm{g}}_{\mathrm{pl}}$) defined in eq (4.10). $P^{\mathrm{g}}_{\max} = 3.75\,\mathrm{cmH_2O}$ and $P^{\mathrm{g}}_{\min} = -3.75\,\mathrm{cmH_2O}$ when gravity is accounted for [155] and $P^{\mathrm{g}}_{\max}$ and $P^{\mathrm{g}}_{\min}$ are set to zero when gravitational effects are ignored. The circulatory system is subjected to an external pressure equivalent to $P^{\mathrm{g}}_{\mathrm{pl}}$ and to the bloods gravitational pressure

$$P^{\mathrm{g}}_{\mathrm{bld}} = \rho_{\mathrm{bld}}\langle \mathbf{x} - \mathbf{x}_0, \mathbf{g}\rangle, \tag{5.1}$$

where ρ_{bld} is the density of blood, $\mathbf{x}$ the 3D coordinates of any point, $\mathbf{x}_0$ a reference point equivalent to $\mathbf{x}_{\mathrm{c}}$ in Section 4.1.2 and $\mathbf{g}$ is the gravitational field. at the terminals of the pulmonary veins the atrium is supposed to have a zero pressure. The gravitational field is taken to be $9.8\mathbf{n}_{\mathrm{g}}\,\mathrm{m/s^2}$ when gravitational effects are considered and $\mathbf{g} = \mathbf{0}$ when the gravitational effects are ignored, where $\mathbf{n}_{\mathrm{g}}$ is the orientation vector of the gravitational field. Furthermore, all simulations are discretized in time with a time step of $\Delta t = 1\,\mathrm{ms}$ and computed until a periodic steady-state is observed.

All example were simulated using the supercomputer of the Institute for Computational Mechanics[8]. The coupled 3D-0D lung was simulated using 64 *Intel(R) Xeon(R) CPU E5-2670 (2.60GHz)* processors, whereas the fully 0D lung was simulated using 8 *Intel(R) Xeon(R) CPU E5-2670 (2.60GHz)* processors. The coupled 3D-0D lung example required 3.5 days to simulate 1 physical second. The fully 0D lung example required 8 hours to simulate 1 physical second.

5.1. Relaxed spontaneous breathing

During relaxed spontaneous breathing an adult human being takes 15 breathes per minute. The tracheal pressure is nearly zero and the pleural pressure fluctuates between -8.3 and $-5.3\,\mathrm{cmH_2O}$ at end expiration and peak inspiration, respectively. As such, the respiratory system is subjected to a zero pressure condition at the trachea and an oscillatory pleural pressure at the pleura. The pleural pressure is taken from eq (4.9) as

$$P_{\mathrm{pl}} = 0.5\left(P_{\max} - P_{\min}\right)\left[\cos\left(2t\pi/T + \phi\right) + 1\right] + P_{\min} + P_{\mathrm{pl}}^{\mathrm{g}}, \tag{5.2}$$

where $P_{\max} = -5.3\,\mathrm{cmH_2O}$, $P_{\min} = -5.3\,\mathrm{cmH_2O}$, $T = 4\,\mathrm{s}$ and $\phi = 0\,\mathrm{rad}$. The simulation results are presented in the following three subsections.

5.1.1. Respiratory system

The influence of gravity on the mechanical behavior of a respiratory system during spontaneous breathing is shown in Figure 5.1 and Figure 5.2. The first thing that is observed is that gravity increased the heterogeneity of the bronchial pressure. This is indeed the case since gravitational effects made the alveoli act under different pressure spans. As such the upper alveoli are exposed to a lower pleural pressure and thus their material is operating within the hyper-elastic zone. In other words, gravity increased the ventilation within the lower airways. This is also

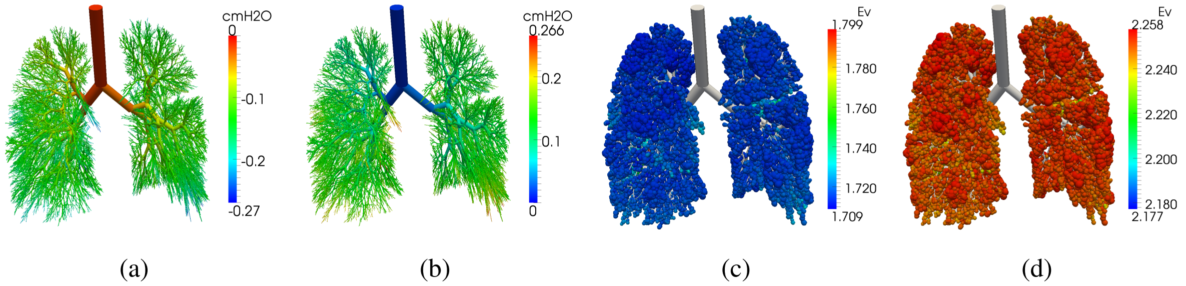

(a) (b) (c) (d)

Figure 5.1.: Results of gravity free spontaneously breathing showing (a) bronchial pressure at maximum tidal inspiration ($t = 13.3\,\mathrm{s}$), (b) bronchial pressure at maximum tidal expiration ($t = 15.3\,\mathrm{s}$), (c) acinar volumetric strain at end expiration ($t = 12\,\mathrm{s}$) and (d) acinar volumetric strain at peak inspiratory volume ($t = 14\,\mathrm{s}$).

---

[8] Institute for Computational Mechanics, Technische Universität München. Address: Boltzmannstr 15, 85747 Garching by Munich, Germany. Website: www.lnm.mw.tum.de

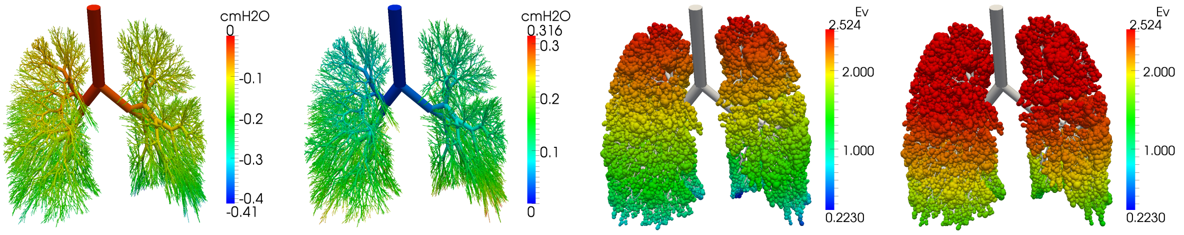

(a) (b) (c) (d)

Figure 5.2.: Results of an upright spontaneously breathing showing (a) bronchial pressure at maximum tidal inspiration ($t = 13.3\,\mathrm{s}$), (b) bronchial pressure at maximum tidal expiration ($t = 15.3\,\mathrm{s}$), (c) acinar volumetric strain at end expiration ($t = 12\,\mathrm{s}$) and (d) acinar volumetric strain at peak inspiratory volume ($t = 14\,\mathrm{s}$).

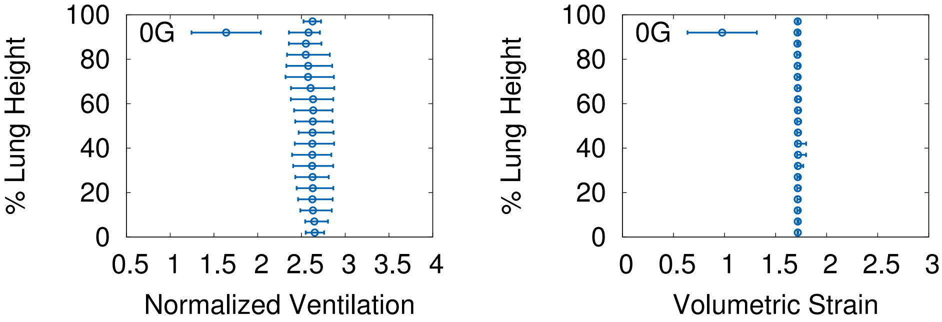

(a) (b)

Figure 5.3.: Lung height distribution of (a) normalized ventilation and (b) volumetric strain in a gravity free spontaneously breathing lung. 0G: no gravity.

observed after comparing the results in Figure 5.1(a-b) and Figure 5.1(c-d) with the results in Figure 5.2(a-b) and Figure 5.2(c-d), respectively. The gravity, firstly, decreased the fluctuation of pressure within the upper bronchi and increased it withing the lower bronchi. Secondly, gravity led to lower alveolar strain fluctuations in the upper part of the lung and higher alveolar strain fluctuations in the lower part of the lung. Furthermore, the detailed normalized ventilation and volumetric strain results of Figure 5.3 and Figure 5.4 showed that gravity led indeed to a more heterogeneous ventilation of the lung and a better ventilation of the lower sections of the lung.

5.1.2. Circulatory system

Figure 5.5 and Figure 5.6 show the effect of gravity flow and pressure within the circulatory system of a spontaneously breathing lung. Interestingly, gravity had a negligible effect on the flow rate values such as the sum of flow of blood through capillaries and the flow into the left atrium (see Figure 5.5(a) versus Figure 5.6(a)). Furthermore, the space averaged pressure values at various sections of the lung are also more or less not effected by gravity (see Figure 5.5(b) versus Figure 5.6(b)). However, a clear increase in pressure fluctuation is observed in Figure 5.6(b).

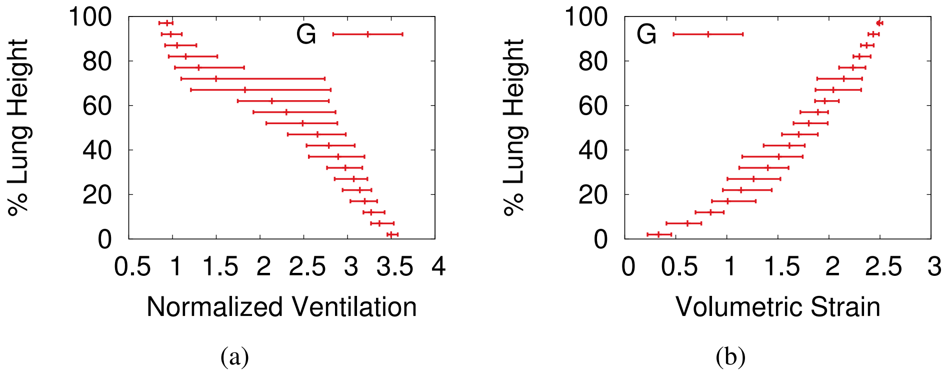

(a) (b)

Figure 5.4.: Lung height distribution of (a) normalized ventilation and (b) volumetric strain in an upright spontaneously breathing lung. G: with gravity.

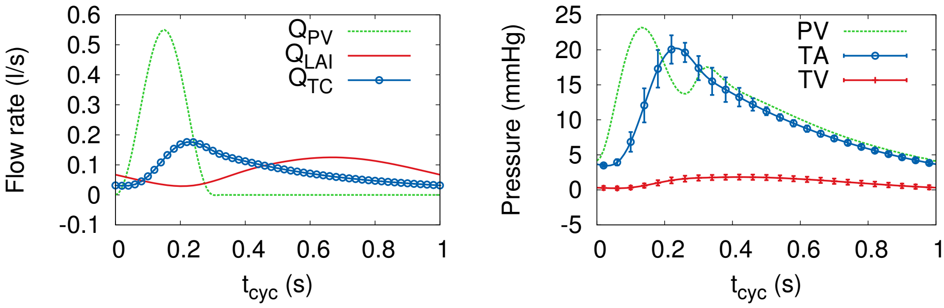

(a) (b)

Figure 5.5.: Space averaged pulmonary circulation results of a gravity free spontaneously breathing lung showing (a) flow rate values and (b) pressure values in different regions of the lung . Q_{PV}: flow at pulmonary valve; Q_{LAI}: flow at left atrium inlet; Q_{TC}: total sum of flow in capillaries; PV: pulmonary valve; TA: terminal arteries; TV: terminal veins.

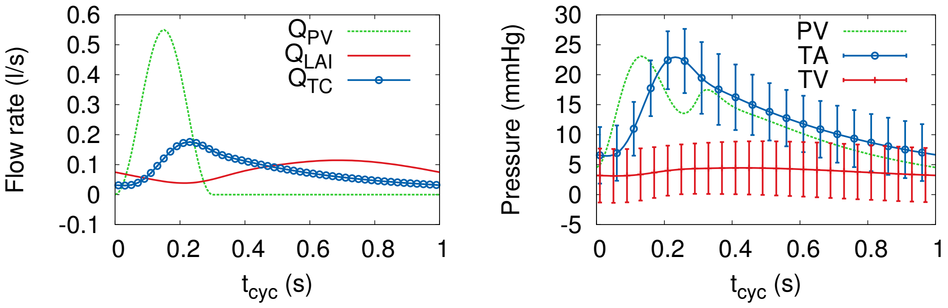

(a) (b)

Figure 5.6.: Space averaged pulmonary circulation results of an upright spontaneously breathing lung showing (a) flow rate values and (b) pressure values in different regions of the lung . Q_{PV}: flow at pulmonary valve; Q_{LAI}: flow at left atrium inlet; Q_{TC}: total sum of flow in capillaries; PV: pulmonary valve; TA: terminal arteries; TV: terminal veins;

This suggested that gravity led to an increased heterogeneity within the lung, but no further details could be concluded from Figure 5.6(b).

A deeper look into the spatial distribution of the mechanical variables of the circulatory system is detailed in Figure 5.7 and Figure 5.8. Indeed a clear heterogeneity in the circulatory

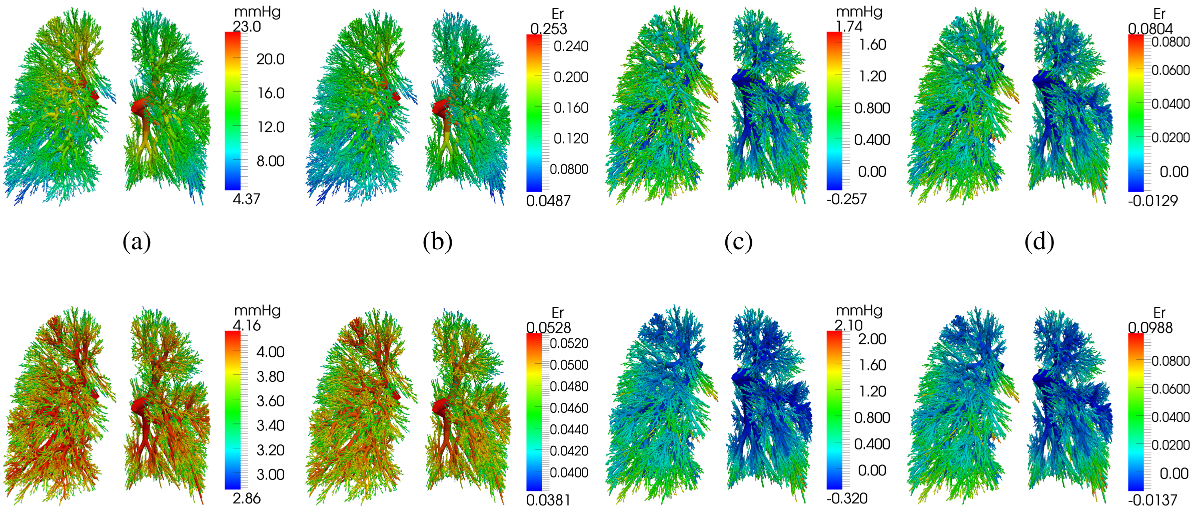

(a) (b) (c) (d)

(e) (f) (g) (h)

Figure 5.7.: Results of gravity free spontaneously breathing showing (a) peak systolic arterial pressure, (b) peak systolic arterial radial strain, (c) peak systolic venous pressure, (d) peak systolic venous radial strain, (e) end diastolic arterial pressure, (f) end diastolic arterial radial strain, (g) end diastolic venous pressure and (h) end diastolic venous radial strain.

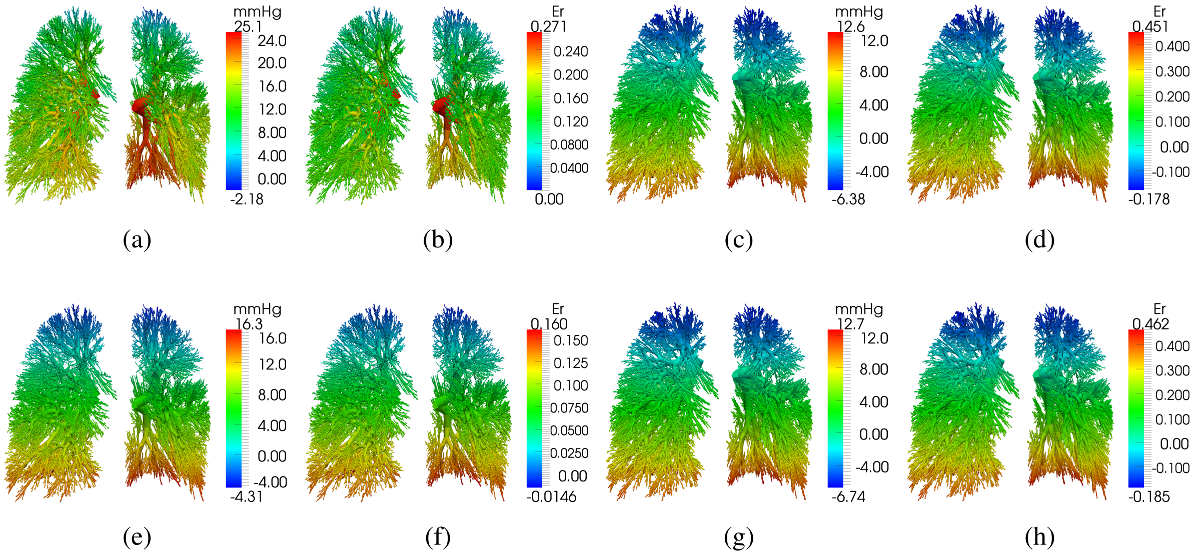
mmHg
25.1
24.0
20.0
16.0
12.0
8.00
4.00
0.00
-2.18
Er
0.271
0.240
0.200
0.160
0.120
0.0800
0.0400
0.00
mmHg
12.6
12.0
8.00
4.00
0.00
-4.00
-6.38
Er
0.451
0.400
0.300
0.200
0.100
0.00
-0.100
-0.178
mmHg
16.3
16.0
12.0
8.00
4.00
0.00
-4.00
-4.31
Er
0.160
0.150
0.125
0.100
0.0750
0.0500
0.0250
0.00
-0.0146
mmHg
12.7
12.0
8.00
4.00
0.00
-4.00
-6.74
Er
0.462
0.400
0.300
0.200
0.100
0.00
-0.100
-0.185

(a) (b) (c) (d)

(e) (f) (g) (h)

Figure 5.8.: Results of an upright spontaneously breathing showing (a) peak systolic arterial pressure, (b) peak systolic arterial radial strain, (c) peak systolic venous pressure, (d) peak systolic venous radial strain, (e) end diastolic arterial pressure, (f) end diastolic arterial radial strain, (g) end diastolic venous pressure and (h) end diastolic venous radial strain.

system due to gravitational effects is again observed. Furthermore, it can be clearly observed in Figure 5.8 that gravity made the blood vessels in the lower part of the circulatory system more distended whereas the blood vessels of the upper part more compressed. In other words, gravity made the blood flow more in the lower part of the circulatory system than the upper one.

5.1.3. Oxygen transport

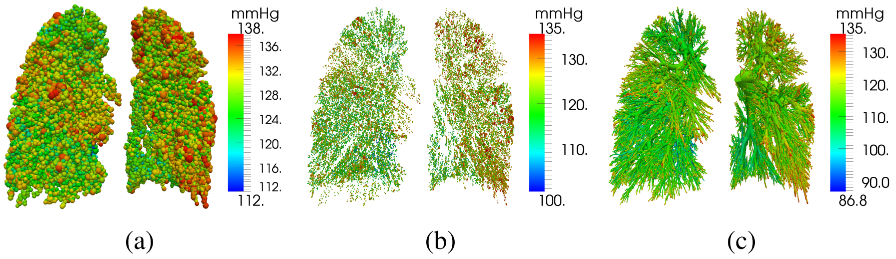
mmHg
138.
136.
132.
128.
124.
120.
116.
112.
112.
mmHg
135.
130.
120.
110.
100.
mmHg
135.
130.
120.
110.
100.
90.0
86.8

(a) (b) (c)

Figure 5.9.: P_{O_2} results of gravity free spontaneously breathing lung showing (a) respiratory zone, (b) capillary network and (c) pulmonary veins.

The spatial distribution of P_{O_2} in a spontaneously breathing lung are shown in Figure 5.9 and Figure 5.10. Gravitational effects are again observed by comparing the upper and lower region of the lung within the presented results. Figure 5.9 shows a more heterogeneous distribution of

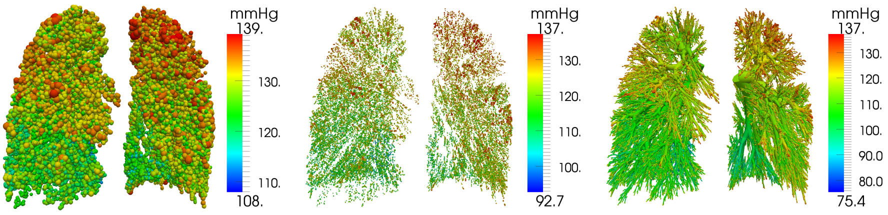

(a) (b) (c)

Figure 5.10.: P_{O_2} results of an upright spontaneously breathing lung showing (a) respiratory zone, (b) capillary network and (c) pulmonary veins.

P_{O_2} when compared to Figure 5.10. The reduced P_{O_2} values in the lower regions of Figure 5.10(a-c) confirmed that due to gravity most blood flowed within the lower lung regions. Thus due to gravity, most of the O_2 supply came from the lower alveolar regions.

5.2. Mechanical ventilation - Supine position

When patients are not able to breath, MV becomes a necessity for their survival. Many mechanical ventilators are invented and investigated the past decades to improve ventilation techniques and ventilation complications such as VALI and VILI [4]. All ventilators are common in two followings: they enforce air through the trachea and their main task is to maintain blood P_{O_2} at vital levels. Ventilators are divided into volume controlled and pressure controlled ones. Recently many preventative ventilation techniques are introduced to protect the lung. However, all of these techniques relied on the tracheal pressure and blood P_{O_2}, as such information about local ventilation and local over straining are and still are not available.

In this section, the entire lung is tested under volume controlled mechanical ventilation. The ventilator is modeled as

$$\begin{cases} Q_\mathrm{t} = 500/T_\mathrm{q}\,\mathrm{ml} & (N_\mathrm{cyc}-1)\,T \leq t < (N_\mathrm{cyc}-1)\,T + T_\mathrm{q} \\ Q_\mathrm{t} = 0.0\,\mathrm{ml} & (N_\mathrm{cyc}-1)\,T + T_\mathrm{q} \leq t < (N_\mathrm{cyc}-1)\,T + T_\mathrm{q} + T_0 \\ P_\mathrm{t} = 0.0\,\mathrm{cmH_2O} & (N_\mathrm{cyc}-1)\,T + T_\mathrm{q} + T_0 \leq t < (N_\mathrm{cyc})\,T \end{cases},$$

where $T = 4\,\mathrm{s}$ is the total period of a mechanical ventilation cycle, $N_\mathrm{cyc} \in \mathbb{N}$ the ventilation cycle number, $T_\mathrm{q} = 1.5\,\mathrm{s}$ the period of time of the air enforced into the lung, $T_0 = 0.25\,\mathrm{s}$ the period of time in which air is trapped inside the lung, Q_t the tracheal flow rate and P_t the tracheal pressure. The pleural pressure is taken from eq (4.12) as

$$P_\mathrm{pl} = P^0_\mathrm{pl} + b_\mathrm{p} V_{\mathrm{VC_p}} + c_\mathrm{p} e^{\left(d_\mathrm{p} V_{\mathrm{VC_p}}\right)} + P^\mathrm{g}_\mathrm{pl},$$

where $V_{\mathrm{VC_p}} = (V - V_\mathrm{R})\,/\,(V_\mathrm{TLC} - V_\mathrm{R})$ is the percentile vital capacitance, V_TLC the total lung capacitance and V_R is the residual volume. The model pleural space model is fitted to the measurements reported by [57] and yielded the following parameters

$$\begin{aligned} P_{\mathrm{pl}}^{0} &= -9.772\,\mathrm{cmH_2O}, \\ b_{\mathrm{p}} &= 20.344\,\mathrm{cmH_2O}, \\ c_{\mathrm{p}} &= -33.382\,\mathrm{cmH_2O}, \\ d_{\mathrm{p}} &= -7.686. \end{aligned}$$

The direction of the gravitational field is set such that the patient is in supine position. The results of the experiments are presented in the following three subsections.

5.2.1. Respiratory system

The difference between ventilating lungs in healthy and diseased states are detailed in Figure 5.11 and Figure 5.12, respectively. Two things are here observed, the tracheal and the bronchial pressure increased in the diseased lung and the heterogeneities increased too.

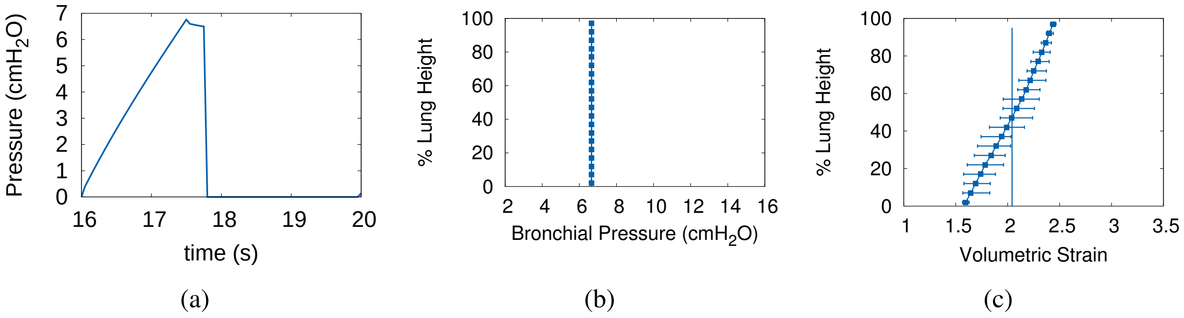

(a) (b) (c)

Figure 5.11.: Peak bronchial pressure of mechanically ventilated lung in supine position at $t = 17.5\,\mathrm{s}$ shown for (a) healthy lung and (b) diseased lung.

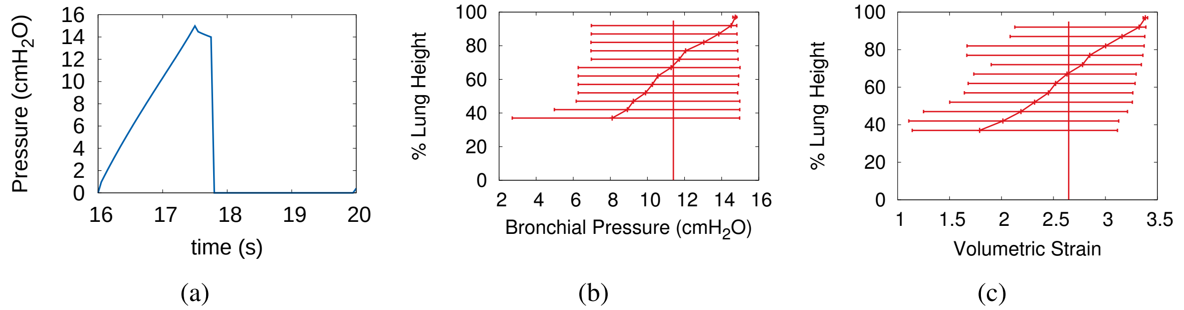

(a) (b) (c)

Figure 5.12.: Acinar volumetric strains of mechanically ventilated lung in supine position, at maximum bronchial pressure at $t = 17.5\,\mathrm{s}$, shown for (a) healthy lung and (b) diseased lung.

Since both healthy and sick lungs are ventilated with the same amount of air, the acini of the sick lung had thus to compete more for volume. A deeper look into the spatial distribution of the peak bronchial pressure and peak acinar volumetric strain, detailed in Figure 5.13 and Figure 5.14, showed that the increased heterogeneity is indeed due to an increase in volume competition between the neighboring acini. This is well illustrated in Figure 5.13(c) and Figure 5.14(c), where the volume competition appeared in both healthy and diseased lung however it is more dominant inside the sick lung. As such, the *in silico* model did indeed capture volume competition between neighboring acini. Furthermore, the peak bronchial pressure in Figure 5.12(a) is not critical by medical standards, however a clear local over straining of the healthy acini is observed in Figure 5.14(b). Thus the *in silico* model predicted a possible local volutrauma.

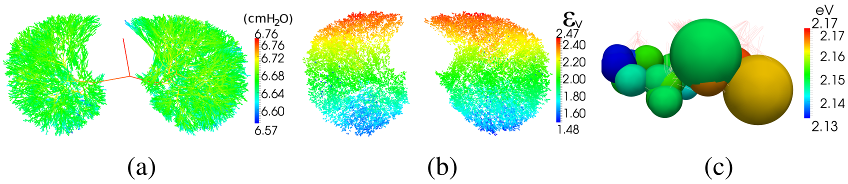

(a) (b) (c)

Figure 5.13.: Results of the mechanically ventilated healthy lung showing (a) peak bronchial pressure (b) peak volumetric acinar strain and (c) a zoomed in section of volume competing acini.

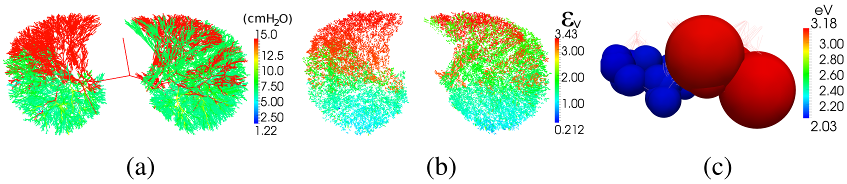

(a) (b) (c)

Figure 5.14.: Results of the mechanically ventilated sick lung showing (a) peak bronchial pressure (b) peak volumetric acinar strain and (c) a zoomed in section of volume competing acini.

5.2.2. Oxygen transport

The P_{O_2} spatial distributions of the mechanically ventilated healthy and diseased lungs are shown in Figure 5.15 and Figure 5.16, respectively. Comparing the sick lung with the healthy one, it is clearly observed that only the blood within the healthy section is oxygenated. The average blood P_{O_2} returned back to the heart is 111 mmHg for the healthy lung and 70 mmHg for the diseased one. The low blood P_{O_2} in the sick lung is due to the fact that the diseased section of the lung is exposed to de-recruited acini. As such, in the sick lung the low P_{O_2} blood mixed gradually with the high P_{O_2} blood the closer it approached to the heart.

5.3. Coupled 3D/0D ventilatory system

To test the coupling approach developed in this work, the setup of Figure 4.4 in Section 4.4 is tested under no gravity and relaxed spontaneous breathing conditions. The inlet of the trachea

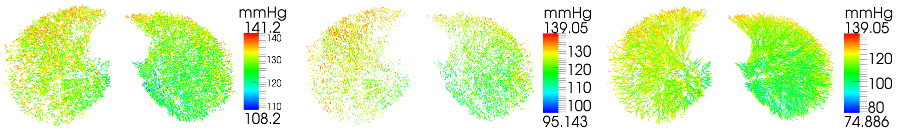

(a) (b) (c)

Figure 5.15.: Distribution of P_{O_2} results in a healthy mechanically ventilated lung showing (a) the respiratory zone, (b) blood capillaries and (c) pulmonary veins.

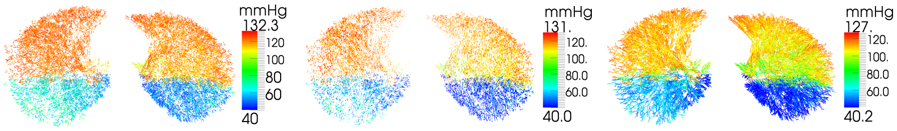

(a) (b) (c)

Figure 5.16.: Distribution of P_{O_2} results in a sick mechanically ventilated lung showing (a) the respiratory zone, (b) blood capillaries and (c) pulmonary veins.

is assumed to have zero pressure. The pleural space is modeled using the following pleural pressure

$$P_{\mathrm{pl}} = P_{\mathrm{pl_{max}}} + \frac{\Delta P_{\mathrm{pl}}}{2}\left(1 - \cos\left(2\pi t/T + \phi\right)\right) \tag{5.3}$$

where $P_{\mathrm{pl_{max}}} = -530.0\,\mathrm{Pa}$, $\Delta P_{\mathrm{pl}} = -330.0\,\mathrm{Pa}$, $T = 4\,\mathrm{s}$ and $\phi = \pi/11$. The velocity profiles at the boundaries are assumed to have a parabolic shape, as described by eq (4.17), since all outlet airways exhibit low Womersley numbers (maximum 1.3). Two simulations are then performed: the first simulation assumed that boundary A (tracheal inlet) developed a flat velocity profile, the second assumed that boundary A develops a parabolic velocity profile. Such a choice for the boundary A is depicted to present the sensitivity of the results on the method developed in Section 3.8 and Section 4.4. The two coupled 3D-0D setups are simulated for two respiratory cycles. Each time step is solved iteratively until the pressure and the velocity norms converges to $10^{-6}\,\mathrm{Pa}$ and $10^{-6}\,\mathrm{mm/s}$, respectively.

Figures 5.17 and 5.18 show the results of the fully coupled 3D-0D lung model for a flat and parabolic velocity profile, respectively. In both cases, the maximum amount of inspired air at the tracheal inlet is approximately $0.45\,\mathrm{l}$ with an approximate peak flow rate of $380\,\mathrm{ml/s}$. The total bronchial pressure drop, depicted in Figure 5.19, is approximately $16\,\mathrm{Pa}$ at peak expiration and $-16\,\mathrm{Pa}$ at peak inspiration. The flow rate and the total bronchial pressure drop are similar when comparing Figures 5.17 and 5.18. The 3D-0D boundaries match perfectly and the inlet pressure profiles are correctly obtained. This is clearly observed in Figures 5.17 and 5.18, where boundaries B, C, D, E and F show a perfect match between the pressure on the 3D surface and pressure and the 0D side of the coupling boundary. Boundary A in Figure 5.17 did not match the prescribed zero pressure during the inspiration phase. Nevertheless, the mismatch is much smaller than the one observed in Figure 4.31 where Neumann inertial terms are not treated. An interesting observation is that the tracheal flow rate in Figure 4.31 is similar to the one reported in Figures 5.17 and Figure 5.18. This is because the air is driven by the acinar region where

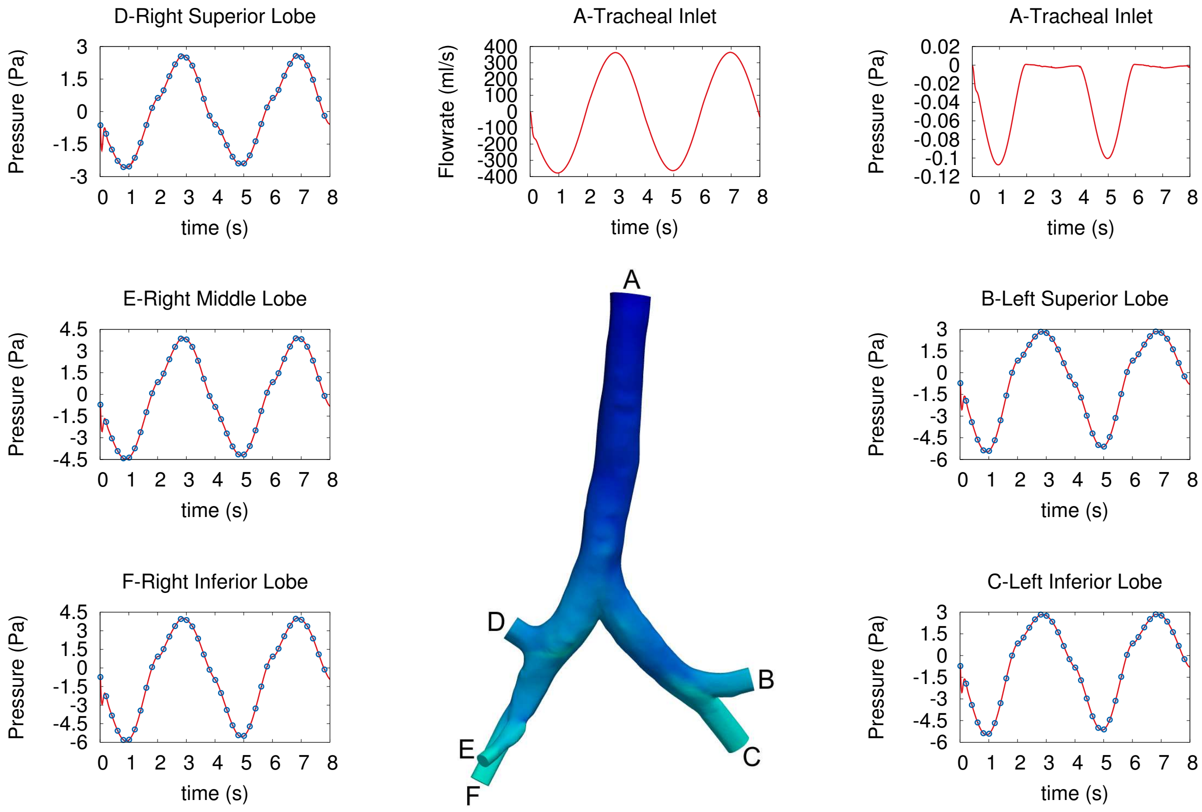

Figure 5.17.: Natural respiration results for case where Neumann conditions are fully treated and a flat velocity profile at the tracheal inlet is assumed (line values: pressure and flow rate values on 3D boundary, dotted values: pressure values on the 0D boundary).

the trans-pulmonary pressure is dominated by the pleural pressure, which in turn is two orders of magnitude higher than the airway pressure. In addition to that, the flow rate on a coupled boundary is controlled by the 3D problem whereas the pressure is controlled by the 0D problem. As such, during inspiration the 0D model kept on reducing the pressure on its side such that the acini get the correct flow rate dictated by the pleural pressure. This is clearly observed in Figure 4.31 from the tracheal pressure values during inspiration. Similarly, during expiration the pressure on the 0D side had to increase to create enough pressure drop on the 3D side that allowed the pleural controlled flow rate to come out of the trachea.

Figures 5.21, 5.22, and 5.23 detail the boundary velocity profiles of the results presented in Figure 5.18 for peak values of inspiration, partial reversed, and expiration flow rates, respectively. At peak inhalation, only the tracheal inlet exhibited (positive) inflow ($u_n^{\text{in}} > 0$), whereas the remaining boundaries had $u_n^{\text{in}} = 0$. Thus, a parabolic velocity profile is observed at the inlet, whereas the outlets developed more complicated profiles with secondary flow as observed in Figure 5.21. At the moment breathing changed from inspiration to expiration, vortices and secondary flows are expected to occur. Thus, partial reversed flow on the Neumann boundaries is expected. The velocity profiles in Figure 5.22 show that the coupling approach in this work did indeed allow partial reversed flows. At peak exhalation all boundaries except the tracheal “inlet”

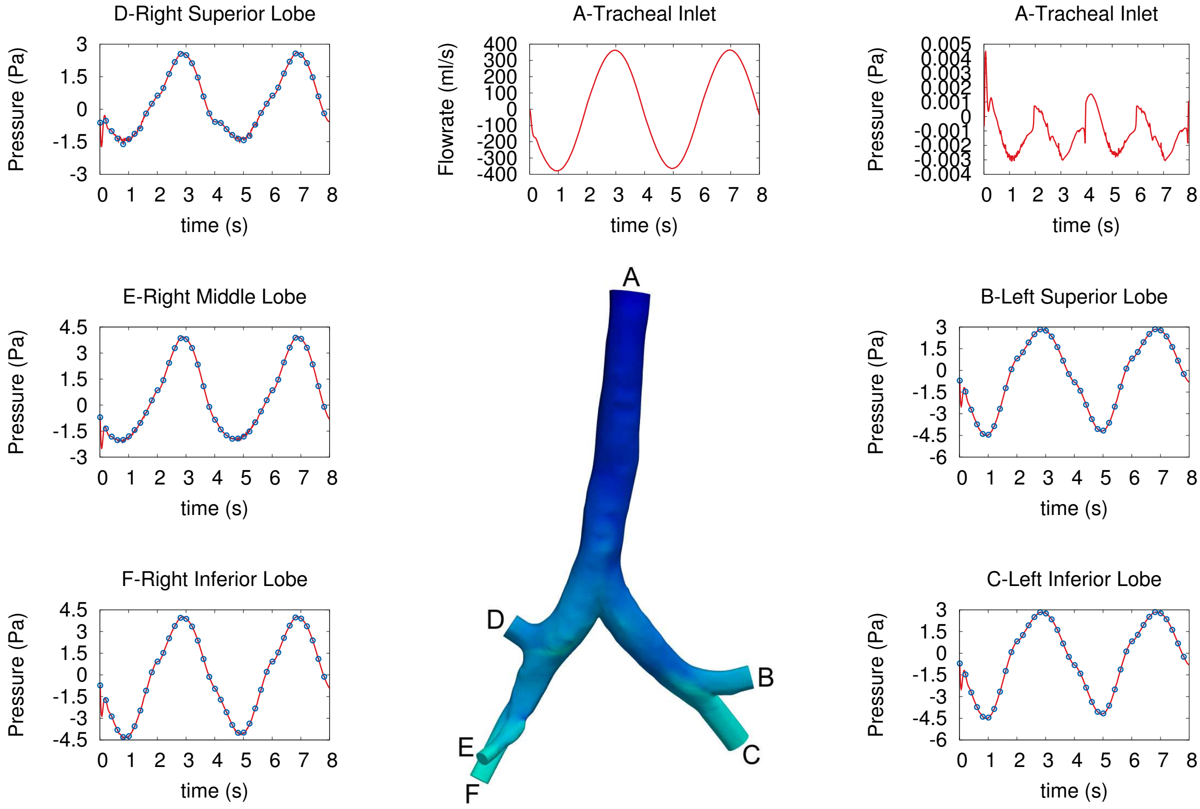

Figure 5.18.: Natural respiration results for case where Neumann conditions are fully treated and a parabolic velocity profile at the tracheal inlet is assumed (line values: pressure and flow rate values on 3D boundary, dotted values: pressure values on the 0D boundary).

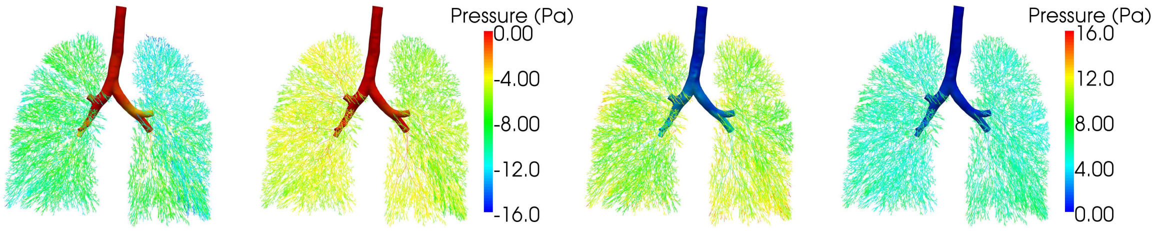
Pressure (Pa)
0.00
-4.00
-8.00
-12.0
-16.0
Pressure (Pa)
16.0
12.0
8.00
4.00
0.00

Figure 5.19.: Pressure values at t= 5 (upper left), 5.5 (upper right), 7 (lower left) and 7.5 s (lower right).

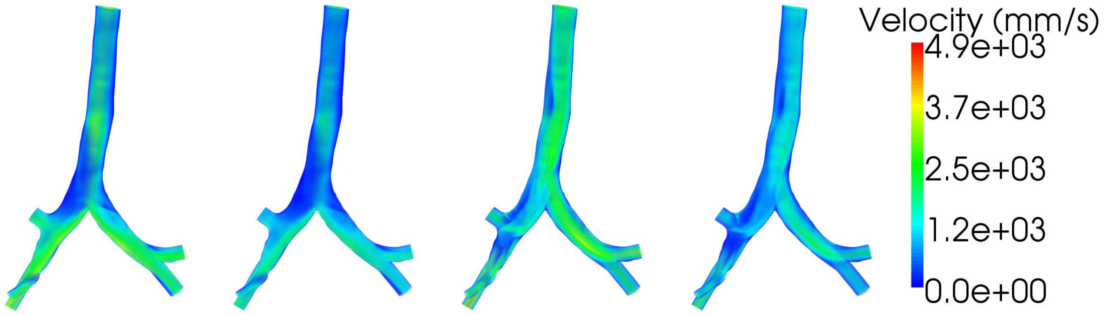
Velocity (mm/s)
4.9e+03
3.7e+03
2.5e+03
1.2e+03
0.0e+00

Figure 5.20.: 3D tracheobronchial velocities at t= 5, 5.5, 7 and 7.5 s.

exhibit inflow. Hence, only the tracheal inlet develops a rather complicated flow profile with secondary flows; see Figure 5.23. All remaining boundaries exhibit parabolic velocity profiles.

In short, the examples above show that the coupling approach developed in this work is stable, easy to implement and weakly enforced. Furthermore, it guarantee pressure match between the 3D and reduced-d domains.

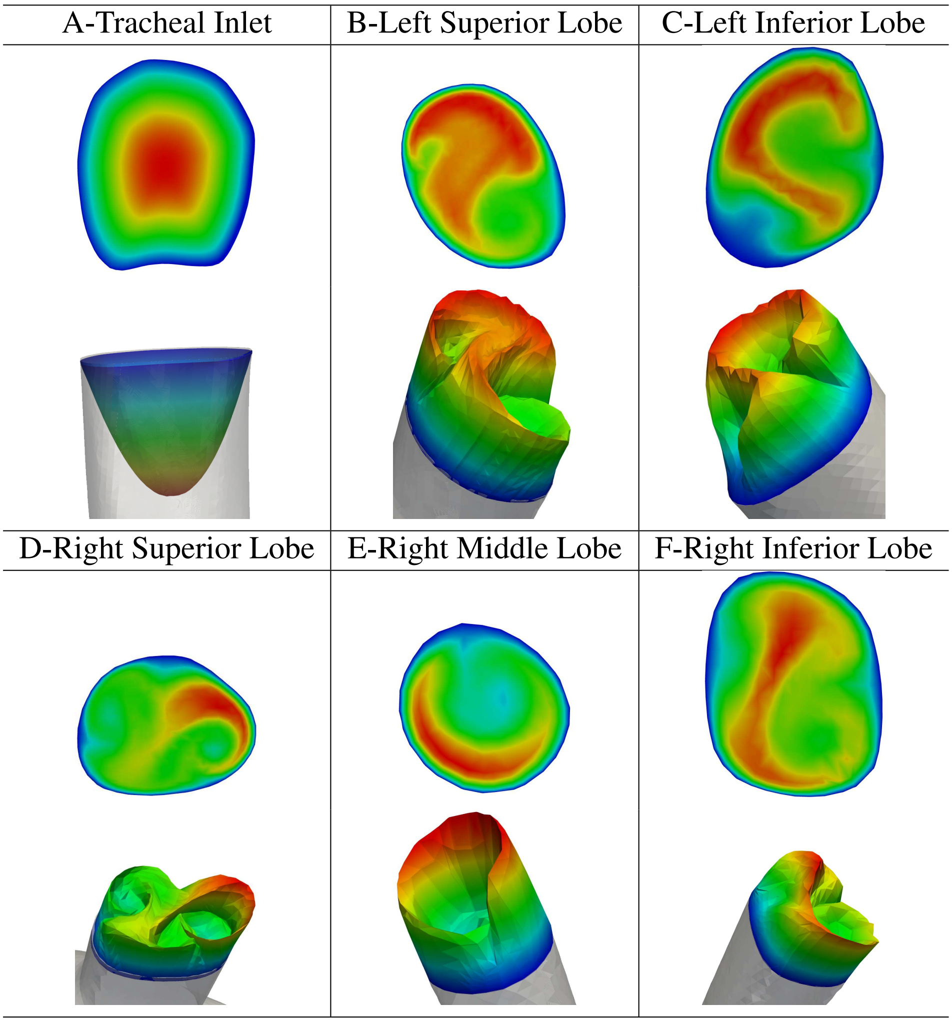
A-Tracheal Inlet B-Left Superior Lobe C-Left Inferior Lobe

D-Right Superior Lobe E-Right Middle Lobe F-Right Inferior Lobe

Figure 5.21.: Velocity profiles at different 3D boundaries at peak inspiration (time = 1 s). Red and blue colors indicate highest and lowest velocity values at a boundary, respectively.

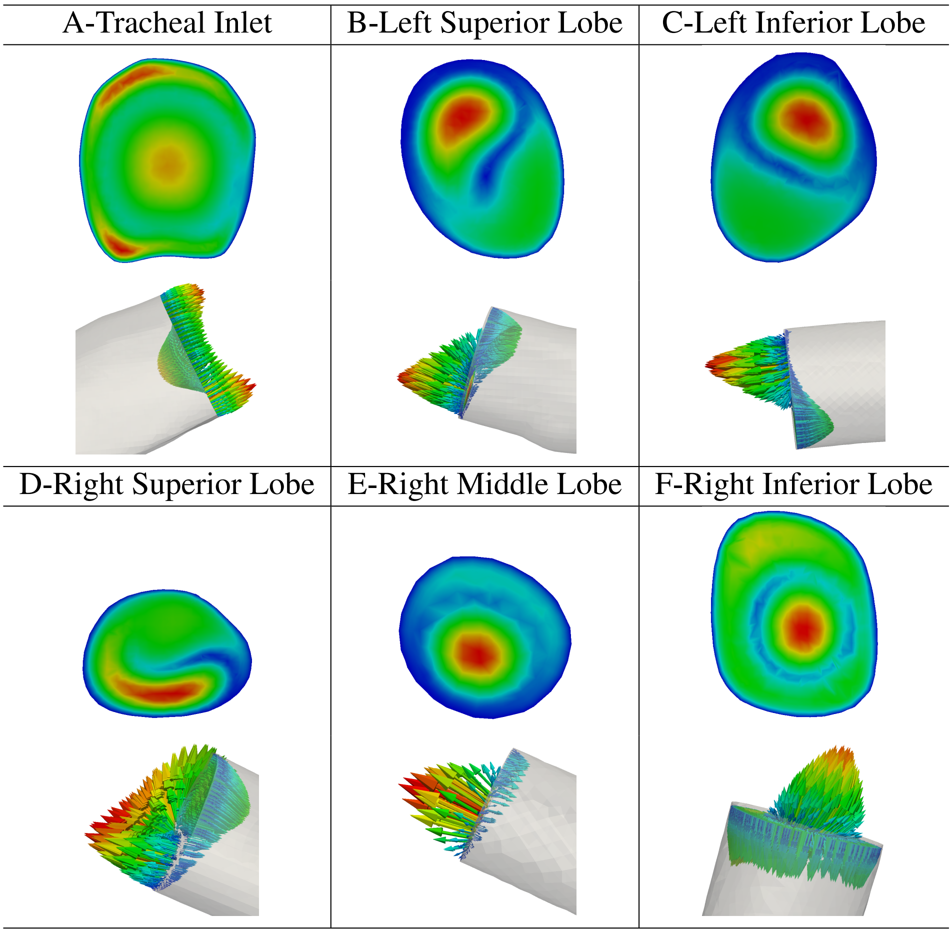
A-Tracheal Inlet
B-Left Superior Lobe
C-Left Inferior Lobe
D-Right Superior Lobe
E-Right Middle Lobe
F-Right Inferior Lobe

Figure 5.22.: Velocity profiles at different 3D boundaries showing partially reversed flow (time = 1.95 s). Red and blue colors indicate highest and lowest velocity values at a boundary, respectively.

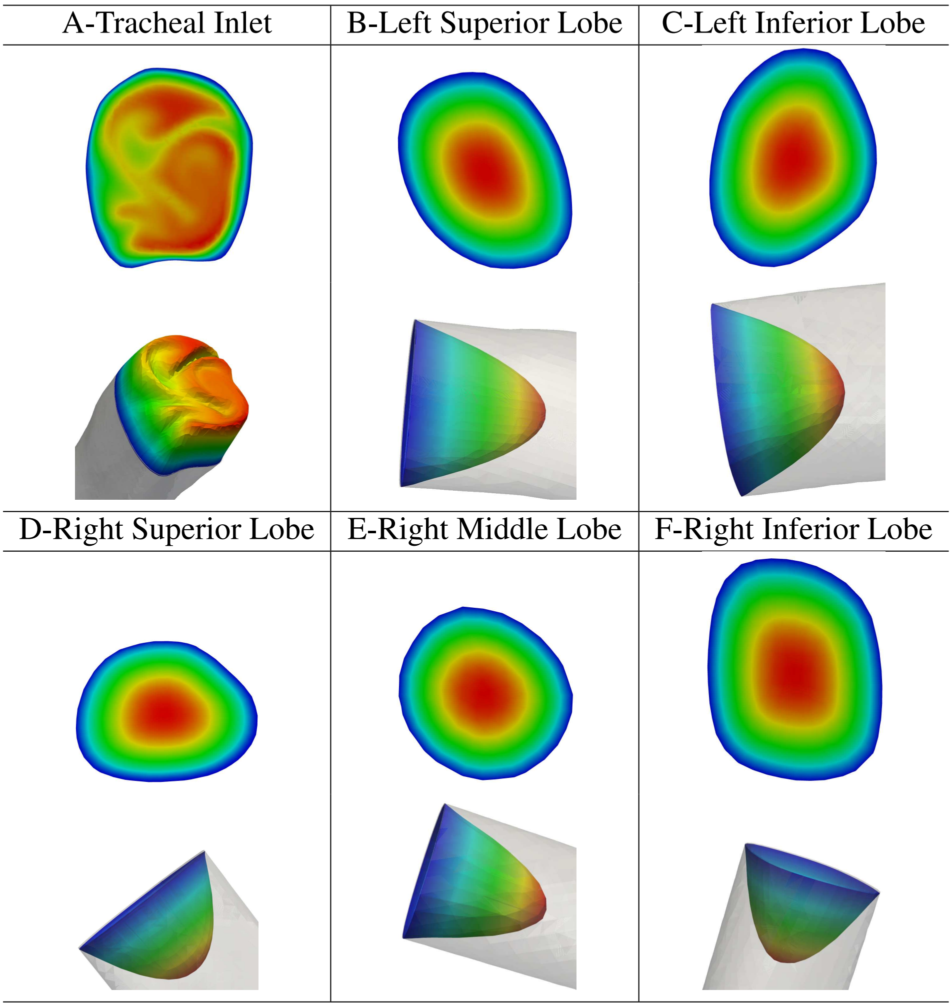
A-Tracheal Inlet
B-Left Superior Lobe
C-Left Inferior Lobe
D-Right Superior Lobe
E-Right Middle Lobe
F-Right Inferior Lobe

Figure 5.23.: Velocity profiles at different 3D boundaries at peak expiration (time = 3 s). Red and blue colors indicate highest and lowest velocity values at a boundary, respectively.

6. Summary and Discussion

> ”I think the in discussion of natural problems we ought to begin not with the scriptures, but with experiments, and demonstrations.”
>
> - Galileo Galilei

6.1. Comprehensive model of the human

This work aimed to development of a novel comprehensive multi-scale model of the entire-lung by combining together 3D, 1D and 0D models of the various lung components. The lung was divided into two main parts, the respiratory system and the circulatory system. Each of the major systems was broken down to three components. In the respiratory system, the author distinguished between the conducting/dead zone, the respiratory zone and the parenchymal inter-acinar tissue. The conducting zone made up 17 generations of airways and the respiratory zone included trees of the alveolar ducts. The inter-acinar tissue carried the information about the neighboring acini, thus allowing the neighboring acini to interact and compete for the same volume. In the circulatory system,three components were distinguished: the pulmonary arteries, the pulmonary capillaries and the pulmonary veins. The interaction between the pulmonary circulation and the respiratory system was established via the oxygen exchange interface between the respiratory zone and the pulmonary capillaries. Furthermore, gravitational effects and pleural pressure variations were included. In regions where local flow effects were the main interest, the author modeled the airways and blood vessels using 3D fluid and fluid-structure interaction models. For the remaining sections of the lung, 1D and 0D models were used. These models were coupled to the trimmed 3D boundaries using a novel coupling approach that guarantee stability and pressure matching at the sides of the coupling boundary.

6.2. Anatomically representative model

Anatomically, the human entire-lung was constructed from patient-specific CT-images. The CT-images provided only the geometry of few bronchial generations and the major lung lobes. However, considering pulmonary morphology and anatomy, 4 algorithms were developed to generate the missing lung components. The generated sections of the lung were validated against measurements from human anatomy. The conducting airway region, also known as dead zone, was found to be $133\,\mathrm{ml}$ in volume which was close to the $150\,\mathrm{ml}$ volume reported in anatomy [56]. The generated respiratory region was found to have 797 million alveoli, which fitted the morphologic measurements of Ochs et al. [106]. Furthermore, each acinus within the respiratory zone was sutured to it’s neighboring acinus via an inter-acinar linker. The blood vessels were generated from the airways geometries using a novel approach such that all arteries grew along the conducting airways and all veins grew in between the airway bifurcations. The algorithm was constructed such that arteries, airways and veins do not overlap. Arterial and venous radii were evaluated such their total volume fitted to the measurements reported by Velentin [146] and their geometry followed the generation power law measured Weibel [154]. In total, the total volume of arteries and veins were $135\,\mathrm{ml}$ and $235\,\mathrm{ml}$, respectively. The capillary networks were generated using the morphological measurements of Townsley [140] and the physiological information of Uylings [144]. In total the capillary networks allowed the pulmonary circulation to grow another 13 to 18 generations with a 10% variation in the terminating radii. Last but not least, an oxygen exchange interface was constructed by connecting capillary networks with their neighboring acini. In total, the oxygen interface yielded $85.9\,\mathrm{m}^2$ of gas exchange surface area, this value matched the anatomical range of $50 - 150\,\mathrm{m}^2$ reported by West [155].

6.3. Parameter identification and physiological results

The physical parameters of each of the lung components were identified inversely and validated against measurements from physiology. In the dead zone 4 parameters were identified, the airway resistance, the airway compliance, the wall visco-elastance and the air momentum/inertia. The airway resistance was tuned to the model of van Ertbruggen [147] and validated using the total bronchial pressure against 3D experiments and the measurements of Pedley et al. [111]. The airway wall compliance was evaluated by firstly constructing the airway wall thickness using the measurement of Montaudon et al. [98] and then fitting the compliance model of this work to the measured trumpet model of Lambert et al. [81]. The viscous effects were modeled mathematically and fitted to the measurements reported by Ito et al. [70]. The contribution of the different airway parameters was investigated under relaxed and extreme ventilation conditions with a peak trans-mural pressure of $15\,\mathrm{cmH_2O}$, ventilation frequencies of $\{0.25, 1, 4\}\,\mathrm{Hz}$ and tidal volumes of $\{0.25, 0.5, 1\}\,\mathrm{l}$. The acini were constructed by filling them with nonlinear visco-hyper-elastic alveolar ducts. Each alveolar duct was reduced down to a 4-element Maxwell model, which was then fitted to the PV-curves of the human *in silico* model of Denny and Schroter [29]. The model was then filled inside the lung geometry and tested under an *in silico* spirometry test. The various lung volumes such as RV, FRV, TV and TLC matched the ones measured in physiology by Needham et al. [103]. The inter-acinar dependencies were firstly validating using a two acinar toy problem. The volume competition between the two neighboring acini matched the analytic one. A further validation of the inter-acinar dependencies was performed on the entire respiratory system, where the pleural pressure was only subjected onto the pleural acini. Again, the inter-acinar dependencies showed lung volumes that matched the physiological measurements. In the circulatory system a fixed wall elastance was assumed such that the veins were 4 times more compliant than the arteries [56]. The wall thickness was found using the empirical model described by Olufsen et al. [109]. A simple optimization was performed by varying the elastance until a physiological systolic and diastolic pulmonary pressure was obtained. As was expected from physiology, the main flow resistance within the circulatory system was observed within the capillary networks, whereas the compliance within the large arteries and veins. The blood/air oxygen interface diffusion model was taken from Keener [72] and shown to reproduce physiological values by being validated against simplified two chamber and five chamber entire lung models. For the 3D/Reduced-D coupling, a pressure mismatch was observed for the classical stable coupling, as such a novel correction term was suggested such that it compensates for the Neumann inertial term dominance during inflow. The correction term was intensively investigated and validated against idealized geometries where an analytic solution of the boundary was known. Furthermore, the correction term was extended to complex problems and shown, using the complex respiratory geometry of the entire lung, to be consistent with the FEM formulation, easy to implement and guaranty the matching pressure at the opposite coupling interfaces.

6.4. Deeper insight into regional ventilation, volume competition and heterogeneities

All of the lung components were assembled together to produce a novel entire lung model. The entire lung was investigated under a group of *in silico* experiments for purpose of gaining a deeper insight into lung ventilation and its sensitivity to external and internal conditions. The investigated external conditions were gravitational effects, patients posture and tracheal/atmospheric pressure/flow rate. The considered internal conditions were pleural pressure and lungs' state of health. A common observation for all of the experiments was that lungs were never evenly ventilated. Various ventilation heterogeneities were observed. In general heterogeneities became more observed during MV and even more observable during the diseased state. A deeper look into local spatial variations showed that elevated heterogeneities within the sick lung were due to volume competition among neighboring acini. The main reason this was more observable in diseased state was because the diseased lung was ventilated with the same tidal volume as the the healthy one. However, the diseased lung had fewer recruited alveoli, thus more volume restrictions.

Interestingly, the volume competition was achieved purely from a physical modeling and was by no means biased within the acinar model. Alveolar collapse was not observed due to the segmoidal stiffness of 0D acinar model that prevented such a behavior. However, the clear volume competition between neighboring acini in the mechanically ventilated sick lung suggested that, contrary to some skeptical views [62], collapsing alveoli might after all exist. Thus showing a local damaging within the collapsed acini (in this work the acini were compressed but not collapsed).

6.5. Prediction of volutrauma and hypoxia

Interesting effects were observed when comparing the acinar straining and bronchial pressure between the mechanically ventilated healthy and diseased lungs. The results showed that while the bronchial pressure levels within the diseased lung were still within the safe ventilation levels, the acinar volumetric strain was close to the peak strain. The reason this happened was because some acini lost their volumes to their dominant neighbors, who in turn had to sustain a bigger volume of air and thus more volume strain. In other words, a local volutrauma was predicted where a baro-trauma was not observed.

Furthermore, the mechanically ventilated diseased lung showed a hypoxia. Although, such an observation can be easily estimated using simple estimation approach and did not require a complex model like the one developed in this work. The complex model gave a deeper insight into the local hypoxia and local oxygen ventilation. This can be used for further investigation of the efficiency of mechanical ventilation regimes.

6.6. Stability of coupled 3D/reduced-D problems and boundary pressure matching

The novel 3D/reduced-D coupling was implemented in a systemic way. Firstly, a Dirichlet-to-Neumann coupling was chosen as the coupling approach. Secondly, a consistent Galerkin method was used to distinguish between coupling conditions during outflow and inflow. Thirdly, the boundaries were shown to be stable during inflow and outflow, however the consistent method lead to a significant pressure mismatch between the 3D and the reduced-D corresponding boundaries. Thus, finally, a boundary pressure correction term, that was consistent with the method and easy to implement, was introduced to guarantee the matching of the boundary. The coupling method was validated against analytic solutions and shown to reproduce the correct physics, correct flow and correct pressure values. Furthermore, an intensive study was performed to compare the behavior of the developed coupling approach between hemodynamic flows and respiratory flow. The results showed that while the pressure correction term can be totally ignored in blood flow, it may not be ignored in respiratory flow.

7. Outlook and Limitations

> ”Even a mistake may turn out to be the one thing necessary to a worthwhile achievement.”
>
> - Henry Ford

7.1. Outlook

Optimization of ventilation profiles

The comprehensive lung model developed in this work successfully reproduces physiology, gives a deep insight into local ventilation, and captures volutrauma when it is not predictable. The next step is to put it into a real life application and investigate under various ventilation regimes for the purpose of optimizing ventilation profiles.

Airway-Airway interaction, blood vessels-airway interaction, and alveolar recruitment

In the current work volume inter-dependencies were modeled only for acini. However, the volume competition is not only due competition between neighboring alveoli but may also be observed between neighboring airways and blood vessels. In the current work the pleural pressure was volumetrically interpolated and applied in form of external pressure on both conducting airways and blood vessels. Thus volume competition between airways and blood vessels was not modeled. The author believes this might answer few open question to air trapping and terminal airway de-recruitment. Since terminal airways are more compliant and thus easier to collapse [81].

Model the left atrium

In the current work the left atrium was modeled as a zero pressure. Thus the flow results at the atrium showed only a diastolic peak but no systolic peak and no back flows due to atrial contraction [26; 49]. While the author believes that such effects might be too minor due to the large compliance of the venous bed, it would be important to validate that, since back flow means that the blood might be exposed for different time scales to O_2 exchange interface.

7.2. Limitations

Space filling of conducting airways

One limitation of this work is the space filling algorithm used to generate the conducting airways. The algorithm was adopted from Tawhai et al. [137], who tested it on a lung geometry under TLC. However, the lung used in this work was under FRV. This meant that, unlike the geometry used by Tawhai et al. [137], the geometry in this work has many concave regions in which the space filling algorithm simply fails. This can be easily noticed in the detailed results of Figure 7.1. While the mean length-to-radius values agreed with the one measured in morphology, the outlays in Figure 7.1(c) were very large and did not agree with the morphological measurements of Weibel [154]. To solve this problem, the length-to-radius ratio is restricted to the values reported in [154] and four trails are performed: the first three trials the length-to-radius ratio is not allowed to exceed 6.5, 7.5 and 15, whereas in the last trail the length-to-radius ratio is not restricted. The results of the four trials are shown in Figure 7.2. It is observed that the restrictions have prohibited the airway tree from filling the lobar space in general and the concave regions in particular (see the bottom part of the lung in Figure 7.2(a-c)).

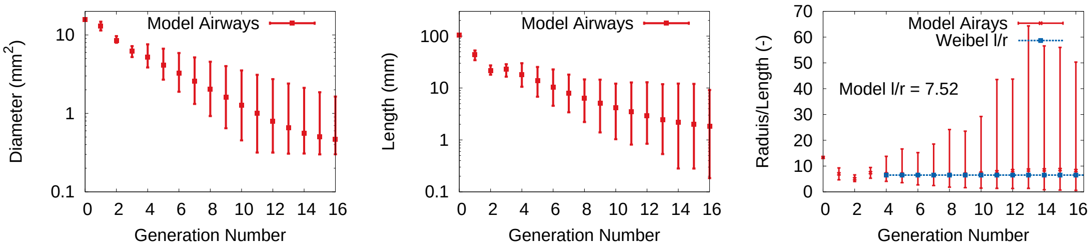

(a) (b) (c)

Figure 7.1.: Generated conducting airway (a) diameters, (b) lengths and (c) length-to-radius ratios.

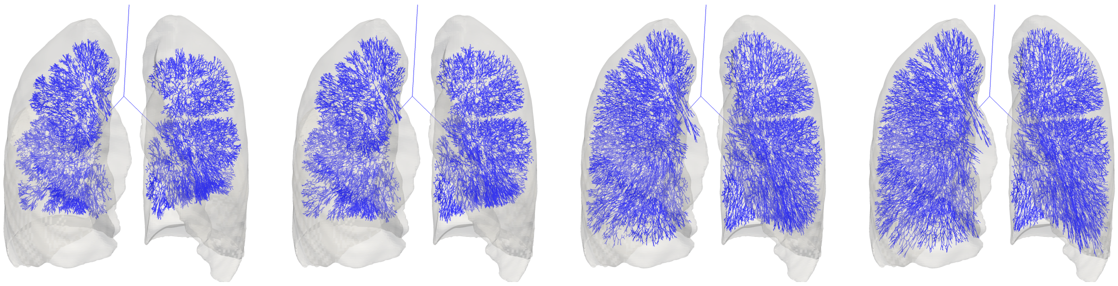

(a) (b) (c) (d)

An alternative solution would be to grow the tree in a bottom-up style. This means that firstly the acini are evenly distributed evenly among the lung lobes, then the tree is built bottom-up starting from the acini and ending at the lobar inlet. However, such a model defies morphology and anatomy of human lungs. It is important to note that the morphogenesis of airways develops from center to periphery while lungs are growing [152]. This means that, in principle, the model of Tawhai [137] does indeed mimic the morphogenesis of airways, however is not suitable for lungs with concave surfaces (i.e. with low lung volume). As such, the author suggests the following approach to be further investigated

1. Fill the lung lobes with evenly distributed cloud of points.
2. Grow the lung using the algorithm of Section 2.2.
3. Use the images registration method of Glaunés et al. [51] to match the terminal point with the evenly distributed clouds.
4. Model the airways as elastic bar elements.
5. Stretch the airway tree from the terminal airway nodes to there corresponding image registered nodes.

It would also make more sense to make the airway ”bar elements” more stiff towards the terminals and less stiff the lower the airway generation number is. That is because, lower generation numbers have larger variations among their length-to-radius ratios [154].

A. Numerical discretization of the 3D flow domain

The 3D flow domain is solved using the residual-based variational multiscale finite element method (RBVMM) of Gravemeier et al. [52] for the incompressible Navier-Stokes. The RBVMM is formulated from eq (3.1) and eq (3.2) as follows: find $p^h \in \mathcal{S}_p^h$ and $\mathbf{u}^h \in \mathcal{S}_{\mathbf{u}}^h$ such that

$$\left(q^h, \nabla \cdot \mathbf{u}^h\right)_\Omega + \sum_{e=1}^{n_{\text{el}}} \left(\nabla q^h, \tau_{\text{Mp}} \mathcal{R}_{\text{M}}^h\right)_{\Omega^e} = 0 \quad \forall\, q^h \in \mathcal{V}_p^h \tag{A.1}$$

$$\begin{aligned}
&\left(\mathbf{v}^h, \frac{\partial \mathbf{u}^h}{\partial t}\right)_\Omega + \left(\mathbf{v}^h, \mathbf{u}^h \cdot \nabla \mathbf{u}^h\right)_\Omega - \left(\nabla \cdot \mathbf{v}^h, p^h\right)_\Omega \\
&+ \left(\varepsilon\left(\mathbf{v}^h\right), 2\nu\varepsilon\left(\mathbf{u}^h\right)\right)_\Omega - \left(\mathbf{v}^h, u_n^h \mathbf{u}^h\right)_{\Gamma_{\text{N}}^{\text{in}}} \\
&+ \sum_{e=1}^{n_{\text{el}}} \left(\nabla \cdot \mathbf{v}^h, \tau_{\text{C}} \mathcal{R}_{\text{C}}^h\right)_{\Omega^e} + \sum_{e=1}^{n_{\text{el}}} \left(\mathbf{u}^h \cdot \nabla \mathbf{v}^h, \tau_{\text{Mu}} \mathcal{R}_{\text{M}}^h\right)_{\Omega^e} \\
&= \left(\mathbf{v}^h, \mathbf{f}\right)_\Omega + \left(\mathbf{v}^h, \mathbf{h}\right)_{\Gamma_{\text{N}}} \quad \forall\, \mathbf{v}^h \in \mathcal{V}_{\mathbf{u}}^h,
\end{aligned} \tag{A.2}$$

where q^h and $\mathbf{v}^h$ are weighting functions introduced for pressure and velocity, respectively. The weighting and solution function spaces are denoted by $\mathcal{V}_p^h$, $\mathcal{V}_{\mathbf{u}}^h$, $\mathcal{S}_p^h$, and $\mathcal{S}_{\mathbf{u}}^h$. Furthermore, $(\cdot,\cdot)$ denotes the L_2-inner products over various domains and boundaries in (A.1)-(A.2). The domain Ω is discretized by n_{el} finite elements Ω^e with characteristic element length h.

The crucial term for that must be taken into account during n- or outflow Neumann boundaries is the second term in the second line of eq (A.2), which came naturally from integration by part and is only active at inflow boundaries. The reader is referred to the work of Gravemeier et al. [53] and Hughes et al. [64] for a more detailed derivation of this term. Note that this term is usually not included, since there usually is no Neumann part of the inflow boundary $\Gamma_{\text{N}}^{\text{in}}$. The difference of the present formulation and the one proposed by Kim et al. [74] is that they used the traction according to eq (3.4) instead of the total momentum flux according to eq (3.5).

Additionally, a Pressure-Stabilizing Petrov-Galerkin (PSPG) (second term on left-hand side in eq (A.1)), a grad-div, and a Streamline Upwind Petrov-Galerkin (SUPG) term (third line in eq (A.2)) are included. The definitions for stabilization parameters τ_{C}, τ_{Mp}, and τ_{Mu} used in this study are the same as the ones used by Gravemeier et al. [53].

B. Numerical discretization of 1D pipe flow domain

Eq (3.11) and eq (3.12) are solved using the second order Taylor-Galerking finite element method, which in turn is equivalent to Lax-Wendroff method in finite difference [33]. This is achieved by discretizing the 1D degrees of freedom, ($\mathbf{U}$) in eq 3.12, in time using Taylor expansion for $\mathbf{U}^{n+1}$, where $n = 0$, 1, ..., Δt is the time step size, and $t^n = n\Delta t$. The truncated Taylor series of $\mathbf{U}^{n+1}$ yielded the following

$$\mathbf{U}^{n+1} = \mathbf{U}^n + \Delta t \left(\frac{\partial \mathbf{U}}{\partial t}\right)^n + \frac{\Delta t^2}{2}\left(\frac{\partial^2 \mathbf{U}}{\partial t^2}\right)^n + \mathcal{O}\left(\Delta t^3\right) \tag{B.1}$$

Substituting eq (3.12) in eq (B.1) yielded

$$\mathbf{U}^{n+1} = \mathbf{U}^n + \Delta t \left(\frac{\partial \mathbf{F}^n_{LW}}{\partial x} + \mathbf{S}^n_{LW}\right) - \frac{\Delta t^2}{2}\left[\mathbf{S}^n_{\mathbf{U}}\frac{\partial \mathbf{F}^n}{\partial x} - \frac{\partial}{\partial x}\left(\mathbf{H}^n\frac{\partial \mathbf{F}^n}{\partial x}\right)\right] \tag{B.2}$$

where

$$\mathbf{F}^n_{LW} = \mathbf{F}^n + \frac{\Delta t}{2}\mathbf{H}^n\mathbf{S}^n \quad ; \quad \mathbf{S}^n_{LW} = \mathbf{S}^n + \frac{\Delta t}{2}\mathbf{S}^n_{\mathbf{U}}\mathbf{S}^n$$

and

$$\mathbf{S}^n_{\mathbf{U}} = \frac{\partial \mathbf{S}}{\partial \mathbf{U}}^n .$$

Spatially, eq (B.1) is discretized using Galerking finite-element method as following: Let an artery with length l, i.e. $x \in [0, l]$, be divided into N elements with $[x_i, xi + 1]$ nodes, where $i = 0, 1, \ldots N$ and $x_{i+1} = x_i + l_i$, such that $\sum_{i=0}^{N-1} l_i = l$, where l_i is the local element size. Let V_h be the space of piece wise linear finite-element functions and $\mathbf{V}_h = [V_h]^2$, while $\mathbf{V}^0_h = \{\mathbf{v}_h \in \mathbf{V}_h | \mathbf{v}_h = \mathbf{0}$ at $x = 0$ and $x = l\}$. Let $\mathbf{L}^2\left(0, l\right)$ be the scalar product defined as

$$\langle \mathbf{u}, \mathbf{v}\rangle_{\Omega_i} = \int_{x_i}^{x_{i+1}} \mathbf{u} \cdot \mathbf{v} dz$$

$$\begin{aligned}\langle \mathbf{U}^{n+1}_l, \psi_l\rangle_{\Omega_e} = \quad & \langle \mathbf{U}^n_l, \psi_l\rangle_{\Omega_e} + \Delta t \langle \mathbf{F}_{LW}\left(\mathbf{U}^n_l\right), \tfrac{d\psi_l}{dx}\rangle_{\Omega_e} - \tfrac{\Delta t^2}{2}\langle \mathbf{S}_{\mathbf{U}}\left(\mathbf{U}^n_l\right) \tfrac{\partial F\left(\mathbf{U}^n_l\right)}{\partial x}, \psi_l\rangle_{\Omega_e} \\ & - \tfrac{\Delta t^2}{2}\langle \mathbf{H}\left(\mathbf{U}^n_l\right) \tfrac{\partial \mathbf{F}\left(\mathbf{U}^n_l\right)}{\partial x}, \tfrac{d\psi_l}{dx}\rangle_{\Omega_e} + \Delta t \langle \mathbf{S}_{LW}\left(\mathbf{U}^n_l\right), \psi_l\rangle_{\Omega_e},\end{aligned}$$

where $\psi_l \in \mathbf{V}^0_l$ is a weighting function.

C. Numerical discretization of 0D pipe flow domain

All of the 0D pipe models are discretized in time using backward Euler scheme

R model

Each 0D resistive element (R) is discretized as following

$$\Delta P^{n+1} = R_{\mu}^{n+1} Q^{n+1},$$

thus yielding the following FEM problem

$$\begin{bmatrix} \frac{-1}{R_{\mu}^{n+1}} & \frac{1}{R_{\mu}^{n+1}} \\ \frac{1}{R_{\mu}^{n+1}} & \frac{-1}{R_{\mu}^{n+1}} \end{bmatrix} \begin{bmatrix} P_{\text{in}} \\ P_{\text{out}} \end{bmatrix}^{n+1} = \begin{bmatrix} -Q \\ Q \end{bmatrix}^{n+1}.$$

RC model

Each 0D complaint-resistive element (RC) is discretized as following

$$\begin{cases} C\frac{\left(P_{\text{in}}^{n+1}-P_{\text{in}}^{n}\right)}{\Delta t} - C\frac{\left(\tilde{P}^{n+1}-\tilde{P}^{n}\right)}{\Delta t} + Q_{\text{out}}^{n+1} - Q_{\text{in}}^{n+1} = 0 \\ R_{\mu}^{n+1} Q_{\text{out}}^{n+1} + P_{\text{out}}^{n+1} - P_{\text{in}}^{n+1} = 0 \end{cases}$$

thus yielded the following FEM model:

$$\begin{bmatrix} \frac{-1}{R_{\mu}^{n+1}} - \frac{C}{\Delta t} & \frac{1}{R_{\mu}^{n+1}} \\ \frac{1}{R_{\mu}^{n+1}} & \frac{-1}{R_{\mu}^{n+1}} \end{bmatrix} \begin{bmatrix} P_{\text{in}} \\ P_{\text{out}} \end{bmatrix}^{n+1} = \begin{bmatrix} -Q_{\text{in}}^{n+1} - \frac{C}{\Delta t}\left(\tilde{P}^{n+1} - \tilde{P}^{n}\right) - \frac{C}{\Delta t}\left(P_{\text{in}}^{n}\right) \\ Q_{\text{out}}^{n+1} \end{bmatrix}.$$

RLC model

Each 0D inductive complaint-resistive element (RLC) is discretized as following

$$\begin{cases} C\frac{\left(P_{\text{in}}^{n+1}-P_{\text{in}}^{n}\right)}{\Delta t} - C\frac{\left(\tilde{P}^{n+1}-\tilde{P}^{n}\right)}{\Delta t} + Q_{\text{out}}^{n+1} - Q_{\text{in}}^{n+1} = 0 \\ I\frac{Q_{\text{out}}^{n+1}-Q_{\text{out}}^{n}}{\Delta t} + R_{\mu}^{n+1} Q_{\text{out}}^{n+1} + P_{\text{out}}^{n+1} - P_{\text{in}}^{n+1} = 0 \end{cases}$$

thus yielded the following FEM model:

$$\begin{bmatrix} \frac{-1}{R_\mu^{n+1}+I/\Delta t}-\frac{C}{\Delta t} & \frac{1}{R_\mu^{n+1}+I/\Delta t} \\ \frac{1}{R_\mu^{n+1}+I/\Delta t} & \frac{-1}{R_\mu^{n+1}+I/\Delta t} \end{bmatrix} \begin{bmatrix} P_{\text{in}} \\ P_{\text{out}} \end{bmatrix}^{n+1} =$$

$$\begin{bmatrix} -Q_{\text{in}}^{n+1}+Q_{\text{out}}^{n}\frac{I}{I+\Delta t R_\mu^{n+1}}-\frac{C}{\Delta t}\left(\tilde{P}^{n+1}-\tilde{P}^{n}\right)-\frac{C}{\Delta t}\left(P_{\text{in}}^{n}\right) \\ Q_{\text{out}}^{n+1}-\frac{I}{I+\Delta t R_\mu^{n+1}} \end{bmatrix}.$$

RLC-viscous model

Each 0D visco-elastic inductive complaint-resistive element (RLC-visc) is discretized as following:

$$\begin{cases} C\frac{\left(P_{\text{in}}^{n+1}-P_{\text{in}}^{n}\right)}{\Delta t}-C\frac{\left(\tilde{P}^{n+1}-\tilde{P}^{n}\right)}{\Delta t}-C\frac{\left(R_{\text{vis}}^{n+1}Q_{\text{in}}^{n+1}-R_{\text{vis}}^{n+1}Q_{\text{in}}^{n+1}\right)}{\Delta t}+C\frac{\left(R_{\text{vis}}^{n+1}Q_{\text{out}}^{n+1}-R_{\text{vis}}^{n+1}Q_{\text{out}}^{n+1}\right)}{\Delta t}+Q_{\text{out}}^{n+1}-Q_{\text{in}}^{n}=0 \\ I\frac{Q_{\text{out}}^{n+1}-Q_{\text{out}}^{n}}{\Delta t}+R_\mu Q_{\text{out}}^{n+1}+P_{\text{out}}^{n+1}-P_{\text{in}}^{n+1}=0 \end{cases}$$

thus yielded the following FEM model:

$$\begin{bmatrix} \frac{-C}{K_{\text{vis}}}-\frac{1}{K_{\text{I}}} & \frac{1}{K_{\text{I}}} \\ \frac{1}{K_{\text{I}}} & \frac{-1}{K_{\text{I}}} \end{bmatrix} \begin{bmatrix} P_{\text{in}} \\ P_{\text{out}} \end{bmatrix}^{n+1} =$$

$$\begin{bmatrix} -Q_{\text{in}}^{n+1}+Q_{\text{out}}^{n}\left(\frac{-CR_{\text{vis}}}{\Delta t K_{\text{vis}}}+\frac{I}{\Delta t K_{\text{I}}}\right)+Q_{\text{in}}^{n}\left(\frac{CR_{\text{vis}}}{\Delta t K_{\text{I}}}\right)-\frac{C}{K_{\text{vis}}}\left(\frac{\tilde{P}^{n+1}-\tilde{P}^{n}}{\Delta t}\right)+P_{\text{in}}^{n}\left(\frac{-C}{\Delta t K_{\text{vis}}}\right) \\ Q_{\text{out}}^{n+1}-\frac{I}{\Delta t K_{\text{I}}}Q_{\text{out}}^{n}, \end{bmatrix}$$

where

$$K_{\text{I}}=\frac{I}{\Delta t}+R_\mu$$

and

$$K_{\text{vis}}=1+\frac{CR_{\text{vis}}}{\Delta t}.$$

D. Numerical discretization of 0D parenchyma domain

The parenchyma is also discretized using time implicit backward Euler.

D.1. 0D acinus

Discretizing eq (3.26) in time yielded:

$$N_{\mathrm{ad}} K_p^{n+1} P_{\mathrm{tp}}^{n+1} + N_{\mathrm{ad}} K_p^{n} P_{\mathrm{tp}}^{n+1} = K_q^{n+1} Q^{n+1} + K_q^{n} Q^{n} + N_{\mathrm{ad}} P_{\mathrm{nonlin}},$$

where

$$P_{\mathrm{nonlin}} = \frac{B}{E_2} \frac{\mathrm{d}P_{\mathrm{E}_1}}{\mathrm{d}t} + P_{\mathrm{E}_1} \tag{D.1}$$

and

$$\begin{aligned} K_p^{n+1} &= \frac{B}{E_2 \Delta t} + 1 \quad ; \quad K_p^{n} = -\frac{B}{E_2 \Delta t} \\ K_q^{n+1} &= \frac{BBa}{E_2 \Delta t} + Ba + B \quad ; \quad K_q^{n} = -\frac{BBa}{E_2 \Delta t} \\ P_{\mathrm{nonlin}} &= \dot{P}_1^{n+1} \frac{B}{E_1} + P_1^{n+1}. \end{aligned}$$

Eq (D.1) is linearized using the Taylor series as:

$$\begin{aligned} P_1^{j+1} &= P_1^{j} + {\frac{\partial P_1}{\partial V_i}}^{j} \left(V_i^{j+1} - V_i^{j}\right) \\ \dot{P}_1^{j+1} &= \dot{P}_1^{j} + {\frac{\partial \dot{P}_1}{\partial V_i}}^{j} \left(V_i^{j+1} - V_i^{j}\right), \end{aligned}$$

where V_i is the volume of an alveolar duct and $\dot{P}_1 = \partial P_1 / \partial t$. The volume of an alveolar duct is discretized as following

$$V_i^{n+1} = \frac{\Delta t}{2} \left(Q_i^{n+1} + Q_i^{n}\right) + V_i^{n}.$$

Finally the linearized eq (3.26) yielded

$$N K_{\mathrm{p}}^{n+1} P^{n+1} + N K_{\mathrm{p}}^{n} P^{n+1} = \left(K_{\mathrm{q}}^{n+1} + K_{\mathrm{lin}}^{n+1}\right) Q^{n+1} + K_{\mathrm{q}}^{n} Q^{n} + N P_{\mathrm{lin}}, \tag{D.2}$$

where

$$\begin{aligned} K_{\text{lin}}^{n+1} &= \left(\frac{\partial {P_1}^j}{\partial V_i} + \frac{B}{E_1} \frac{\partial {\dot{P}_1}^j}{\partial V_i} \right) \left(\frac{\Delta t}{2} \right) \\ P_{\text{lin}} &= P_1^j + \frac{B}{E_1} \dot{P}_1^j + \left(\frac{B}{E_1} \frac{\partial {\dot{P}_1}^j}{\partial V_i} + \frac{\partial {P_1}^j}{\partial V_i} \right) \left(q_i^n \frac{\Delta t}{2} + V_i^n - V_i^j \right). \end{aligned}$$

Finally, eq (3.26) yielded the following FEM model:

$$\mathbf{K}_{\text{ac}} \mathbf{P}^{n+1} = \mathbf{Q}^{n+1} + \mathbf{LHS}^n, \tag{D.3}$$

where

$$\mathbf{K}_{ac} = \begin{bmatrix} -K_{ac} & K_{ac} \\ K_{ac} & -K_{ac} \end{bmatrix}, \ \mathbf{p} = \begin{bmatrix} P_{\text{a}} \\ P_{\text{pl/intr}} \end{bmatrix}, \ \mathbf{Q} = \begin{bmatrix} -Q \\ Q \end{bmatrix}; \ \mathbf{LHS}^n = \begin{bmatrix} -\text{LHS}^n \\ \text{LHS}^n \end{bmatrix}.$$

where

$$K_{ac} = \frac{N K_p^{n+1}}{K_q^{n+1} + K_{\text{lin}}^{n+1}}, \ P_{\text{tp}} = P_{\text{a}} - P_{\text{pl/intr}}$$

and

$$\text{LHS}^n = -\frac{N K_p^n}{K_q^{n+1} + K_{\text{lin}}^{n+1}} P_{\text{tp}}^n + \frac{K_q^n}{K_q^{n+1} + K_{\text{lin}}^{n+1}} Q^n + \frac{N}{K_q^{n+1} + K_{\text{lin}}^{n+1}} P_{\text{lin}}.$$

D.2. 0D inter-acinar linker

Each inter-acinar linker of eq (4.11) yielded the following FEM model:

$$\begin{bmatrix} \frac{1}{N_i^{\text{neig}}} & -\frac{1}{N_j^{\text{neig}}} \\ -\frac{1}{N_i^{\text{neig}}} & \frac{1}{N_j^{\text{neig}}} \end{bmatrix} \begin{bmatrix} P_i \\ P_j \end{bmatrix} = \begin{bmatrix} 0 \\ 0 \end{bmatrix},$$

where N_i^{neig} and N_j^{neig} are the total number of neighborhoods of the inter-acinar linker's points i and j, respectively.

E. Numerical discretization of 0D impedance tree domain

The tree-generated impedance model is originally developed for arterial flow by Olufsen et al. [109]. Comerford et al. [22] extended the impedance model to pulmonary problems. This is achieved by first eliminating the convective terms in eq (3.10) and then linearizing it to yield the following:

$$C\frac{\partial P}{\partial t}+\frac{\partial Q}{\partial t}=0,$$

where C is the capacitance, P pressure and Q volumetric flow rate within a compliant pipe. The airway capacitance is found to be

$$C=\frac{2\pi r_{\mathrm{aw}}^{3}}{E_{\mathrm{aw}}h_{\mathrm{aw}}}, \tag{E.1}$$

where r_{aw} is the airway radius, E_{aw} the airway wall Young's modulus of elasticity and h_{aw} the airway wall thickness. Knowing that flow in lower airways is laminar, a Womersley flow profile is assumed and the upstream impedance of an airway is evaluated from the downstream impedance as

$$Z\left(0,\omega\right)=\frac{ig^{-1}\sin\left(\omega L/c\right)+Z\left(L,\omega\right)\cos\left(\omega L/c\right)}{\cos\left(\omega L/c\right)+igZ\left(L,\omega\right)\sin\left(\omega L/c\right)} \tag{E.2}$$

where $g=C\cdot c$, with wave speed

$$c=\sqrt{\frac{A_0\left(1-F_j\right)}{\rho C}},$$

where F_j is the fraction of first and zeroth Bessel function as calculated from the Womersley solution. The total impedance is recursively summed up from individual impedances as

$$\frac{1}{Z_P}=\frac{1}{Z_L}+\frac{1}{Z_R}, \tag{E.3}$$

where the subscripts P, L, and R stand for parent, left daughter, and right daughter airway branches, respectively. Finally the impedance trees is calculated at the root from which the impedance tree is grown. The impedance is first transformed into the time domain via inverse Fourier transformation:

$$z\left(t\right)=\frac{1}{T}\sum_{-T/2}^{T/2}Z\left(\omega_n\right)e^{i\omega_n t} \tag{E.4}$$

and then the pressure is calculated by the convoluting of flow rate and impedance.

$$P\left(t\right)=\int_{t-\tau}^{\tau}Q\left(t\right)z\left(t-\tau\right)d\tau. \tag{E.5}$$

F. Radial mapping of a non-circular convex surface to circular surface

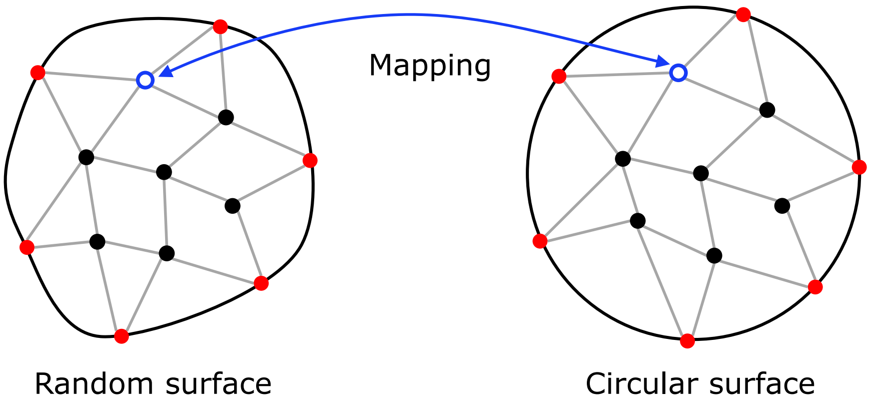
Mapping
Random surface
Circular surface

Figure F.1.: Mapping mesh nodes of a random convex surface onto a circular surface showing border nodes are colored in red, internal nodes colored in black, and a mapped node colored in white and blue.

To map the nodes of a non-circular convex surface onto the a circular surface, the algorithm developed of Mynard and Nithiarasu [101] is used. The mapping algorithm is detailed in Algorithm 6 and illustrated in Figure F.2.

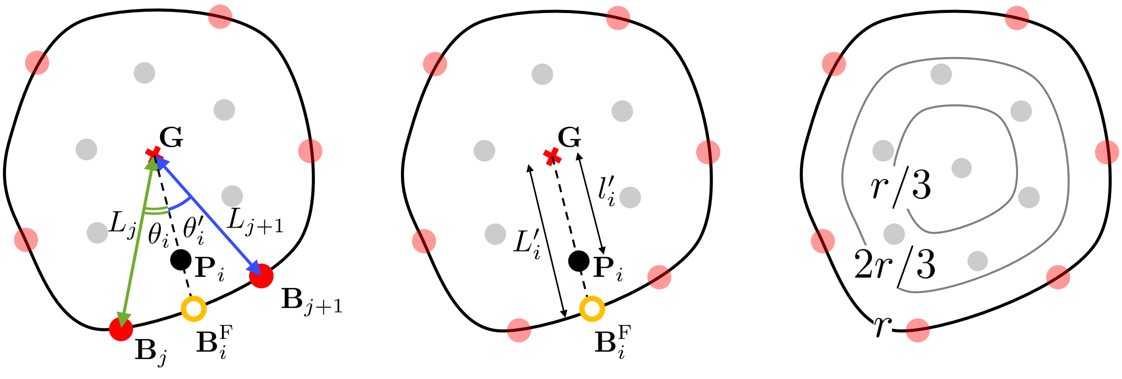
G
L_j
θ_i
θ'_i
L_{j+1}
$\mathbf{P}_i$
$\mathbf{B}_{j+1}$
$\mathbf{B}_j$
$\mathbf{B}_i^\mathrm{F}$
G
l'_i
L'_i
$\mathbf{P}_i$
$\mathbf{B}_i^\mathrm{F}$
$r/3$
$2r/3$
r

(a) (b) (c)

Figure F.2.: Mapping mesh nodes of a random convex surface onto a circular surface via (a) step 1, (b) step 2, and (c) step 3.

Algorithm 6 Map non-circular convex surface onto a circular surface

```
Evaluate surface area ($A$) of the noncircular geometry
Evaluate average surface radius $r = \sqrt{A/\pi}$
Find the center of mass $\mathbf{G}$
loop Loop over all nodes
    Detect boundary nodes (see red nodes in Figure F.2(a))
end loop
loop over all internal nodes
    Get node $\mathbf{P}_i$
    Find 2 neighboring boarder nodes ($\mathbf{B}_j$ and $\mathbf{B}_{j+1}$), such that $\mathbf{P}_i$ is inside $\triangle(\mathbf{G}, \mathbf{B}_j, \mathbf{B}_{j+1})$ (see Figure F.2(a))
    Evaluate $\theta_i = \angle(\mathbf{B}_j, \mathbf{G}, \mathbf{P}_i)$ and $\theta'_i = \angle(\mathbf{B}_{j+1}, \mathbf{G}, \mathbf{P}_i)$
    Find distances $L_j = |\mathbf{G} - \mathbf{B}_j|_2$ and $L_{j+1} = |\mathbf{G} - \mathbf{B}_{j+1}|_2$ (see Figure F.2(b))
    Find a fictitious boundary node $\mathbf{B}^{\mathrm{F}}_i = \left(\frac{\theta'}{\theta+\theta'}\right)\mathbf{B}_j + \left(\frac{\theta}{\theta+\theta'}\right)\mathbf{B}_{j+1}$
    Evaluate $L'_i = \left|\mathbf{B}^{\mathrm{F}}_i - \mathbf{G}\right|_2$ and $l'_i = |\mathbf{P}_i - \mathbf{G}|_2$ and
    Set the radial coordinate of $\mathbf{P}_i$ to $r_i = \left(\frac{l'_i}{L'_i}\right) r$ (see Figure F.2(c))
end loop
```

Bibliography

[1] J. Alastruey, *Numerical modelling of pulse wave propagation in cardiovascular system: development, validation and clinical apptications*, Ph.D. thesis, Departments of Aeronautics and Bioengineering, Imperial College London (2006).

[2] J. Alastruey, K. Parker, J. Peiro, S. Byrd, S. Sherwin, *Modelling the circle of willis to assess the effects of anatomical variations and occlusions on cerebral flows*, Journal of Biomechanics **40** (2007) 1794–1805.

[3] J. Alastruey, K.H. Parker, J. Peiró, S.J. Sherwin, *Lumped parameter outflow models for 1-D blood flow simulations: Effect on pulse waves and parameter estimation*, Communications in Computational Physics **4** (2008) 317–336.

[4] American Thoracic Society, European Society of Intensive Care Medicine, Societé de Réanimation Langue Française, *International consensus conferences in intensive care medicine. ventilator-associated lung injury in ARDS*, Intensive Care Medicine **25** (1999) 1444–1452.

[5] A. Avolio, *Multi-branched model of the human arterial system*, Medical & Biological Engineering & Computing **18** (1980) 709–718.

[6] U. Barkow, A. Strohmaier, *CT-images*, Tech. rep., Medical Office Diagnostische Radiologie, Stuttgart, Germany (2007).

[7] J. Bates, K. Lutchena, *The interface between measurement and modeling of peripheral lung mechanics*, Respiratory Physiology and Neurobiology **148** (2005) 153–164.

[8] J.H.T. Bates, *Lung Mechanics: An Inverse Modeling Approach*, Cambridge University Press, 2009.

[9] Y. Bazilevs, J.R. Gohean, T.J. Hughes, R.D. Moser, Y. Zhang, *Patient-specific isogeometric fluid-structure interaction analysis of thoracic aortic blood flow due to implantation of the Jarvik 2000 left ventricular assist device*, Computer Methods Applied Mechanics and Engineering **198** (2009) 3534–3550.

[10] C. Bertoglio, A. Caiazzo, *A tangential regularization method for backflow stabilization in hemodynamics*, Journal of Computational Physics **In press** (2014) n.a–n.a.

[11] C. Bertoglio, A. Caiazzo, M.A. Fernandez, *Fractional-step schemes for the coupling of distributed and lumped models in hemodynamics*, SIAM Journal on Scientific Computing **35** (2013) B551B575.

[12] C. BERTOGLIO, P. MOIREAU, J.F. GERBEAU, *Sequential parameter estimation for fluidstructure problems: Application to hemodynamics*, International Journal for Numerical Methods in Biomedical Engineering **28** (2012) 4.

[13] P.J. BLANCO, R.A. FEIJÒO, S.A. URQUIZA, *A unified variational approach for coupling 3D–1D models and its blood flow applications*, Computer Methods in Applied Mechanics and Engineering **196** (2007) 4391–4410.

[14] P.J. BLANCO, S.A. URQUIZA, R.A. FEIJÒO, *Assessing the influence of heart rate in local hemodynamics through coupled 3D-1D-0D modelsbraack2007*, International Journal for Numerical Methods in Biomedical Engineering **26** (2010) 890–903.

[15] M. BRAACK, E. BURMAN, V. JOHN, G. LUBE, *Stabilized finite element methods for the generalized oseen problem*, Computer Methods in Applied Mechanics and Engineering **196** (2007) 853–866.

[16] J.S. BRODY, E.J. STEMMLER, A.B. DUBOIS, *Longitudinal distribution of vascular resistance in the pulmonary arteries, capillaries, and veins*, The Journal of Clinical Investigation **47** (1968) 783–799.

[17] R.K. CALAY, J. KURUJAREON, A.E. HOLDO, *Numerical simulation of respiratory flow patterns within human lung*, Respiratory Physiology **130** (2002) 201–221.

[18] D. CARNEY, J. DIROCCO, G. NIEMAN, *Dynamic alveolar mechanics and ventilator-induced lung injury*, Critical care medicine **33** (2005) S122–S128.

[19] D. CHEMLA, V. CASTELAIN, M. HUMBERT, J.L. HÉBERT, G. SIMONNEAU, Y. LECARPENTIER, P. HERVÉ, *New formula for predicting mean pulmonary artery pressure using systolic pulmonary artery pressure*, CHEST Journal **126** (2004) 1313–1317.

[20] J.J. COALSON, R.J. KING, V.T. WINTER, T.J. PRIHODA, A.R. ANZUETO, J.I. PETERS, W.G. JOHANSON, *O2- and pneumonia-induced lung injury. i. pathological and morphometric studies*, Journal of Applied Physiology **67** (1989) 346–356.

[21] A. COMERFORD, G. BAUER, W.A. WALL, *Nanoparticle transport in a realistic model of the tracheobronchial region*, International Journal for Numerical Methods in Biomedical Engineering **26** (2010) 904–914.

[22] A. COMERFORD, C. FÖRSTER, W.A. WALL, *Structured tree impedance outflow boundary conditions for 3D lung simulations*, Journal of Biomechanical Engineering **132** (2010) 081002.

[23] A. COMERFORD, V. GRAVEMEIER, W.A. WALL, *An algebraic variational multiscalemultigrid method for large-eddy simulation of turbulent pulsatile flows in complex geometries with detailed insight into pulmonary airway flow*, International Journal for Numerical Methods in Fluids **71** (2013) 1207–1225.

[24] M. Cressoni, P. Cadringher, C. Chiurazzi, M. Amini, E. Gallazzi, A. Marino, M. Brioni, E. Carlesso, D. Chiumello, M. Quintel, G. Bugedo, L. Gattinoni, *Lung inhomogeneity in patients with acute respiratory distress syndrome*, American Journal of Respiratory and Critical Care Medicine **189** (2014) 149–158.

[25] J.W. De Backer, W.G. Vos, C.D. Gorle, P. Germonpré, B. Partoens, F.L. Wuyts, P.M. Parizel, W. De Backer, *Flow analyses in the lower airways: patient-specific model and boundary conditions.*, Medical Engineering and Physics Journal **30** (2008) 872.

[26] S.F. de Marchi, M. Bodenmüller, D.L. Lai, C. Seiler, *Pulmonary venous flow velocity patterns in 404 individuals without cardiovascular disease*, Heart **85** (2001) 23–29.

[27] E. Denny, R.C. Schroter, *The mechanical behavior of mammalian lung alveolar duct model*, Journal of Biomechanical Engineering **117** (1995) 254–261.

[28] E. Denny, R.C. Schroter, *Relationships between alveolar size and fiber distribution in a mammalian lung alveolar duct model*, Journal of Biomechanical Engineering **119** (1997) 289–297.

[29] E. Denny, R.C. Schroter, *Viscoelastic behavior of a lung alveolar duct model*, Journal of Biomechanical Engineering **122** (2000) 143–151.

[30] M. Denny, *Air and Water: The biology and Physics of Life's Media*, Princeton University, 1993.

[31] K. DeVault, A.G. Pierre, V. Novak, S.O. Mette, G. Vernières, P. Zhao, *Blood flow in the circle of willis: Modeling and calibration*, Multiscale Model Simulation **7** (2008) 888–909.

[32] J.D. DiRocco, L.A. Pavone, D.E. Carney, C.J. Lutz, L.A. Gatto, S.K. Landas, G.F. Nieman, *Dynamic alveolar mechanics in four models of lung injury*, Intensive Care Medicine **32** (2006) 140–148.

[33] J. Donea, *A taylor-galerkin method for convective transport problem*, International Journal for Numerical Methods in Engineering **20** (1984) 101–119.

[34] A. Donovan, *Antoine Lavoisier: Science, Administration and Revolution*, vol. 5, Cambridge University Press, 1996.

[35] M.A. Fernandez, V. Milsic, A. Quarteroni, *Analysis of a geometrical multiscale blood flow model based on the coupling of odes and hyperbolic pdes*, Multiscale Modeling and Simulation **4** (2005) 215–236.

[36] C.A. Figueroa, C.A. Taylor, V. Yeh, A.J. Chiou, C.K. Zarins, *Effect of curvature on displacement forces acting on aortic endografts: a three dimensional computational analysis*, Journal of Endovascular Therapy **16** (2009) 284–294.

[37] L. Formaggia, J.F. Gerbeau, F. Nobile, A. Quarteroni, *On the coupling of 3D and 1D Navier-Stokes equation for flow problems in compliant vessels*, Computer Methods in Applied Mechanics and Engineering **191** (2001) 561–582.

[38] L. Formaggia, D. Lamponi, A. Quarteroni, *One-dimensional models for blood flow in arteries*, Journal of Engineering Mathematics **47** (2003) 251–276.

[39] L. Formaggia, A. Moura, F. Nobile, *On the stability of the coupling of 3D and 1D fluid-structure interaction models for blood flow simulations*, ESAIM: M2AN **41** (2007) 743–769.

[40] L. Formaggia, A. Moura, F. Nobile, *On the stability of the coupling of 3D and 1D fluid-structure interaction models for blood flow simulations*, ESAIM: M2AN **41** (2007) 743–769.

[41] L. Formaggia, F. Nobile, A. Quarteroni, A. Veneziani, *Multiscale modelling of the circulatory system: a preliminary analysis*, Computing and Visualization in Science **2** (1999) 75–83.

[42] R.K. Freitas, W. Schröder, *Numerical investigation of the three-dimensional flow in a human lung model*, Journal of Biomechanics **41** (2008) 2446–2457.

[43] Y.C. Fung, *Biomechanics. Motion, Flow, Stress and Growth*, Springer-Verlag, New York, 1990.

[44] T.C. Gasser, G.A. Holzapfel, *Modeling plaque fissuring and dissection during balloon angioplasty interventiongee*, Annals of Biomedical Engineering **35** (2007) 711–723.

[45] M.W. Gee, C. Förster, W.A. Wall, *A computational strategy for prestressing patient specific biomechanical problems under finite deformation*, International Journal for Numerical Methods in Biomedical Engineering **26** (2010) 52–72.

[46] M.W. Gee, U. Küttler, W.A. Wall, *Truly monolithic algebraic multigrid for fluid-structure interaction*, International Journal for Numerical Methods in Engineering **85** (2010) 987–1016.

[47] M.W. Gee, C. Reeps, H.H. Eckstein, W.A. Wall, *Prestressing in finite deformation abdominal aortic aneurysm simulation*, Journal of Biomechanics **42** (2009) 1732–1739.

[48] T. Gemcia, V. Ponyavin, Y. Chena, H. Chen, R. Collins, *Computational model of airflow in upper 17 generations of human respiratory tract*, Journal of Biomechanics **41** (2008) 2047–2054.

[49] F. Gentile, A. Manterof, A. Lippolis, M. Ornaghi, M. Azzollinii, P. Barbier, L. Beretta, F. Casazza, R. Cornof, F. Faletraf, E. Giagnoni, C. Gualtierottitt, S. Lombrosoff, R. Mattioli, A. Morabito, M. Pepi, S. Todd, A. Pezzanof, *An echo 2d colour doppler cooperative study*, European Heart Journal **18** (1997) 148–164.

[50] H.L. GILLIS, K.R. LUTCHEN, *How heterogeneous bronchoconstriction affects ventilation distribution in human lungs: A morphometric model*, Annals of Biomedical Engineering **27** (1999) 14–22.

[51] J. GLAUNÈS, A. TROUVÉ, L. YOUNES, *Diffeomorphic matching of distributions: A new approach for unlabelled point-sets and sub-manifolds matching*, IEEE Computer Society Conference on Computer Vision and Pattern Recognition **2** (2004) 712–718.

[52] V. GRAVEMEIER, W.A. WALL, *Residual-based variational multiscale methods for laminar, transitional and turbulent variable-density flow at low mach number*, International Journal for Numerical Methods in Fluids **65** (2011) 1260–1278.

[53] V. GRAVEMEIER, L. YOSHIHARA, A. COMERFORD, M. ISMAIL, W.A. WALL, *A novel formulation for Neumann inflow boundary conditions in biomechanics*, International Journal for Numerical Methods in Biomedical Engineering **28** (2012) 560–573.

[54] A.S. GREEN, *Modelling peak-flow wall shear stress in major airways of the lung*, Journal of Biomechanics **37** (2004) 661–667.

[55] O.C. GRUNER, *A treatise on the Canon of medicine of Avicenna: incorporating a translation of the first book*, Luzac, 1973.

[56] A.C. GUYTON, J.E. HALL, *Medical Physiology*, Elsevier Saunders, 2005.

[57] R. HARRIS, *Pressure-volume curves of the respiratory system*, Respiratory Care **50** (2005) 78–99.

[58] K.C. HIGH, J.S. ULTMAN, S.R. KARL, *Mechanically induced pendelluft flow in a model airway bifurcation during high frequency oscillation*, Journal of Biomechical Engineering **113** (1991) 342–347.

[59] R. HOLLINGHAM, *Blood and Guts: A History of Surgery*, Random House, 2008.

[60] K. HORSFIELD, G. DART, D.E. OLSON, G.F. FILLEY, G. CUMMING, *Models of the human bronchial tree*, Journal of Applied Physiology **31** (1971) 207–217.

[61] W. HUANG, R.T. YEN, M. MCLAURINE, G. BLEDSOE, *Morphometry of the human pulmonary vasculature*, Journal of Applied Physiology **81** (1996) 2123–2133.

[62] R.D. HUBMAYR, *Perspective on lung injury and recruitment: a skeptical look at the opening and collapse story.*, American Journal of Respiratory and Critical Care Medicine **165** (2002) 1647–53.

[63] T.J.R. HUGHES, L.P. FRANCA, M. HULBERT, *A new finite element formulation for computational fluid dynamics: VIII. the Galerkin/least-squares method for advective-diffusive equations*, Computer Methods in Applied Mechanics and Engineering **73** (1989) 173–189.

[64] T.J.R. HUGHES, G.N. WELLS, *Conservation properties for the Galerkin and stabilised forms of the advection-diffusion and incompressible Navier-Stokes equations*, Computer Methods in Applied Mechanics and Engineering **194** (2005) 1141–1159.

[65] J.D. HUMPHREY, C.A. TAYLOR, *Intracranial and abdominal aortic aneurysms: Similarities, differences, and need for a new class of computational models*, Annual Review of Biomedical Engineering **10** (2008) 221–46.

[66] M. ISMAIL, A. COMERFORD, W.A. WALL, *Coupled and reduced dimensional modelling of respiratory mechanics during spontaneous breathing*, International Journal for Numerical Methods in Biomedical Engineering **in press** (2013) n.a–n.a.

[67] M. ISMAIL, M.W. GEE, W.A. WALL, *Adjoint-based inverse analysis of windkessel parameters of patient-specific vascular models*, Journal of Computational Physics, **244** (2013) 113–130.

[68] M. ISMAIL, V. GRAVEMEIER, A. COMERFORD, W.A. WALL, *A stable approach for coupling multidimensional cardiovascular and pulmonary networks based on a novel pressure-flowrate or pressure-only Neumann boundary condition formulation*, International Journal for Numerical Methods in Biomedical Engineering **in press** (2013) n.a–n.a.

[69] M. ISMAIL, L. YOSHIHARA, C. ROTH, A. COMERFORD, W.A. WALL, *A comprehensive computational human lung model incorporating inter-acinar dependencies: Application to spontaneous breathing and mechanical ventilation*, Journal of Medical Physics **Submitted** (2014) n.a–n.a.

[70] S. ITO, A. MAJUMDAR, H. KUME, K. SHIMOKATA, K. NARUSE, K. LUTCHEN, D. STAMENOVIC, B. SUKI, *Viscoelastic and dynamic nonlinear properties of airway smooth muscle tissue: roles of mechanical force and the cytoskeleton*, Americal Journal of Physiologiy - Lung Cellular and Molecular Physiology **290** (2006) 1227–1237.

[71] S. KABILAN, C.L. LIN, E.A. HOFFMAN, *Characteristics of airflow in a CT-based ovine lung: a numerical study*, Journal of Applied Physiology **102** (2006) 1469–1482.

[72] J. KEENER, J. SNEYD, *Mathematical Physiology*, Springer Verlag, 1998.

[73] H.J. KIM, C.A. FIGUEROA, T.J.R. HUGHES, K.E. JANSEN, C.A. TAYLOR, *Augmented lagrangian method for constraining the shape of velocity profiles at outlet boundaries for three-dimensional finite element simulations of blood flow*, Computer Methods in Applied Mechanics and Engineering **198** (2009) 3551–3566.

[74] H.J. KIM, I.E. VIGNON-CLEMENTEL, C.A. FIGUEROA, J.F. LADISA, K.E. JANSEN, J.A. FEINSTEIN, C.A. TAYLOR, *On coupling a lumped parameter heart model and a three-dimensional finite element aorta model*, Annals of Biomedical Engineering **37** (2009) 2153–69.

[75] J.M. KINSMAN, *The history of the study of respiration*, Presented to the Innominate Society.

[76] C. KLEINSTREUER, Z. ZHANG, *An adjustable triple-bifurcation unit model for air-particle flow simulations in human tracheobronchial airways*, Journal of Biomechanical Engineering **131** (2009) 021007.

[77] C. KLEINSTREUER, Z. ZHANG, Z. LI, W.L. ROBERTS, C. ROJAS, *A new methodology for targeting drug-aerosols in the human respiratory system*, International Journal of Heat and Mass Transfer **51** (2008) 5528–5589.

[78] R. KLINKE, H.C. PAPE, S. SILBERNAGL, *Lehrbuch der Physiologie*, Georg Thieme, 2005.

[79] A.P. KUPRAT, S. KABILAN, J.P. CARSON, R.A. COREY, D.R. EINSTEIN, *A bidirectional coupling procedure applied to multiscale respiratory modeling*, Journal of Computational Physics **244** (2013) 148–167.

[80] U. KÜTTLER, M.W. GEE, C. FÖSTER, A. COMERFORD, W.A. WALL, *Coupling strategies for biomedical fluid-structure interaction problems*, International Journal for Numerical Methods in Biomedical Engineering **26** (2010) 305–321.

[81] R.K. LAMBERT, T.A. WILSON, R.E. HYATT, J.R. RODARTE, *A computational model for expiratory flow*, Journal of Applied Physiology **52** (1982) 44–56.

[82] C.L. LIN, M.H. TAWHAI, G. MCLENNAN, E.A. HOFFMAN, *Characteristics of the turbulent laryngeal jet and its effect on airflow in the human intra-thoracic airways*, Respiratory Physiology and Neurobiology **157** (2007) 295–309.

[83] C.L. LIN, M.H. TAWHAI, G. MCLENNAN, E.A. HOFFMAN, *Computational fluid dynamics: Multiscale simulation of gas flow in subject-specific models of the human lung*, IEEE Engineering in Medicine and Biology Society **28** (2009) 25–33.

[84] Y. LIU, R.M.C. SO, C.H. ZHANG, *Modeling the bifurcating flow in a human lung airway*, Journal of Biomechanics **35** (2002) 465–473.

[85] K.R. LUTCHEN, Z. HANTOS, F. PETAK, A. ADAMICZA, B. SUKI, *Airway inhomogeneities contribute to apparent lung tissue mechanics during constriction*, American Journal of Physiology **80** (1996) 1841–1849.

[86] B. MA, K.R. LUTCHEN, *An anatomically based hybrid computational model of the human lung and its application to low frequency oscillatory mechanics*, Annals of Biomedical Engineering **34** (2006) 1691–1704.

[87] B. MA, B. SUKI, J.H.T. BATES, *Effects of recruitment/derecruitment dynamics on the efficacy of variable ventilation*, Journal of Applied Physiology **110** (2011) 1319–1326.

[88] A. MAIER, M. ESSLER, M.W. GEE, H.H. ECKSTEIN, W.A. WALL, C. REEPS, *Correlation of biomechanics to tissue reaction in aortic aneurysms assessed by nite elements and 18F-fluorodeoxyglucose-PET/CT*, International Journal of Numerical Methods in Biomedical Engineering **28** (2012) 456–471.

[89] A. Maier, M.W. Gee, C. Reeps, H.H. Eckstein, W.A. Wall, *Impact of calcifications on patient-specific wall stress analysis of abdominal aortic aneurysms*, Biomechanics and Modeling in Mechanobiology **9** (2010) 511–521.

[90] A. Maier, M.W. Gee, C. Reeps, J. Pongratz, H.H. Eckstein, W.A. Wall, *A comparison of diameter, wall stress, and rupture potential index for abdominal aortic aneurysm rupture risk prediction*, Annals of Biomedical Engineering **38** (2010) 3124–3134.

[91] A. Majumdar, A.M. Alencar, S.V. Buldyrev, Z. Hantos, K.R. Lutchen, H.E. Stanley, B. Suki, *Relating airway diameter distributions to regular branching asymmetry in the lung*, Physical Review Letters **95** (2005) 168101.

[92] A.C.I. Malossi, P.J. Blanco, S. Deparis, *A two-level time step technique for the partitioned solution of one-dimensional arterial networks*, Computer Methods in Applied Mechanics and Engineering **237240** (2012) 212 – 226.

[93] A.C.I. Malossi, P.J. Blanco, S. Deparis, A. Quarteroni, *Algorithms for the partitioned solution of weakly coupled fluid models for cardiovascular flows*, International Journal for Numerical Methods in Biomedical Engineering **27** (2011) 2035–2057.

[94] G. Marini, A. Maier, C. Reeps, H.H. Eckstein, W.A. Wall, M.W. Gee, *A continuum description of the damage process in the arterial wall of abdominal aortic aneurysms*, International Journal for Numerical Methods in Biomedical Engineering **28** (2012) 87–99.

[95] J. Mead, T. Takishima, D. Leith, *Stress distribution in lungs: a model of pulmonary elasticity*, Journal of applied physiology **28** (1970) 596–608.

[96] M.E. Moghadam, Y. Bazilevs, T.Y. Hsia, I.E. Vignon-Clementel, A.I. Marsden, *A comparison of outlet boundary treatments for prevention of backflow divergence with relevance to blood flow simulations*, Computational Mechanics **48** (2011) 277–291.

[97] M.E. Moghadam, I.E. Vignon-Clementel, R. Figliola, A.I. Marsden, *A modular numerical method for implicit 0D/3D coupling in cardiovascular finite element simulations*, Journal of Computational Physics (2012) 3534–3550.

[98] M. Montaudon, P. Desbarats, P. Berger, G. De Dietrich, R. Marthan, F. Laurent, *Assessment of bronchial wall thickness and lumen diameter in human adults using multi-detector computed tomography: comparison with theoretical models*, Journal of Anatomy **211** (2007) 579–588.

[99] C.D. Murray, *The physiological principle of minimum work applied to the angle of branching of arteries*, The Journal of General Physiology **9** (1926) 835–841.

[100] J.P. Mynard, *One-dimensional blood flow modelling with the locally conservative galerkin (lcg) method*, Master's thesis, school of Engineering at Swansea University (2007).

[101] J.P. Mynard, P. Nithiarasu, *A 1D arterial blood flow model incorporating ventricular pressure, aortic valve and regional coronary flow using the locally conservative Galerkin (lcg) method*, Communications in Numerical Methods in Engineering **24** (2008) 367–417.

[102] P. Nardinicchi, G. Pontrelli, L. Teresi, *A one-dimensional model for blood flow in prestressed vessels*, European Journal of Mechanics A/Solids **24** (2005) 23–33.

[103] C.D. Needham, M.C. Rogan, I. McDonald, *Normal standards for lung volumes, intrapulmonary gas-mixing, and maximum breathing capacity*, Thorax **9** (1954) 313–325.

[104] N. Nowak, P.P. Kakade, A.V. Annapragada, *Computational fluid dynamics simulation of airflow and aerosol deposition in human lungs*, Annals of Biomedical Engineering **31** (2003) 374–390.

[105] G. Nucci, S. Tessarin, C. Cobelli, *A morphometric model of lung mechanics for time-domain analyses of alveolar pressures during mechanical ventilation.*, Annals of Biomedical Engineering **30** (2002) 537–545.

[106] M. Ochs, J.R. Nyengaard, A. Jung, L. Knudsen, M. Voigt, T. Wahlers, J. Richter, H.J.G. Gundersen, *The number of alveoli in the human lung*, American Journal of Respiratory and Critical Care Medicine **169** (2004) 120–124.

[107] M.S. Olufsen, A. Nadim, *On desiving lumped models for blood flow and pressure in the systemic arteries*, Mathematical Biosciences and Engineering **1** (2004) 61–80.

[108] M.S. Olufsen, A. Nadim, L.A. Lipsitz, *Dynamics of cerebral blood flow regulation explained using a lumped parameter model*, American Journal of Physiology Regulatory, Integrative and Comparative Physiology **282** (2002) 611–622.

[109] M.S. Olufsen, C.S. Peskin, W.Y. Kim, E.M. Pedersen, A. Nadim, J. Larsen, *Numerical simulation and experimental validation of blood flow in arteries with structured-tree outflow conditions*, Annals of Biomedical Engineering **28** (2000) 12811299.

[110] T.J. Pedley, *Pulmonary fluid dynamics*, Annual Review of Fluid Mechanics **9** (1977) 229–274.

[111] T.J. Pedley, R.C. Schroter, M.F. Sudlow, *The prediction of pressure drop and variation of resistance within the human bronchial airways*, Respiratory Physiology **9** (1970) 387–405.

[112] M. Probst, M. Lülfesmann, M. Nicolai, M. Bücker, M. Behr, C.H. Bischof, *Sensitivity of optimal shapes of artificial grafts with respect to flow parameters*, Computer Methods in Applied Mechanics and Engineering **199** (2010) 997–1005.

[113] A. Protti, M. Cressoni, A. Santini1, A. Langer, C. Mietto, D. Febres, M. Chierichetti, S. Coppola, S. Conte, G.and Gatti, O. Leopardi, S. Masson, L. Lombardi, M. Lazzerini, E. Rampoldi, P. Cadringher, L. Gattinoni,

Lung stress and strain during mechanical ventilation. any safe threshold?, American Journal of Respiratory and Critical Care Medicine **183** (2011) 1354–1362.

[114] A. QUARTERONI, A. VENEZIANI, *Analysis of a geometrical multiscale model based on the coupling of ode and pde for blood flow simulations*, Multiscale Modeling and Simulation **1** (2003) 173–195.

[115] M. RAGALLER, T. RICHTER, *Acute lung injury and acute respiratory distress syndrome*, Journal of Emergencies, Trauma and Shock **3** (2010) 43–51.

[116] M.L. RAGHAVAN, D.A. VORP, *Toward a biomechanical tool to evaluate rupture potential of abdominal aortic aneurysm: identification of a finite strain constitutive model and evaluation of its applicability*, Journal of Biomechanics **33** (2000) 475–482.

[117] S. RAUSCH, D. HABERTHÜR, M. STAMPANONI, J.C. SCHITTNY, W.A. WALL, *Local strain distribution in real three-dimensional alveolar geometries*, Annals of Biomedical Engineering **39** (2011) 2835–2843.

[118] S. RAUSCH, C. MARTIN, B. BORNEMANN, S. UHLIG, W.A. WALL, *Material model of lung parenchyma based on living precision-cut lung slice testing*, Journal of the Mechanical Behavior of Biomedical Materials **4** (2011) 583–592.

[119] S.M.K. RAUSCH, *Computational and experimental modeling of lung parenchyma*, Ph.D. thesis, Technische Universität München (2012).

[120] C. REEPS, M.W. GEE, A. MAIER, M. GURDAN, H.H. ECKSTEIN, W.A. WALL, *The impact of model assumptions on results of computational mechanics in abdominal aortic aneurysm*, Journal of Vascular Surgery **51** (2010) 679 – 688.

[121] P. REYMOND, F. MERENDA, F. PERREN, D. RÜFENACHT, N. STERGIOPULOS, *Validation of a one-dimensional model of the systemic arterial tree*, Heart and Circulation Physiology - American journal of Physiology **297** (2009) H208–H222.

[122] D.B. REYNOLDS, J.S. LEE, *Modeling study of the pressure-flow relationship of the bronchial tree (abstract)*, Fed. Proc. **38** (1979) 1444.

[123] F. ROHRER, *Flow resistance in human air passages and the effect of irregular branching of the bronchial system on the respiratory process in various regions of the lungs*, Arch Ges Physiol **162** (1915) 225–299.

[124] W. RUAN, *A coupled system of odes and quasilinear hyperbolic pdes arising in a multiscale blood flow model*, Journal of Mathematical Analysis and Applications **343** (2008) 778–798.

[125] S. SHERWIN, L. FORMAGGIA, J. PEIRÓ, V. FRANKE, *Computational modelling of 1D blood flow with variable mechanical properties and its application to the simulation of wave propagation in the human arterial system*, International Journal for Numerical Methods in Fluids **43** (2003) 673–700.

[126] S. SHERWIN, V. FRANKE, J. PEIRÓ, K. PARKER, *One-dimensional modelling of a vascular network in space-time variables*, Journal of Engineering Mathematics **47** (2003) 217–250.

[127] R.L. SPILKER, C.A. TAYLOR, *Tuning multidomain hemodynamic simulations to match physiological measurements*, Annals of Biomedical Engineering **38** (2010) 2635–2648.

[128] J.S. STROUD, S.A. BERGER, D. SALONER, *Numerical analysis of flow through a severely stenotic carotid artery bifurcation*, Journal of Biomechanics Engineering **124** (2002) 9–20.

[129] B. SUKI, J.H.T. BATES, *Lung tissue mechanics as an emergent phenomenon*, journal of Applied Physiology **110** (2011) 1111.

[130] B. SUKI, R.H. HABIB, A.C. JACKSON, *Wave propagation, input impedance, and wall mechanics of the calf trachea from 16 to 1,600 hz*, American Journal of Physiology **75** (1993) 2755–2766.

[131] B. SUKI, A. MAJUMDAR, M.A. NUGENT, J.H.T. BATES, *In silico modeling of interstitial lung mechanics: implications for disease development and repair*, Drug Discovery Today. Disease Models **4** (2007) 139–145.

[132] A. SWILLENS, L. LANOYE, J. DE BACKER, N. STERGIOPULOS, P.R. VERDONCK, F. VERMASSEN, P. SEGERS, *Effect of an abdominal aortic aneurysm on wave reflection in the aorta*, IEEE transactions on biomedical engineering **55** (2008) 1602–1611.

[133] D. TAULBEE, C.P. YU, *A theory of aerosol decomposition in human respiratory tract*, Journal of applied physiology **38** (1975) 77–85.

[134] M.H. TAWHAI, C.L. LIN, *Image-based modeling of lung structure and function*, Journal of Magnetic Resonance Imaging **32** (2010) 1421–1431.

[135] M.H. TAWHAI, M.P. NASH, E.A. HOFFMAN, *An imaging-based computational approach to model ventilation distribution and soft-tissue deformation in the ovine lung.*, Academic Radiology **13** (2006) 113.

[136] M.H. TAWHAI, M.P. NASH, C.L. LIN, E.A. HOFFMAN, *Supine and prone differences in regional lung density and pleural pressure gradients in the human lung with constant shape*, Journal Applied Physiology **107** (2009) 912–920.

[137] M.H. TAWHAI, A.H. PULLAN, P.J. HUNTER, *Generation of an anatomically based three-dimensional model of the conducting airways*, Annals of Biomedical Engineering **28** (2000) 793–802.

[138] C.A. TAYLOR, M.T. DRANEY, J.P. KU, D. PARKER, B.N. STEELE, K. WANG, C.K. ZARINS, *Predictive medicine: computational techniques in therapeutic decision-making*, Computer Aided Surgery **4** (1999) 231–247.

[139] G. THEWS, *Die Sauerstoffdiffusion in der Lunge. Ein Verfahren zur Berechnung der O2-Diffusionszeiten, der Kontaktzeit und des O2-Diffusionsfaktors*, Pflüger's Archiv für die gesamte Physiologie des Menschen und der Tiere **265** (1957) 154–171.

[140] M.I. TOWNSLEY, *Structure and composition of pulmonary arteries, capillaries and viens*, Comprehensive Physiology **2** (2013) 675–709.

[141] S. UHLIG, *Ventilation-induced lung injury and mechanotransduction: stretching it too far?*, American Journal of Physiology - Lung Cellular and Molecular Physiology **282** (2002) 892–896.

[142] U. UHLIG, S. UHLIG, *Comprehensive Physiology*, chap. Ventilation-Induced Lung Injury, John Wiley & Sons, Inc., 2011.

[143] S.A. URQUIZA, P.J. BLANCO, M.J. VENERE, R.A. FEIJOO, *Multidimensional modelling for the carotid artery blood flow*, Computer Methods in Applied Mechanics and Engineering **195** (2006) 4002–4017.

[144] H.B.M. UYLINGS, *Optimization of diameters and bifurcation angles in lung and vascular tree structures*, Bulletin of mathematical biology **39** (1977) 509–520.

[145] V.G. V. MELICHER, *A numerical solution of one dimensional blood flow model - moving grid approach*, Jornal of Computational and Applied Mathematics **215** (2008) 512–520.

[146] J. VALENTIN, *Basic anatomical and physiological data for use in radiological protection: reference values: {ICRP} publication 89*, Annals of the {ICRP} **32** (2002) 1 – 277.

[147] C. VAN ERTBRUGGEN, C. HIRSCH, M. PAIVA, *Anatomically based three-dimensional model of airways to simulate flow and particle transport using computational fluid dynamics*, Journal of Applied Physiology **98(3)** (2005) 970–980.

[148] I. VIGNON-CLEMENTEL, C. FIGUEROA, K. JANSEN, C.A. TAYLOR, *Outflow boundary conditions for three-dimensional finite element modeling of blood flow and pressure in arteries*, Computer Methods in Applied Mechanics and Engineering **195** (2006) 3776–3796.

[149] W.A. WALL, T. RABCZUK, *Fluid structure interaction in lower airways of CT-based lung geometries*, International Journal for Numerical Methods in Fluids **57** (2008) 653–675.

[150] W.A. WALL, L. WIECHERT, A. COMERFORD, S. RAUSCH, *Towards a comprehensive computational model for the respiratory system*, International Journal for Numerical Methods in Biomedical Engineering **26** (2010) 807–827.

[151] J.J. WANG, K. PARKER, *Wave propagation in a model of the arterial circulation*, Journal of Biomechanics **37** (2004) 457–470.

[152] E. WEIBEL, *Symmorphosis: on form and function in shaping life*, Harvard University Press, 2000.

[153] E.R. WEIBEL, *Morphometry of the human lung*, Springer-Verlag, 1963.

[154] E.R. WEIBEL, *The Pathway for oxygen: Structure and Functiona in Mammalian Respiratory System*, Harvard University Press, 1984.

[155] J.B. WEST, *Respiratory Physiology: The Essentials*, Lippincott Williams and Wilkins, 2008.

[156] N. WESTERHOF, J.W. LANKHAAR, B.E. WESTERHOF, *The arterial windkessel*, Journal of Medical and Biological Engineering and Computing **47** (2009) 131–141.

[157] L. WIECHERT, *Computational modeling of multi-field and multi-scale phenomena in respiratory mechanics*, Ph.D. thesis, Technische Universität München (2011).

[158] L. WIECHERT, R. METZKE, W. WALL, *Modeling the mechanical behavior of lung tissue at the micro-level*, Journal of Engineering Mechanics **135** (2009) 434–438.

[159] M.F.O. WILMER W. NICHOLS, *McDonald's blood flow in arteries*, Hodder Arnold, 2005.

[160] T. WINKLER, J.G. VENEGAS, *Complex airway behavior and paradoxical responses to bronchoprovocation*, Journal of Applied Physiology **103** (2007) 655–663.

[161] J.R. WOMERSLEY, *Method for the calculation of velocity, rate of flow and viscous drag in arteries when the pressure gradient is known*, journal of Physiology **127** (1955) 553–563.

[162] G. XIA, M.H. TAWHAI, E.A. HOFFMAN, C.L. LIN, *Airway wall stiffening increases peak wall shear stress: a fluid-structure interaction study in rigid and compliant airways*, Annals of Biomedical Engineering **38** (2010) 1836–1853.

[163] N. XIAO, J. ALASTRUEY, C. ALBERTO FIGUEROA, *A systematic comparison between 1-D and 3-D hemodynamics in compliant arterial models*, International Journal for Numerical Methods in Biomedical Engineering **30** (2014) 2040–7947.

[164] Y. YIN, J. CHOI, E.A. HOFFMAN, M.H. TAWHAI, C.L. LIN, *Simulation of pulmonary air flow with a subject-specific boundary condition*, Journal of Biomechanics **43** (2010) 2159–2163.

[165] Z. ZHANG, C. KLEINSTREUER, *Species heat and mass transfer in a human upper airway model*, International Journal of Heat and Mass Transfer **46** (2003) 4755–4768.

[166] Z. ZHANG, C.Z. KLEINSTREUER, *Transient airflow structures and particle transport in a sequentially branching lung airway model*, Physics of Fluids **14** (2002) 862–880.

[167] Z. ZHANG, C.Z. KLEINSTREUER, *Airflow structures and nano-particle deposition in a human upper airway model*, Journal of Computational Physics **198** (2004) 178–210.

Curriculum Vitae

Personal Information

First Name: Mahmoud
Family Name: Ismail
Date of Birth: 10th February 1986, Dalhoun (Lebanon)

Education

2008-2014	**PhD in Mechanical Engineering**, *Technische Universität München*, Munich (Germany)
2007-2008	**M.Sc. with Honours in Computational Mechanics**, *Elite Network of Bavaria*, Munich/Erlangen (Germany)
2006-2008	**M.Sc. in Computational Mechanics**, *Technische Universität München*, Munich (Germany)
2003-2006	**B.Sc. in Mechatronics Engineering**, *Hariri Canadian University*, Mechref (Lebanon)
2003	**Lebanese Baccalaureate in Life Sciences**, *Iman High School*, Baakleen (Lebanon)

Working Experience

2008-2014	**Research and Teaching Assistant**, *Institute for Computational Mechanics, TUM*, Munich (Germany)
2007-2008	**Student Research Assistant**, *Technische Universität München*, Munich (Germany): - LabView Programmer, Institute for Machine Elements - Lab Tutor, Chair for Structural Dynamics - C++ Program, Chair for Computation in Engineering
2004-2006	**Teacher Assistant and Lab Tutor**, *Institute for Mechatronics, HCU*, Mechref (Lebanon)
2005	**Mechatronics Trainee**, *YL-e GmbH*, Beirut (Lebanon)

Reports of the Institute for Computational Mechanics, TUM

19 (2014) Mahmoud Ismail:
Reduced dimensional modeling of the entire human lung.

18 (2013) Florian Henke:
An extended finite element method for turbulent premixed combustion.

17 (2012) Markus Gitterle:
A dual mortar formulation for finite deformation frictional contact problems including wear and thermal coupling.

16 (2012) Andreas Maier:
Computational modeling of rupture risk in abdominal aortic aneurysms.

15 (2012) Georg Bauer:
A coupled finite element approach for electrochemical systems.

14 (2012) Alexander Popp:
Mortar methods for computational contact mechanics and general interface problems.

13 (2012) Thomas Klöppel:
A finite element model for the human red blood cell.

12 (2012) Sophie Rausch:
Computational and experimental modeling of lung parenchyma.

11 (2011) Christian Cyron:
Micromechanical continuum approach for the analysis of biopolymer networks.

10 (2011) Lena Wiechert:
Computational modeling of multi-field and multi-scale phenomena in respiratory mechanics.

9 (2010) Peter Gamnitzer:
Residual-based variational multiscale methods for turbulent flows and fluid-structure interaction.

8 (2010) Axel Gerstenberger:
An XFEM based fixed grid approach to fluid-structure interaction.

7 (2009) **Ulrich Küttler:**
Effiziente Lösungsverfahren für Fluid-Struktur-Interaktions-Probleme.

6 (2009) **Moritz Frenzel:**
Advanced structural finite element modeling of arterial walls for patient-specific geometries.

5 (2007)* **Christiane Förster:**
Robust methods for fluid-structure interaction with stabilised finite elements.

4 (2004)* **Tobias Erhart:**
Strategien zur Numerischen Modellierung transienter Impaktvorgänge bei nichtlinearem Materialverhalten.

3 (2004)* **Michael Gee:**
Effiziente Lösungsstrategien in der nichtlinearen Schalenmechanik.

2 (2003)* **Volker Gravemeier:**
The variational multiscale method for laminar and turbulent incompressible flow.

1 (2001)* **Daniel Mok:**
Partitionierte Lösungsverfahren in der Strukturdynamik und der Fluid-Struktur-Interaktion.

---

[*] This dissertation was supervised by Prof. Dr.-Ing. Wolfgang A. Wall at the Institute for Structural Mechanics at the University of Stuttgart and is published in the respective report series.